



Study of charmless $B^0_{d,s} \rightarrow h+h'-\pi^0$ decays in LHCb

Diego Alejandro Roa Romero

► To cite this version:

Diego Alejandro Roa Romero. Study of charmless $B^0_{d,s} \rightarrow h+h'-\pi^0$ decays in LHCb. Other [cond-mat.other]. Université Blaise Pascal - Clermont-Ferrand II, 2013. English. NNT : 2013CLF22355 . tel-00872114

HAL Id: tel-00872114

<https://theses.hal.science/tel-00872114>

Submitted on 11 Oct 2013

HAL is a multi-disciplinary open access archive for the deposit and dissemination of scientific research documents, whether they are published or not. The documents may come from teaching and research institutions in France or abroad, or from public or private research centers.

L'archive ouverte pluridisciplinaire **HAL**, est destinée au dépôt et à la diffusion de documents scientifiques de niveau recherche, publiés ou non, émanant des établissements d'enseignement et de recherche français ou étrangers, des laboratoires publics ou privés.

UNIVERSITÉ BLAISE PASCAL
U.F.R. Sciences et Technologies

ÉCOLE DOCTORALE DES SCIENCES FONDAMENTALES
N° 749

THÈSE

présentée pour obtenir le grade de

Docteur d'Université
SPÉCIALITÉ : PHYSIQUE DES PARTICULES

par

Diego Alejandro Roa Romero

Study of charmless $B_{d,s}^0 \rightarrow h^+ h'^- \pi^0$ decays in LHCb

Soutenue publiquement le 24 mai 2013, devant la commission d'examen :

Président :	Alain FALVARD	
Examineurs :	Frédéric BLANC	
	Régis LEFÈVRE	
	Jussara MIRANDA	Rapporteur
	José OCARIZ	Rapporteur
	Pascal PERRET	

Acknowledgements

This work has been made with the participation of several people. First of all, I want to thank my supervisor, Régis Lefèvre. He not only helped me with the development of this thesis work but also took care of me when I just arrived in France with total generosity. Many thanks!

Then I want to thank my thesis director, Pascal Perret, who gave me the opportunity to come to work in France and have the chance to make what I like with a wonderful group of people.

Thanks to the members of the jury. First to Jussara Miranda who flew from Brazil to Clermont-Ferrand to attend my thesis presentation. To Frédéric Blanc for the interest he has in this work as demonstrated by his smart questions and suggestions. Special thanks to José Ocariz. I am happy this thesis bring him back to the time he worked on BaBar. His comments made me think and learn many things about the physics of the Standard Model.

Thanks to the people of the Laboratoire de Physique Corpusculaire de Clermont-Ferrand, starting from Alain Falvard, director of the laboratory and president of the thesis jury. Through his help, I received special support from the laboratory during the last part of my thesis.

Thanks to the people of the LHCb team at the laboratory, Olivier Deschamps, Stéphane Monteil, Valentin Niess, Eric Cogneras, Hervé Chanal, Ziad Ajaltouni, Luigi Li Gioi and Marc Grabalosa. Their support on all kind of problems, from physics to everyday life, was of great help. Thanks also to the students of the team, Marwa Jahjah, Krzysztof Sobczak, Mostapha Hoballa and Marouen Baalouch, we were always happy to help each other.

I made many friends at the laboratory and in Clermont-Ferrand. Patricio Cenicerros the best friend here and witness of the most difficult times of the thesis. Reina Camacho Toro and Daniela Paredes, we shared very good times. I remember the lunches we spent talking about Latin American politics. Mónica Cardona, Mónica Huertas, Jazmin Porras and Geoffrey

Gilles, my very good friends in Clermont-Ferrand. There were also people special to me with who I shared unique moments those last years, Michelle Luise Nicol and Karen Nicol. I am also very grateful to my old friends, Gustavo Orozco, Tatiana Gonzáles, Luz Stella Gómez, Luisa Fernanda Trujillo, Edna Carolina Suárez and Maria Elena Gavilán, because they are always ready to listen to me and give me their advices.

Finally, thanks to my family. To my sisters, Angela Marcela and Zulima Consuelo, and brother, César. I know I always can count on you. To my parents, Luis Eduardo and Aura, you are my principal motivation and I am so happy that you are here to share with you this achievement.

A todos ustedes muchas gracias.

Abstract

This thesis work is about the identification of charmless three-body decays of neutral B mesons with a π^0 in the final state ($B_{d,s}^0 \rightarrow h^+ h'^- \pi^0$) through the analysis of a 1.0 fb^{-1} data sample collected in 2011 by the LHCb experiment at the LHC. Those modes are sensitive to CKM parameters and allow to test Standard Model predictions related to CP violation. Some of them, such as $B_s^0 \rightarrow K^- \pi^+ \pi^0$ and $B_s^0 \rightarrow K^+ K^- \pi^0$, have not been observed previously.

This is the first analysis with energetic π^0 in LHCb. To evaluate the detector performance for π^0 , $D^{*+} \rightarrow D^0(\rightarrow K^- \pi^+ \pi^0) \pi^+$ decays have been selected. This provides a clean and high statistics sample of neutral pions used to study their energy calibration as well as the effectiveness of the π^0/γ separation tool of the experiment. Radiative decays are indeed the most dangerous backgrounds for the study of $B_{d,s}^0 \rightarrow h^+ h'^- \pi^0$ modes.

To select $B_{d,s}^0 \rightarrow h^+ h'^- \pi^0$ events, a dedicated trigger algorithm has been implemented. It complements the standard online selections and significantly improves the efficiency. Offline, obvious backgrounds, mainly from charm decays, are rejected applying simple criteria. The sample is then further purified using a multivariate classifier. At last, information from the ring imaging Cherenkov detectors allows to separate $\pi^+ \pi^- \pi^0$, $K^\pm \pi^\mp \pi^0$ and $K^+ K^- \pi^0$ final states.

A simultaneous fit of the reconstructed B mass spectra in the three subsamples is used to extract the signal yields. It accounts for the different backgrounds remaining as well as for the signal crossfeeds from one subsample to the other. The $B^0 \rightarrow \pi^+ \pi^- \pi^0$, $B^0 \rightarrow K^+ \pi^- \pi^0$ and $B_s^0 \rightarrow K^+ K^- \pi^0$ contributions are clearly established. This is the first observation of the $B_s^0 \rightarrow K^+ K^- \pi^0$ decay mode.

Keywords : LHCb experiment, CKM matrix, CP violation, flavour physics, charmless B decays, energetic π^0 .

Résumé

Ce travail de thèse porte sur l'identification des désintégrations sans charme de mésons beaux neutres en trois corps dont un π^0 ($B_{d,s}^0 \rightarrow h^+ h'^- \pi^0$) en analysant l'échantillon de données de 1.0 fb^{-1} collecté en 2011 par l'expérience LHCb au LHC. Ces modes sont sensibles aux paramètres de la matrice CKM et permettent de tester certaines prédictions du Modèle Standard liées à la violation de CP. Plusieurs d'entre eux, tels que $B_s^0 \rightarrow K^- \pi^+ \pi^0$ et $B_s^0 \rightarrow K^+ K^- \pi^0$, n'ont pas été observés précédemment.

Il s'agit de la première analyse avec des π^0 énergétiques dans LHCb. Pour évaluer les performances du détecteur relatives au π^0 , des désintégrations $D^{*+} \rightarrow D^0 (\rightarrow K^- \pi^+ \pi^0) \pi^+$ ont été sélectionnées. Un échantillon de pions neutres relativement pur et de grande statistique a ainsi pu être extrait. Il est utilisé pour étudier leur étalonnage en énergie ainsi que l'efficacité de l'outil de séparation π^0/γ de l'expérience. Les désintégrations radiatives constituent en effet le bruit de fond le plus dangereux pour l'étude des modes $B_{d,s}^0 \rightarrow h^+ h'^- \pi^0$.

Pour sélectionner les événements $B_{d,s}^0 \rightarrow h^+ h'^- \pi^0$, un algorithme dédié a été mis en place au niveau du système de déclenchement. Il complète les sélections en ligne standards et permet d'augmenter significativement l'efficacité. Sur les événements enregistrés, les bruits de fond évidents, issus principalement de désintégrations de mésons charmés, sont rejetés en appliquant des critères simples. L'échantillon est alors purifié davantage en utilisant une analyse multivariée. Enfin, les informations des détecteurs Cherenkov permettent de séparer les états finals $\pi^+ \pi^- \pi^0$, $K^\pm \pi^\mp \pi^0$ et $K^+ K^- \pi^0$.

Un ajustement simultané des spectres de masse reconstruite du méson beau dans les trois sous-échantillons est utilisé pour extraire les nombres d'événements de signal. Il tient compte des différents bruits de fond restants ainsi que des migrations du signal d'un sous-échantillon à l'autre. Les contributions des modes $B^0 \rightarrow \pi^+ \pi^- \pi^0$, $B^0 \rightarrow K^+ \pi^- \pi^0$ et $B_s^0 \rightarrow K^+ K^- \pi^0$ sont clairement établies. Il s'agit de la première observation du mode de désintégration $B_s^0 \rightarrow K^+ K^- \pi^0$.

Mots clefs : expérience LHCb, matrice CKM, violation de CP, physique des saveurs, désintégration sans charme des mésons beaux, π^0 énergétiques.

Contents

Acknowledgements

Abstract

Résumé

Introduction	1
1 The CKM Matrix and the unitarity triangle	3
1.1 The Standard Model of Fundamental Particles	3
1.2 Quark mixing and CKM Matrix	5
1.3 Representations of the CKM Matrix	6
1.4 Modules of the CKM matrix elements	8
1.4.1 $ V_{ud} $	8
1.4.2 $ V_{us} $	8
1.4.3 $ V_{cd} $	8
1.4.4 $ V_{cs} $	8
1.4.5 $ V_{cb} $	9
1.4.6 $ V_{ub} $	9
1.4.7 $ V_{td} $ and $ V_{ts} $	9
1.4.8 $ V_{tb} $	10
1.5 Unitarity Triangle	10
1.5.1 α angle	11
1.5.2 β angle	12
1.5.3 γ angle	12
1.6 CKM global fit in the Standard Model	12
2 Charmless three body decays of B mesons	15
2.1 Measurement of α	15
2.1.1 α from $B \rightarrow \pi\pi$ and $B \rightarrow \rho\rho$ decays	16

2.1.2	α from $B^0 \rightarrow \pi^+\pi^-\pi^0$ decays	18
2.1.3	α from $B^0 \rightarrow K^+\pi^-\pi^0$ decays	21
2.2	γ from $B_s^0 \rightarrow K^-\pi^+\pi^0$ decays	24
2.3	Other charmless three body decays	25
2.3.1	$B_{d,s}^0 \rightarrow K^0 h^+ h'^-$	25
2.3.2	$B^0 \rightarrow K^- K^+ \pi^0$	26
2.3.3	$B_s^0 \rightarrow K^- K^+ \pi^0$	26
2.4	Radiative decays and specific backgrounds	27
2.5	Conclusion	27
3	The LHCb experiment	29
3.1	The LHC	29
3.2	The LHCb Experiment	30
3.2.1	VELO	34
3.2.2	Magnet	35
3.2.3	Tracking System	36
3.2.4	RICH detectors	38
3.2.5	Calorimeters	39
3.2.6	Muon Chambers	40
3.2.7	Trigger	41
3.3	The LHCb Software	44
3.4	Luminosity Measurements in LHCb	44
4	Particle identification	47
4.1	Charged particles identification	47
4.2	Photon Reconstruction	48
4.3	π^0 reconstruction	51
4.3.1	Resolved π^0	52
4.3.2	Merged π^0	53
4.4	$D^0 \rightarrow K^-\pi^+\pi^0$ study	53
4.4.1	Stripping	54
4.4.2	Monte Carlo results	54
4.4.3	$D^{*+} \rightarrow D^0 \pi^+$ selection	56
4.4.4	Results on data	57
4.4.5	π^0/γ discrimination	59
4.5	Summary	65
5	Selection of $B_{d,s}^0 \rightarrow h^+ h'^- \pi^0$ events	67
5.1	Introduction	67
5.1.1	Monte Carlo samples	67
5.1.2	Extraction of the expected yields	70

5.1.3	Selection strategy	71
5.2	Trigger selection	73
5.3	Stripping Selection	75
5.4	Final Selection	76
5.4.1	Tracks identification	77
5.4.2	Specific backgrounds peaking in the $m_{h+h'}$ spectra	78
5.4.3	Additional cuts	81
5.4.4	Preselection efficiency	84
5.4.5	Multivariate analysis	84
5.4.6	Radiative background	91
5.5	Summary	99
6	Estimation of the $B_{d/s}^0 \rightarrow h^+ h'^- \pi^0$ signal yields	101
6.1	Signal and background PDFs	101
6.1.1	Signal	102
6.1.2	Crossfeed	104
6.1.3	Partially reconstructed background	104
6.1.4	Combinatorial background	106
6.2	Fit Model	106
6.2.1	Parametrisation of the PDFs	109
6.2.2	Crossfeed Contributions	109
6.2.3	Free parameters	111
6.3	Optimization of the BDT cut	111
6.4	Unblinding the $K^+ K^- \pi^0$ signal region	117
6.5	Signal yields	120
6.5.1	Final fit	120
6.5.2	First observation of the $B_s^0 \rightarrow K^+ K^- \pi^0$ mode	123
6.5.3	Crossfeed contributions	125
6.5.4	Results	125
6.6	Dalitz distributions	126
6.7	Summary	128
	Conclusion	131
A	π^0 calibration from $D^0 \rightarrow K \pi \pi^0$ decays	133
B	Stripping Selection	137

Introduction

One of the main outcomes of relativistic quantum mechanics is the existence of antiparticles and antimatter. The CP violation phenomenon is the fact that particles and antiparticles have different behaviors. In the Standard Model of particle physics it is related with the electroweak charged currents, in particular how they couple to quark eigenstates. This is modelled by the CKM matrix. Measuring the parameters of the CKM matrix and checking that it gives a coherent description of the various CP violation phenomena is a very important test of the Standard Model.

Electroweak hadron decays stand as a source of information on CP violation. Decays of b-hadrons in particular can be used to measure parameters of the CKM matrix. The LHCb experiment at the Large Hadron Collider has been designed for high precision studies in the beauty and charm sectors. This covers not only CP violation but also indirect searches of new physics beyond the Standard Model.

In this work, the 1.0 fb^{-1} dataset collected by LHCb in 2011 is analysed to extract charmless three body decays of neutral b-mesons with π^0 in the final state. A dedicated selection is implemented. The sample is then divided in three different sub-samples corresponding to $\pi^+\pi^-\pi^0$, $K^\pm\pi^\mp\pi^0$ and $K^+K^-\pi^0$ final states. As $B^0 \rightarrow \pi^+\pi^-\pi^0$ decays can be used to measure the CKM angle α , a first motivation is to see how well those events can be selected. Another motivation is that decays such as $B_s^0 \rightarrow K^+K^-\pi^0$ have not been observed previously. A simultaneous fit of the reconstructed B mass spectra in the three samples is employed to estimate the various signal yields and to extract the corresponding Dalitz distributions.

Due to the interest in decays containing π^0 , a complementary work consisted in the extraction of a clean and high statistics sample of π^0 designing a selection dedicated to $D^*(2010)^+ \rightarrow D^0(\rightarrow K^-\pi^+\pi^0)\pi^+$ decays. This sample is used to check the π^0 energy calibration and to calibrate the π^0/γ discrimination in the experiment.

The thesis is organized as follows. The first chapter gives a short theoretical introduction on the quark mixing, the CKM matrix and the unitarity triangle. Chapter 2 discusses how

$B_{d/s}^0 \rightarrow h^+ h'^- \pi^0$ decays can be used to measure the angles α and γ of the unitarity triangle. In the third chapter, the LHC and the LHCb experiment are presented. Chapter 4 is organized around particle identification in LHCb. The selection of $D^{*+} \rightarrow D^0(\rightarrow K^- \pi^+ \pi^0) \pi^+$ decays is described together with the results on the π^0 energy calibration and the π^0/γ discrimination. Chapter 5 presents the selection of $B_{d/s}^0 \rightarrow h^+ h'^- \pi^0$ decays and the particle identification criteria used to form the $\pi^+ \pi^- \pi^0$, $K^\pm \pi^\mp \pi^0$ and $K^+ K^- \pi^0$ samples. Finally in chapter 6, the simultaneous fit implemented to analyze the data is described and the results are discussed in terms of yields and Dalitz plots.

CHAPTER 1

The CKM Matrix and the unitarity triangle

In this chapter, a brief review of the Standard Model of particle physics is proposed, introducing the quark-mixing phenomena and the need of the definition of the CKM matrix. Then the different representations of the CKM matrix are described and the properties related to its unitarity are studied. The unitarity triangle is finally defined and a short description of how the parameters of the CKM matrix are measured is given.

1.1 The Standard Model of Fundamental Particles

The Standard Model of particle physics is currently the best answer to the question of how the universe works at the microscopic level. It is possible to draw an analogy between the universe and a building. In order to build a house or even a simple wall, it is necessary to have bricks and cement to glue them together. In the case of fundamental particles, one can imagine that the role of bricks is played by fermions, and the role of glue is played by gauge bosons. In fact, fermions which are the constituents of matter interact through forces that are carried by gauge bosons [1].

Fermions, which are particles of spin 1/2, occur in two types, quarks and leptons. Leptons have integer electric charge and quarks have fractional charge. There are six quarks and leptons organized in three generations. The set of quarks can be represented as

$$\begin{pmatrix} u & c & t \\ d & s & b \end{pmatrix}, \quad (1.1)$$

where each column stands for one generation. The letters in the array refers to the quarks “up”, “down”, “charm”, “strange”, “top” and “bottom”. From that it is possible to name

all quarks of the upper row as the “up” type quarks and the ones of the lower row as the “down” type quarks. In the case of leptons the picture becomes

$$\begin{pmatrix} \nu_e & \nu_\mu & \nu_\tau \\ e & \mu & \tau \end{pmatrix}, \quad (1.2)$$

where in the lower row the electron, muon and tau are listed. The upper row refers to the corresponding electron, muon and tau neutrinos.

Three types of interaction are considered in the Standard Model: electromagnetic, strong and weak interactions. Gravity, expected to be negligible at the microscopic level, still remains beyond the model. All the fermions are sensitive to the weak interaction. Only quarks undergo the strong force. The electromagnetic interaction is perceived by all the particles except the neutrinos, which do not carry any electric charge and only interact through the weak interaction. Moreover the weak force acts only on the left-handed particles and the right-handed anti-particles following an SU(2) symmetry. According to this symmetry, the particles are organized in pairs or “doublets”. Each doublet defines the generations which are the columns of the arrays of the expressions 1.1 and 1.2. The right-handed particles and left-handed anti-particles are not affected by the weak interaction and are considered as singlets of the corresponding SU(2) symmetry.

There are different force carriers depending on the interaction. In the case of the electromagnetic force, the carrier is the photon, which is massless. For the strong force, there are eight gluons, also massless. Finally for the weak force, the carriers are the W^\pm and Z bosons, that are almost two orders of magnitude heavier than the proton. It has been shown that the electromagnetic and weak interactions can be unified in the so-called electroweak interaction. In this case, the W^\pm and Z bosons are massive while the photon is not. In order to obtain that result without affecting the fundamental symmetry of the interaction, it is necessary to apply a mechanism of spontaneous symmetry breaking including a scalar boson field: the Higgs field. In the Standard Model, the Higgs boson is responsible for the masses of the particles.

It has been mentioned that fermions are organized in doublets defined according to the way they participate in weak interaction: charged currents couple a charged lepton with its neutrino or an “up” type quark with its “down” type partner [2]. Charged currents are responsible of processes such as the pion decay $\pi^+ \rightarrow \mu^+ \nu_\mu$ ($\pi^- \rightarrow \mu^- \bar{\nu}_\mu$) as can be seen in the diagram of figure 1.1.

In this scheme, the weak interaction only couples particles of the same doublet. However, processes like the kaon decay, $K^+ \rightarrow \mu^+ \nu_\mu$ ($K^- \rightarrow \mu^- \bar{\nu}_\mu$), do not follow this rule. This decay processes through the same diagram as the one of figure 1.1 replacing the \bar{d} anti-quark by an

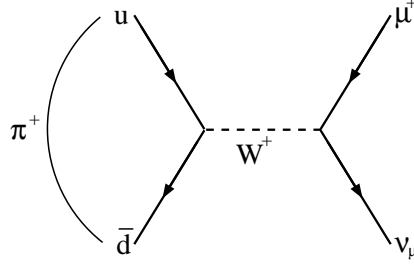


Figure 1.1: Tree-level Feynman diagram of the pion decay.

\bar{s} anti-quark leading to a $u\bar{s} \rightarrow W^+$ vertex. This is a signature of quark interactions beyond the doublets used to organize the three generations [3].

1.2 Quark mixing and CKM Matrix

The quark mixing comes from the fact that the quark states used to express the composition of hadrons (mass eigenstates) are not eigenstates of the weak interactions [4]. The starting point is the part of the quark lagrangian related to the Yukawa couplings of left-handed and right-handed quarks to the Higgs field:

$$\mathcal{L}_q^Y = -Y_U^{ij} \bar{Q}_{Li} \phi U_{Rj} - Y_D^{ij} \bar{Q}_{Li} \phi^* D_{Rj} + h.c. , \quad (1.3)$$

where ϕ is the Higgs field SU(2) doublet, $\bar{Q}_{Li} = (\bar{U}_{Li}, \bar{D}_{Li})$ are the left-handed quark field doublets, $U_{(D)R}$ are the right-handed quark field singlets, $Y_{U[D]}$ are 3×3 complex matrices, and the i and j indices denote the generation (i and j go from 1 to 3). Once the Higgs field acquires a vacuum expectation value v , mass terms arise:

$$\mathcal{L}_q^Y = -\frac{Y_U^{ij}}{\sqrt{2}} v \bar{U}_{Li} U_{Rj} - \frac{Y_D^{ij}}{\sqrt{2}} v \bar{D}_{Li} D_{Rj} + h.c. . \quad (1.4)$$

This expression defines the mass matrices $\mathcal{M}_{U[D]} = -Y_{U[D]}^{ij} v / \sqrt{2}$. All this has been done in the weak interaction basis, where $U_{Li}, D_{Li}, U_{Ri}, D_{Ri}$ are eigenstates. In this basis the $\mathcal{M}_{U[D]}$ matrices are not diagonal. It is possible to diagonalize them using unitary matrices $T_{L,U}, T_{R,U}, T_{L,D}, T_{R,D}$:

$$\mathcal{M}_{U[D]}^{diag} = T_{L,U[D]} \mathcal{M}_{U[D]} T_{R,U[D]}^\dagger . \quad (1.5)$$

One can then introduce $U_{R[L]}^m$ and $D_{R[L]}^m$, the mass eigenstates, as

$$U_{R[L]}^m = T_{R[L],U} U_R, \quad D_{R[L]}^m = T_{R[L],D} D_R . \quad (1.6)$$

This transformation of the quark fields leaves unchanged the electromagnetic and neutral weak currents: at first order, there is no Flavour Changing Neutral Currents (FCNC). This is not the case for charged currents:

$$\bar{U}_L \gamma^\mu D_L = \bar{U}_L^m T_{L,U} \gamma^\mu T_{L,D}^\dagger D_L^m . \quad (1.7)$$

In this equation the product of two unitary matrices appears, defining $V = T_{L,U} T_{L,D}^\dagger$. This matrix is the Cabibbo-Kobayashi-Maskawa (CKM) matrix. In the Standard Model, quark mixing is fully described by the CKM matrix.

The CKM matrix is the source of CP violation in the Standard Model. This fact arises from the CP transformations of the part of the lagrangian related to weak charged currents (for any quark field ψ):

$$\mathbf{CP} \mathcal{L}_q^W = \mathbf{CP} \frac{g}{\sqrt{2}} \bar{\psi}_i V_{ij} (1 - \gamma^5) \gamma^\mu \psi_j W_\mu^+ + \mathbf{CP} \frac{g}{\sqrt{2}} \bar{\psi}_i V_{ij}^* (1 - \gamma^5) \gamma^\mu \psi_j W_\mu^- . \quad (1.8)$$

No CP violation would require the first term of 1.8 to be transformed in the second and vice versa, this is not the case as the factor V_{ij} is complex [5]: V_{ij}^* is not equal to V_{ij} .

1.3 Representations of the CKM Matrix

In the most general representation form, the CKM matrix can be written as

$$V_{CKM} = \begin{pmatrix} V_{ud} & V_{us} & V_{ub} \\ V_{cd} & V_{cs} & V_{cb} \\ V_{td} & V_{ts} & V_{tb} \end{pmatrix} . \quad (1.9)$$

A complex $n \times n$ matrix has $2n^2$ real parameters. Unitarity implies that only n^2 are independent. In addition, the phases of the up and down types quark fields can be rotated freely, by transformations such as $\psi \rightarrow e^{i\phi} \psi$. It implies that the CKM matrix can be multiplied by diagonal matrices containing phases only in the diagonal as the overall phase is irrelevant. $2n - 1$ relative phases can be removed this way. This means there are only $(n - 1)^2$ independent physical parameters. Orthogonal transformation matrices contain $\frac{1}{2}n(n - 1)$ real parameters which are rotation angles. The number of complex phases in the matrix is then

$$(n - 1)^2 - \frac{1}{2}n(n - 1) = \frac{1}{2}(n - 2)(n - 1) . \quad (1.10)$$

In the case of two generations ($n = 2$) there is only one rotation angle and no complex phase, so no CP violation. In the case of three generations, there are three rotation angles and one complex phase. This is the case of the CKM matrix and the complex phase is the source of

CP violation in the quark sector of the Standard Model.

With three rotation angles θ_{12} , θ_{13} , θ_{23} and a complex phase δ_{13} , the CKM matrix can be represented as [6]

$$V_{CKM} = \begin{pmatrix} c_{12}c_{13} & s_{12}c_{13} & s_{13}e^{-i\delta_{13}} \\ -s_{12}c_{23} - c_{12}s_{23}s_{13}e^{i\delta_{13}} & c_{12}c_{23} - s_{12}s_{23}s_{13}e^{i\delta_{13}} & s_{23}c_{13} \\ s_{12}s_{23} - c_{12}c_{23}s_{13}e^{i\delta_{13}} & -c_{12}s_{23} - s_{12}c_{23}s_{13}e^{i\delta_{13}} & c_{23}c_{13} \end{pmatrix},$$

with $c_{ij} = \cos\theta_{ij}$ and $s_{ij} = \sin\theta_{ij}$ ($i, j = 1, 2, 3$).

An earlier model about quark mixing was developed by Cabbibo [3]. It was a two generation scheme and the main parameter was λ , which is the sinus of the Cabbibo mixing angle

$$\lambda = 0.22. \quad (1.11)$$

As done by Wolfenstein [7], the CKM matrix can be developed in powers of λ . With respect to the standard parametrization, it is possible to do so introducing three new parameters, A , ρ and η , defined according to the following expressions:

$$\begin{aligned} s_{23} &= A\lambda^2, \\ s_{13}e^{-i\delta_{13}} &= A\lambda^3(\rho - i\eta). \end{aligned} \quad (1.12)$$

One then obtains the following representation valid up to $\mathcal{O}(\lambda^6)$ [8]:

$$V_{CKM} = \begin{pmatrix} 1 - \frac{1}{2}\lambda^2 - \frac{\lambda^4}{8} & \lambda & A\lambda^3(\rho - i\eta) \\ -\lambda + \frac{A^2\lambda^5}{2}(1 - 2\rho) - iA^2\lambda^5\eta & 1 - \frac{1}{2}\lambda^2 - \lambda^4(\frac{1}{8} + \frac{A^2}{2}) & A\lambda^2 \\ A\lambda^3(1 - (1 - \frac{\lambda^2}{2})(\rho - i\eta)) & -A\lambda^2(1 - \frac{\lambda^2}{2})(1 + \lambda^2(\rho + i\eta)) & 1 - \frac{A^2\lambda^4}{2} \end{pmatrix}. \quad (1.13)$$

It can be noticed that the flavour transitions between quarks have a hierarchy depending on the value of the matrix element. Diagonal elements of the CKM matrix have the largest modules and correspond to the coupling of quarks of the same doublet. CP violation depends of the value of η (the CKM matrix is real for $\eta = 0$). In expression 1.13, η is multiplied at least by a factor λ^3 , reducing CP violation effects in quark processes. In the Standard Model it can be shown that CP violation effects are proportional to $F_u F_d J$ where

$$\begin{aligned} F_u &= (m_u^2 - m_c^2)(m_c^2 - m_t^2)(m_t^2 - m_u^2), \\ F_d &= (m_d^2 - m_s^2)(m_s^2 - m_b^2)(m_b^2 - m_d^2), \\ J &= \text{Im}[V_{us}V_{cd}V_{cs}^*V_{ub}^*] = c_{12}c_{23}c_{13}^2s_{12}s_{13}s_{23}\sin\delta_{13} = A^2\lambda^6\eta. \end{aligned}$$

J is known as the Jarlskog invariant [9].

1.4 Modules of the CKM matrix elements

In order to determine the values of the CKM matrix elements, accurate measurements have been performed as discussed below.

1.4.1 $|V_{ud}|$

Superallowed transitions are β transitions between two members of an isospin multiplet [10]. The value of $|V_{ud}|$ has been obtained from superallowed nuclear, neutron, and pion decays. Currently, the most precise determination of $|V_{ud}|$ comes from superallowed nuclear β decays. The most recent analysis gives a weighted average of [11]

$$|V_{ud}| = 0.97425 \pm 0.00022 . \quad (1.14)$$

1.4.2 $|V_{us}|$

$|V_{us}|$ may be determined from kaon decays such as $K_S^0 \rightarrow \pi^\pm e^\mp \nu$, $K_L^0 \rightarrow \pi^\pm e^\mp \nu$, $K_L^0 \rightarrow \pi^\pm \mu^\mp \nu$, $K^\pm \rightarrow \pi^0 e^\pm \nu$ and $K^\pm \rightarrow \pi^0 \mu^\pm \nu$. Results from the various decays are consistent. $|V_{us}|$ can also be evaluated from the ratio $|V_{us}|/|V_{ud}|$ obtained from $K^\pm \rightarrow \mu^\pm \nu(\gamma)$ and $\pi^\pm \rightarrow \mu^\pm \nu(\gamma)$ decays where (γ) indicates that radiative decays are included. Combined with lattice QCD calculations of the corresponding form factor [12] or ratio of decay constants [13], respectively, the two methods allow to extract $|V_{us}|$ with similar precision. The two determinations are compatible and their average is [14]

$$|V_{us}| = \lambda = 0.2252 \pm 0.0009 . \quad (1.15)$$

1.4.3 $|V_{cd}|$

There are two ways to measure this element. The first one is to use charm semileptonic decays such as $D^0 \rightarrow \pi^- l^+ \nu$. In this case the precision on the extraction of $|V_{cd}|$ is however limited by the uncertainties on the corresponding form factor given by lattice QCD calculations. The other and more precise possibility is to use di-muon production in deep inelastic scattering of neutrinos and anti-neutrinos beams on nucleons. This production is proportional to the charm cross section off valence d-quarks, i.e. $|V_{cd}|^2$, times the average semileptonic branching fraction of charm mesons. The average value extracted this way is [15, 16]

$$|V_{cd}| = 0.230 \pm 0.011 . \quad (1.16)$$

1.4.4 $|V_{cs}|$

As for $|V_{cd}|$, neutrino and anti-neutrino scattering on nucleons can be used but the extraction of $|V_{cs}|$ is affected by the large uncertainty on the s-quark sea content. The direct measurement comes from semileptonic D^0 or leptonic D_s^\pm decays. Lattice QCD calculations provide

the semileptonic D^0 form factor and the D_s^\pm decay constant. The extraction of $|V_{cs}|$ from semileptonic decays is compatible with the one from leptonic decays but much less precise because of the large uncertainty on the form factor. The combination of the two is [6]

$$|V_{cs}| = 1.006 \pm 0.023 . \quad (1.17)$$

1.4.5 $|V_{cb}|$

$|V_{cb}|$ is obtained from semileptonic B decays into charm. Inclusive and exclusive determinations give compatible results with similar uncertainties. The combination is [6]

$$|V_{cb}| = (40.9 \pm 1.1) \times 10^{-3} . \quad (1.18)$$

1.4.6 $|V_{ub}|$

This value can also be obtained from inclusive semi-leptonic decays of B mesons of the type $B \rightarrow X_u l \bar{\nu}$. The extraction is however complicated by the large background of $B \rightarrow X_c l \bar{\nu}$. It is possible to perform the measurements in kinematic regions where the charm background is forbidden. However in such region there is a non perturbative contribution from the motion of the b quark inside the B meson. This is considered within the so-called shape function, which can be extracted at leading order of Λ_{QCD}/m_b ¹ from the photon energy spectrum in $B \rightarrow X_s \gamma$. The extraction of $|V_{ub}|$ from exclusive channels is less precise because the form factors are more complicated to calculate. Inclusive and exclusive determinations of $|V_{ub}|$ are marginally compatible (at the 3σ level). A combination of the two gives [6]

$$|V_{ub}| = (4.15 \pm 0.49) \times 10^{-3} . \quad (1.19)$$

1.4.7 $|V_{td}|$ and $|V_{ts}|$

Those parameters are not accessible from tree-level decays of the top quark as the top quark is experimentally selected using t to b transitions. Their determination is performed using $B - \bar{B}$ oscillations, which are mediated by box diagrams with a dominant top quark contribution. The precision is limited by uncertainties on hadronic effects determined for lattice QCD. The current determinations are [6]

$$|V_{td}| = (8.4 \pm 0.6) \times 10^{-3} \text{ and } |V_{ts}| = (42.9 \pm 2.6) \times 10^{-3} . \quad (1.20)$$

¹In QCD the asymptotic freedom is a consequence of the non-Abelian nature of the theory. The QCD coupling constant $\alpha_s(Q)$ which is function of the transferred momentum Q is small for high values of Q : $\alpha_s(Q) \rightarrow 0$ as $Q \rightarrow \infty$. Thus, perturbation theory can be safely used for large Q . In perturbative theory, Λ_{QCD} is the scale at which $\alpha_s(Q)$ diverges: $\alpha_s(Q) \rightarrow \infty$ as $Q \rightarrow \Lambda_{QCD}$. It then sets the scale for which $\alpha_s(Q)$ becomes large and perturbative QCD irrelevant. Λ_{QCD} is of the order of 200 MeV. Here this has to be compared to the b quark mass m_b , about $4.8 \text{ GeV}/c^2$ for the pole mass.

1.4.8 $|V_{tb}|$

The usual determination of this parameter assumes unitarity of the CKM matrix and uses the ratio of the branching fractions

$$R = \frac{\mathcal{B}(t \rightarrow Wb)}{\mathcal{B}(t \rightarrow Wq)} = \frac{|V_{tb}|^2}{\sum_q |V_{tq}|^2} \quad q = b, s, d . \quad (1.21)$$

Unitarity implies that this ratio is equal to $|V_{tb}|^2$. The most recent measurement gives $|V_{tb}| > 0.92$ at 95% confidence level [17]. The direct determination of $|V_{tb}|$ without assuming unitarity is possible using single top production. The average value is [6]

$$|V_{tb}| = 0.89 \pm 0.07 . \quad (1.22)$$

1.5 Unitarity Triangle

The CKM matrix is unitary by definition. This property implies some interesting relations among its elements:

$$\sum_j V_{ij} V_{jk} = \delta_{ik} \quad i, k = 1, 2, 3 . \quad (1.23)$$

This corresponds to nine relations. With respect to CP violation, the interesting relations are the ones for which $i \neq k$ ($\delta_{ik}=0$). Since the V_{ij} elements are complex numbers, it is possible to draw a geometrical representation of those relations on the complex plane leading to triangles. All the triangles have the same area but different forms. This area is equal to $J/2$ (where J is, as previously mentioned, the Jarlskog invariant). One may notice here that no CP violation would mean flat triangles.

Among the six triangles associated to CP violation, two of them have two sides of length $\sim \mathcal{O}(\lambda)$ and one side of length $\sim \mathcal{O}(\lambda^5)$. Two others have two sides of the order λ^2 and one of the order λ^4 [4]. Finally the last two have all three sides of the same order $\sim \mathcal{O}(\lambda^3)$. The formulas related with those triangles are

$$V_{td}V_{ud}^* + V_{ts}V_{us}^* + V_{tb}V_{ub}^* = \delta_{ut} = 0 , \quad (1.24)$$

$$V_{ud}V_{ub}^* + V_{cd}V_{cb}^* + V_{td}V_{tb}^* = \delta_{db} = 0 . \quad (1.25)$$

Those triangles are associated with B meson physics. Their angles are relatively large, meaning large asymmetries in some B decays. The triangle of equation 1.25 is the most commonly used.

Using the parametrization of equation 1.13 and dividing equation 1.25 by $V_{cd}V_{cb}^*$, the triangle has its apices at $z = 0$, $z = 1$ and $z = \bar{\rho} + i\bar{\eta}$ with:

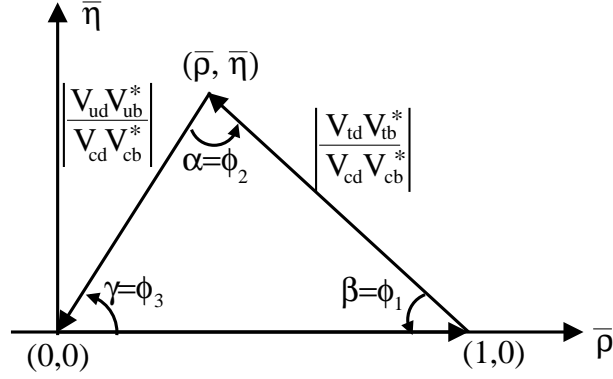


Figure 1.2: Unitary triangle of the CKM matrix.

$$\bar{\rho} = \rho \left(1 - \frac{\lambda^2}{2}\right), \quad (1.26)$$

$$\bar{\eta} = \eta \left(1 - \frac{\lambda^2}{2}\right). \quad (1.27)$$

Figure 1.2 shows the unitary triangle in the complex plane $\bar{\rho} - \bar{\eta}$. The internal angles of the unitary triangle are denoted by α , β and γ :

$$\alpha = \arg \left(-\frac{V_{td} V_{tb}^*}{V_{ud} V_{ub}^*} \right), \quad (1.28)$$

$$\beta = \arg \left(-\frac{V_{cd} V_{cb}^*}{V_{td} V_{tb}^*} \right), \quad (1.29)$$

$$\gamma = \arg \left(-\frac{V_{ud} V_{ub}^*}{V_{cd} V_{cb}^*} \right). \quad (1.30)$$

The present status of the measurements of those angles is discussed in the following paragraphs.

1.5.1 α angle

As presented in the next chapter, the measurements of α come from $B \rightarrow \pi\pi$, $B \rightarrow \rho\pi$ and $B \rightarrow \rho\rho$ decay channels. α is extracted thanks to isospin analyses of the SU(2) related modes ($B^0 \rightarrow h^+ h'^-$, $B^0 \rightarrow h^0 h'^0$ and $B^+ \rightarrow h^+ h'^0$ with $h^{(\prime)} = \rho$ or π). In the case of $B \rightarrow \pi\pi$ and $B \rightarrow \rho\rho$, α is obtained with an eight fold ambiguity between 0 and π . On the other hand, a full Dalitz analysis of the $B \rightarrow \rho\pi$ mode allows a theoretically clean and ambiguity free

determination of α . The $B \rightarrow \rho\pi$ analysis is experimentally more difficult but has already been applied on BaBar and Belle data: the combinations of those results gives $\alpha = (120_{-7}^{+11})^\circ$. Combining the three decay channels α is measured as [18]

$$\alpha = (88.7_{-4.2}^{+4.6})^\circ . \quad (1.31)$$

1.5.2 β angle

$\sin 2\beta$ is extracted from the time-dependent CP asymmetry of B^0 - \bar{B}^0 decays to a common final state. The cleanest channels are $b \rightarrow c\bar{c}s$ decays to CP eigenstates such as $B^0 \rightarrow J/\psi K_{S,L}$. BaBar and Belle performed precise measurements of $\sin 2\beta$. The world average is [6]

$$\sin 2\beta = 0.679 \pm 0.020 . \quad (1.32)$$

This measurement can also be done with penguin dominated $b \rightarrow sq\bar{q}$ decays such as $B^0 \rightarrow \phi K^0$ or $B^0 \rightarrow \eta' K^0$. Those modes have the same phase as $b \rightarrow c\bar{c}s$ ones up to corrections suppressed by λ^2 . Therefore, the main interest in these modes is not to measure $\sin 2\beta$ but to check the consistency of the Standard Model. Deviations from the measurement in $b \rightarrow c\bar{c}s$ modes would be an indication of new physics.

1.5.3 γ angle

Unlike α and β , γ is not expected to be affected by physics beyond the Standard Model as it is related to tree level diagrams. γ is extracted from the interference of $b \rightarrow c\bar{u}s$ and $b \rightarrow c\bar{c}s$ transitions in $B^\pm \rightarrow D^0(\bar{D}^0)K^\pm$ modes leading to final states accessible both through D^0 and \bar{D}^0 decays. Three methods are used. The GLW one [19, 20] considers D^0 decays to CP eigenstates such as $\pi^+\pi^-$. The ADS method [21] considers the interferences between Cabibbo-allowed \bar{D}^0 and doubly-Cabibbo-suppressed D^0 decays: $\bar{D}^0 \rightarrow K^+\pi^-$ and $D^0 \rightarrow K^+\pi^-$ for instance. The last method and more precise to date considers three-body decays of the D^0/\bar{D}^0 , such as $K_S^0\pi^+\pi^-$, and extracts the interference from the Dalitz plot [22, 23]. Combining the results obtained with these three methods, the world average is [6]

$$\gamma = (68_{-11}^{+10})^\circ . \quad (1.33)$$

1.6 CKM global fit in the Standard Model

We have seen that in the Standard Model, the CKM matrix results from the Yukawa couplings of quarks with the Higgs field as a consequence of the electroweak spontaneous symmetry breaking mechanism. Precise measurements of the CKM parameters are then crucial. Indeed, checking the coherence of the various measurements constitutes a major test of the Standard Model.

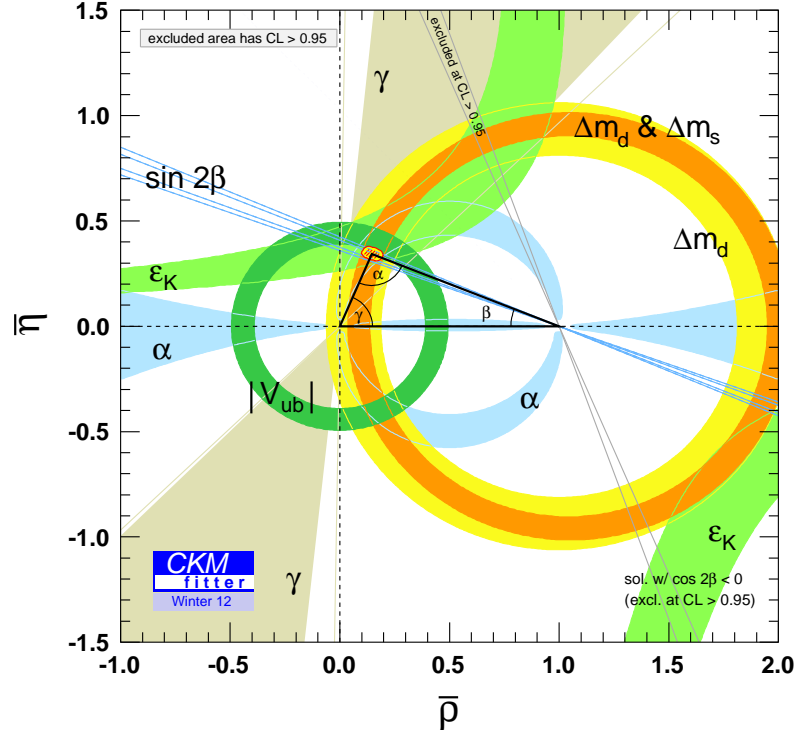
Figure 1.3: Constraints on the $\bar{\rho} - \bar{\eta}$ plane.

Figure 1.3 shows the state of art of the combination of the various constraints on the apex of the unitarity triangle in the $\bar{\rho} - \bar{\eta}$ plane [18]. A first set of constraints comes from the angles α , β and γ . The lengths of the sides of the triangle are also constrained: one is related to $|V_{ub}|$, the other to Δm_d (and Δm_s) the mass difference between the two mass eigenstates which determines the oscillation frequencies of the $B_d^0 - \bar{B}_d^0$ ($B_s^0 - \bar{B}_s^0$) system. Measurements of indirect CP violation (CP violation in mixing and in the interference between decay with and without mixing) in $K_{S,L}^0 \rightarrow \pi^+\pi^-$ and $K_{S,L}^0 \rightarrow \pi^0\pi^0$ provide the last constraint (ϵ_K).

One can see that all the constraints point to the same region. Combining experimental data and theoretical predictions into a global fit, one obtains the Wolfenstein parameters [6]:

$$\begin{aligned} \lambda &= 0.22535 \pm 0.00065, & A &= 0.811^{+0.022}_{-0.012}, \\ \bar{\rho} &= 0.131^{+0.026}_{-0.013}, & \bar{\eta} &= 0.345^{+0.013}_{-0.014}. \end{aligned} \quad (1.34)$$

The phase of the CKM matrix is established as the dominant source of CP violation in the quark sector of the Standard Model. There is still room for sizable contributions of New Physics. In some extensions of the Standard Model the constraints are indeed much weaker than the ones presented in figure 1.3 [24]. To test the Standard Model more precisely the uncertainties have to be reduced, specially on the angles α and γ which are the less well constrained experimentally. In the next chapter, we will discuss how charmless three body decays of B mesons can contribute to this field.

CHAPTER 2

Charmless three body decays of B mesons

In summer 1977, a group of physicists discovered the Υ meson at FERMILAB [25]. Later on, it was found that this particle is the bounded state of a bottom (b) quark and its anti-particle (\bar{b}) [26]. The particles composed of a \bar{b} anti-quark and an up, down, strange or charm quark define the family of B mesons. The first evidence of B mesons was found in 1981 in CLEO and the first observation of charmless hadronic B meson decays was also made there [27].

The theoretical analysis of this kind of decay stands in the fact that non perturbative QCD effects occur at long distances, allowing the factorization of perturbative and non perturbative QCD effects and the posterior development of effective QCD theories [28]. There are three popular approaches: QCD factorization (QCDF) [29], perturbative QCD (pQCD) [30] and soft-collinear effective theory (SCET) [31].

This chapter presents a short review of how the measurements of the angles of the unitarity triangle can be performed using charmless three body decays of B mesons. This is followed by a brief section about radiative decays, which are an important source of background for the charmless decays involving π^0 in the final state.

2.1 Measurement of α

The CKM angle α does not appear directly as a weak phase of any decay channel but can be extracted as $\beta + \gamma = \pi - \alpha$. $B \rightarrow \pi\pi$, $B \rightarrow \rho\rho$ and $B \rightarrow \rho\pi$ modes involve both $V_{ub}(\gamma)$ in tree level weak processes and $V_{td}(\beta)$ in penguin processes as well as in the $B^0 - \bar{B}^0$ oscillations for the neutral modes. α can be extracted for the interference between those

various contributions.

2.1.1 α from $B \rightarrow \pi\pi$ and $B \rightarrow \rho\rho$ decays

Using the $B \rightarrow \pi\pi$ or $B \rightarrow \rho\rho$ decays, α can be measured from the time dependent and independent CP asymmetries and the branching fractions [32]. The branching fractions of those decays are [6]

$$\mathcal{B}(B^0 \rightarrow \pi^+\pi^-) = (5.15 \pm 0.22) \times 10^{-6} \quad (2.1)$$

$$\mathcal{B}(B^0 \rightarrow \pi^0\pi^0) = (1.62 \pm 0.31) \times 10^{-6} \quad (2.2)$$

$$\mathcal{B}(B^+ \rightarrow \pi^+\pi^0) = (5.70 \pm 0.50) \times 10^{-6} \quad (2.3)$$

$$\mathcal{B}(B^0 \rightarrow \rho^+\rho^-) = (2.42 \pm 0.31) \times 10^{-5} \quad (2.4)$$

$$\mathcal{B}(B^0 \rightarrow \rho^0\rho^0) = (7.30 \pm 2.80) \times 10^{-7} \quad (2.5)$$

$$\mathcal{B}(B^+ \rightarrow \rho^+\rho^0) = (2.40 \pm 0.19) \times 10^{-5} \quad (2.6)$$

For both $B \rightarrow \pi\pi$ and $B \rightarrow \rho\rho$ modes, the time dependent asymmetry can be expressed as

$$S^{ij} \sin(\Delta mt) - C^{ij} \cos(\Delta mt) \text{ with } i, j = +-, 00, +0 \quad (2.7)$$

and

$$C^{ij} = \frac{(|A^{ij}|^2 - |\bar{A}^{ij}|^2)}{(|A^{ij}|^2 + |\bar{A}^{ij}|^2)}, \quad (2.8)$$

$$S^{ij} = \text{Im}(\bar{A}^{ij}/A^{ij}), \quad (2.9)$$

where A^{ij} are the $h^i h^j$ decay amplitudes and h can be either ρ or π . These decay processes have pure electroweak components at tree level and both QCD and electroweak components at penguin level. In this approach, the penguin contributions affects the value of α extracted from the $h^+ h^-$ mode in which it is only possible to obtain an effective value that includes the penguin QCD pollution. This value is known as α_{eff} and can be calculated from [33]

$$\sin(2\alpha_{eff}) = \frac{S^{+-}}{\sqrt{1 - (C^{+-})^2}}. \quad (2.10)$$

This calculation can be complemented using SU(2) symmetry [32]. Since the two final state particles are identical, the total wave function has to be symmetric, allowing only final states with isospin I=0 or I=2. Neglecting electroweak penguins and long distance effects, the tree level contribution can lead both to I=0 and I=2 final states while the penguin one is pure I=0. The A^{ij} amplitudes can be then decomposed as

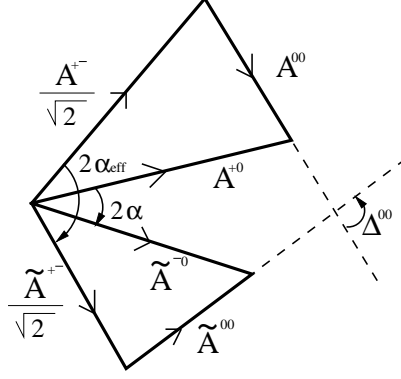


Figure 2.1: Representation of the isospin relations for the decay amplitudes of the $B \rightarrow \pi\pi$ and $B \rightarrow \rho\rho$ modes.

$$\begin{aligned} (1/\sqrt{2})A^{+-} &= A_2 - A_0, \\ A^{00} &= 2A_2 + A_0, \\ A^{+0} &= 3A_2, \end{aligned} \quad (2.11)$$

where A_2 and A_0 are the amplitudes of the isospin states $I=2$ and $I=0$, respectively. The following equations are then obtained

$$(1/\sqrt{2})A^{+-} + A^{00} = A^{+0}, \quad (2.12)$$

$$(1/\sqrt{2})\tilde{A}^{+-} + \tilde{A}^{00} = \tilde{A}^{+0}. \quad (2.13)$$

These relations can be represented as triangles as on figure 2.1. In this figure, one has

$$\tilde{A}^{ij} = \frac{\bar{A}^{ij}}{\sqrt{1 - (C^{ij})^2}}, \quad (2.14)$$

$$\sin(\Delta^{00}) = \frac{S^{00}}{\sqrt{1 - (C^{00})^2}}. \quad (2.15)$$

There is four-fold ambiguity when going from $2\alpha_{eff}$ to 2α as the orientations of A^{00} and \tilde{A}^{00} are unknown. As there is also a two-fold ambiguity going from $\sin(2\alpha_{eff})$ to α_{eff} , this leads to eight mirror solutions between 0 and π .

Applying this isospin analysis to the $B \rightarrow \rho\rho$ modes [34], the final state polarization of the ρ vector meson has to be taken into account, splitting in three the isospin relations given in 2.11, depending of the polarization of the ρ mesons. However the longitudinal polarization

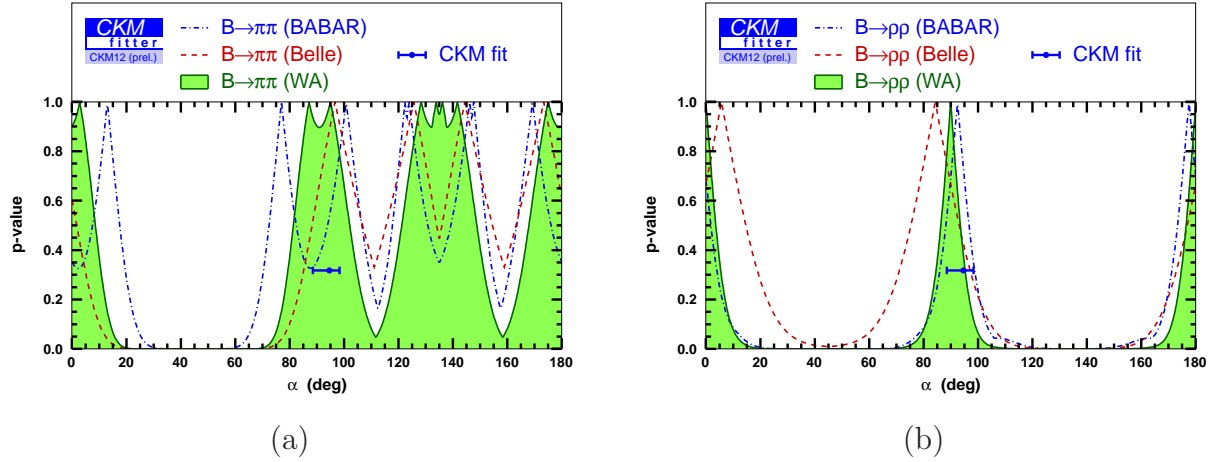


Figure 2.2: Current status of the measurement of α using $B \rightarrow \pi\pi$ (a) and $B \rightarrow \rho\rho$ (b) modes.

almost saturate the $B^0 \rightarrow \rho^+\rho^-$ and $B^+ \rightarrow \rho^+\rho^0$ decays [35] which simplifies the analysis. A first advantage of the $B \rightarrow \rho\rho$ analysis is the large $B^0 \rightarrow \rho^+\rho^-$ and $B^+ \rightarrow \rho^+\rho^0$ branching fractions compared to the $\pi\pi$ counterparts. Another is the small $B^0 \rightarrow \rho^0\rho^0$ branching fraction with respect to the $B^0 \rightarrow \rho^+\rho^-$ and $B^+ \rightarrow \rho^+\rho^0$ ones. This leads to small corrections from $2\alpha_{eff}$ to 2α . A last advantage is that, contrary to the $B \rightarrow \pi\pi$ case, one can measure here S^{00} with a time-dependent analysis of $B^0 \rightarrow \rho^0\rho^0$. As one can see in figure 2.1, this resolves the ambiguities when going from $2\alpha_{eff}$ to 2α leaving only two mirror solutions of α between 0 and π .

Figure 2.2 [18] shows the state of the art of the measurements of α using the two body and quasi-two body decays $B \rightarrow \pi\pi$ and $B \rightarrow \rho\rho$ at B factories. One can see that the extraction from $B \rightarrow \rho\rho$ is more precise and has less ambiguities than the one from $B \rightarrow \pi\pi$. BaBar and Belle data are in good agreement. Their combination is in excellent agreement with the CKM fit.

2.1.2 α from $B^0 \rightarrow \pi^+\pi^-\pi^0$ decays

A complementary analysis to obtain α , developed by Snyder and Quinn [36], comes from the $B^0 \rightarrow \pi^+\pi^-\pi^0$ decay channel. Within an isospin study of the $B^0 \rightarrow \rho\pi$ decay amplitudes, the interferences between the $B^0 \rightarrow \rho^+\pi^-$, $B^0 \rightarrow \rho^-\pi^+$ and $B^0 \rightarrow \rho^0\pi^0$ contributions allow to extract α from a time-dependent analysis of the “Dalitz plot”¹. As for $B \rightarrow \pi\pi$ and $B \rightarrow \rho\rho$, the contributions to the $B \rightarrow \rho\pi$ decays come from tree level electroweak diagrams

¹A Dalitz plot is a representation of a three-body decay in a two-dimensional plot. Usually, the two axis of the plot are the squares of the invariant masses of two of the three possible particle pairs [37].

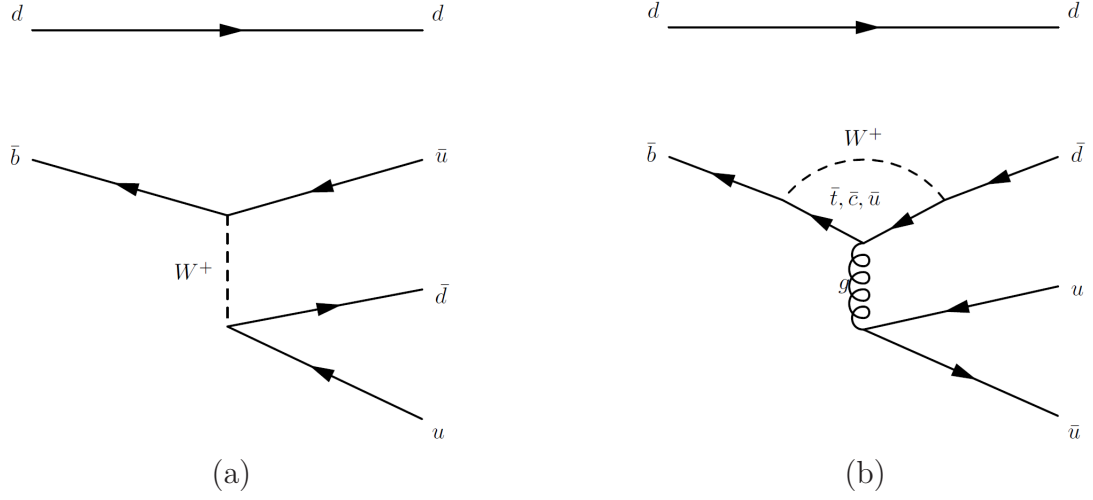


Figure 2.3: Processes contributing to the $B^0 \rightarrow \pi^+ \pi^- \pi^0$ decay. Tree level diagram that represents a weak process ending in $\rho^\pm \pi^\mp$ (a) and penguin level diagram representing a weak-QCD process with $\rho^0 \pi^0$ final state (b).

and both QCD and electroweak penguin diagrams. Figure 2.3 shows two examples of those diagrams.

As for $B \rightarrow \pi\pi$ and $B \rightarrow \rho\rho$, the electroweak penguins as well as the long distance effects are neglected in the isospin analysis. A complication here is coming from the fact that the $\rho^+ \pi^-$ final state is different from the $\rho^- \pi^+$ one. This means the A^{-+} amplitude is different from the A^{+-} one. Defining [38]:

$$\begin{aligned} S_1 &= \sqrt{2}A^{+0}, & S_2 &= \sqrt{2}A^{0+}, \\ S_3 &= A^{+-}, & S_4 &= A^{-+}, & 2S_5 &= A^{00}, \end{aligned} \tag{2.16}$$

one obtains the pentagonal relation

$$S_1 + S_2 = S_3 + S_4 + S_5. \tag{2.17}$$

Separating tree and penguin contributions explicitly, one has

$$\begin{aligned} S_1 &= T^{+0} + 2P_1, \\ S_2 &= T^{0+} - 2P_1, \\ S_3 &= T^{+-} + P_1 + P_0, \\ S_4 &= T^{-+} - P_1 + P_0, \\ S_5 &= T^{0+} + T^{+0} - T^{+-} - T^{-+} - 2P_0, \end{aligned}$$

where T^{ij} represents the tree contribution and P_k the penguin one with the $\rho\pi$ isospin final state k . The total amplitude of the $B^0 \rightarrow \pi^+\pi^-\pi^0$ decay can be written as a linear combination of the three A^{ij} amplitudes

$$A_{3\pi} = \sum_{i,j} f^i A^{ij}, \quad ij = +-, -+, 00. \quad (2.18)$$

Similarly the CP conjugate is

$$\bar{A}_{3\pi} = \sum_{i,j} f^i \bar{A}^{ij}, \quad ij = +-, -+, 00. \quad (2.19)$$

The f^i factors are relativistic Breit-Wigner functions multiplied by phase factors that take into account the polarization of the ρ meson [39] for each of the $\rho(770)$, $\rho(1450)$ and $\rho(1700)$ resonances.

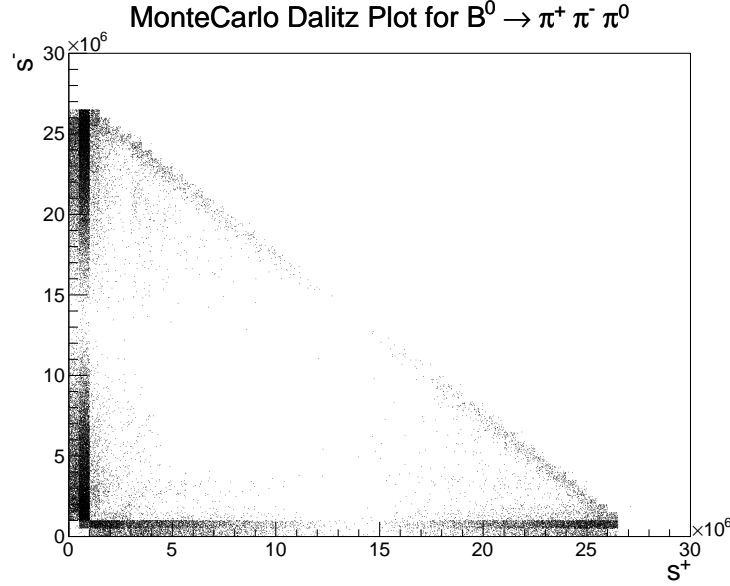
To describe the kinematics of the $B^0 \rightarrow \pi^+\pi^-\pi^0$ decay, there are twelve final-state parameters that are the 4-momentum components of the three pions. Some constraints however reduce the number of degrees of freedom. The B^0 is a scalar, which means there is no privileged direction in its decay: the decay being isotropic, it is possible to choose any value for the three Euler angles. The energy-momentum conservation imposes four relations and the masses of the pions give other three. So finally there is only two degrees of freedom. The standard parametrization of the phase space is to take the squares of the invariant masses of the pairs formed by charged pions and the neutral one: $s^+ = m_{\pi^+\pi^0}^2$ and $s^- = m_{\pi^-\pi^0}^2$. This defines the axes of the Dalitz plot of the three-body decay. Figure 2.4 shows a Dalitz plot obtained simulating 10^5 $B^0 \rightarrow \pi^+\pi^-\pi^0$ Monte Carlo events. The bands represent the ρ resonances. The interferences in the corners allows to extract the tree and penguin components of the decay amplitude.

The $B^0 - \bar{B}^0$ oscillation is a known phenomena [4]. The state of a B meson can change from B^0 to \bar{B}^0 and vice versa during its evolution in time. The decay amplitude as a function of time and phase space has to take into account this feature.

To obtain the temporal evolution, the states of the B mesons are expressed in the mass basis:

$$\begin{aligned} |B_L\rangle &= p|B^0\rangle + q|\bar{B}^0\rangle, \\ |B_H\rangle &= p|B^0\rangle - q|\bar{B}^0\rangle, \end{aligned}$$

where L stands for “light” and H for “heavy”. The factors p and q are such that $|p|^2 + |q|^2 = 1$. From this definition derives $m = \frac{M_H + M_L}{2}$, $\Gamma = \frac{\Gamma_H + \Gamma_L}{2}$ and $\Delta m = M_H - M_L$.

Figure 2.4: Simulated $B^0 \rightarrow \pi^+ \pi^- \pi^0$ Dalitz plot.

When the B meson initial state is B^0 , the decay amplitude is given by

$$M(t, s^+, s^-) = e^{-\frac{\Gamma t}{2}} \left\{ \cos\left(\frac{\Delta m t}{2}\right) A_{3\pi}(s^+, s^-) + i \frac{q}{p} \sin\left(\frac{\Delta m t}{2}\right) \bar{A}_{3\pi}(s^+, s^-) \right\}. \quad (2.20)$$

In the case of a \bar{B}^0 initial state, one has

$$\bar{M}(t, s^+, s^-) = e^{-\frac{\Gamma t}{2}} \left\{ \cos\left(\frac{\Delta m t}{2}\right) \bar{A}_{3\pi}(s^+, s^-) + i \frac{p}{q} \sin\left(\frac{\Delta m t}{2}\right) A_{3\pi}(s^+, s^-) \right\}. \quad (2.21)$$

The Dalitz plot method is to fit the probability distributions from $M(t, s^+, s^-)$ and $\bar{M}(t, s^+, s^-)$ expressions on the experimental distributions. One has to measure s^+ and s^- as well as the decay proper time and to tag the initial flavour of the B meson as B^0 or \bar{B}^0 . Figure 2.5 presents simulated Dalitz distributions for different proper time intervals and for an initial B^0 .

This method has already been applied on data from the BaBar [39] and Belle [40] experiments. Figure 2.6 shows the results obtained for α using the three decays modes $\pi\pi$, $\rho\rho$ and $\rho\pi$. At the 2σ level, the $\rho\pi$ determination agrees with the $\rho\rho$ one. It allows to favor one of the two $\rho\rho$ mirror solutions. The combined measurements of BaBar and Belle using the three decay modes is $(88.5^{+4.7}_{-4.4})^\circ$ [18].

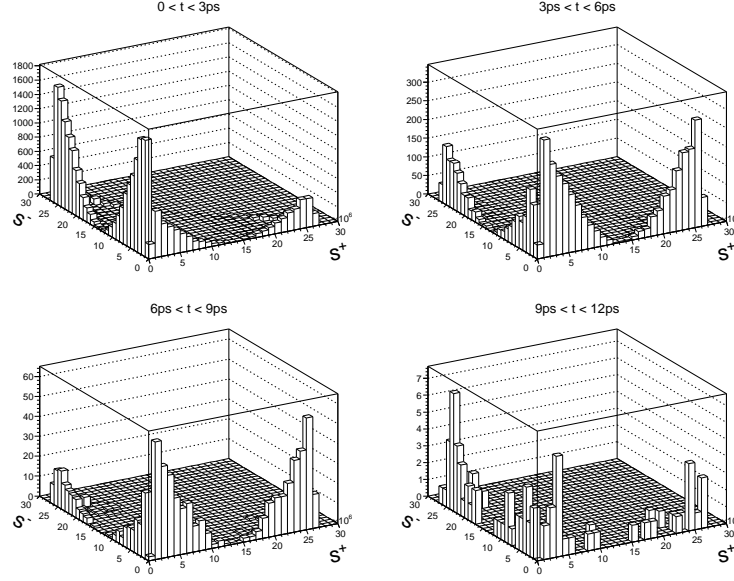


Figure 2.5: Simulated Dalitz distributions for different proper time intervals and for a B^0 in the initial state.

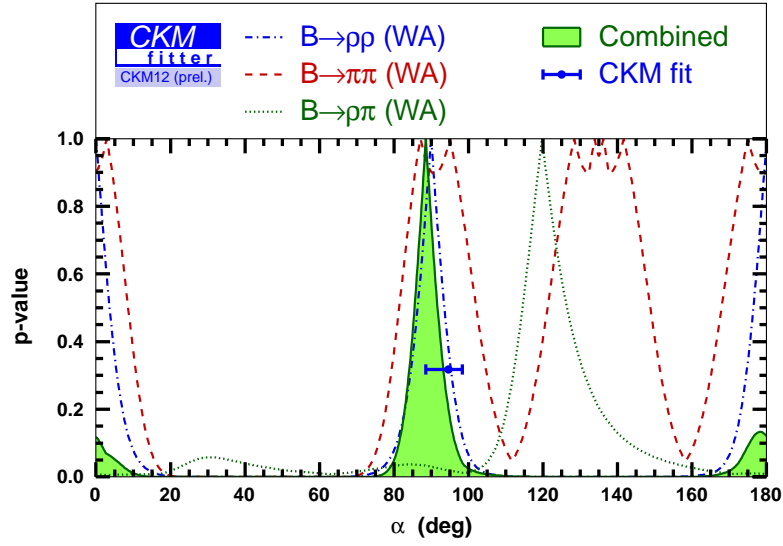


Figure 2.6: Extraction of α combining the measurements from $B_d^0 \rightarrow \rho\rho$ (blue), $B_d^0 \rightarrow \pi\pi$ (red) and $B_d^0 \rightarrow \rho\pi$ (dark green). The combination appears in light green.

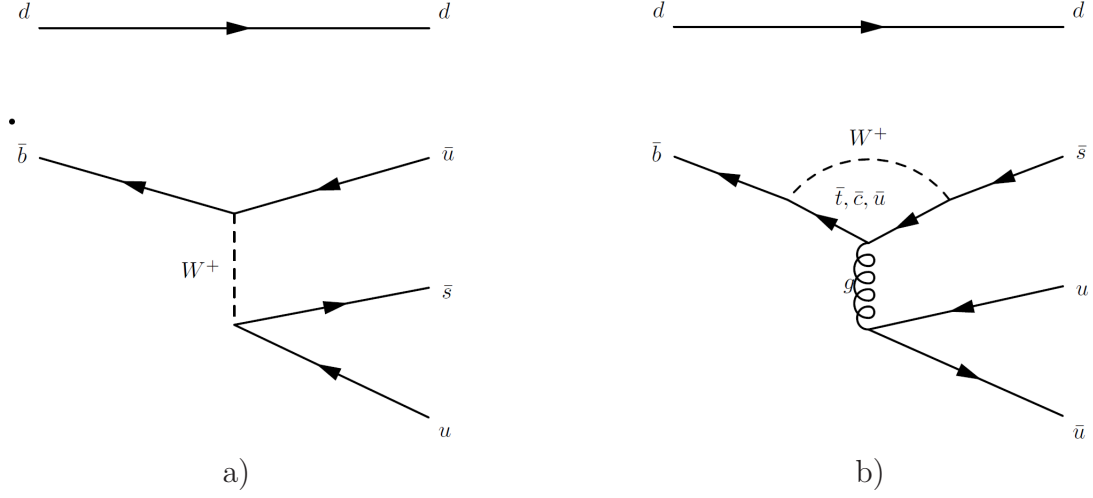


Figure 2.7: Processes contributing to the $B^0 \rightarrow K^+ \pi^- \pi^0$ decay. a) Tree level diagram that represents a weak process ending in $K^{*+} \pi^-$. b) Penguin level diagram representing a weak-QCD process with $K^{*0} \pi^0$ final state.

2.1.3 α from $B^0 \rightarrow K^+ \pi^- \pi^0$ decays

A possible extraction of α comes from the Dalitz analyses of the $B^0 \rightarrow K^+ \pi^- \pi^0$ mode. This decay was first observed in Belle and its branching fraction is [6, 41]

$$\mathcal{B}(B^0 \rightarrow K^+ \pi^- \pi^0) = (3.78 \pm 0.32) \times 10^{-5} . \quad (2.22)$$

It involves tree level electroweak contributions as well as penguin electroweak and QCD contributions. Figure 2.7 shows two examples of diagrams. The decay amplitude can be written in a general way as [42]

$$A(B^0 \rightarrow K^+ \pi^- \pi^0) = e^{i\gamma} T - P , \quad (2.23)$$

where T represents the electroweak tree terms and P represents the penguin part.

The $B^0 \rightarrow K^+ \pi^- \pi^0$ decay may proceed through intermediate resonances such as the isospin multiplet $B^0 \rightarrow K^{*0} \pi^0$, $K^{*+} \pi^-$ and $K^{*-} \pi^+$. The quantities

$$A^0 = A(K^{*+} \pi^-) + \sqrt{2} A(K^{*0} \pi^0) , \quad (2.24)$$

$$\bar{A}^0 = A(K^{*-} \pi^+) + \sqrt{2} A(\bar{K}^{*0} \pi^0) \quad (2.25)$$

are free from QCD penguin contributions. Neglecting electroweak penguins in 2.23 it could be possible to get α from the ratio [43]

$$R^0 = \frac{q}{p} \frac{\bar{A}^0}{A^0} = e^{-2i\beta} e^{-2i\gamma} = e^{2i\alpha} . \quad (2.26)$$

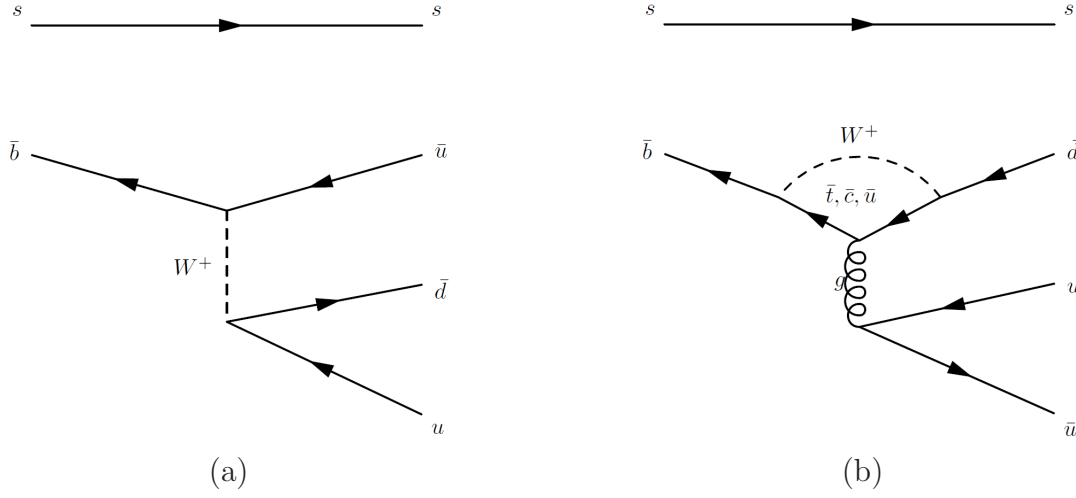


Figure 2.8: Processes contributing to the $B_s^0 \rightarrow K^- \pi^+ \pi^0$ decay. (a) Tree level diagram that represents a weak process ending in $K^{*-} \pi^+$ or $K^- \rho^+$. (b) Penguin level diagram representing a weak-QCD process with $K^{*0} \pi^0$ final state.

This quantity can be extracted from a Dalitz analysis of the $B^0 \rightarrow K^+ \pi^- \pi^0$ and $\bar{B}^0 \rightarrow K^- \pi^+ \pi^0$ decays [44]. However the penguin terms are not negligible and extracting α from this measurement would rely on the SU(3) flavour symmetry [45]. This leads to relatively large theoretical uncertainties. In addition, the quantities A^0 and \bar{A}^0 defined in 2.24 and 2.25 were found to be consistent with 0 in BaBar studies [46]. It was then not possible to measure α from $B^0 \rightarrow K^+ \pi^- \pi^0$ decays. However, this method can still be applied to similar decays as discussed in the next section.

2.2 γ from $B_s^0 \rightarrow K^- \pi^+ \pi^0$ decays

The $B_s^0 \rightarrow K^- \pi^+ \pi^0$ decay can be used in an analog way to obtain γ . Here also there are tree level electroweak contributions as well as QCD and electroweak penguins. Example diagrams are shown in figure 2.8.

The main advantage in this case is that the electroweak penguins are negligible. The expressions [47]

$$A_s^0 = A(B_s^0 \rightarrow K^{*-} \pi^+) + \sqrt{2} A(B_s^0 \rightarrow \bar{K}^{*0} \pi^0) , \quad (2.27)$$

$$\bar{A}_s^0 = A(\bar{B}_s^0 \rightarrow K^{*+} \pi^-) + \sqrt{2} A(\bar{B}_s^0 \rightarrow K^{*0} \pi^0) , \quad (2.28)$$

in which QCD penguin contributions cancel out, are then almost only related to the elec-

troweak tree level. The CKM angle γ can be obtained from

$$R^s = \frac{q_s}{p_s} \frac{\bar{A}_s^0}{A_s^0} = e^{-2i\beta_s} e^{-2i\gamma} \simeq e^{-2i\gamma} \quad (2.29)$$

A_s^0 and \bar{A}_s^0 can be extracted experimentally from the $B_s^0 \rightarrow K^-\pi^+\pi^0$ Dalitz distributions. It is then necessary to fix the phase difference between $A(B_s^0 \rightarrow K^{*-}\pi^+)$ and $A(\bar{B}_s^0 \rightarrow K^{*+}\pi^-)$. A Dalitz analysis of the $B_s^0 \rightarrow K_s^0\pi^+\pi^-$ decay can provide this information through the resonant contribution $B_s^0 \rightarrow K^{*-}(\bar{K}^0\pi^-)\pi^+$ and its CP conjugate.

2.3 Other charmless three body decays

As discussed, charmless three-body decays can be used to measure the CKM angles. Those channels also offer a direct way to study CP violation phenomena looking at their asymmetries. They also give clues about the dynamics of the B hadronic decays in general.

Studies of B_s^0 decays are particularly interesting. If B^0 and B^+ mesons were extensively studied at B-factories, this is not the case of the B_s^0 . The main reason is that at B-factories the B mesons are produced through the intermediate $\Upsilon(4S)$ resonance which does not decay to B_s^0 . In Belle some data were taken at the $\Upsilon(5S)$ which has a branching fraction of 20% to $B_s^*\bar{B}_s^*$ [48]. Only about 1000 $B_s^*\bar{B}_s^*$ pairs were produced during those dedicated runs. In addition, studies of $B_s^0 - \bar{B}_s^0$ oscillations require a high boost and can not be conducted at B-factories. Hadron collider data first from the Tevatron and now the LHC clearly supersede B-factories ones from what concerns the B_s^0 . Some of the B_s^0 branching fractions have been calculated using QCDF and pQCD. Reference [49] gives in particular predictions for the branching fractions of decays leading to $B_s^0 \rightarrow \pi^+\pi^-\pi^0$, $B_s^0 \rightarrow K^-\pi^+\pi^0$ and $B_s^0 \rightarrow K^+K^-\pi^0$ final states. The predictions are reported in table 2.1. They are affected by large uncertainties related to the choice of the scale and to uncertainties on hadronic inputs and CKM matrix elements. The predicted branching fractions are very small for $B_s^0 \rightarrow \pi^+\pi^-\pi^0$ final states as well as for $B_s^0 \rightarrow \bar{K}^{*0}\pi^0$ and $B_s^0 \rightarrow \phi\pi^0$ modes, $O(10^{-7})$. They range for 4×10^{-6} to 25×10^{-6} for the other modes.

2.3.1 $B_{d,s}^0 \rightarrow K^0 h^+ h'^-$

Other interesting charmless three-body decays are those including K_S^0 in the final state: $B_{d,s}^0 \rightarrow K_S^0\pi^+\pi^-$, $B_{d,s}^0 \rightarrow K_S^0 K^\pm \pi^\mp$ and $B_{d,s}^0 \rightarrow K_S^0 K^+ K^-$. A Dalitz analysis of the $B_{d,s}^0 \rightarrow K_S^0\pi^+\pi^-$ and $B_{d,s}^0 \rightarrow K_S^0 K^+ K^-$ final state may allow to measure the weak phase of the $B^0 - \bar{B}^0$ mixing in $b \rightarrow q\bar{q}s$ transitions ($q = d, s$). Under the assumption that $b \rightarrow c\bar{c}s$ transitions are dominated by Standard Model processes, a significative difference between

Mode	QCDF($\times 10^{-6}$)	pQCD ($\times 10^{-6}$)
$B_s^0 \rightarrow K^{*-}\pi^+$	$8.7^{+5.9}_{-4.9}$	$7.6^{+3.0}_{-2.3}$
$B_s^0 \rightarrow K^-\rho^+$	$24.5^{+15.2}_{-12.9}$	$17.8^{+7.9}_{-5.9}$
$B_s^0 \rightarrow \bar{K}^{*0}\pi^0$	$0.25^{+0.46}_{-0.22}$	$0.07^{+0.05}_{-0.02}$
$B_s^0 \rightarrow K^{*+}K^-$	$4.1^{+9.5}_{-3.2}$	$6.0^{+2.5}_{-1.9}$
$B_s^0 \rightarrow K^{*-}K^+$	$5.5^{+15.1}_{-4.7}$	$4.7^{+2.7}_{-1.6}$
$B_s^0 \rightarrow \phi\pi^0$	$0.12^{+0.05}_{-0.05}$	$0.16^{+0.06}_{-0.05}$
$B_s^0 \rightarrow \rho^-\pi^+$	≈ 0.003	$0.22^{+0.06}_{-0.08}$
$B_s^0 \rightarrow \rho^+\pi^-$	≈ 0.003	$0.24^{+0.07}_{-0.08}$
$B_s^0 \rightarrow \rho^0\pi^0$	≈ 0.003	$0.23^{+0.07}_{-0.08}$

Table 2.1: Theoretical branching fractions for B_s^0 decays.

$b \rightarrow q\bar{q}s$ and $b \rightarrow c\bar{c}s$ transitions would be a hint of New Physics contributions. The LHCb collaboration have performed a deep study of these channels and measured the $B_s^0 \rightarrow K_S^0\pi^+\pi^-$, $B^0 \rightarrow K_S^0K^\pm\pi^\mp$, $B_s^0 \rightarrow K_S^0K^\pm\pi^\mp$, $B^0 \rightarrow K_S^0K^+K^-$, $B_s^0 \rightarrow K_S^0K^+K^-$ branching fractions relative to $B^0 \rightarrow K_S^0\pi^+\pi^-$ one [50].

2.3.2 $B^0 \rightarrow K^-K^+\pi^0$

This decay has not been observed. The decay mode $B^0 \rightarrow \phi\pi^0$ is dominated by electroweak penguins. The branching fraction predicted from QCDF is of the order of 10^{-9} [51]. For what concerns $B^0 \rightarrow K^{*-}K^+$ and $B^0 \rightarrow K^-K^{*+}$, the electroweak penguin contributions are less important and the pure annihilation process is dominating. The expected branching fractions are of the order of 10^{-8} [51].

2.3.3 $B_s^0 \rightarrow K^-K^+\pi^0$

Just as the last case, this decay has not been observed yet. Theoretical predictions for resonant intermediate states are found in table 2.1. According to [52], the principal contribution

for the $B_s^0 \rightarrow \phi\pi^0$, $B_s^0 \rightarrow K^{*+}K^-$ and $B_s^0 \rightarrow K^{*+}K^-$ decays is from electroweak diagrams at tree level.

2.4 Radiative decays and specific backgrounds

The study of charmless three body decays of B mesons including a π^0 in the final state is a difficult task. The branching fractions are small and the potential backgrounds relatively large. The b-hadron radiative decays constitute the most dangerous backgrounds as their reconstructed B mass is expected to peak in the signal region. Their final states are very close to the signal one as energetic π^0 and photons are not easy to distinguish. We will see in chapter 4 that the clusters of the two photons from the π^0 decay can not be separated in the calorimeters when the π^0 has an important boost.

Radiative decays of B mesons were first observed by CLEO in 1993, in the mode $B^0 \rightarrow K(892)^0\gamma$. The physics of weak radiative decays is associated with two principal processes at the quark level: electromagnetic penguins and W-exchange or W annihilation accompanied by a bremsstrahlung photon emission. Two types of decays, dominated by electromagnetic penguin diagrams [53], are particularly relevant here:

$$b \rightarrow s\gamma \Rightarrow B \rightarrow K^*\gamma, \quad B_s^0 \rightarrow \phi\gamma \quad (2.30)$$

$$b \rightarrow d\gamma \Rightarrow B \rightarrow \rho\gamma, \quad B^0 \rightarrow \omega\gamma, \quad B_s^0 \rightarrow K^{*0}\gamma. \quad (2.31)$$

$b \rightarrow s\gamma$ and $b \rightarrow d\gamma$ transitions proceed through flavour changing neutral currents. They are thus very sensitive to physics beyond the Standard Model. In the Standard Model, the decays listed in equation 2.30 are related to V_{ts} and the ones in 2.31 to V_{td} . The mentioned CKM parameters can not be measured using these decays individually because of large uncertainties on the form factors. Most of the uncertainties cancels out considering the ratios of branching fractions of the decays of 2.30 and 2.31. In this case the parameter accessible is $|V_{td}/V_{ts}|$ [54, 55].

The $B^0 \rightarrow K^*(892)^0\gamma$ branching fraction has been measured at B factories, the combination is $(4.33 \pm 0.15) \times 10^{-5}$ [6]. Another important channel is $B^0 \rightarrow K_2^*(1430)^0\gamma$ which has a branching fraction of $(1.24 \pm 0.24) \times 10^{-5}$ [6]. The $B_s^0 \rightarrow \phi\gamma$ branching fraction has been recently measured in LHCb as $(3.3 \pm 0.3) \times 10^{-5}$ [56]. The $b \rightarrow d\gamma$ decays have only been studied in B factories so far. The average $B^0 \rightarrow \rho^0\gamma$ branching fraction is $(8.6 \pm 1.5) \times 10^{-7}$ [6].

2.5 Conclusion

The charmless three-body decays of B mesons with a π^0 in the final state can be used to measure the angles α and γ of the unitarity triangle. Studies at B-factories have been performed in that sense. Similar studies can be performed at LHCb where higher statistics are expected. In addition, they can be extended to decays of the B_s^0 meson which was not reachable at B-factories. In this chapter the charmless three body decays of B meson have been presented as an important source of information on CP violation. The next chapter introduces the experimental facility used in this study, the Large Hadron Collider and LHCb, the experiment itself.

CHAPTER 3

The LHCb experiment

Precise studies of CP violation in the $B_d^0 - \bar{B}_d^0$ system were done at the B-factories [57, 58]. In B-factories, two electron beams collide with asymmetric energies at the $\Upsilon(4S)$ resonance to produce boosted and coherent pairs of B mesons. In addition to the coherence of the produced pairs, another advantage is the clean environment which lead to clear signal signatures and low backgrounds. Even if more than one billion $B\bar{B}$ pairs were recorded at B-factories, results could still be statistically limited given the rarity of the corresponding processes. Much higher statistics could be reached in an hadronic collider at high energy such as the LHC. In addition, this allows to access not only the B^0 (\bar{B}^0) and B^\pm but also the B_s^0 (\bar{B}_s^0) and the b-baryons. This chapter presents the LHCb experiment which was designed to study beauty and charm physics at the LHC. In the first part, the LHC accelerator is presented. This is followed by a general introduction to the LHCb experiment. The sub-detectors of LHCb as well as the trigger and software framework are then described. Finally a brief description of the luminosity measurement at LHCb is given.

3.1 The LHC

The biggest particle accelerator ever built is the Large Hadron Collider (LHC). It consists of a circular tunnel of 27 km, located underground at the french-swiss border [59]. This machine has been designed for proton-proton collisions. Two beams of protons travel inside the tunnel in opposite directions inside two different pipes. Each beam consists in sets of grouped protons called bunches, each one containing 10^{11} protons on average. There are more than 1000 bunches in each beam. The collisions occur in determined places around the rings, called interaction points, where the two bunches cross each other. This is where the detectors are located. There are four principal experiments at the LHC. The ATLAS

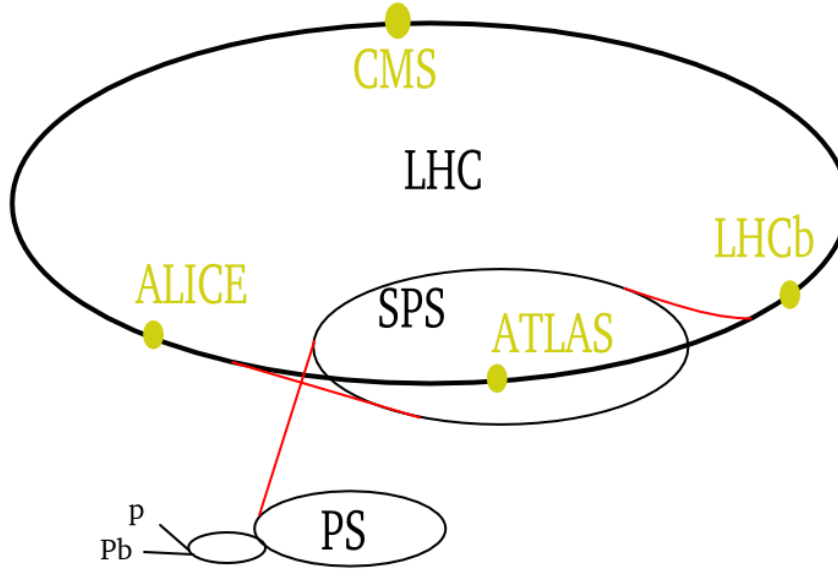


Figure 3.1: General view of the LHC.

and CMS detectors [60, 61] are general purpose experiments, mainly designed to search for the Higgs boson and for direct evidence of physics beyond the Standard Model. The ALICE experiment [62] is dedicated to the reconstruction of heavy ions collisions in order to study the formation of the quark-gluon plasma. Finally the LHCb experiment, in which this work took place, is designed for precision measurements on beauty and charm physics, specially the study of CP violation in this sector [63].

To reach those challenging physics goals, it is necessary to accumulate a big amount of data at collision energies never achieved before. In 2010-2011 LHC ran at a center of mass energy of 7 TeV. The center of mass energy was increased to 8 TeV in 2012. The protons are injected from the Super Proton Synchrotron (SPS) at the energy of 450 GeV. Inside the LHC, protons are accelerated to reach their final energy: 3.5 TeV in 2010-2011, 4 TeV in 2012. A general view of the LHC complex can be found in figure 3.1.

3.2 The LHCb Experiment

The idea of building an experiment dedicated to b-physics at the LHC comes from the fact that this machine is a copious producer of b-hadrons. The energies and luminosities reached at the LHC allows to have by far the largest production of those particles in the world. To

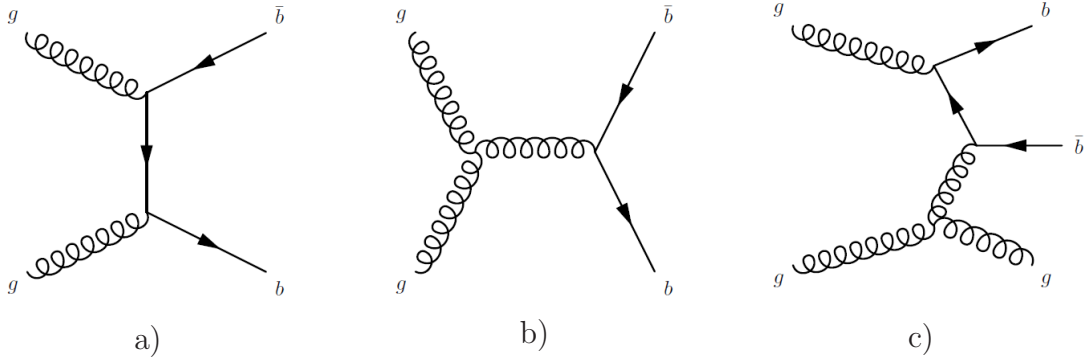


Figure 3.2: Feynman diagrams of processes related to $b\bar{b}$ production at the LHC, gluon fusion (a), gluon splitting (b) and flavour excitation (c).

benefit from this, it is necessary to carefully consider the production process of b-hadrons in the LHC environment. At LHC energies the main processes contributing to the heavy quark production are gluon-gluon fusion, flavour excitation and gluon splitting. The Feynman diagrams of these processes are shown in figure 3.2. The $b\bar{b}$ cross section is dominated by configurations in which one of the partons is much harder than the other. The b and \bar{b} quarks are then boosted along the direction of the hardest parton: their directions are close to the direction of one of the beams. As shown on figure 3.3, the b and \bar{b} -hadrons are consequently produced predominantly in the same forward cone.

According to this verification, the LHCb experiment has been built as a single arm forward spectrometer. The acceptance is from 10 to 300 mrad in the horizontal plane (bending plane) and 250 mrad in the vertical plane (non bending plane). The experiment has been optimized to reconstruct b-hadrons falling within its acceptance and tag their initial b-quark flavour. Figure 3.4 shows a general view of the LHCb detector.

The nominal interaction point defines the center of the coordinate system. The x , y and z axes form a right handed orthogonal system: the x axis is horizontal and orthogonal to the beam direction, the y axis is vertical and the z axis is parallel to the beam direction. As shown on figure 3.4, the y axis is directed upward and the z axis from the interaction point to the end of the spectrometer. The polar angle θ is the opening angle with respect to the z axis.

The design of any particle accelerator as the LHC is dictated by the cross sections of the physics phenomena to be observed. As the theory predicts smaller cross sections, the machine has to increase the luminosity. This is the case for searches of the Higgs boson and of new particles not present in the Standard Model. Hence, in the interaction point of ATLAS and CMS, the LHC delivers as much instantaneous luminosity as possible. This leads to increase the average number of proton-proton collisions per bunch crossing. Increasing the number

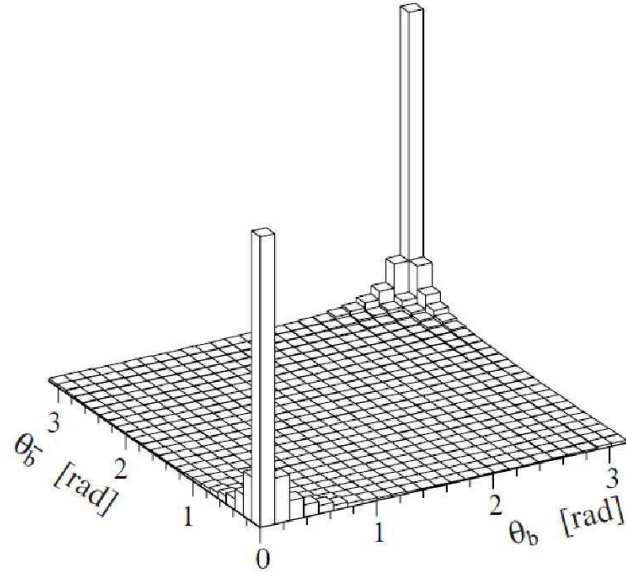


Figure 3.3: Polar angles of the b and \bar{b} -hadrons produced at the LHC, as obtained from a PYTHIA simulation.

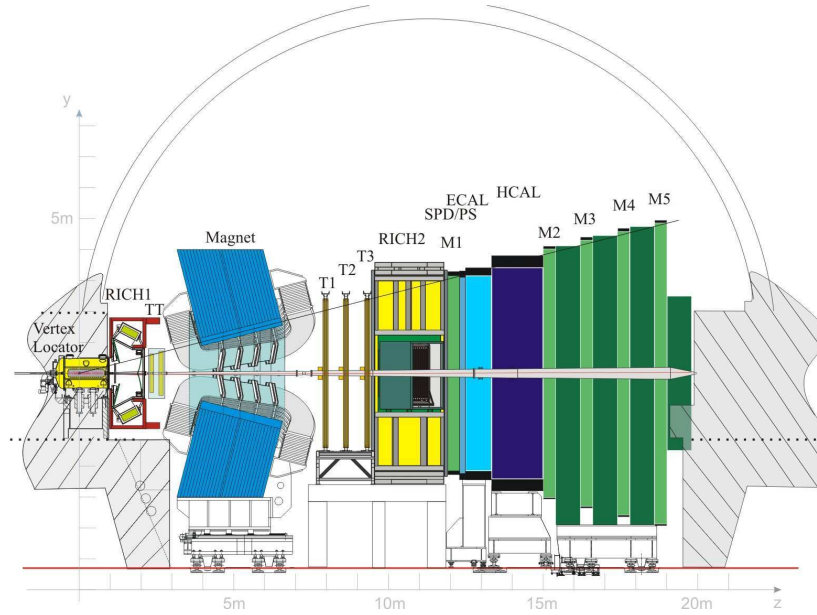


Figure 3.4: General schematic view of the LHCb detector.

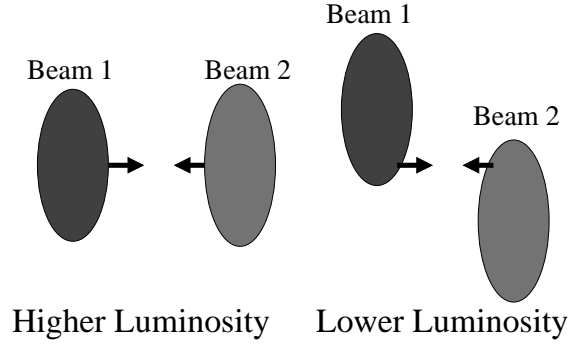


Figure 3.5: The concept of the luminosity leveling.

Year	Peak Lumi. ($\times 10^{32} \text{cm}^{-2} \text{s}^{-1}$)	μ	Integrated Lumi. (fb^{-1})
2010	1.7	2.5	0.04
2011	3.7	1.5	1.10
2012	4.0	1.7	2.08

Table 3.1: Data taking conditions and recorded luminosity in LHCb during the three years of LHC running. μ refers to the average multiplicity of visible interactions per bunch crossing.

of proton-proton collisions has a cost, it increases the multiplicity of particles in the event and makes the event reconstruction more difficult. This is more critical in the forward region where the occupancy is higher. In LHCb, the flavour tagging is for instance particularly impacted. Another important point is that for an event with multiple proton-proton interactions there could be an ambiguity in associating a b-hadron to the right production vertex as the b-hadrons reconstructed in the experiment have very forward directions. Therefore, LHCb is running at lower luminosity than ATLAS or CMS. The beam is less focused and the method of luminosity leveling by beam separation is used [64]. Luminosity leveling consists in moving the proton beams relative to each other modifying the effective crossing area. Figure 3.5 shows the concept.

Thanks to the luminosity leveling, LHCb runs with stable instantaneous luminosity, this means stable average number of visible interactions per bunch crossing. The data taking conditions and the luminosities integrated at LHCb [65, 66] during the three years of running are reported in table 3.1.

The identification of b-hadron decays in LHCb relies on the following:

- Vertex reconstruction: as b-hadrons fly a few millimeters before decaying, the reconstruction of primary vertices (proton-proton interaction point, where the b-hadron is produced) and secondary vertices (where the b-hadron decays) is of major importance to distinguish between tracks from b-hadrons and tracks directly produced in the proton-proton interaction as well as to check that selected tracks point back to a common decay vertex. Vertices are reconstructed by the vertex locator (VELO).
- Momentum/energy measurements: measurements of the momentum of the b-hadron decay products allows to reconstruct the mass of the b-hadron candidate and of eventual intermediate resonances. Excellent invariant mass resolutions are required to reject as much background as possible. The momentum of charged particles are measured by the tracking system. The calorimeters are used to measure the energy of neutral particles.
- Particle identification: another way to select a given process is to identify the final state particles. The two ring imaging Cherenkov detectors (RICH) allows to separate pions, kaons and protons. Electrons, protons and π^0 are identified in the calorimeters, muons in the muon chambers.

3.2.1 VELO

The VELO has been developed for the reconstruction of primary and secondary vertices. It provides the measurements of flight distance and of impact parameters (IP, distance of closest approach of a track to a vertex). It has a single hit precision of $\sim 4 \mu\text{m}$ [67, 68] requiring high precision on its alignment. The detector consists of 21 stations positioned perpendicular to the direction of the beam. It is located near the interaction region within a vacuum maintained by a dedicated vessel. The stations are approximately circular in shape and $300 \mu\text{m}$ thick. Each station is divided in two halves completely independent. A hole of 7 mm of radius allows the passage of the beams. The VELO stations are between $z = -18 \text{ cm}$ and $z = 88 \text{ cm}$. This is shown in figure 3.6.

Each half station is composed of two types of sensors: the r -sensors and the ϕ -sensors. The r -sensors consist in semi-circles centred on the beam axis. This allows the determination of the r coordinate which is the distance to the beam axis. The ϕ -sensors are divided radially to determine the ϕ -coordinate defined as the angle with respect to the x axis in the (x, y) plane. The z coordinate is obtained from the position of the station. This cylindrical geometry is used for the VELO because it gives better performances for tracks and vertices reconstruction. After the injection of the beams in the LHC, the beams are not fully focused. They are stabilized on their nominal orbits after the acceleration of the protons to their final energies. For this reason, the VELO stations are opened retracting each half station by 3 cm as one can see on figure 3.6. The VELO may be closed only after stabilization of the beams. It can be fully operated in both positions, opened or closed. Two additional stations, called

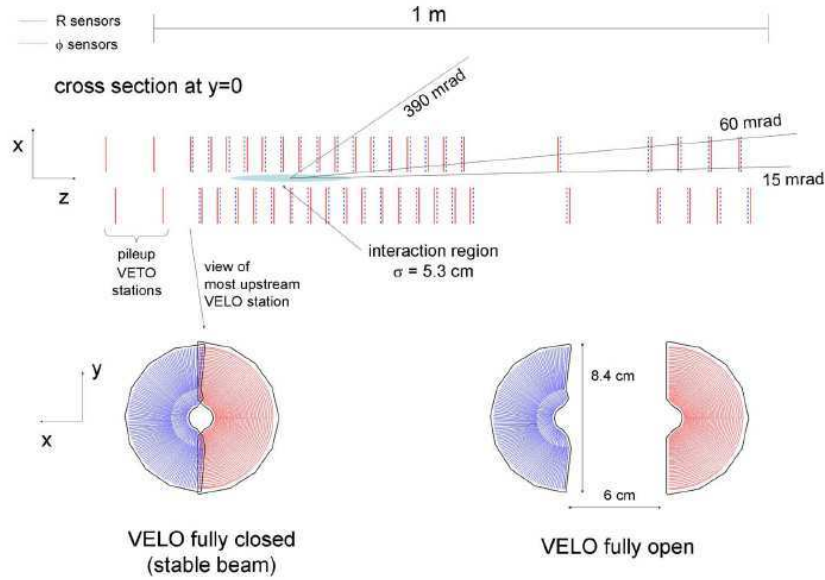


Figure 3.6: Cross section in the (x,z) plane of the VELO silicon sensors at $y = 0$, with the detector in the fully closed position. The front face of the first modules is also illustrated in both closed and open positions.

pile-up stations, constituted by r-sensor modules, are placed upstream of the interaction point to allow a fast determination of the number of primary vertices that can be used in the first trigger level. Figure 3.7 shows some of the key performances of the VELO [69]. For Primary Vertices (PV), the x and y resolutions vary from 10 to 40 μm depending of the number of associated tracks. In z the resolution varies from 60 to 250 μm . For tracks with transverse momentum (p_T) greater than 1 GeV/c, the IP resolution is better than 40 μm .

3.2.2 Magnet

The measurement of the momentum of the charged particles is computed from the curvature of their trajectories in a magnetic field, as usual in detectors of high energy physics. In LHCb, the magnetic field is provided by a dipole of 1600 tons. The average value of the integrated magnetic field is 3.6 Tm. The field is in the vertical direction bending charged particles in the horizontal plane. The polarity of the dipole is regularly changed to reduce systematic uncertainties on CP asymmetries related to potential asymmetries of the detector.

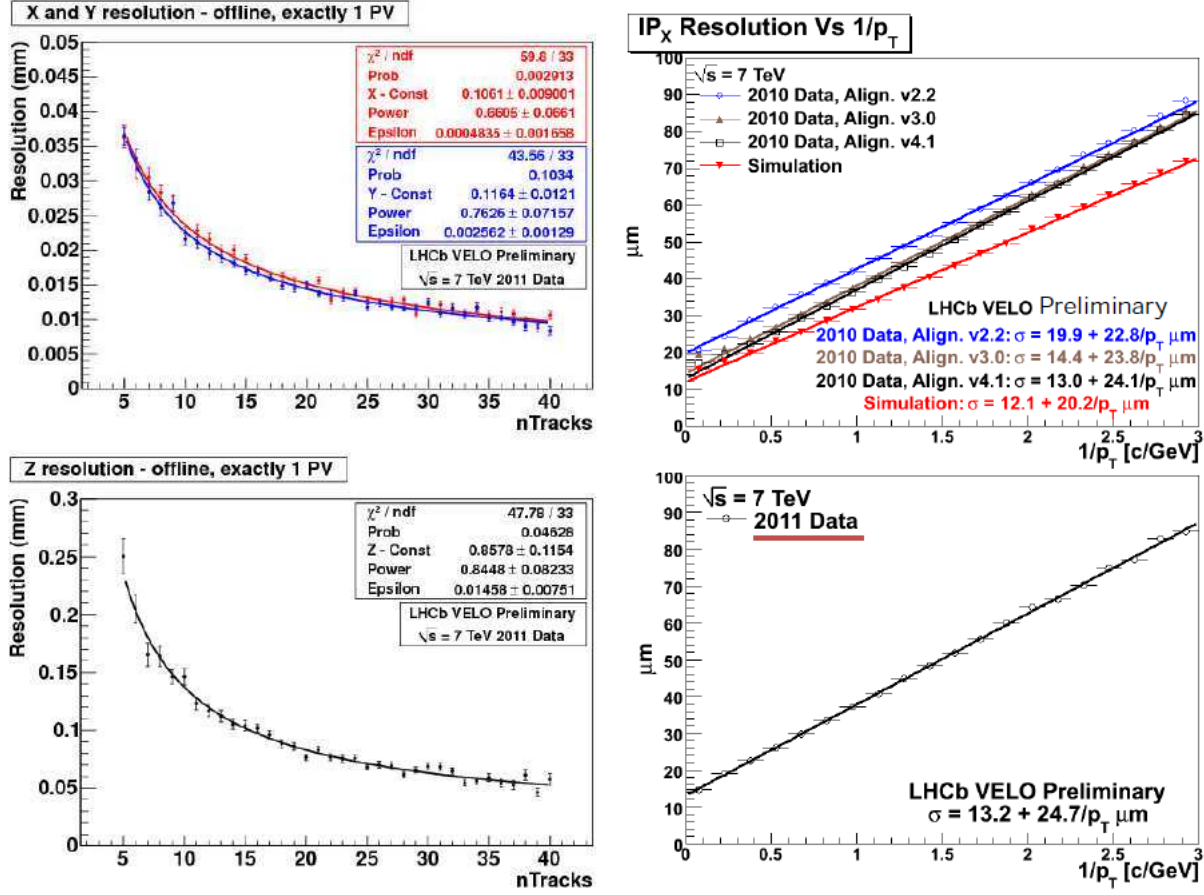


Figure 3.7: VELO performances. Primary vertex x (red) and y (blue) resolutions (Top left). Primary vertex z resolution (Bottom left). IP resolution with 2010 (Top right) and 2011 (Bottom right) data.

3.2.3 Tracking System

The VELO is completed by four tracking stations. The first one, TT, upstream of the magnet and the other three downstream of the magnet. These are T1, T2 and T3, composed of two type of detectors, the Inner Tracker (IT) and Outer Tracker (OT). A general view of the tracking stations can be seen in figure 3.8.

The TT

The Tracker Turicensis is a silicon microstrip tracker detector. It consists on four tracking layers allowing a fast momentum determination (with a precision of about 20%). The first and fourth layers have vertical readout strips, while the second and the third have rotated strips

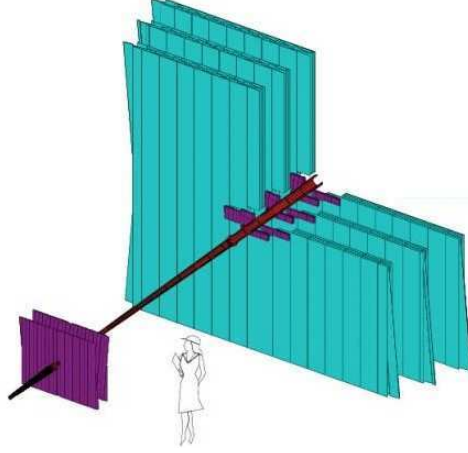


Figure 3.8: General view of the tracking stations with TT and IT in purple and OT in blue.

by a stereo angle of $+5^\circ$ and -5° respectively [70]. The hit resolution of silicon microstrips detectors is mainly related to the distance between strips, often called the strip pitch. In the case of the TT, the pitch is $183\ \mu\text{m}$ [71].

The Inner Tracker

In the tracking stations T1-T3, different technologies are used in the inner and the outer regions. This configuration was chosen because the inner region corresponds to the highest particle density. The Inner Tracker (IT) is designed with the same technology as the TT. Each IT station consists of a set of four overlapping “boxes”. As for TT, each station has four detection layers, two with vertical strips, two with stereo angles of $\pm 5^\circ$ [72]. The pitch in the IT is $198\ \mu\text{m}$ [71]. Although the IT covers only 1.3% of T1-T3 area, about 20% of the charged particles have their paths in the IT region.

The Outer Tracker

The outer tracker (*OT*) is a drift-time detector, designed as an array of individual straw tube modules. Each module is made of two layers of tubes put together in the same orientation. An OT station is made of four plans of modules, two with straw oriented vertically, two with stereo angles of $\pm 5^\circ$. Within a layer, the tube pitch is $5.25\ \text{mm}$ [73]. The tubes are filled with a mixture of 70% argon and 30% CO_2 . The drift time is shorter than 50 ns. This gives a manageable spillover from previous bunch crossings in the context of the experiment.

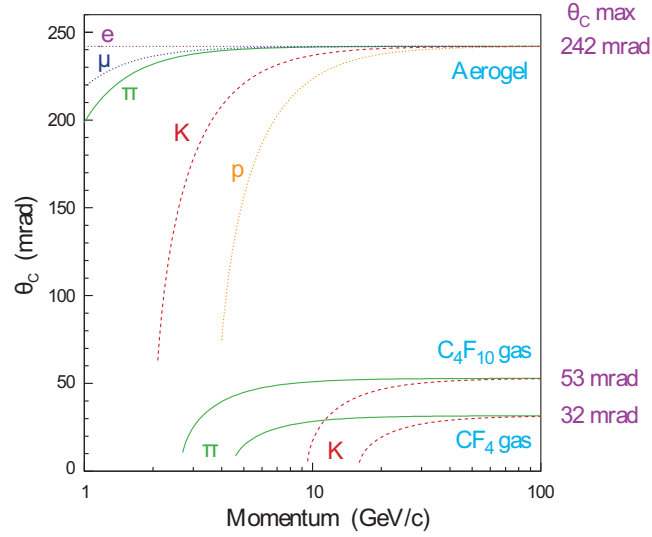


Figure 3.9: Theoretical Cherenkov angle according to the momentum and the kind of the charged particle for the different media used in the RICH detectors.

Tracking Performance

On 2011 data, the tracking efficiency is measured to be about 98% [74]. The momentum resolution $\delta p/p$ varies from 0.4% at 5 GeV/c to 0.6% at 100 GeV/c.

3.2.4 RICH detectors

The RICH detectors use the Cherenkov effect to identify charged particles. The Cherenkov effect is the fact that photons are emitted by a charged particle moving in a dielectric medium with a speed greater than the speed of light in that medium. The photons are emitted in a cone around the direction of the charged particle. The cone opening angle depends on the speed of the particle. Knowing the momentum (measured by the tracking system) and the speed of a particle, one has access to its mass and can then identify it [75]. In LHCb, the Cherenkov photons are guided by a series of spherical mirrors to a photon detector plane, located outside the detector acceptance. The Cherenkov photons form a ring on the detector plane and the radius of the ring is directly related to the angle of the Cherenkov cone.

Figure 3.9 shows the Cherenkov angle as a function of the particle momentum for different particles and for the different media used in the RICH detectors. Given that tracks with higher momentum have on average directions more forward than the lower momentum ones, two RICH detectors with different dielectric media are used in LHCb.

Figure 3.10 shows the configuration of the RICH detectors. RICH1 is located upstream of the magnet in the region between the VELO and the TT. It uses silica aerogel and C_4F_{10} and allows charged particle identification for momenta between 1 and 60 GeV/c. It covers polar angles from 25 to 300 mrad in the bending plane and to 250 mrad in the non bending plane. RICH2 is downstream of the magnet, after T3, and covers polar angles from 15 mrad to 120 mrad in the bending plane and to 100 mrad in the non bending plane. It uses CF_4 as dielectric medium and its momentum coverage goes from 15 GeV/c to 100 GeV/c.

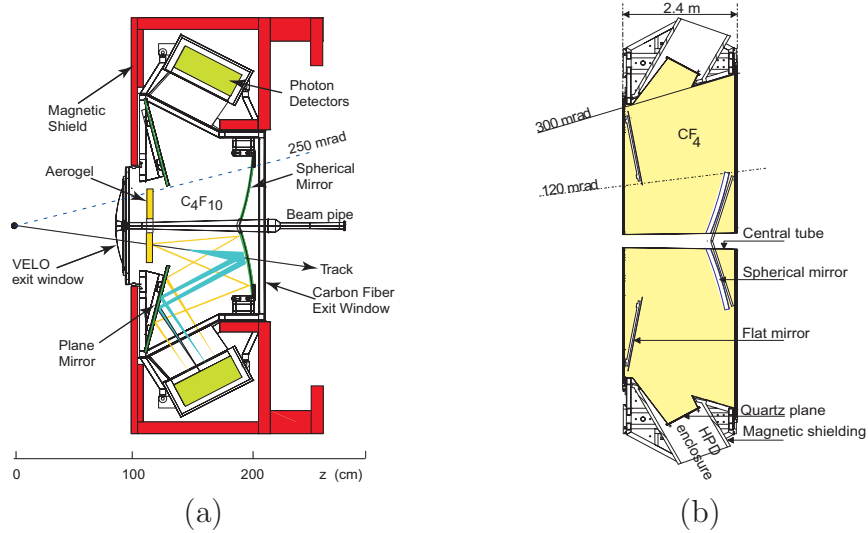


Figure 3.10: Schema of the RICH detectors, RICH1 (a) and RICH2 (b).

3.2.5 Calorimeters

The calorimeter system provides measurements of energy and positions of hadrons, electrons and photons. It stops all the particles produced in the collision except the muons (and neutrinos). Particles will lose all their energy by interacting with the calorimeters creating particle showers. The LHCb calorimeters are sampling calorimeters consisting of a succession of plates of passive material, to degrade the energy of the incoming particles, and of scintillator plates, to sample the energy of the shower. They are divided in independent cells providing the position of the particles [76]. The calorimeter system is divided in four stages in order to allow a first particle discrimination used in particular in the first trigger level. The most upstream device is the Scintillator Pad Detector (SPD) followed by the preshower (PS), the Electromagnetic Calorimeter (ECAL) and the Hadronic Calorimeter (HCAL).

One of the tasks of the calorimeter system is the identification of photons, electrons and π^0 . The various stages of the calorimeter have been introduced in this respect. The SPD and

the PS are 15 mm thick scintillator pads. A lead layer of 12 mm (2.5 radiation length) is placed between the SPD and the PS to start the electromagnetic showers. The distinction between charged and neutral particles is done in the SPD which only detects the passage of charged particles. The discrimination between charged pions and photons or electrons uses the preshower technique. About 92% of the electron ($1 - e^{-2.5}$) and 86% of the photon ($1 - e^{-2.5 \times 7/9}$) start their showers in the lead in between the SPD and the PS and deposit more energy in the PS than a Minimum Ionizing Particle (MIP). For the first level trigger, the corresponding cut is at 5 MIP.

The ECAL makes use of the “shashlik” design [76] alternating 66 layers of lead and polystyrene for a total length corresponding to 25 radiation lengths [76]. The ECAL sampling fraction (fraction of energy deposited in the active material) is 16%. The electromagnetic showers can be measured with a resolution of $\sigma(E)/E = 10\%/\sqrt{E} \oplus 1\%$ where the “ \oplus ” sign means that the summation is in quadrature.

The HCAL uses tiles of iron and polystyrene. To facilitate the readout the tiles are arranged parallel to the beam. The iron tiles are 16 mm thick while the scintillating ones are 4 mm thick. The HCAL has a sampling fraction of 2.7% and corresponds to 5.6 interaction lengths. Its resolution is $\sigma(E)/E = 70\%/\sqrt{E} \oplus 10\%$ [77].

The ECAL and HCAL transverse segmentations are presented in Figure 3.11. The cells are smaller in the inner part where the occupancy is higher. The ECAL is divided in three regions: inner, middle and outer. In the inner part, the cells are $4 \times 4 \text{ cm}^2$ large. Given that the Molière radius of lead is 3.5 cm, a smaller segmentation would not improve much the localization of the showers. In the middle and outer part, the cell sizes are $6 \times 6 \text{ cm}^2$ and $12 \times 12 \text{ cm}^2$ respectively. The SPD and PS segmentations follow the ECAL one with small differences on the cell sizes to respect the projective geometry from the interaction point. The HCAL is divided in two regions, inner and outer, with cell sizes of $13 \times 13 \text{ cm}^2$ and $26 \times 26 \text{ cm}^2$ respectively.

3.2.6 Muon Chambers

As shown in figure 3.12 the muon system consists in five stations called M1 to M5. M1 is placed upstream of the calorimeters in order to improve the transverse momenta measurement for the first trigger level. The downstream stations are separated by 80 cm iron blocks to further filter remaining backgrounds after the calorimeters.

Except for the inner region of M1 where the particle flux is the highest, Multi-Wire Proportional Chambers (MWPC) are used. In the MWPC, two non conducting plates form a 5 mm gap. Vertical conducting strips lie on the surface of one of the plates. In the middle of the gap, conducting wires are placed vertically each 2 mm. Each strip is associated to

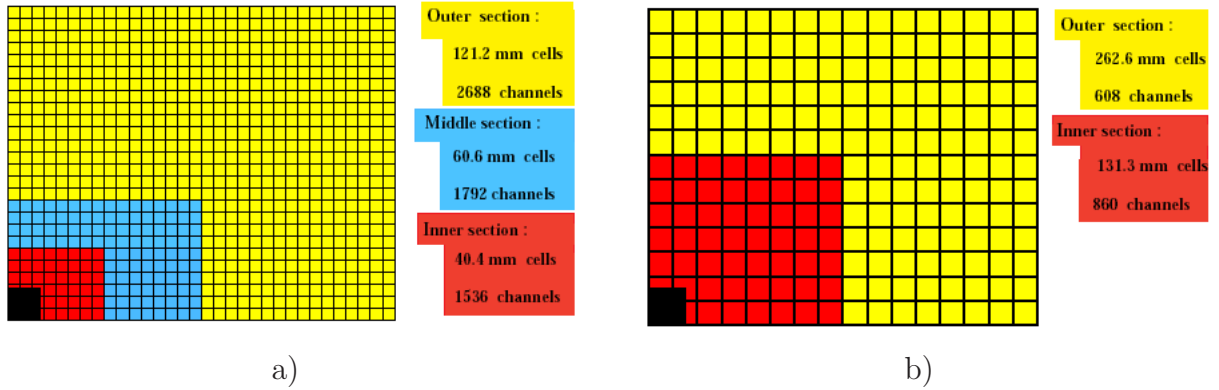


Figure 3.11: ECAL (a) and HCAL (b) transverse segmentations. Each figure corresponds to a quarter of the calorimeter area. The black region in the beam area is not instrumented. For the ECAL, each square corresponds to one outer cell, four middle cells or nine inner cells. For the HCAL, each square corresponds to one outer cells or four inner cells.

a given number of wires (4 to 42) which depends on the width of the strip. The strips are segmented longitudinally: a segment and its associated wires compose a “pad” [78]. The pad size depends on the distance to the beam. The innermost chambers have the smallest pad size, which means the highest granularity. The pad size in x and y varies from $1 \times 2.5 \text{ cm}^2$ to $25 \times 30 \text{ cm}^2$. The MWPC are filled with a mixture of Argon, CO_2 and CF_4 and the electric field in the gap is around 5 kV/cm.

The inner region of M1 is composed of triple-GEM (Gas Electron Multiplier) detectors which are more suitable given the high particle flux in this area. In this case, three copper foils are placed in between the anode and cathode plates. These foils are pierced of holes, to increase the electron flux of the ionizing shower. The electric field is 3.5 kV/cm between the cathode and the first copper foil as well as between the foils. It is set to 5 kV/cm between the last foil and the anode. The gas mixture used is also $\text{Ar} - \text{CO}_2 - \text{CF}_4$ [79]. The pad size in the triple-GEM is the same as the one in the innermost MWPC, i.e. $1 \times 2.5 \text{ cm}^2$ in x and y .

3.2.7 Trigger

The trigger system has to select on-line interesting events reducing the rate from the rate of visible collisions produced at the interaction point to the rate that can be sustained by the storage system. The rate of visible collisions is given by

$$\frac{\mathcal{L}\sigma_{vis}}{\mu}(1 - e^{-\mu}) , \quad (3.1)$$

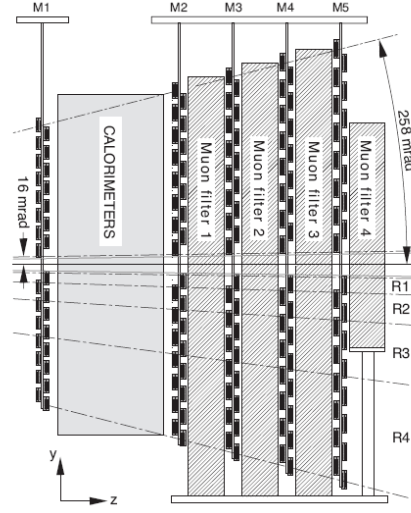


Figure 3.12: Schematic view of the muon stations.

where \mathcal{L} is the instantaneous luminosity; $\sigma_{vis} \sim 60$ mb is the visible interaction cross section, where interactions are considered to be visible if they give at least two tracks reconstructed in the VELO pointing to the interaction region; as already introduced, μ is the average number of visible interactions per bunch crossing. The factor $e^{-\mu}$ accounts for the fraction of bunch crossing with no visible interaction. Given the running conditions in 2011 and 2012 (see table 3.1), the rate of visible collisions was about 12 MHz. This has to be compared to the 3 kHz of events that are written in the storage system. LHCb has two levels of trigger, the Level 0 trigger and the High Level Trigger.

Level-0 Trigger

The first trigger level, called Level 0 (L0), is a hardware trigger integrated within the detector's front-end electronics. The L0 trigger operates synchronously with the 40 MHz LHC clock and a fixed latency of $4 \mu\text{s}$. It reduces the rate to about 1 MHz at which the entire detector may be read out. The L0 information is coming from the pile-up sensors of the VELO, the calorimeters and the muon system. It is sent to the Level 0 Decision Unit (L0DU) where the L0 selection algorithms are run.

The pile-up system has been implemented to reject events with several primary vertices. It uses the information of the pile-up stations of the VELO. Given that the experiment is running at higher μ than foreseen in the design, events with pile-up are not rejected and the pile-up system does not contribute to physics triggers. It is used to trigger on beam-gas events providing the number of hits in the pile-up stations, which are the only detector ele-

ments upstream of the interaction point. As we will see at the end of the chapter, beam-gas events are used in the determination of the luminosity [81].

The L0 calorimeter trigger system uses information from the four components of the calorimeter, SPD, PS, ECAL and HCAL. It computes the transverse energy deposited in 2×2 clusters. Then the clusters with the largest E_T are selected and identified either as hadron, photon or electron candidates. The hadron candidate is defined from the highest E_T HCAL cluster. The photon candidate is the highest E_T ECAL cluster with at least one PS cell with energy higher than a 5 MIP threshold and no hit in the corresponding SPD cells. The electron candidate is defined as the photon candidate except that at least one hit is required in the SPD cells in front of the PS cells above the 5 MIP threshold. The total number of hits in the SPD is also computed. It is used to reject high multiplicity events which would proportionally take too much time to be processed in the High Level Trigger.

The muon chambers perform a stand-alone muon reconstruction with a p_T resolution of $\sim 25\%$. Tracks are searched combining the pad data from the five muon stations to form towers pointing towards the interaction region. The muon stations are divided in quadrants and there is no exchange of information between the quadrants. In each quadrant, the two muon candidates with highest p_T are selected.

High Level Trigger

The High Level Trigger (HLT) is a fully software trigger. It consists of a C++ application executed on an event filter farm composed of 15000 processors summing about 25000 copies of the application. The HLT application has access to all the data of a given event and runs the selection algorithms, called “trigger lines”, optimized to cover a certain class of events of interest. The HLT processing time per event is close to 30 ms. The HLT reduces the rate from the level 0 output to ~ 3 kHz. For timing reasons, the HLT is divided into two stages, HLT1 and HLT2.

HLT1

HLT1 reduces the level 0 input rate by a factor of about 20. It performs a simplified 3D tracking reconstruction only for high transverse momentum track ($p_T > 1$ GeV/c or so). The selection requires a single high p_T track displaced for all primary vertices (PV) [82]. Along with some track quality requirements, the track should have an IP larger than $125 \mu\text{m}$ with respect to any PV, $p_T > 1.8$ GeV/c and $p > 12.5$ GeV/c. For events triggered by the Level 0 photon and electron lines, the p_T requirement is relaxed to 0.8 GeV/c.

HLT2

In HLT2 a simplified event reconstruction is performed. HLT1 rate allows an HLT2 tracking close to the offline one. Only tracks with $p > 5 \text{ GeV}/c$ and $p_T > 0.5 \text{ GeV}/c$ are reconstructed. The HLT2 runs exclusive and inclusive selections. Special inclusive lines have been developed to trigger on partially reconstructed b-hadron decays. These so-called topological lines [83] are based on displaced vertices with 2, 3 or 4 associated tracks. The topological lines were first implemented as cut based selections. To improve the performances, additional lines using a multivariate approach were then added [84].

3.3 The LHCb Software

LHCb applications are sets of libraries written in C++. They are used in a general framework called GAUDI [85]. The simulation package is called GAUSS [86]. PYTHIA 6.4 [87] with a configuration specific to LHCb is used to generate pp collisions. The hadronic particle decays are described by the EvtGen [88] package in which PHOTOS [89] is used to generate final state radiations. GAUSS then connects the PYTHIA output as input of GEANT 4 [90] which implements the interaction of the particles with the detector and the response of the active materials. The simulation of the digitization of the signals produced in the active materials is performed by the BOOLE application [91]. It includes simulation of the readout electronics as well as of the L0 hardware trigger. The simulation output is digitized data that mimics the real data coming from the detector.

The event reconstruction is performed by the BRUNEL application [93]. The MOORE application [92] can be used to run the HLT selection on reconstructed events. This is especially useful to emulate the HLT response on the simulated data. Finally, DAVINCI [94], the analysis application, computes for each event the variables used in the analysis and stores them in standard files.

3.4 Luminosity Measurements in LHCb

To measure any cross section a determination of the luminosity is mandatory. One has

$$\frac{dn}{dt} = \sigma \mathcal{L} \epsilon , \quad (3.2)$$

where $\frac{dn}{dt}$ is the number of selected events of a given process per unit of time, σ is the process cross section, \mathcal{L} is the instantaneous luminosity and ϵ is the total efficiency, accounting for the detector acceptance as well as the reconstruction and selection efficiencies.

The average instantaneous luminosity of two colliding bunches can be expressed as [95]

$$\mathcal{L} = \frac{f N_1 N_2}{4\pi \sigma_x \sigma_y} , \quad (3.3)$$

where f is the revolution frequency (11245 Hz at the LHC), N_1 and N_2 are the number of protons in the two bunches, σ_x and σ_y are the transverse sizes of the bunch at the interaction point along the x and y axis respectively.

In LHCb two methods to determine the absolute luminosity have been implemented [81]. The *van der Meer* scan in which the beams are moved in transverse directions in order to investigate the beam transverse profiles counting the interaction rate as a function of the beam offsets. In the *beam-imaging gas* method, the high acceptance of the VELO around the interaction point is used to reconstruct beam-gas vertices produced by the collision of protons in the beam with molecules in the remaining gas of the beam pipe. The positions of the beam-gas interactions are used to determine beam angles and profiles [96]. Combining the two methods, the absolute luminosity can be determined with a relative precision of 3.5%. This allows to calculate a reference cross section of visible interactions. Then, dedicated luminosity counters are defined in order to follow the evolution of the instantaneous luminosity during the data taking.

CHAPTER 4

Particle identification

The physics studies performed at LHCb require to distinguish the different b-hadron decay channels. Separating pions, kaons and protons is crucial and motivates the use of RICH detectors. The muons are essentially identified thanks to the muon chambers. For what concerns electrons, photons and neutral pions, the calorimeter is predominant for their identification.

In this work a selection of the $D^0 \rightarrow K^-\pi^+\pi^0$ mode has been developed. The first motivation was to validate the π^0 reconstruction and check the corresponding calibrations. The data sample obtained was then used to calibrate the π^0/γ separation tool of the experiment. This chapter first presents the charged particle identification in LHCb. Photon and π^0 reconstruction are then discussed. The work done around the $D^0 \rightarrow K^-\pi^+\pi^0$ mode is then presented.

4.1 Charged particles identification

In LHCb, the charged particle identification is done combining the information coming from the RICHs, the calorimeters and the muon chambers. For electrons, one of the main criteria is the E/p ratio where E is the energy measured in the calorimeters and p the momentum of the associated track reconstructed in the tracking system. Similarly, the tracks reconstructed in the muon chambers are matched with tracks in the tracking system. Combined likelihoods are defined as [63]

$$\begin{aligned}
\mathcal{L}_e &= \mathcal{L}^{RICH}(e)\mathcal{L}^{CALO}(e)\mathcal{L}^{MUON}(\text{non } \mu) , \\
\mathcal{L}_\mu &= \mathcal{L}^{RICH}(\mu)\mathcal{L}^{CALO}(\text{non } e)\mathcal{L}^{MUON}(\mu) , \\
\mathcal{L}_h &= \mathcal{L}^{RICH}(h)\mathcal{L}^{CALO}(\text{non } e)\mathcal{L}^{MUON}(\text{non } \mu) ,
\end{aligned}$$

where $h = \pi, K$ or p . The particle identification (PID) variables are then defined as the differences in the log-likelihoods with respect to the pion hypothesis:

$$PID_X = \ln(\mathcal{L}_X) - \ln(\mathcal{L}_\pi) , \quad (4.1)$$

where \mathcal{L}_X denotes the likelihood associated to the X hypothesis ($X = e, \mu, K$ or p). The discriminator between two kinds of particles is defined from this. For example, the discriminator between protons and kaons is

$$\Delta \text{Log} \mathcal{L}_{p-K} = PID_p - PID_K = \ln(\mathcal{L}_p) - \ln(\mathcal{L}_K) . \quad (4.2)$$

The $\Delta \text{Log} \mathcal{L}_{X-Y}$ distributions for real pions, kaon or protons are obtained from data using calibration samples of well known decays: $D^{*+} \rightarrow D^0(\rightarrow K^- \pi^+) \pi^+$, $\Lambda \rightarrow p \pi^-$ and $\bar{\Lambda} \rightarrow \bar{p} \pi^+$. These distributions are shown in figure 4.1 [97]. They allow to determine the efficiencies of the PID cuts. Figure 4.2 shows for instance the kaon PID efficiency (kaons identified as kaons) and the corresponding pion misidentification (pions identified as kaons) as a function of the track momentum for two different cuts in $\Delta \text{Log} \mathcal{L}_{K-\pi}$ ($=PID_K$) [99]. The results obtained from Monte Carlo and data are presented. For $PID_K > 0$, the average efficiencies are about 95% and 10% for kaons and pions respectively. A cut at $PID_K > 5$ significantly reduces the average fraction of misidentified pions, which is then $\sim 3\%$, and gives an average kaon efficiency close to 85%.

As the simulation does not perfectly reproduce the performances on data, a data driven calibration procedure is applied. It is based on the calibration samples previously discussed. The efficiencies are usually determined in bins of track momentum and pseudo-rapidity. The track transverse momentum and the number of tracks in the event can also be used. Event-per-event weights corresponding to the different PID efficiencies and misidentification fractions are then evaluated for the sample to be calibrated. The method was first developed on individual tracks. To account for the kinetic correlations between tracks, an event by event solution was finally adopted. More information on the PID efficiency calculation can be found in [50] and [98].

4.2 Photon Reconstruction

The energy from the interaction of photons and electrons with the detector is mainly absorbed in the ECAL. The reconstruction process begins with the identification of cells that have more

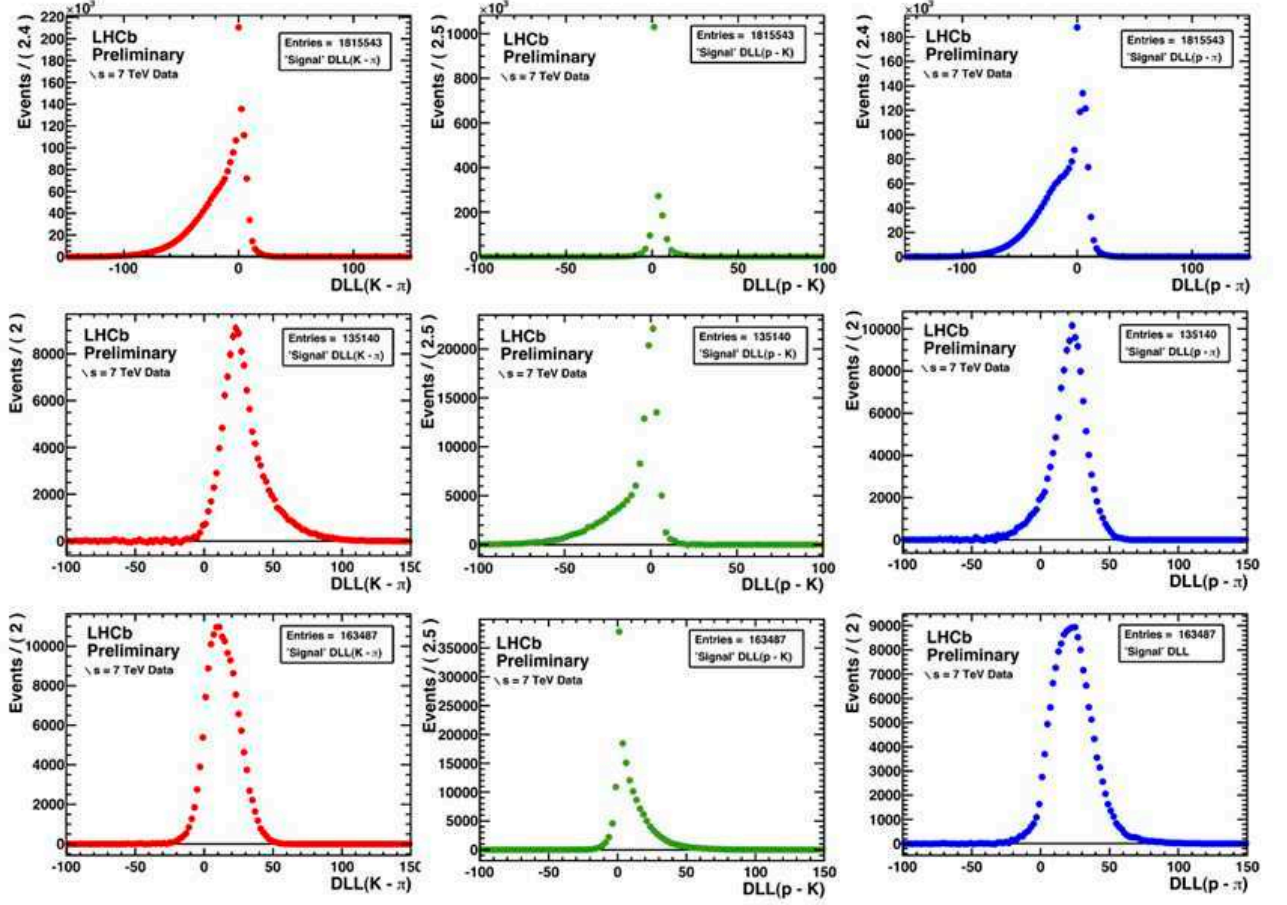


Figure 4.1: $\Delta \text{Log} \mathcal{L}_{K-\pi}$, $\Delta \text{Log} \mathcal{L}_{p-K}$ and $\Delta \text{Log} \mathcal{L}_{p-\pi}$ distributions for pions (top), kaons (middle) and protons (bottom).

energy than all their neighbors. These cells are selected only if the transverse energy is higher than 50 MeV. The selected cell and its neighbors define a “cluster”. To determinate the 4-momentum of the corresponding particle, the cluster total energy and the position of its barycenter are calculated:

$$E = \sum_i E_i, \quad x_b = \frac{1}{E} \sum_i x_i E_i, \quad y_b = \frac{1}{E} \sum_i y_i E_i, \quad (4.3)$$

where E_i represents the energy measured in each cell i of the cluster, x_i and y_i give the position of the middle of the cell.

The geometry of the calorimeter system has been chosen in such a way that the ECAL

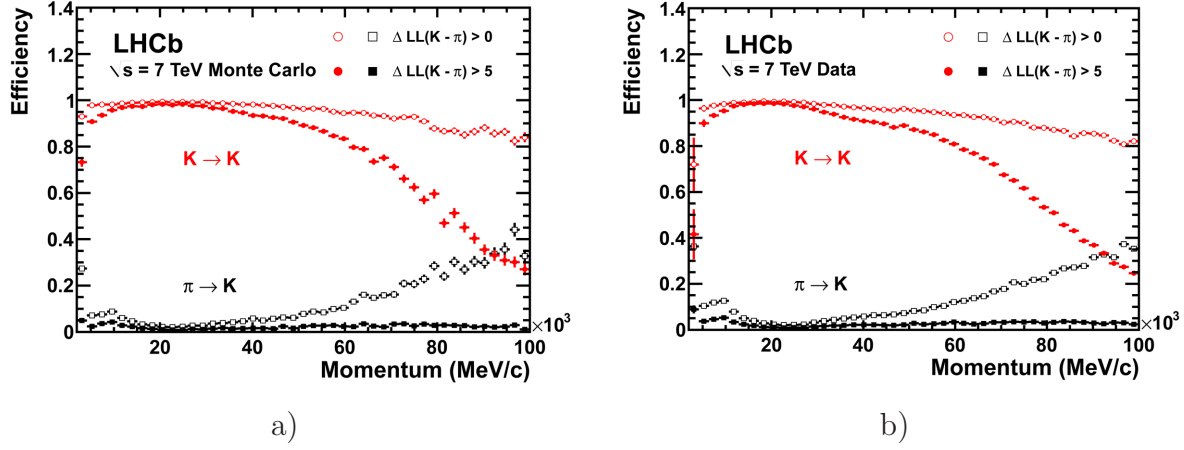


Figure 4.2: Efficiencies for kaons and pions as a function of the track momentum for the cuts $\Delta \text{Log}\mathcal{L}_{K-\pi} > 0$ and 5. (a) Monte Carlo and (b) data.

cells correspond to the PS and SPD cells. The ECAL cluster energy has to be corrected by the amount of energy deposited in the PS cells. Moreover, the granular design of the calorimeter itself introduces intrinsic losses that need to be compensated. These corrections are considered in a single expression:

$$E_c = \alpha E + \beta E_{PS} , \quad (4.4)$$

where E_{PS} is the measured energy in the PS cells. The α and β coefficients are extracted from data and depend on the ECAL region.

As the transverse distribution of the energy in the cluster is not linear, the energy weighted barycenter of equation 4.3 does not correspond to the impact position of the particle [100]. The transverse energy distribution is modelled by a single exponential in a first order approximation:

$$E(r) \sim E_0 e^{-r/b} , \quad (4.5)$$

where r is the relative position inside the cluster and b is obtained from data. In this approach, the position of the barycenter is corrected using a shower shape function according to

$$(x_c - x_0, y_c - y_0) = b \sinh^{-1} \left[\frac{(x_b - x_0, y_b - y_0) \cosh(\Delta_{cell}/2)}{(\Delta_{cell}/2) b} \right] \quad (4.6)$$

where Δ_{cell} is the transverse size of the calorimeter cell. x_0 and y_0 give the position of the central cell of the cluster. More accurate corrections involve additional shower shapes.

A longitudinal correction allows to account for the penetration of the shower in the calorimeter. It is modelled as

$$z_c = z_{ECAL} + \alpha' \ln(E) + \beta'(E_{PS}) , \quad (4.7)$$

where z_{ECAL} is the position of the front face of the electromagnetic calorimeter along the beam axis with respect to the nominal collision point.

In order to discriminate photons from charged particles, the main criteria is the isolation of the cluster with respect to the tracks extrapolated to the ECAL surface. This criteria is implemented defining a bi-dimensional χ^2 as

$$\chi^2(\vec{R}^\perp) = (\vec{R}_{tr}^\perp - \vec{R}^\perp)^T C_{tr}^{-1} (\vec{R}_{tr}^\perp - \vec{R}^\perp) + (\vec{R}_{cl}^\perp - \vec{R}^\perp)^T S^{-1} (\vec{R}_{cl}^\perp - \vec{R}^\perp) \quad (4.8)$$

where \vec{R}_{tr}^\perp is the extrapolation of the track to the surface of the ECAL, C_{tr} is the associated covariance matrix, \vec{R}_{cl}^\perp is the position of the cluster's barycenter in the same plane and S is the second moment matrix of the cluster [100]. For each track, the track matching χ^2 is minimized with respect to the variable \vec{R}^\perp . The smallest value over all the tracks is used to distinguish neutral particles clusters (large χ^2) from charged particles ones (low χ^2).

The track matching χ^2 is complemented with information from the SPD and PS detectors and the energy spread in the ECAL cluster to define the photon identification likelihood estimator. The commonly used variable is a transformation of this likelihood estimator, defined between 0 and 1 and called γ CL (CL stands for confidence level even if it is not really a confidence level).

Due to the material found between the interaction point and the calorimeter, some photons convert in an e^+e^- pair before the calorimeter front face. There are two kinds of converted photons. If the photon conversion occurs before the magnet, the electron trajectories are deflected by the magnetic field and the tracks of the two electrons can be reconstructed. Then the photon information is coming from the reconstruction of the two separated electrons. If the conversion happens after the magnet, the electrons end up in a single ECAL cluster and the converted photon can be identified using the signal left in the SPD. A cluster with no matching tracks but with a deposit in the SPD is the signature of a converted photon. Dedicated calibrations are determined for converted photons.

4.3 π^0 reconstruction

(98.823 \pm 0.034)% of the π^0 decay in two photons [6]. The π^0 signature in the ECAL depends on its kinematics, the higher is the momentum of the π^0 the closer the two photons are at the entry of the calorimeter. These two photons can then produce two separated clusters or

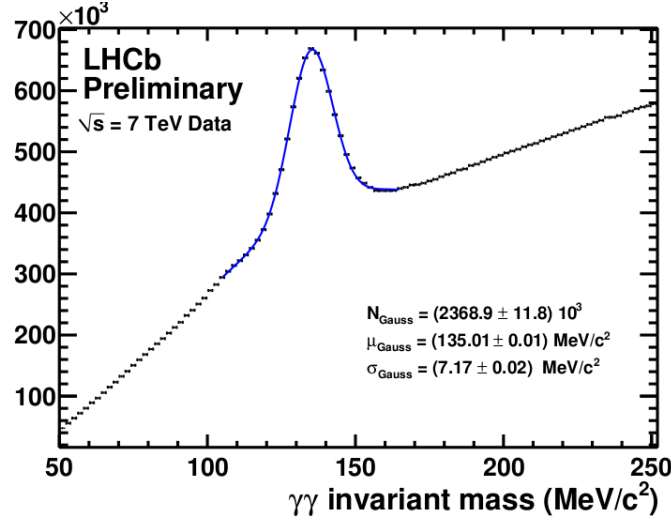


Figure 4.3: $m_{\gamma\gamma}$ distribution for non converted photons using LHCb data of summer 2010.

share a single cluster in which their individual signals are not clearly distinguishable. The π^0 are classified as resolved π^0 in the former case and as merged π^0 in the latter one.

The p_T spectrum of merged π^0 starts around 2 GeV/c. Considering the $B^0 \rightarrow \pi^+\pi^-\pi^0$ Dalitz plot (see figure 2.4), events in the corners have one particle close to rest in the B^0 rest frame. If this particle is the π^0 , events are in the corner close to the origin. Hence this corner is mainly populated with resolved π^0 while merged π^0 dominate in the other corners and the diagonal.

4.3.1 Resolved π^0

To reconstruct resolved π^0 , a loop over the photons is done, pairing the photons and comparing the resultant invariant mass, $m_{\gamma\gamma}$, with the π^0 mass. Only photons with $p_T > 200$ MeV/c and with a track matching $\chi^2 > 4$ are taken into account [100]. $m_{\gamma\gamma}$ is required to be in the range 105 to 165 MeV/c². Using those criteria and according to the simulation, the global reconstruction and identification efficiency of resolved π^0 (with respect to events such as the true γ are both in the ECAL acceptance, both with $p_T > 200$ MeV/c, and pointing to ECAL cells separated by at least one cell) is about 50% for $B^0 \rightarrow \pi^+\pi^-\pi^0$ decays [100]. Figure 4.3 shows the $m_{\gamma\gamma}$ distribution for non converted photons obtained with the LHCb data of summer 2010 (~ 3.4 nb⁻¹). The fitted parameters of the resolved π^0 peak are reported in the figure.

4.3.2 Merged π^0

Each electromagnetic cluster is split in two sub-clusters defined from the two most energetic cells. An algorithm is applied to evaluate the amount of energy corresponding to each sub-cluster. This algorithm calculates the barycenter of each sub-cluster using the transverse shower shape of individual photons. The positions of the two barycenters depend on the energy sharing between the two sub-clusters, which itself depends on the positions of the two barycenters. According to that, the calculation is done using an iterative procedure [100]. Finally each of the two sub-clusters is reconstructed as a single photon cluster (see section 4.2).

After the preparation of the two photon sub-clusters, the following criteria are applied to identify the cluster as coming from a π^0 .

- The cluster is identified as coming from a neutral particle requiring a track matching $\chi^2 > 1$.
- The cluster energy has to be compatible with the π^0 hypothesis. To assure that, a cut is applied on the minimal distance between the impacts of the two photons on the ECAL front face

$$d_{\gamma\gamma} = 2 \times z_{ECAL} \times m_{\pi^0} / E_{\pi^0} < 1.8 \Delta_{cell} , \quad (4.9)$$

where Δ_{cell} is the transverse size of the calorimeter cell, m_{π^0} is the reconstructed π^0 mass, E_{π^0} is the π^0 energy and z_{ECAL} is the position of the ECAL front face with respect to the interaction point.

- The reconstructed π^0 mass is required to be in the range 75 to 195 MeV/ c^2 .

The merged π^0 identification benefits of a relative low combinatorics compared to that of resolved π^0 . Simulation studies showed that the global reconstruction and selection efficiency of merged π^0 from $B^0 \rightarrow \pi^+ \pi^- \pi^0$ decays is about 70% (with respect to events for which the true γ are both in the ECAL acceptance, both with $p_T > 200$ MeV/ c , and pointing to the same ECAL cell or to two adjacent cells) [100]. It is lower when one or the two photons are converted and reaches $\sim 80\%$ if both photons are not converted.

4.4 $D^0 \rightarrow K^- \pi^+ \pi^0$ study

The goal of the selection of $D^0 \rightarrow K^- \pi^+ \pi^0$ decays is to provide a clear data sample of π^0 . This sample can then be used to study the π^0 energy calibration and the performances of the discrimination between photons and merged π^0 in the experiment. The high branching fraction of the $D^0 \rightarrow K^- \pi^+ \pi^0$ process, $(13.9 \pm 0.5)\%$ [6], allows to get a high statistics sample with low backgrounds. The 1 fb $^{-1}$ dataset collected in LHCb in 2011 is used in this study.

For Monte Carlo studies, a simulated sample of $D^0 \rightarrow K^- \pi^+ \pi^0$, reproducing the data taking condition in 2011, is also considered.

4.4.1 Stripping

In Chapter 3, it was discussed that the high collision rate at the LHC requires the implementation of a trigger to reduce the amount of data stored. The recorded data are first treated centrally. LHCb uses a process called “stripping” to reduce the size of the data sample as well as the CPU consumption of the various analyses. As for the trigger, the selections are implemented in lines, each line acting as a preselection for further analyses of given modes. Running over events which passed the trigger, each line should have a processing time lower than 1 ms per event and a selection rate lower than 5×10^{-4} .

The stripping selection of $D^0 \rightarrow K^- \pi^+ \pi^0$ decays we have implemented uses topological and kinematic criteria reported in table 4.1. The first set of cuts concerns the K^- and π^+ tracks. Good quality tracks are required looking at the track fit probability. The two tracks are requested not to come from a primary vertex (PV) by cutting on their minimal impact parameter (IP) χ^2 with respect to any PV. PID cuts on the K^- and π^+ tracks are also imposed. Transverse momentum (p_T) cuts are applied to the tracks and to the π^0 . In the case of resolved π^0 , a minimal γ CL cut is imposed to the two photons. The K^- , π^+ and π^0 are combined to form a D^0 candidate.

The K^- and π^+ are requested to form a good secondary vertex checking the D^0 vertex fit probability. The D^0 candidate is required to point to a PV using its minimal IP χ^2 with respect to any PV. The D^0 flight distance (FD) is then defined as the distance between the corresponding PV and the D^0 end vertex. As it should be significant, a FD χ^2 cut is used. The D^0 direction angle (θ_{DIRA}) defined as the angle between the direction of flight of the D^0 candidate, from the PV to the D^0 end vertex, and the D^0 momentum is requested to be small. Finally a relatively large D^0 mass window is used.

4.4.2 Monte Carlo results

Figure 4.4 shows the reconstructed D^0 mass distribution for merged and resolved π^0 as obtained applying the stripping selection to the $D^0 \rightarrow K^- \pi^+ \pi^0$ Monte Carlo sample. The reconstructed D^0 candidates are requested to be matched to true $D^0 \rightarrow K^- \pi^+ \pi^0$ decays. The peaks are fitted by two Crystal Balls [101] in the case of merged π^0 and by a Gaussian plus a Crystal Ball for resolved π^0 . A first order polynomial is added to account for misreconstructed events.

Description	cut
Tracks fit probability	$> 10^{-6}$
Tracks minimum IP χ^2	> 16
Tracks p_T (merged π^0)	$> 0.3 \text{ GeV}/c$
Tracks p_T (resolved π^0)	$> 0.6 \text{ GeV}/c$
Kaon PID_K	> 0
Pion PID_K	< 5
Resolved π^0 p_T	$> 1 \text{ GeV}/c$
Merged π^0 p_T	$> 2 \text{ GeV}/c$
For γ from resolved π^0 : γ_1 and γ_2 CL	> 0.2
D^0 vertex fit probability	$> 10^{-3}$
D^0 minimum IP χ^2	< 9
D^0 FD χ^2	> 64
$D^0 \cos \theta_{DIRA}$	> 0.9999
$m_{K^- \pi^+ \pi^0}$	1.6 to 2.1 GeV/c^2

Table 4.1: Cuts implemented in the $D^0 \rightarrow K^- \pi^+ \pi^0$ stripping line.

A Crystal Ball probability density function (PDF) is given by

$$f(x; \mu, \sigma, \alpha, n) = N \begin{cases} \exp\left(-\frac{(x-\mu)^2}{2\sigma^2}\right) & \text{for } \frac{x-\mu}{\sigma} > -\alpha \\ A \cdot \left(B - \frac{x-\mu}{\sigma}\right)^{-n} & \text{for } \frac{x-\mu}{\sigma} \leq -\alpha \end{cases}, \quad (4.10)$$

where

$$A = \left(\frac{n}{|\alpha|}\right)^n \exp\left(-\frac{|\alpha|^2}{2}\right), \quad (4.11)$$

$$B = \frac{n}{|\alpha|} - |\alpha|, \quad (4.12)$$

and N is a normalization factor:

$$N = \frac{1}{\sigma(C + D)}, \quad (4.13)$$

with

$$C = \frac{n}{|\alpha|} \frac{1}{n-1} \exp\left(-\frac{|\alpha|^2}{2}\right) \quad (4.14)$$

and

$$D = \sqrt{\frac{\pi}{2}} \left[1 - \text{erf}\left(\frac{|\alpha|}{\sqrt{2}}\right) \right]. \quad (4.15)$$

The merged π^0 PDF uses two Crystal Balls with left handed tails ($\alpha > 0$) sharing the same μ , α and n parameters but with different σ . In order to have similar shapes in data and Monte Carlo, the n and α parameters as well as the relative fractions of the two Crystal Balls are here fixed to the fitted values on the data sample (see section 4.4.4) which has much higher statistics.

For resolved π^0 a Crystal Ball with a right handed tail ($\alpha < 0$) is combined with a Gaussian. The right handed tail of the Crystal Ball could be explained by resolved π^0 for which the two photons clusters overlap a bit. Again, the relative fractions of the two distributions as well as the n and α parameters of the Crystal Ball are here fixed to the fitted values on data. The Crystal Ball and the Gaussian do not have the same μ and σ . Using the same μ values, one would not get a good fit of the high statistics data sample. The ratio μ_{CB}/μ_G is also fixed to the fitted value on data.

The 4-momentum of the π^0 has to be corrected to obtain the right D^0 mass peak value. For this Monte Carlo sample the components of the π^0 4-momentum are increased by 1.1% in the case of merged π^0 and by 0.6% in the case of resolved π^0 . The statistical uncertainties on those corrections are of the order of 0.1%.

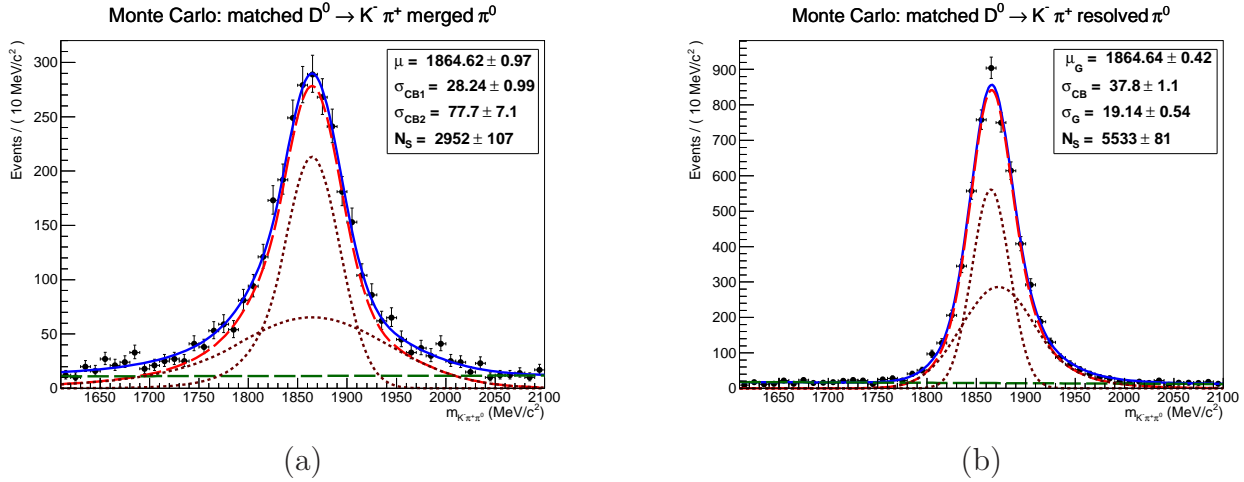


Figure 4.4: $K^- \pi^+ \pi^0$ invariant mass for the $D^0 \rightarrow K^- \pi^+ \pi^0$ Monte Carlo events passing the stripping selection for merged π^0 (a) and resolved π^0 (b). The solid blue line represents the fitted PDF. The dashed lines are the different components of the PDF.

Description	cut
No muon hit for any track	isMuon = 0
Tracks ghost probability	< 0.2
π from D^* track fit probability	> 10^{-6}
π from D^* minimum IP χ^2	< 16
D^* vertex fit probability	> 10^{-2}
D^* minimum IP χ^2	< 16
D^* FD χ^2	< 16
D^* and D^0 p_T	> 4 GeV/c
$ m_{D^{*+}} - m_{D^0} - 145.421 $	< 2 MeV/ c^2

Table 4.2: Cuts implemented in the selection of $D^{*+} \rightarrow D^0(\rightarrow K^- \pi^+ \pi^0) \pi^+$ decays.

4.4.3 $D^{*+} \rightarrow D^0 \pi^+$ selection

To improve the signal over background ratio, the $D^0 \rightarrow K^- \pi^+ \pi^0$ ($\bar{D}^0 \rightarrow K^+ \pi^- \pi^0$) candidates from the stripped data sample are requested to come from $D^{*+} \rightarrow D^0 \pi^+$ ($D^{*-} \rightarrow \bar{D}^0 \pi^-$) decays. This is a standard way to clean out the D^0 sample. It has for example been used in the study of CP violation in D^0 decays [102].

Table 4.2 shows the cuts used in the $D^{*+} \rightarrow D^0 \pi^+$ selection. The three tracks, the charged kaon and pion from the D^0 decay as well as the soft charged pion from the D^{*+} , are requested not to have associated hits in the muon chambers (isMuon = 0) and to have a small ghost probability. A ghost is a fake track reconstructed from hits of other tracks [103]. The soft pion track is requested to be of good quality and to come from a PV, cutting on the track fit probability and on the minimum IP χ^2 with respect to any PV. The D^{*+} candidate is requested to have a good end vertex and to decay at the level of a PV, checking the D^{*+} vertex fit probability, its minimum IP χ^2 and its FD χ^2 with respect to the associated PV. Transverse momentum cuts are applied to both the D^0 and the D^{*+} to reduce the combinatorial background.

Figure 4.5 shows a zoom of the $m_{D^{*+}} - m_{D^0}$ distribution obtained around the expected value, (145.421 ± 0.010) MeV/ c^2 [6]. The final $D^{*+} \rightarrow D^0 \pi^+$ selection cut is then to require this mass difference to be compatible with the expectation from the PDG within 2 MeV/ c^2 . This allows to reject a large fraction of the background.

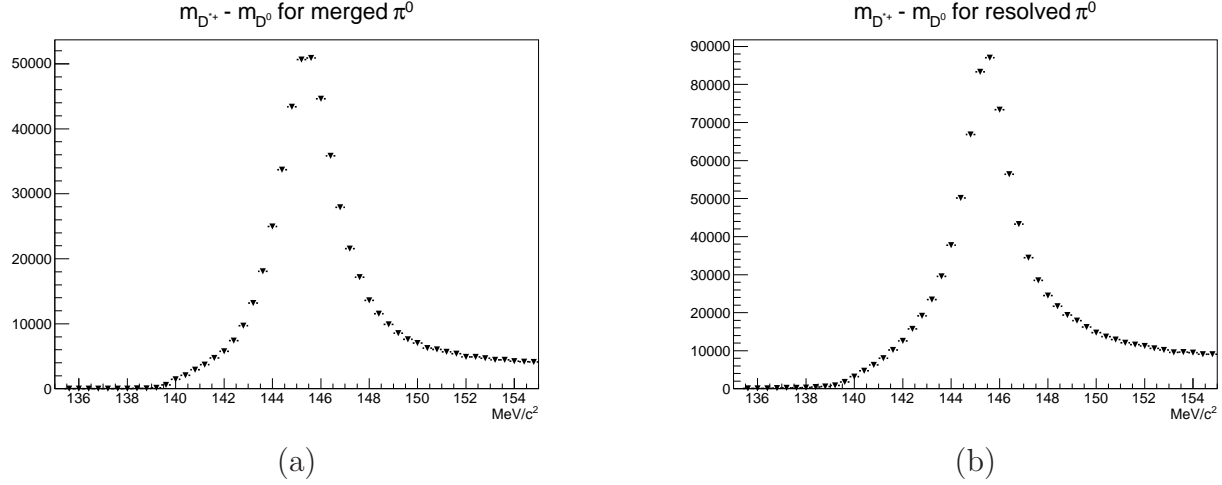


Figure 4.5: Distribution of $m_{D^{*+}} - m_{D^0}$ for the data events passing the D^{*+} selection (but the $m_{D^{*+}} - m_{D^0}$ cut) for merged π^0 (a) and resolved π^0 (b).

4.4.4 Results on data

Figure 4.6 shows the fit of the $K^- \pi^+ \pi^0$ invariant mass distribution as obtained from the $D^{*+} \pi^-$ data sample for events with merged and resolved π^0 . To fit those distributions, the signal model was adjusted on this high statistics data sample. It was then validated using a Monte Carlo sample of $D^0 \rightarrow K^- \pi^+ \pi^0$ as reported in section 4.4.2. The signal is the sum of two Crystal Balls with the same μ , α and n parameters but different σ in the case of merged π^0 . For resolved π^0 , the sum of a Crystal Ball and a Gaussian is used. The combinatorial background is modelled by a first order polynomial.

A small contribution from $D^0 \rightarrow K^- \pi^+$ events appears at high $m_{K^- \pi^+ \pi^0}$. The shape of this contribution is extracted from data using $D^0 \rightarrow K^- \pi^+$ events in the $D^{*+} \pi^-$ sample. Figure 4.7 shows the $m_{K^- \pi^+}$ distribution close to the D^0 mass. In this figure, the $D^0 \rightarrow K^- \pi^+$ component is modelled by a Gaussian in the case of merged π^0 events, by a Crystal Ball in the case of resolved π^0 events. The background in both cases is modelled by an exponential. We then use events with $m_{K^- \pi^+} > 1835 \text{ MeV}/c^2$, this corresponds to about 3σ away from the peak in the $D^0 \rightarrow K^- \pi^+$ mass distribution, and reconstruct their $m_{K^- \pi^+ \pi^0}$ spectrum as shown in figure 4.8. The $K^- \pi^+ \pi^0$ mass distributions for events with merged and resolved π^0 are fitted using two gaussians. These shapes are then used for the global $m_{K^- \pi^+ \pi^0}$ fits of figure 4.6. One can see that for merged π^0 events this contribution is found to be negligible.

The invariant mass distributions of figure 4.6 have been obtained after applying corrections to the π^0 4-momentum as explained in Appendix A. Those corrections are obtained consid-

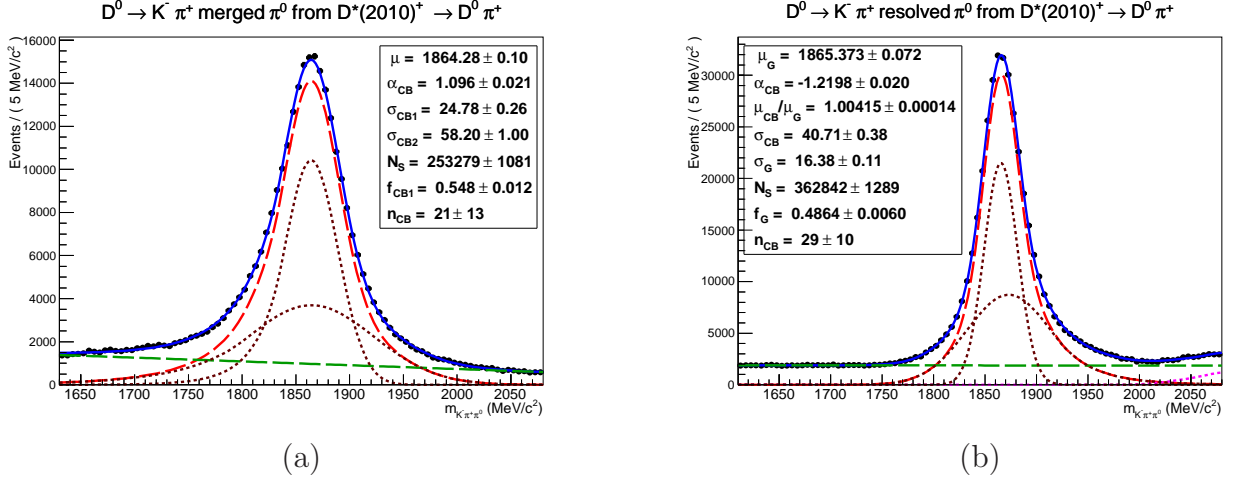


Figure 4.6: $K^- \pi^+ \pi^0$ invariant mass distribution for data events with merged π^0 (a) and resolved π^0 (b). The solid blue lines represent the fitted PDF. The signal contribution is the long dashed red line. The two signal components correspond to the short dashed brown lines. The long dashed green line is the combinatorial background component and the short dashed magenta line the $D^0 \rightarrow K^- \pi^+$ one.

ering six $D^{*+} \rightarrow D^0 \pi^+$ sub-samples for merged and resolved π^0 . For merged π^0 , the six sub-samples are defined according to the position of the π^0 in the ECAL (inner, middle and outer) and to the presence or not of any signal in the associated SPD cells. For resolved π^0 , they are made of events with both γ in the same ECAL region (inner, middle or outer) and both γ converted or not. If figure 4.6, the fitted peak values are not exactly the PDG D^0 mass. However, one would get the right mass changing the π^0 4-momentum by only about 0.1%.

4.4.5 π^0/γ discrimination

A tool has been developed in LHCb to discriminate between photons and merged π^0 . The first motivation was to remove part of the backgrounds with π^0 in the final state in the studies of B meson radiative decays. In our case, the tool may be used to reject some of the backgrounds from radiative decays.

In the π^0/γ separation tool, the relevant information from the calorimeters is combined in a multivariate analysis [104]. The tool uses the shape of the electromagnetic shower in the

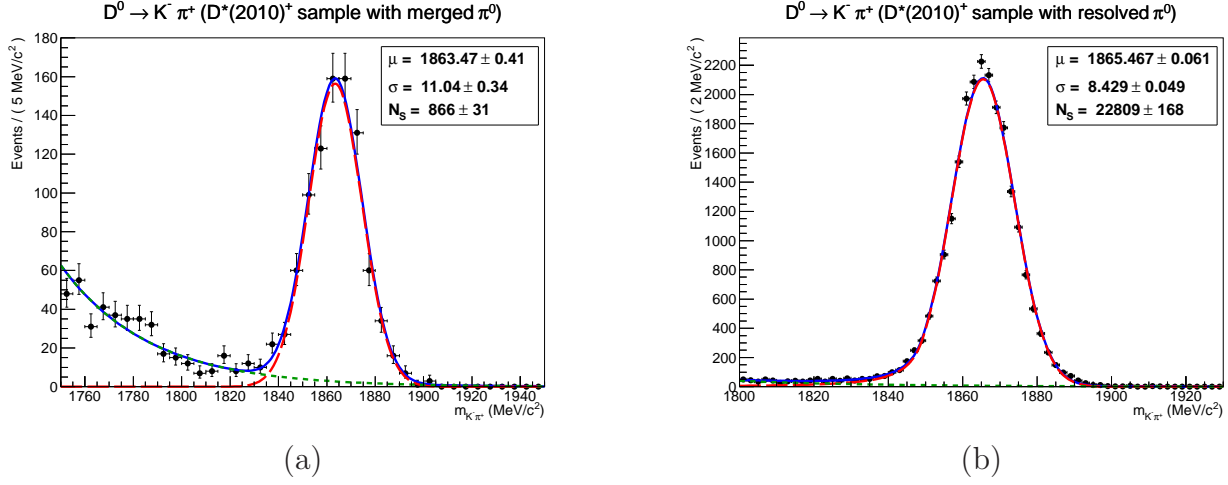


Figure 4.7: $K^- \pi^+$ invariant mass distribution close to the D^0 mass for events with merged π^0 (a) and resolved π^0 (b). The solid blue line represents the fitted PDF. The long dashed red line is the $D^0 \rightarrow K^- \pi^+$ component. The short dashed green line corresponds to the combinatorial background.

ECAL and the PS. The shower shape variables are defined from the quantities

$$\begin{aligned}
 S_{xx} &= \sum_i E_i (x_i - x_b)^2 / E_{cl} , \\
 S_{yy} &= \sum_i E_i (y_i - y_b)^2 / E_{cl} , \\
 S_{xy} &= \sum_i E_i (x_i - x_b)(y_i - y_b) / E_{cl} ,
 \end{aligned}$$

where i is the cell index in the cluster, E_i the cell energy, x_i and y_i the positions of the center of the cell in x and y , x_b and y_b the position of the barycenter of the cluster in x and y , and

$$E_{cl} = \sum_i E_i \quad (4.16)$$

the cluster energy. The ECAL shower shape variables are

- $r2 = S_{xx} + S_{yy}$, related with the spread of the shower;
- $1 - r2/r4$ with $r4 = \sum_i E_i ((x_i - x_b)^4 + (y_i - y_b)^4) / E_{cl}$, informing about the importance of the tails;
- $|S_{xy} / \sqrt{S_{xx} S_{yy}}|$, measuring the correlation in x and y ;

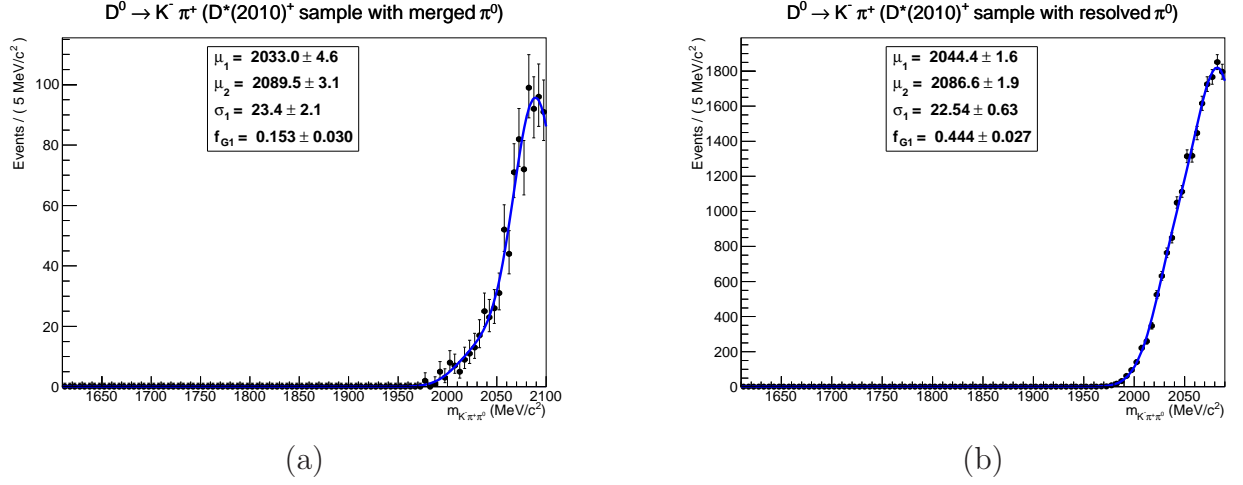


Figure 4.8: $K^- \pi^+ \pi^0$ invariant mass distribution for events with merged π^0 (a) and resolved π^0 (b) and $m_{K^- \pi^+} > 1835$ MeV/ c^2 .

- $\sqrt{1 - 4(S_{xx}S_{yy} - S_{xy}^2)/(S_{xx} + S_{yy})^2}$, describing the squashiness of the shower.

Two additional ECAL variables are used:

- E_{seed}/E_{cl} ,
- $(E_{2nd} + E_{seed})/E_{cl}$,

where E_{seed} and E_{2nd} are the energies measured in the ECAL cells with maximum and second maximum energies in the cluster.

Analogous variables are considered for the PS:

- r^2 and $|S_{xy}/\sqrt{S_{xx}S_{yy}}|$ as defined from PS cells;
- E_{max}/E_{sum} and E_{2nd}/E_{sum} with E_{max} (E_{2nd}) the energy measured in the PS cells with maximum (second maximum) energy in the cluster and E_{sum} the sum of the energies measured in the PS cells of the cluster.

In addition, the multiplicities of PS cluster cells above four different energy thresholds (0, 15, 30, and 45 MeV) are used.

The multivariate analysis has been implemented in TMVA [105, 106] and uses a multi-layer perceptron [107]. The neural network is trained using $B^0 \rightarrow K^{*0} \gamma$ and $B^0 \rightarrow K^+ \pi^- \pi^0$ Monte

Carlo samples respectively for photons and merged π^0 .

To calibrate the π^0/γ separation tool, data samples of merged π^0 and photons are taken respectively from $D^{*+} \rightarrow D^0(K^- \pi^+ \pi^0)\pi^+$ and $B^0 \rightarrow K^* \gamma$ candidates. The selection of $D^{*+} \rightarrow D^0(K^- \pi^+ \pi^0)\pi^+$ events has been presented previously. The $B^0 \rightarrow K^* \gamma$ selection is discussed in the following.

$B^0 \rightarrow K^{*0} \gamma$ selection

The selection of $B^0 \rightarrow K^{*0} \gamma$ events has been developed for measurements of the ratio of branching fractions $\mathcal{B}(B^0 \rightarrow K^{*0} \gamma)/\mathcal{B}(B_s^0 \rightarrow \phi \gamma)$ and of the direct CP asymmetry in $B^0 \rightarrow K^{*0} \gamma$ [56, 108]. Table 4.3 presents the cuts used. Most of the variables have already been introduced in 4.4.1. The helicity angle θ_H is the angle between the momentum of the B^0 candidate and the momentum of any of the K^{*0} decay products in the K^{*0} rest frame. Considering angular momentum conservation in the decays of spinless B^0 meson, the helicity angle is expected to follow a $\sin^2 \theta_H$ distribution for $B^0 \rightarrow V \gamma$ modes, where V is a vector meson. It should follow a $\cos^2 \theta_H$ function for $B^0 \rightarrow V \pi^0$ modes. The helicity angle cut therefore allows to reduce the pollution from $B^0 \rightarrow V \pi^0$ events in which the π^0 is misidentified as a photon. The B^0 vertex isolation $\Delta\chi^2$ is the minimal change in χ^2 of the B^0 end vertex fit when adding any other track in the event to this vertex. Requiring the B^0 vertex to be isolated allows to reduce the background from partially reconstructed decays of b-hadrons. Figure 4.9 presents the $K^+ \pi^- \gamma$ invariant mass distribution for events passing the $B^0 \rightarrow K^{*0} \gamma$ selection. This figure is taken from [56].

Calibration of the π^0/γ separation tool

To calibrate the π^0/γ discriminant, the remaining backgrounds in the $D^{*+} \rightarrow D^0(K^- \pi^+ \pi^0)\pi^+$ and $B^0 \rightarrow K^{*0} \gamma$ data samples are statistically subtracted using the sPlot technique [109]. A signal sWeight is attributed to each event according to the fit of the D^0 and B^0 reconstructed mass. Those fits are presented in figures 4.6 (a) and 4.9.

Figure 4.10 shows the π^0/γ discriminant distributions as obtained from Monte Carlo and Data. For photons, it accumulates between 0.8 and 1. For merged π^0 , the discriminant is more or less homogeneously distributed between 0 and 1. There is a small peak in the same region as for photons. This is because the most energetic π^0 produce showers very similar to the ones from photons.

From the distributions of figure 4.10 the efficiency curves for γ and π^0 are obtained. These

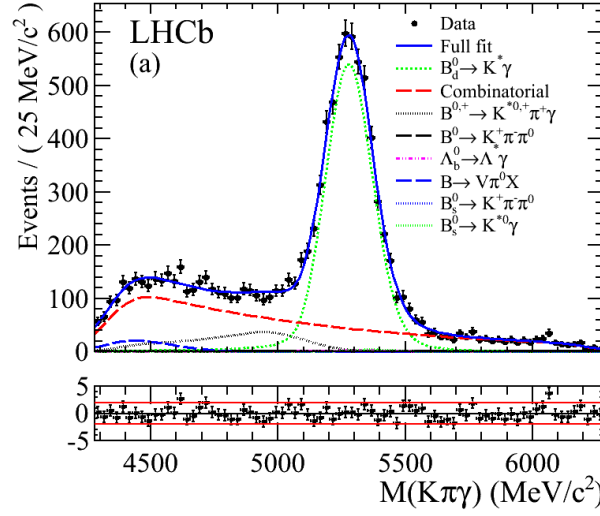


Figure 4.9: $m_{K^+\pi^-\gamma}$ distribution for $B^0 \rightarrow K^*\gamma$ candidates in the LHCb data sample of 2011.

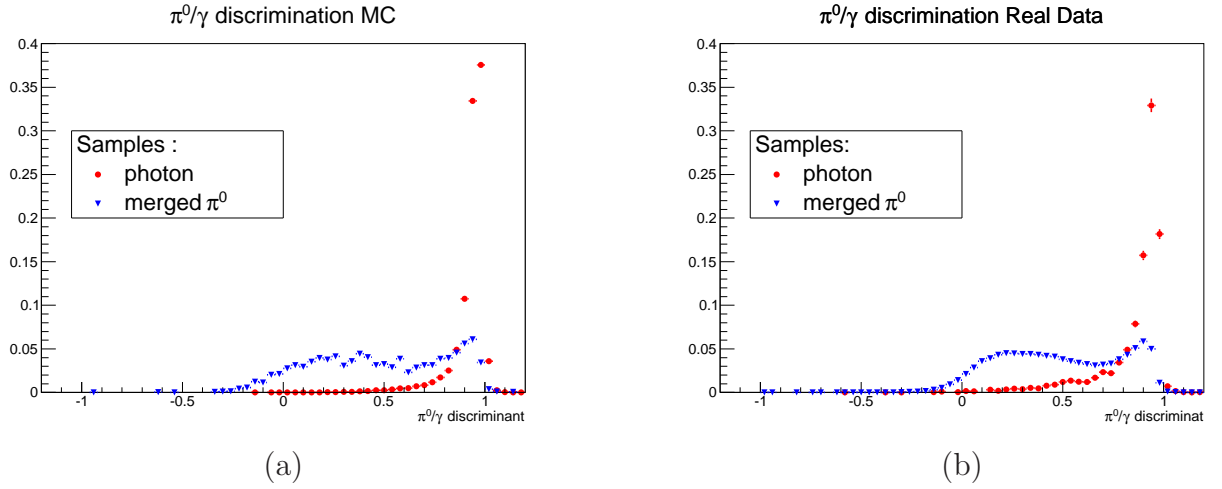


Figure 4.10: Distributions of the π^0/γ discriminant for π^0 from $D^0 \rightarrow K^- \pi^+ \pi^0$ and photons from $B^0 \rightarrow K^{*0}\gamma$ in Monte Carlo (a) and real data (b).

Description	cut
Tracks fit χ^2/ndof	< 5
Tracks minimum IP χ^2	> 25
Tracks p_T	$> 0.5 \text{ GeV}/c$
At least one track with p_T	$> 1.2 \text{ GeV}/c$
Kaon PID _K	> 5
Kaon PID _K -PID _p	> 2
Pion PID _K	< 0
Reconstructed $m_{K^{*0}}$ - PDG $m_{K^{*0}}$	$< 50 \text{ MeV}/c^2$
K^{*0} vertex fit χ^2	< 9
γ transverse energy	$> 2.6 \text{ GeV}$
γ CL	> 0.25
B^0 p_T	$> 3 \text{ GeV}/c$
B^0 minimum IP χ^2	< 9
B^0 FD χ^2	> 100
B^0 θ_{DIRA}	$< 20 \text{ mrad}$
B^0 $ \cos \theta_H $	< 0.8
B^0 vertex isolation $\Delta\chi^2$	> 2

Table 4.3: Selection of $B^0 \rightarrow K^{*0}\gamma$ candidates.

are presented in figure 4.11. For π^0 , they are similar in data and simulation. This is not the case for photons for which a higher tail is found on data. Requiring the π^0/γ discriminant to be lower than 0.8 corresponds in data to an efficiency of around 80% for merged π^0 and 20% for photons. Figure 4.12 shows the evolution of the π^0 and photon efficiency for this cut as a function of the π^0/γ p_T . The merged π^0 efficiency decreases with the π^0 p_T : as already mentioned the most energetic π^0 are difficult to distinguish from photons.

4.5 Summary

The π^0 reconstruction is essential in the analysis of charmless three body decays of B mesons with π^0 in the final state. The charged particle identification is also necessary to distinguish among the different decay channels.

A selection of $D^{*+} \rightarrow D^0(K^-\pi^+\pi^0)\pi^+$ events has been implemented. It allows to extract a clean and very high statistics sample of π^0 . Using the data collected in 2011 one gets about 2.5×10^5 and 3.6×10^5 signal events with merged π^0 and resolved π^0 respectively. This sample

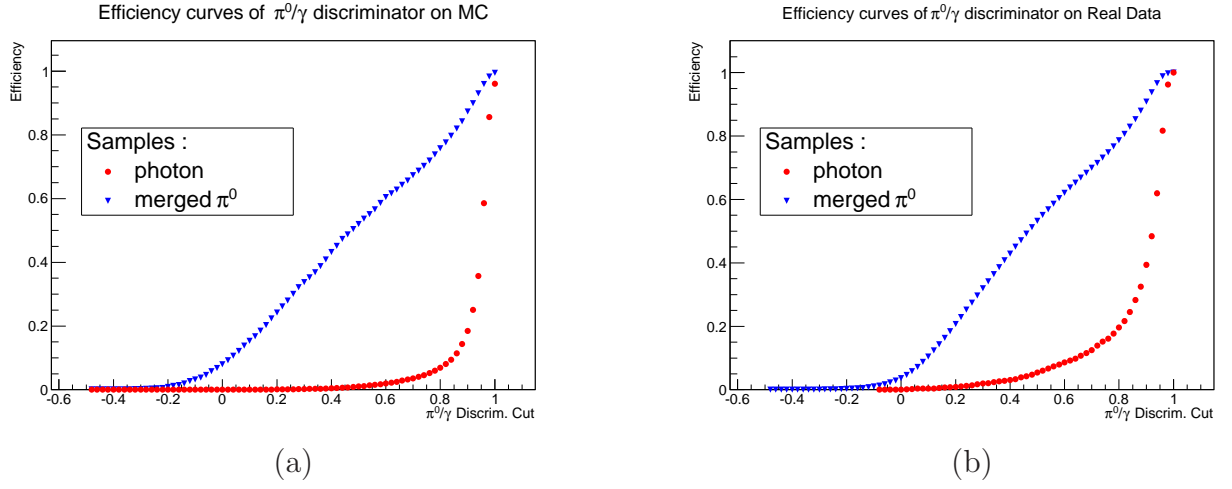


Figure 4.11: Efficiency curves of the π^0/γ discriminator (asking the discriminator to be lower than the running value) for π^0 from $D^0 \rightarrow K^-\pi^+\pi^0$ events and photons from $B^0 \rightarrow K^{*0}\gamma$ events in Monte Carlo (a) and real data (b).

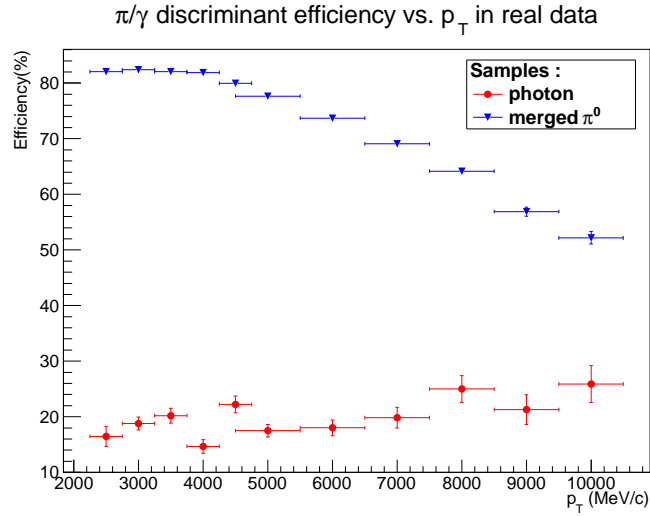


Figure 4.12: Efficiency for merged π^0 from $D^0 \rightarrow K^-\pi^+\pi^0$ events and photons from $B^0 \rightarrow K^{*0}\gamma$ events, requiring the π^0/γ discriminant to be lower than 0.8, as a function of the π^0/γ p_T .

has been used to evaluate corrections on the π^0 energy calibration and to calibrate the π^0/γ discriminant of the experiment.

Selection of $B_{d,s}^0 \rightarrow h^+ h'^- \pi^0$ events

Charmless B decays are characterized by small branching fractions. Dedicated selections have to be implemented to extract them from the various physics processes occurring at the LHC. In this chapter the selection of charmless three-body decays with a π^0 in the final state is described. The data recorded in 2011 is used in this analysis. The sample corresponds to 1 fb^{-1} of proton-proton collisions collected at $\sqrt{s} = 7 \text{ TeV}$. The chapter starts by an introduction discussing the Monte Carlo samples that are used, how the expected yields will be evaluated and the selection strategy. The different steps of the selection are then presented: first at the level of the trigger, next for the stripping and at last the final selection.

5.1 Introduction

5.1.1 Monte Carlo samples

Samples of fully simulated events are used to study the signals and the specific backgrounds. They were generated according to the data taking conditions of 2011 in LHCb: a center of mass energy of 7 TeV and a mean number of visible interactions per bunch crossing μ of 1.7 (MC11a). They are mainly used to give an idea of the efficiencies of each selection stage guiding the design of the selection.

The list of Monte Carlo samples used is shown in table 5.1. It can be divided in three sets: signal, partially reconstructed background and radiative background. For the signal, the resonant samples include Dalitz models of the decays. The $B^0 \rightarrow \pi^+ \pi^- \pi^0$ resonant sample also includes CP violation, it corresponds to what has been presented in section 2.1.2. The resonant samples will be used to tune the selection. However, considering the fact that the efficiency varies along the Dalitz plane, they only give indicative efficiencies which correspond

to their own Dalitz models and not to the Dalitz distributions that will be obtained from data.

To get a better estimate of the efficiencies, they have to be mapped in the Dalitz plane. This is the purpose of the square Dalitz samples. Those do not contain any Dalitz model. They give flat distributions in the so-called square Dalitz plane. A square Dalitz plane is just a transformation of the Dalitz plane defining

$$m' = \frac{1}{\pi} \arccos \left(2 \frac{m_{+-} - m_{+-}^{\min}}{m_{+-}^{\max} - m_{+-}^{\min}} - 1 \right) \text{ and } \theta' = \frac{1}{\pi} \theta_{+-} \quad (5.1)$$

where m_{+-} is the $h^+ h'^-$ invariant mass, $m_{+-}^{\max} = m_{B_{d/s}^0} - m_{\pi^0}$, $m_{+-}^{\min} = m_{h^+} + m_{h'^-}$, and θ_{+-} the helicity angle defined as the angle between the h^+ and the negative B momentum in the rest frame of the “particle” obtained from the addition of the h^+ and h'^- 4-momenta.

Square Dalitz plots have some advantages compared to the standard Dalitz ones. The boundaries of the Dalitz plot are very important since they are usually quite populated and since the interferences between light mesons take place here. In Dalitz plots, large variations occur over small areas. In square Dalitz plots, the region corresponding to low mass resonances and to their interferences are expanded. In addition, they have the shape of a rectangle (m' and θ' are between 0 and 1) so there is no need to define curved edge of bins on the boundaries.

To increase the effective statistics of the square Dalitz samples, they are produced using tight cuts at the generator level:

- h^+ and h'^- polar angles (θ) between 5 and 400 mrad;
- both photons from the π^0 in the calorimeter acceptance;
- h^+ and h'^- $p_T > 495$ MeV/c;
- π^0 $p_T > 800$ MeV/c;
- $B_{d/s}$ $p_T > 2.5$ GeV/c.

All events passing the selection presented in the following of this chapter satisfy those generator level cuts, so they do not introduce any bias. In fact, the square Dalitz samples do not give flat distributions in the square Dalitz plane because of the tight cuts used at the generator level. This is not an issue because the events cut at the generator level would have in any case been cut during the selection. However, to make sure we really start from flat distributions, generator level only square Dalitz samples were produced requiring only the polar angle of the b hadron to be lower than 400 mrad at the generator level. This cut do not bias the square Dalitz distributions.

Table 5.1 gives for each sample the number of events generated and the efficiency of the generator level cuts. The efficiencies are around 7% for the tight cuts of the square Dalitz samples and 33% when only requiring $\theta_{b\text{-hadron}} < 400$ mrad as for their generator level only counterparts. The $\Lambda_b \rightarrow \Lambda(1520)\gamma$ also only use this cut.

Sample	Statistics	Generator eff. (%)
$B^0 \rightarrow \pi^+\pi^-\pi^0$ (resonant, CPV)	1012496	17.15 ± 0.01
$B^0 \rightarrow K^+\pi^-\pi^0$ (resonant)	1027495	16.02 ± 0.05
$B_s^0 \rightarrow K^-\pi^+\pi^0$ (resonant)	1033000	16.15 ± 0.05
$B^0 \rightarrow \pi^+\pi^-\pi^0$ (square Dalitz)	2039488	6.47 ± 0.03
$B^0 \rightarrow K^+\pi^-\pi^0$ (square Dalitz)	1842988	6.66 ± 0.03
$B_s^0 \rightarrow K^-\pi^+\pi^0$ (square Dalitz)	1874493	6.78 ± 0.03
$B_s^0 \rightarrow K^+K^-\pi^0$ (square Dalitz)	2034491	7.38 ± 0.03
$B^0 \rightarrow \pi^+\pi^-\pi^0$ (gen. level)	2160000	32.86 ± 0.03
$B^0 \rightarrow K^+\pi^-\pi^0$ (gen. level)	3160000	32.82 ± 0.03
$B_s^0 \rightarrow K^-\pi^+\pi^0$ (gen. level)	2660000	32.75 ± 0.03
$B_s^0 \rightarrow K^+K^-\pi^0$ (gen. level)	1520000	32.83 ± 0.03
$B^0 \rightarrow \rho^+\rho^-$	497997	14.29 ± 0.05
$B^+ \rightarrow \rho^+\rho^0$	496997	15.00 ± 0.05
$B^0 \rightarrow \rho^0\gamma$	1803990	22.35 ± 0.06
$B^0 \rightarrow K^*\gamma$	7537965	23.41 ± 0.09
$B_s^0 \rightarrow \phi\gamma$	6888469	20.11 ± 0.06
$\Lambda_b \rightarrow \Lambda(1520)\gamma$	516000	33.21 ± 0.08
$\Lambda_b \rightarrow \Lambda(1670)\gamma$	1064492	24.44 ± 0.06

Table 5.1: Monte Carlo samples used in the analysis for signal (top), partially reconstructed background (middle) and radiative background (bottom). The second column shows the generated Monte Carlo statistics and the third one lists the efficiency of the generator level cuts.

For the other decays, the charged particles and the photons from the π^0 are required to have polar angles in the ranges 10 to 400 mrad and 5 to 400 mrad, respectively. Those cuts are applied for charged particles and π^0 directly coming from the b-hadron or from the promptly decaying resonances. For $B \rightarrow \rho\rho$ and resonant signal samples, the generator level efficiencies are between 14 and 17%. They are higher for the radiative decays, 20 to 24%, as there is no requirement on the photon. With respect to those standard cuts, the tight cuts applied for the square Dalitz samples allow to increase the effective statistics by more than a factor 2.

5.1.2 Extraction of the expected yields

The expected number of events from any specific decay of B mesons is extracted according to

$$N_{exp} = 2 \times \mathcal{L} \times \sigma_{b\bar{b}} \times f_q \times \mathcal{B} \times \epsilon_{tot} . \quad (5.2)$$

\mathcal{L} is the integrated luminosity, 1fb^{-1} for 2011. $\sigma_{b\bar{b}}$ is the production cross section of pairs of $b\bar{b}$ quarks, which LHCb measured as $(284 \pm 20 \pm 49)\mu\text{b}$ [110] for pp collisions at $\sqrt{s} = 7\text{ TeV}$. f_q is the hadronization fraction of a \bar{b} quark into $\bar{b}q$ meson, where q can be d , u or s . f_q is replaced by $f_{\Lambda_b^0}$ if a Λ_b^0 baryon is produced. Reliable predictions of these hadronization fractions are not possible because the calculation is beyond the scope of the perturbative regime. They have to be determined experimentally. LHCb have performed measurements of the ratios $f_s/(f_d + f_u)$, $f_{\Lambda_b^0}/(f_d + f_u)$ and f_s/f_d [111]. For instance the measured value of f_s/f_d is 0.256 ± 0.020 . \mathcal{B} is the product of the branching fractions of the considered b decay and subsequent decays, $\mathcal{B}(B^0 \rightarrow \pi^+\pi^-\pi^0) \times \mathcal{B}(\pi^0 \rightarrow \gamma\gamma)$ for instance. ϵ_{tot} is the global reconstruction and selection efficiency of the decay.

Table 5.2 reports the measured branching fractions relevant here [6]. The $B^0 \rightarrow \phi\gamma$ branching fraction, is taken from the ratio $\mathcal{B}(B^0 \rightarrow K^{*0}\gamma)/\mathcal{B}(B_s^0 \rightarrow \phi\gamma)$ measured in LHCb [108]. LHCb has also reported an estimation of the $\Lambda_b^0 \rightarrow \Lambda^*\gamma$ branching fraction [108]:

$$\mathcal{B}(\Lambda_b^0 \rightarrow \Lambda^*(pK)\gamma) \times \frac{f_{\Lambda_b^0}}{f_d} = (4.2 \pm 0.7) \times 10^{-6} , \quad (5.3)$$

where Λ^* stands for the $\Lambda(1520)$ and further massive baryon resonances promptly decaying to pK^- final state. Assuming from isospin symmetry $f_{\Lambda_b^0}/f_d$ to be one half of $f_{\Lambda_b^0}/(f_d + f_u)$ [112] one obtains the $\Lambda_b \rightarrow \Lambda^*\gamma$ branching fraction presented in table 5.2. The $B_s^0 \rightarrow h^+h'\pi^0$ modes have not been observed yet: some predictions were already reported in table 2.1.

The efficiency may be written as

$$\epsilon_{tot} = \epsilon_{gen} \times \epsilon_{trig} \times \epsilon_{strip} \times \epsilon_{sel} . \quad (5.4)$$

ϵ_{gen} is the generator efficiency, calculated at the generator level as the fraction of generated events passing the generator level cuts.

The ϵ_{strip} factor is the stripping efficiency. The stripping selection is the first offline selection applied to reduce the size of the data samples to be further analyzed. The stripping efficiency is computed from Monte Carlo as the ratio between the number of events selected in the stripping over the number of simulated events.

The ϵ_{trig} factor is the trigger efficiency. It is evaluated from Monte Carlo through the emulation of the trigger. Here it is defined as the fraction of stripped events passing the trigger.

Decay channel	Branching fraction ($\times 10^{-5}$)
$B^0 \rightarrow \rho^0 \pi^0$	0.2 ± 0.05
$B^0 \rightarrow \rho^\pm \pi^\mp$	2.3 ± 0.23
$B^0 \rightarrow K^+ \pi^- \pi^0$	3.78 ± 0.32
$B^0 \rightarrow \rho^+ \rho^-$	2.42 ± 0.31
$B^+ \rightarrow \rho^+ \rho^0$	2.40 ± 0.19
$B^0 \rightarrow \rho^0 \gamma$	0.086 ± 0.015
$B^0 \rightarrow K^*(892)^0 \gamma$	4.33 ± 0.15
$B^0 \rightarrow K_2^*(1430)^0 \gamma$	1.24 ± 0.24
$B_s^0 \rightarrow \phi \gamma$	3.3 ± 0.3
$\Lambda_b \rightarrow \Lambda^* \gamma$	$0.75^{+0.01}_{-0.05}$

Table 5.2: Measured branching fractions relevant in this study, including the already observed $B^0 \rightarrow h^+ h'^- \pi^0$ decays.

This definition is not the usual, normally the trigger efficiency is obtained from the events passing the whole offline selection. This is however equivalent when considering the overall efficiency. The definition chosen here allows to separate the trigger from the optimization of the final selection.

ϵ_{sel} accounts for the efficiency of the additional selection cuts with respect to the stripping selection. As the RICH performances are not very well reproduced in the simulation, ϵ_{sel} is written as

$$\epsilon_{sel} = \epsilon_{selNoPID}^{MC} \times \epsilon_{PID}^{Data} . \quad (5.5)$$

$\epsilon_{selNoPID}^{MC}$ accounts for all the cuts additional to the stripping ones, except the particle identification criteria, and is obtained from the simulation as the fraction of stripped events passing those cuts. The efficiency of the particle identification cuts, ϵ_{PID}^{Data} , is obtained from data using dedicated calibration samples as discussed in 4.1.

5.1.3 Selection strategy

The main characteristic of b-hadrons is their relatively long lifetime (~ 1.5 ps, except for the B_c^\pm which lifetime is about three times smaller). Given the excellent vertexing resolution of the VELO and the important boosts of the b-hadrons produced at the LHC ($\beta\gamma$ typically of the order of ten), it is possible to distinguish the primary vertex (PV), where the b-hadron is produced, from the secondary vertex where its decay takes place. Another important characteristic of b-hadrons is their high masses (~ 5 GeV/c²) compared to other hadrons. This drives the kinematics of the decay: most of the mass of the b-hadron is transformed in

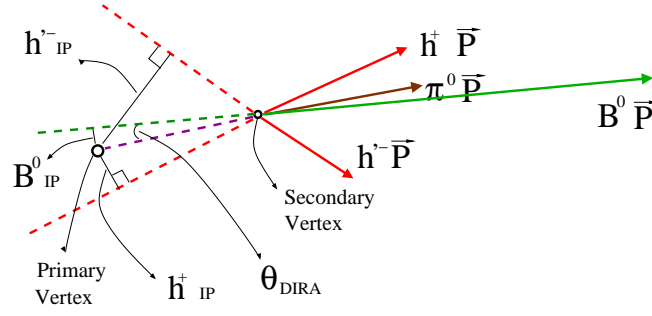


Figure 5.1: Representation of a $B^0 \rightarrow h^+ h'^- \pi^0$ event.

kinetic energy of the decay products which tend to scatter in directions with large angles with respect to the direction of flight of the b-hadron. As a result, the b-hadron decay products have typically high transverse momenta. In the particular case of $B_{d,s}^0 \rightarrow h^+ h'^- \pi^0$ decays, the final state consists of two tracks and a π^0 . The main selection criteria are (see figure 5.1):

- The two tracks should be of good quality. It can be tested looking at the χ^2/ndof of the track fit.
- The two tracks must not come from a PV, meaning that the impact parameter (IP) of their trajectories with respect any PV has to be large.
- The two tracks should form a secondary vertex. The χ^2 of the vertex fit has to be small.
- The B meson has to come from a PV. Its reconstructed IP has to be small with respect to this point.
- The flight distance (FD) of the B^0 is the distance between the primary and secondary vertices. It has to be significant, of the order of few millimeters considering the B^0 lifetime and its typical boost.
- The direction of flight of the B^0 from the primary to the secondary vertices should match the direction of the momentum of the B^0 , obtained as the vector sum of the momentum of the final particles. The matching is measured by the angle between the direction of flight of the B^0 and the direction of the momentum of the B^0 . This so-called direction angle (θ_{DIRA}) has to be small, no more than a few dozen milliradians.
- The transverse momentum (p_T) of the final particles is high, over hundreds of MeV/c.
- The 3-body invariant mass has to be in the B^0 mass range.

Selection criterion	AllL0 line	Photon Line
VELO track IP	$> 125 \mu\text{m}$	
VELO track hits	> 9	
Missed VELO track hits	< 3	
Track p	$> 12.5 \text{ GeV}/c$	$> 8.0 \text{ GeV}/c$
Track p_T	$> 1.5 \text{ GeV}/c$	$> 0.8 \text{ GeV}/c$
Track fit χ^2/ndof	< 3	< 5
Track minimum IP χ^2	> 36	

Table 5.3: Selection cuts of the Hlt1 lines Hlt1TrackAllL0 and Hlt1TrackPhoton.

The selection is done in three stages, first the trigger, then a dedicated stripping selection followed by the final selection. The final selection implements some cuts to reject specific backgrounds and a multivariate analysis method to improve the purity rejecting most of the combinatorial background. Particle identification criteria are finally used to separate the different $h^+h'^-\pi^0$ samples, i.e. $\pi^+\pi^-\pi^0$, $K^\pm\pi^\mp\pi^0$ and $K^+K^-\pi^0$.

5.2 Trigger selection

The L0 and Hlt1 triggers are based on standard LHCb trigger lines which were described in Chapter 3. At L0 the event is required to trigger one of the L0Photon, L0Electron or L0Hadron lines. In the Hlt1 the single track trigger lines *Hlt1TrackPhoton* or *Hlt1TrackAllL0* [113] are used.

Table 5.3 shows the selection cuts of those Hlt1 lines. The track quality is evaluated with the number of hits in the VELO, the number of missing hits and the χ^2/ndof of the track fit. The track is required to have significant IP with respect to the PV and sufficient momentum (p) and p_T .

The cuts reported in table 5.3 seem to be tight, in particular the kinematic ones. However one should consider that these conditions are applied to each individual track, meaning that a single track fulfilling the criteria is enough to trigger on the event. This is the case for most of the $b\bar{b}$ events. The efficiency of the single track lines has been investigated in Monte Carlo B meson decay samples [113]. The efficiencies found are from 71% for $B_s^0 \rightarrow \phi\gamma$ to 88% for $B^+ \rightarrow h^+h^+h^-$. In the particular case of $B^0 \rightarrow \pi^+\pi^-\pi^0$ the Hlt1 trigger efficiency is shown in table 5.5.

The Hlt2 lines considered here are the standard topological lines *Hlt2Topo2BodySimple*, *Hlt2Topo2BodyBBDT* and a dedicated line *Hlt2B2HHPi0_Merged*. The topological lines were

Observable	Cut
Tracks p_T	$> 0.5 \text{ GeV}/c$
Tracks p	$> 5 \text{ GeV}/c$
Tracks fit χ^2/ndof	< 2.4
Tracks minimum IP χ^2	> 9
Tracks DOCA	$< 0.2 \text{ mm}$
$\pi^0 p_T$	$> 2.5 \text{ GeV}/c$
B p_T	$> 3 \text{ GeV}/c$
B end vertex χ^2	< 10
B IP χ^2	< 25
B θ_{DIRA}	$< 16 \text{ mrad}$
B FD χ^2	> 100
B mass	$4.2 \text{ to } 6.4 \text{ GeV}/c^2$

Table 5.4: Selection cuts of the Hlt2B2HHPi0_Merged trigger line. DOCA is the distance of closest approach between two tracks.

explained in Chapter 3. The additional line has been designed and implemented for this study to improve the Hlt2 efficiency for events with a merged π^0 . In those events, the π^0 carries most of the energy of the B meson, then the tracks have lower transverse momentum and the topological lines are less efficient. The cuts used in this dedicated line are reported in table 5.4. The cuts in the tracks p and p_T are imposed by the trigger tracking reconstruction. As it requires calorimeter reconstruction which takes some additional CPU time, this line runs only on events triggered by the L0 photon or electron lines from which most of the signal events with a merged π^0 are coming.

Trigger categories

In LHCb, events passing the trigger can be separated in three categories.

- Trigger Independent of Signal (TIS): events selected by the trigger independently of the signal decay products. The rest of the event allows to fire the trigger.
- Trigger On Signal (TOS): events for which the signal decay products satisfied by themselves, independently of the rest of the event, the trigger requirements.
- Trigger On Both (TOB): events triggered partially on the signal decay products and partially on the rest of the events, this last category is mutually exclusive of the two first.

Most of the signal events are in the TOS category which is also the cleanest one. For signals with clean signatures and sufficient statistics, the TIS category may be used to evaluate the trigger efficiency on data considering the overlap between the TIS and TOS categories. The TIS efficiency is then

$$\epsilon_{TIS} = \frac{N^{TIS\&TOS}}{N^{TOS}}. \quad (5.6)$$

Similarly, the TOS efficiency is

$$\epsilon_{TOS} = \frac{N^{TIS\&TOS}}{N^{TIS}}. \quad (5.7)$$

The global trigger efficiency can be evaluated from the TIS one as

$$\epsilon_{TRIG} = \epsilon_{TIS} \frac{N^{TRIG}}{N^{TIS}}. \quad (5.8)$$

In this analysis, events are required to be in the TOS category for each trigger level:

- L0: Photon, Electron or Hadron lines;
- Hlt1: TrackAllL0 or TrackPhoton lines;
- Hlt2:
 - Merged π^0 : Topo2BodySimple or Topo2BodyBBDT or B2HHPi0_Merged lines;
 - Resolved π^0 : Topo2BodySimple or Topo2BodyBBDT lines.

This allows to remove an important fraction of the background ($\sim 60\%$ for resolved and $\sim 40\%$ for merged π^0 events) for a limited loss of signal efficiency ($\sim 10\%$). For illustration, table 5.5 shows the trigger efficiencies at each trigger level for $B^0 \rightarrow \pi^+\pi^-\pi^0$ Monte Carlo events passing the stripping selection (see next section). The global trigger efficiency is around 40% for signal events with a merged π^0 and a bit smaller than 30% for those with a resolved π^0 . The Hlt2 trigger efficiency for merged π^0 without the *Hlt2B2HHPi0_Merged* line is $46.2 \pm 0.7\%$. The achieved efficiency using this line is $72.9 \pm 0.6\%$ as reported in table 5.5.

5.3 Stripping Selection

As already mentioned in 4.4.1, stripping selections are run centrally in LHCb to reduce the size of the data sample as well as the CPU consumption of the various analyses. We have designed a stripping line dedicated to charmless B decays to $h^+h'^-\pi^0$. The cuts used are reported in table 5.6 and the corresponding plots are presented in appendix B. The cuts on

Trigger Level	π^0 merged eff.	π^0 resolved eff.
L0	79.8 ± 0.4 %	52.7 ± 0.6 %
Hlt1	71.2 ± 0.5 %	76.4 ± 0.7 %
Hlt2	72.9 ± 0.6 %	68.2 ± 0.9 %
Global	41.4 ± 0.5 %	27.5 ± 0.5 %

Table 5.5: Trigger efficiencies on $B^0 \rightarrow \pi^+\pi^-\pi^0$ Monte Carlo events passing the stripping selection.

Observable	merged π^0	resolved π^0
Tracks p_T	> 0.5 GeV/c	
Tracks p	> 5 GeV/c	
Tracks fit χ^2 probability	$> 10^{-6}$	
Tracks minimum IP χ^2	> 25	
π^0 p_T	> 2.5 GeV/c	> 1.5 GeV/c
Minimum γ CL	-	> 0.2
B p_T	> 3 GeV/c	> 2.5 GeV/c
B end vertex χ^2 probability	$> 10^{-3}$	
B minimum IP χ^2	< 9	
B θ_{DIRA}	< 10 mrad	
B FD χ^2	> 64	
B mass	4.2 to 6.4 GeV/ c^2	

Table 5.6: Selection cuts of the $B_{d,s}^0 \rightarrow h^+h'^-\pi^0$ stripping line.

the tracks p and p_T correspond to the ones used in the trigger, which are imposed by the trigger tracking reconstruction.

Table 5.7 shows the stripping efficiencies for the different Monte Carlo samples. In the case of merged π^0 , the efficiencies for the radiative decays are of the same order as the ones for the signal modes. This is because merged π^0 and energetic photons have similar signatures. Table 5.7 also presents the trigger efficiencies, defined with respect to events passing the stripping selection.

5.4 Final Selection

The data sample obtained thanks to the stripping selection is treated as follows:

- Identify the two tracks as π^\pm or K^\pm to divide the sample in three interesting sub-

Sample	Merged π^0		Resolved π^0	
	Stripp Eff. (%)	Trigg Eff. (%)	Stripp Eff. (%)	Trigg Eff. (%)
$B^0 \rightarrow \pi^+\pi^-\pi^0$	0.859 ± 0.009	41.4 ± 0.5	0.669 ± 0.008	27.5 ± 0.5
$B^0 \rightarrow K^+\pi^-\pi^0$	0.963 ± 0.010	44.1 ± 0.5	0.908 ± 0.009	24.6 ± 0.4
$B_s^0 \rightarrow K^-\pi^+\pi^0$	1.333 ± 0.011	42.2 ± 0.4	1.054 ± 0.010	20.6 ± 0.4
$B^0 \rightarrow \rho^+\rho^-$	0.537 ± 0.010	38.5 ± 0.9	0.396 ± 0.009	23.1 ± 0.9
$B^+ \rightarrow \rho^+\rho^0$	0.603 ± 0.011	37.1 ± 0.9	0.446 ± 0.009	15.8 ± 0.8
$B_s^0 \rightarrow \phi\gamma$	1.137 ± 0.004	39.1 ± 0.2	0.097 ± 0.001	14.1 ± 0.4
$B^0 \rightarrow \rho^0\gamma$	1.570 ± 0.009	40.0 ± 0.3	0.135 ± 0.003	14.5 ± 0.7
$B^0 \rightarrow K^{*0}\gamma$	1.467 ± 0.004	40.5 ± 0.1	0.128 ± 0.001	13.9 ± 0.3
$\Lambda_b \rightarrow \Lambda(1520)\gamma$	0.875 ± 0.013	40.6 ± 0.7	0.076 ± 0.004	12.6 ± 1.7
$\Lambda_b \rightarrow \Lambda(1670)\gamma$	1.296 ± 0.011	41.7 ± 0.4	0.111 ± 0.003	14.5 ± 1.0

Table 5.7: Stripping and trigger efficiencies for the different Monte Carlo samples.

samples, $\pi^+\pi^-\pi^0$, $K^\pm\pi^\mp\pi^0$ and $K^+K^-\pi^0$;

- Identify specific backgrounds peaking in the $h^+h'^-$ mass spectra and apply simple cuts to reject them;
- Reduce the combinatorial background using a multivariate analysis.

Those three steps are described hereafter. Finally, radiative backgrounds are discussed. Those are the most dangerous backgrounds as they are peaking in the signal region considering the reconstructed B mass. We will see that we have to limit ourselves to high $m_{h^+h'^-}$ regions where their contributions are negligible while they dominate at low $m_{h^+h'^-}$.

5.4.1 Tracks identification

The division of the data sample in the different $B_{d,s}^0 \rightarrow h^+h'^-\pi^0$ channels is done using the track PID discussed in Chapter 4. Considering the kinematic similarities between the $B_{d,s}^0 \rightarrow h^+h'^-\pi^0$ and $B_{d,s}^0 \rightarrow K_S^0 h^+h'^-$ decays, we use in this work the same PID cuts and assume the same PID efficiencies as in the $B_{d,s}^0 \rightarrow K_S^0 h^+h'^-$ study documented in [50]. The PID cuts applied to π^\pm and K^\pm candidates are reported in table 5.8. As the PID here only relies on the RICHs, the tracks are first required to have associated RICH information (hasRich=1). The cuts in the difference log-likelihoods then concerns the K/π separation and the rejection of proton tracks.

According to the discussion of Chapter 4, the PID cut efficiencies have to be determined on data using calibration samples. As reported in table 5.9, the calibration data are limited

Candidate	π^\pm	K^\pm
Rich Information		hasRich = 1
Kaon Requirement	PID _K < 0	PID _K > 5
Proton Requirement	PID _p < 10	PID _p - PID _K < 10

Table 5.8: PID cuts applied to π^\pm and K^\pm candidates.

Observable	Cuts
momentum	$p < 100 \text{ GeV}/c$
pseudo-rapidity	$1.5 < \eta < 5$

Table 5.9: Kinematic cuts applied on tracks corresponding to the fiducial region of the calibration data.

in momentum and pseudo-rapidity. Those kinematic cuts are then applied to the tracks of the $h^+h'^-\pi^0$ samples. The PID is in any case less performant for tracks above 100 GeV/c, especially for what concerns the K/p separation.

Table 5.10 shows the various identification and misidentification efficiencies corresponding to the cuts of table 5.8. The uncertainties reported in this table correspond to the sum in quadrature of the statistical uncertainty due to the finite statistics in the Monte Carlo and in the calibration samples, the systematic uncertainty related to the PID calibration method itself, and the systematic uncertainty estimated to account for PID efficiency variations across the Dalitz plane [50]. The statistical uncertainty is negligible. The systematic uncertainty related to efficiency variations in the Dalitz plane is the dominant contribution. As explained in 4.1, the efficiencies are calculated per event, considering both tracks to account for the kinematic correlations between the tracks. Depending of the mode, the efficiency with both tracks correctly identified is between 73 and 79%. The efficiencies corresponding to one misidentified track are between 2 and 8%. For both tracks misidentified, the efficiencies are around 1 to 2 per mille.

5.4.2 Specific backgrounds peaking in the $m_{h^+h'^-}$ spectra

To investigate potential backgrounds, the two body invariant mass spectra combining either the two tracks or a track with the reconstructed π^0 are studied. For the tracks, the pion, kaon and proton hypothesis were tried. Specific backgrounds were found peaking in the $m_{\pi^+\pi^-}$, $m_{K^\pm\pi^\mp}$, $m_{K^+K^-}$, and $m_{p\pi^-}$ ($m_{\bar{p}\pi^+}$) spectra. Nothing was found in the $m_{h^\pm\pi^0}$ ones.

Mode	Eff (%)	Mode	Eff (%)
$\pi\pi \rightarrow \pi\pi$	78.6 ± 2.0	$K\pi \rightarrow \pi K$	0.13 ± 0.03
$\pi\pi \rightarrow K\pi$	4.58 ± 0.92	$K\pi \rightarrow KK$	1.88 ± 0.57
$\pi\pi \rightarrow KK$	0.06 ± 0.04	$KK \rightarrow \pi\pi$	0.18 ± 0.10
$K\pi \rightarrow \pi\pi$	3.87 ± 0.96	$KK \rightarrow K\pi$	7.79 ± 1.36
$K\pi \rightarrow K\pi$	74.5 ± 3.6	$KK \rightarrow KK$	72.3 ± 4.7

Table 5.10: Efficiencies of the PID cuts defined in table 5.8 as obtained in the $B_{d,s}^0 \rightarrow K_S^0 h^+ h'^-$ study of reference [50].

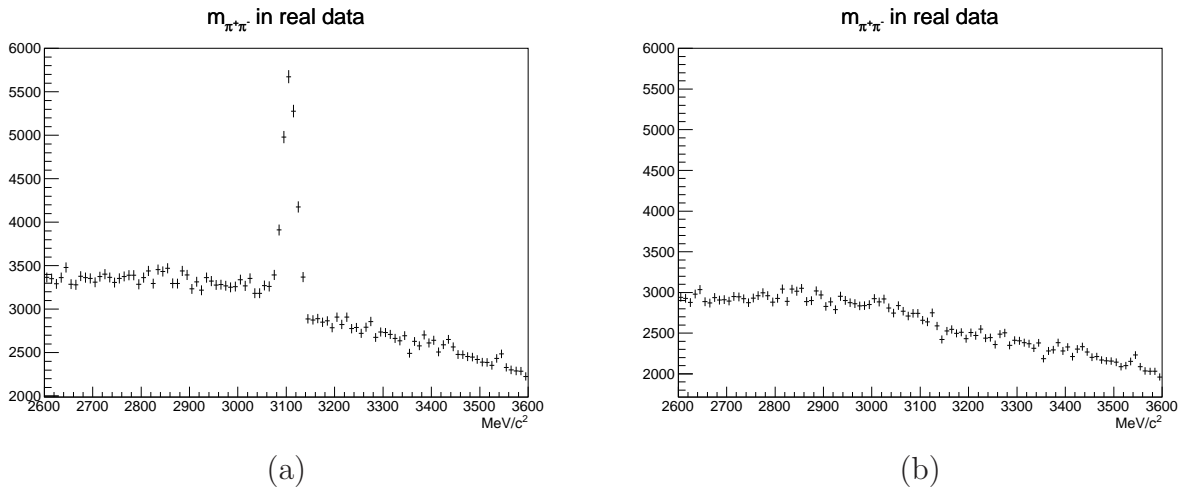


Figure 5.2: Distribution of $m_{\pi^+\pi^-}$ between 2.6 and 3.6 GeV/c^2 without (a) and with (b) the $\text{isMuon} = 0$ requirement.

Figure 5.2 shows the $m_{\pi^+\pi^-}$ distribution between 2.6 and 3.6 GeV/c^2 . There is a clear peak of J/ψ on the left plot. It is easily eliminated, as one can see on the right plot, requiring that both tracks have no associated hits in the muon chambers ($\text{isMuon}=0$). This cut is applied hereafter.

As shown on figure 5.3, the $m_{\pi^+\pi^-}$ spectrum presents in addition to the expected $\rho^0 \rightarrow \pi^+\pi^-$ contribution clear peaks of $K_S^0 \rightarrow \pi^+\pi^-$, $D^0 \rightarrow \pi^+\pi^-$ and even $D^0 \rightarrow K^-\pi^+$ with a misidentified kaon. The $m_{K^\pm\pi^\mp}$ and $m_{K^+K^-}$ distributions also have clear contributions from D^0 two body decays as one can see in figure 5.4. Figure 5.5 shows that a small contamination of $\Lambda \rightarrow p\pi^-$ is also found.

These specific backgrounds are rejected applying the cuts of table 5.11. As already mentioned, tracks with associated hits in the muon chambers are not considered. In addition,

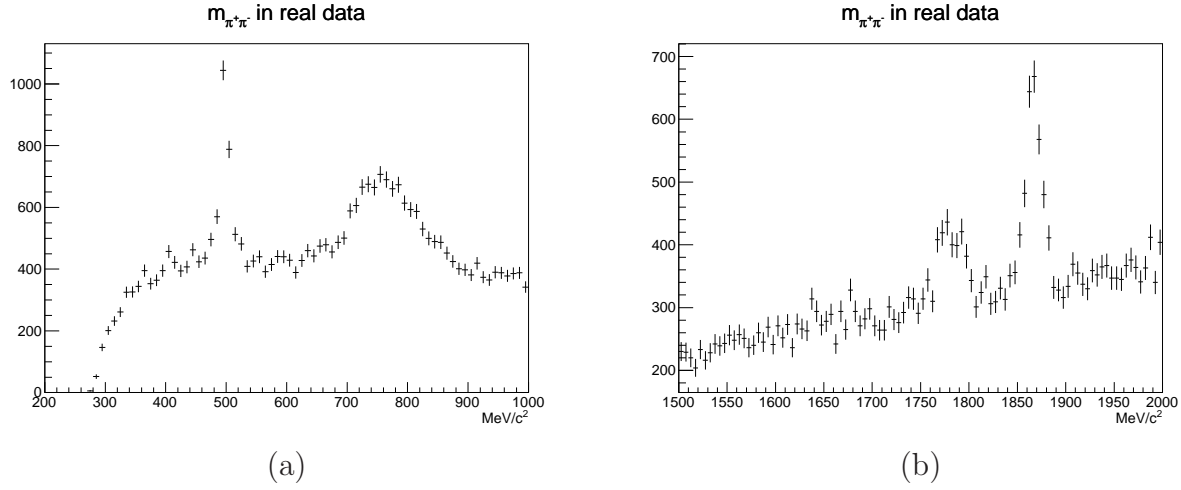


Figure 5.3: Distribution of $m_{\pi^+\pi^-}$ below 1 GeV/c^2 (a) and between 1.5 and 2 GeV/c^2 (b).

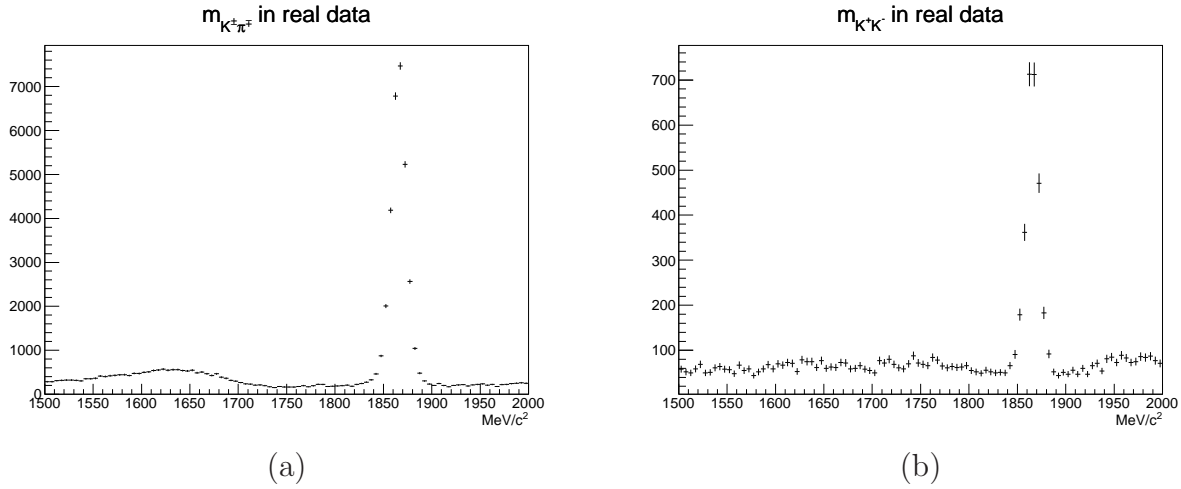
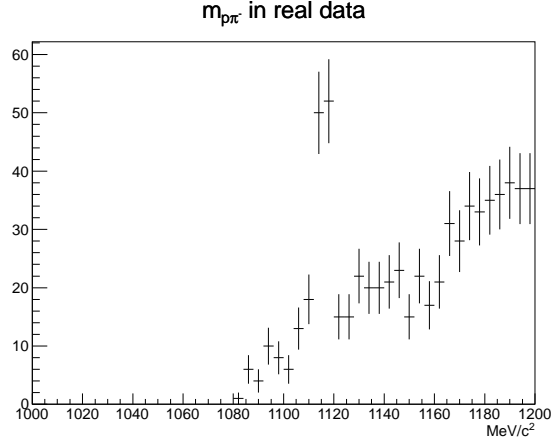


Figure 5.4: Distribution of $m_{K^\pm\pi^\mp}$ (a) and $m_{K^+K^-}$ (b) between 1.5 and 2 GeV/c^2 .

Figure 5.5: Distribution of $m_{p\pi^-}$ below of 1.2 GeV/ c^2 .

Observable	cut
No muon hit for any track	isMuon = 0
$ m_{\pi^+\pi^-} - m_{K_S^0} $	$> 30 \text{ MeV}/c^2$
$ m_{p\pi^-} - m_{\Lambda} $	$> 10 \text{ MeV}/c^2$
$ m_{\pi^+\pi^-} - m_{D^0} $	$> 30 \text{ MeV}/c^2$
$ m_{K^\pm\pi^\mp} - m_{D^0} $	$> 30 \text{ MeV}/c^2$
$ m_{K^+K^-} - m_{D^0} $	$> 30 \text{ MeV}/c^2$

Table 5.11: Cuts to reject specific backgrounds peaking in the $m_{h+h'^-}$ spectra.

vetoed are applied on $K_S^0 \rightarrow \pi^+\pi^-$, $\Lambda \rightarrow p\pi^-$, $D^0 \rightarrow \pi^+\pi^-$, $D^0 \rightarrow K^+\pi^-$, and $D^0 \rightarrow K^+K^-$ decays.

Figure 5.6 shows that the stripped data sample contains a small contamination of $B^0 \rightarrow K^+\pi^-$ events. This contamination can not be removed cutting on the $K^\pm\pi^\mp$ invariant mass as this would bias the $m_{K^\pm\pi^\mp\pi^0}$ distribution. These events produce a small, non peaking contribution at high $m_{K^\pm\pi^\mp\pi^0}$.

5.4.3 Additional cuts

Before applying the multivariate analysis, additional cuts are used to reduce the backgrounds. The first criterion is to reject tracks likely to be fake tracks. A fake or ghost track is a track reconstructed from pseudo-random combinations of hits associated to multiple charged tracks.

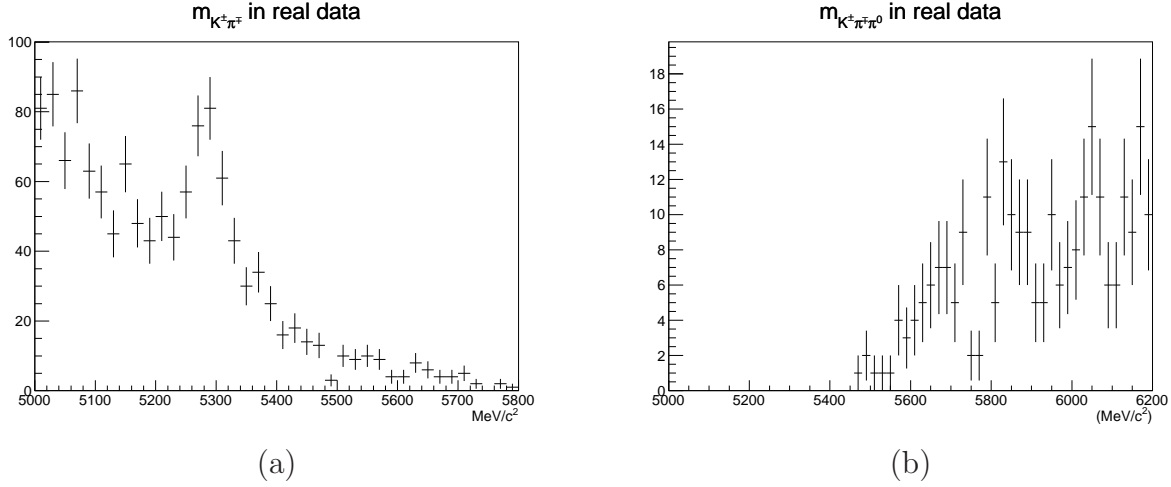


Figure 5.6: Distribution of $m_{K^{\pm}\pi^{\mp}}$ between 5.0 and 5.8 GeV/c^2 (a). $m_{K^{\pm}\pi^{\mp}\pi^0}$ distribution for events with $m_{K^{\pm}\pi^{\mp}}$ between 5220 and 5340 MeV/c^2 (b).

The average ghost rate for long tracks is 27% and for muon tracks is 17%. Ghost tracks typically have low track fit χ^2 probability and missing hits. The standard ghost probability estimator developed in the collaboration [103] is used. This allows to reject part of the combinatorial background associated with misreconstructed tracks.

As we will see in 5.4.5, the multivariate analysis will be designed to reject the combinatorial background, taking as background training sample the high hand of the reconstructed B^0 mass distribution. It will have little effect on partially reconstructed backgrounds. Those are events arising from B decays with one or more decay products in addition to the two tracks and the π^0 of the signal final state. To reduce the contamination from partially reconstructed backgrounds, the isolation of the B^0 decay vertex is considered. The compatibility of any other track in the event with the B^0 end vertex is checked. The track is added to the vertex and the variation of the vertex χ^2 fit is computed. The minimal χ^2 variation ($\Delta\chi_{min}^2$), looping over all the tracks but the initial h^+ and h'^- ones, quantifies the isolation of the B^0 vertex.

Figure 5.7 shows the distribution of the maximum ghost probability of the two tracks and of the square root of the vertex isolation $\Delta\chi_{min}^2$. The signal distributions correspond to Monte Carlo $B^0 \rightarrow \pi^+\pi^-\pi^0$. The background ones have been obtained from real data events passing the stripping selection and having a reconstructed B^0 mass between 5.8 and 6.3 GeV/c^2 . This region is fully dominated by the combinatorial background. On the plots of figure 5.7, the vertical lines represents the cut used. These are reported in table 5.12. Even if the $\Delta\chi_{min}^2$ cut is initially considered to reduce partially reconstructed backgrounds, it also removes a large fraction of the combinatorial background.

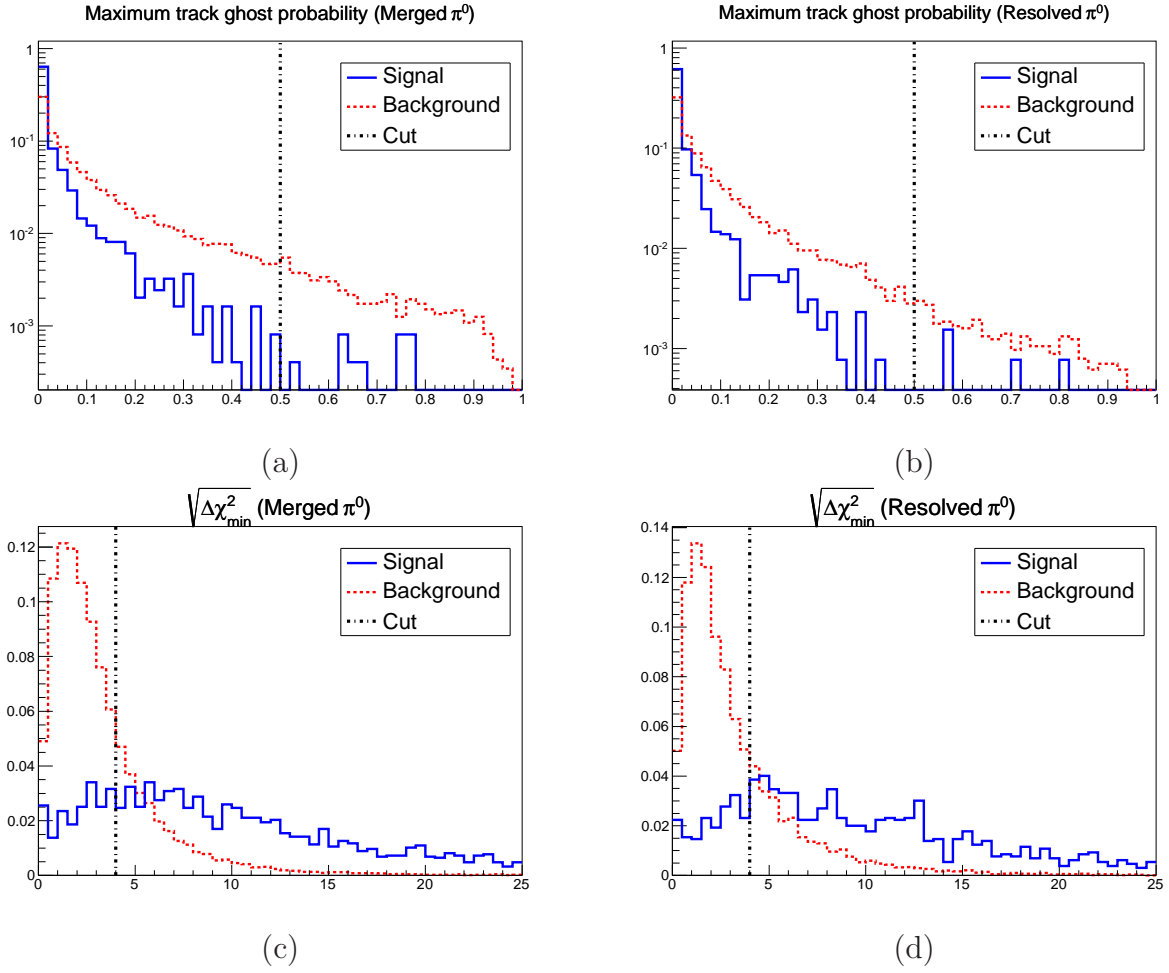


Figure 5.7: Distribution of the maximum ghost probability over the two tracks (top) and of the square root of the vertex isolation $\Delta\chi^2_{min}$ (bottom) for events reconstructed with a merged π^0 (left) and a resolved π^0 (right).

Variable	Cut
Tracks ghost probability	< 0.5
B^0 vertex isolation $\Delta\chi^2_{min}$	> 16

Table 5.12: Additional cuts to reduce combinatorial and partially reconstructed backgrounds.

Sample	Eff Merged (%)	Eff Resolved (%)
$B^0 \rightarrow \pi^+\pi^-\pi^0$	61.13 ± 0.80	62.97 ± 1.12
$B^0 \rightarrow K^+\pi^-\pi^0$	61.74 ± 0.73	62.03 ± 1.01
$B_s^0 \rightarrow K^-\pi^+\pi^0$	60.84 ± 0.64	62.85 ± 1.02
$B^0 \rightarrow \rho^+\rho^-$	56.88 ± 1.54	57.99 ± 2.31
$B^+ \rightarrow \rho^+\rho^0$	29.08 ± 1.36	33.43 ± 2.52
$B^0 \rightarrow \rho^0\gamma$	68.52 ± 0.44	71.87 ± 2.40
$B^0 \rightarrow K^{*0}\gamma$	64.38 ± 0.23	67.92 ± 1.27
$B_s^0 \rightarrow \phi\gamma$	60.23 ± 0.28	55.92 ± 1.60
$\Lambda_b \rightarrow \Lambda(1520)\gamma$	53.00 ± 1.16	46.93 ± 7.12
$\Lambda_b \rightarrow \Lambda(1670)\gamma$	66.36 ± 0.62	69.19 ± 3.52

Table 5.13: Monte Carlo efficiencies of the preselection cuts of tables 5.9, 5.11 and 5.12 in the case of $\pi^+\pi^-\pi^0$ reconstruction.

5.4.4 Preselection efficiency

Tables 5.8, 5.9, 5.11 and 5.12 list all the cuts used between the stripping and the multivariate analysis presented in the next section. The efficiencies of the PID cuts, as extracted from data in the study of $B_{d,s}^0 \rightarrow K_S^0 h^+ h'^-$ decays of reference [50], have already been reported in table 5.10. The efficiencies of the remaining cuts are obtained from the simulation. They are reported in table 5.13. In this table, they were evaluated reconstructing the final state as $\pi^+\pi^-\pi^0$. Almost identical results are found considering the $K^\pm\pi^\mp\pi^0$ and $K^+K^-\pi^0$ reconstructions. For completeness, those are given in tables 5.14 and 5.15.

5.4.5 Multivariate analysis

A multivariate analysis is implemented to improve the signal over background ratio. It intends to reduce the combinatorial background mainly using topological variables. It is trained with Monte Carlo samples for the signal, and data events in the upper part of the reconstructed B^0 mass spectrum for the background.

Multivariate classifiers combine correlated input variables into a discriminant output. They

Sample	Eff Merged (%)	Eff Resolved (%)
$B^0 \rightarrow \pi^+ \pi^- \pi^0$	61.30 ± 0.80	62.99 ± 1.12
$B^0 \rightarrow K^+ \pi^- \pi^0$	62.00 ± 0.73	62.29 ± 1.01
$B_s^0 \rightarrow K^- \pi^+ \pi^0$	61.02 ± 0.64	63.00 ± 1.02
$B^0 \rightarrow \rho^+ \rho^-$	56.71 ± 1.53	58.26 ± 2.30
$B^+ \rightarrow \rho^+ \rho^0$	29.20 ± 1.35	33.43 ± 2.52
$B^0 \rightarrow \rho^0 \gamma$	68.65 ± 0.43	72.32 ± 2.38
$B^0 \rightarrow K^{*0} \gamma$	64.58 ± 0.22	68.12 ± 1.27
$B_s^0 \rightarrow \phi \gamma$	60.36 ± 0.28	56.16 ± 1.60
$\Lambda_b \rightarrow \Lambda(1520) \gamma$	53.05 ± 1.16	45.83 ± 7.19
$\Lambda_b \rightarrow \Lambda(1670) \gamma$	66.55 ± 0.62	69.12 ± 3.52

Table 5.14: Monte Carlo efficiencies of the preselection cuts of tables 5.9, 5.11 and 5.12 in the case of $K^\pm \pi^\mp \pi^0$ reconstruction.

Sample	Eff Merged (%)	Eff Resolved (%)
$B^0 \rightarrow \pi^+ \pi^- \pi^0$	61.23 ± 0.80	62.92 ± 1.12
$B^0 \rightarrow K^+ \pi^- \pi^0$	61.72 ± 0.73	62.00 ± 1.01
$B_s^0 \rightarrow K^- \pi^+ \pi^0$	60.75 ± 0.64	62.86 ± 1.02
$B^0 \rightarrow \rho^+ \rho^-$	56.45 ± 1.53	58.04 ± 2.30
$B^+ \rightarrow \rho^+ \rho^0$	28.86 ± 1.35	33.43 ± 2.52
$B^0 \rightarrow \rho^0 \gamma$	68.47 ± 0.44	72.36 ± 2.39
$B^0 \rightarrow K^{*0} \gamma$	64.39 ± 0.23	68.05 ± 1.27
$B_s^0 \rightarrow \phi \gamma$	60.21 ± 0.28	56.33 ± 1.60
$\Lambda_b \rightarrow \Lambda(1520) \gamma$	52.68 ± 1.16	43.75 ± 7.16
$\Lambda_b \rightarrow \Lambda(1670) \gamma$	66.29 ± 0.62	69.19 ± 3.52

Table 5.15: Monte Carlo efficiencies of the preselection cuts of tables 5.9, 5.11 and 5.12 in the case of $K^+ K^- \pi^0$ reconstruction.

have to be trained over signal and background samples. The training allows to determine the internal parameters of the classifier that maximize the separation between the two samples. Many multivariate methods exist and their relative performances depend on the problem. In this work three methods were tested: Fisher discriminant, artificial neural network and boosted decision trees. Each is briefly described in the following.

The Fisher discriminant [114] identifies the linear projection of the input variables that maximizes the distance between the means of the two classes of events while minimizing the variance within each class. If μ_1 and μ_2 denote the means of the two classes, σ_1^2 and σ_2^2 their variances, the axis onto which the input variables are projected is defined maximizing

$$\frac{|\mu_1 - \mu_2|}{\sigma_1^2 + \sigma_2^2} . \quad (5.9)$$

The Fisher discriminant is a simple and safe classifier. However, it only accounts for linear correlations between the input variables.

An artificial neural network consists in a set of interconnected nodes or neurons by analogy with biological neural networks. Each neuron produces a non-linear response depending on a given set of input signals. The nodes are generally organized in layers, each layer being fully connected to the next one. This type of neural networks is called a multilayer perceptron (MLP). The first layer corresponds to the input variables. The last one consists in a single node which gives the MLP output. There are one or several intermediate layers called hidden layers.

Boosted Decision Trees (BDT) provide another powerful event classifier. A decision tree is a sequence of binary splits of the data. Each split is done according to the input variable that, at this stage, gives the best separation between signal and background when being cut on. The process is repeated until a given number of final nodes is reached. It can also end if all nodes are pure signal or background, or if a node has too few events. Decision trees are known to be powerful but unstable as small changes in the training samples can produce large changes in the tree. They are stabilized thanks to a boosting algorithm. The training events which were misclassified have their weight increased (boosted) to form a new tree. Many trees are built up this way. They are finally combined into a single classifier given by the average of the individual decision trees.

To apply those methods, we used the Toolkit for Multivariate Analysis (TMVA) [105]. TMVA provides a ROOT [106] integrated environment and implements a variety of multivariate classifiers through a common interface. In the following, the preparation of the signal and background samples is discussed.

Sample	Merged	Resolved
Signal	4726	2281
Background	17646	7354

Table 5.16: Yields of the signal and background samples.

Signal and background samples

The signal and background samples are made of events passing the stripping selection and all the preselection but the PID cuts in table 5.8. The PID cuts are not applied as the same multivariate classifier will be used for the different decay modes. The PID variables are not expected to be correlated with the input variables of the multivariate analysis.

For the signal, the $B^0 \rightarrow \pi^+\pi^-\pi^0$ and $B^0 \rightarrow K^+\pi^-\pi^0$ Monte Carlo samples are used. They correspond to the two modes that have already been measured. The events reconstructed in the simulation are required to be matched to Monte Carlo truth decays.

For the background, we take real data events with a reconstructed B^0 mass between 5.8 and 6.3 GeV/ c^2 . This region is fully dominated by the combinatorial background. The signal region as well as the lower hand of the reconstructed B^0 mass spectrum should be avoided as they contain signal-like events from the signal itself and from partially reconstructed backgrounds. In the background sample, the events are reconstructed as $B^0 \rightarrow \pi^+\pi^-\pi^0$. Table 5.16 gives the number of events in the signal and background samples for merged and resolved π^0 . Half of the samples will be used to train the multivariate classifiers, the other half to test them.

Input variables

The information provided by the detector concerns the kinematics of the event, its topology and the identification of the final state particles. The discriminating variables used in the multivariate analysis should be selected carefully. They should have similar behaviors for the different $B_{d,s}^0 \rightarrow h^+h^-\pi^0$ modes that are investigated. Variables involving the kinematics of the decays can not be used as they would bias the measurement in the Dalitz plane. For this reason topological variables are favoured. Table 5.17 gives the list of input variables. Most of them have already been introduced. The only kinematical one is the p_T of the B meson candidate. The FD χ^2 and IP χ^2 of the B meson candidate with respect to its associated PV (the one for which the B IP χ^2 is minimum) are used as well as its θ_{DIRA} angle and the χ^2 probability of its end vertex fit. The minimum IP χ^2 of any of the two tracks with respect to any PV is also considered. The only variable that was not mentioned earlier concerns the maximum distance between any of the two tracks and the B meson candidate line of flight.

Description	Variable
B transverse momentum	$B \ p_T$
B FD significance	$\sqrt{B \text{ FD} \chi^2}$
B IP significance	$\sqrt{B \text{ IP} \chi^2}$
B direction angle	θ_{DIRA}
B end vertex fit probability	$-\log_{10}(B \text{ vertex prob})$
Tracks minimum IP significance	$\sqrt{\min \text{ Tr IP} \chi^2}$ $= \min(\sqrt{\min \text{ IP} \chi^2(h^+)}, \sqrt{\min \text{ IP} \chi^2(h'^-)})$
Tracks maximum distance to the B line of flight	$\max \text{ Tr Dist B}$ $= \max(d_{3D}(h^+, B), d_{3D}(h'^-, B))$
Photons minimum γ CL (resolved π^0 only)	$\min \gamma \text{ CL}$ $= \min(\text{CL}(\gamma_1), \text{CL}(\gamma_2))$

Table 5.17: TMVA input variables. The B flight distance and impact parameter are defined with respect to the associated primary vertex. For each track, the impact parameter corresponds to the minimum impact parameter with respect to any primary vertex.

The B line of flight is evaluated using the space point defined by the primary vertex (\vec{R}_{PV}) and the direction given by the B momentum (\vec{p}_B). For the charged hadron, its momentum (\vec{p}_h) and the B end vertex (\vec{R}_{EV}) are used. The distance between the charged hadron and the B lines of flight is calculated as

$$d_{3D}(h, B) = \frac{\det[(\vec{R}_{EV} - \vec{R}_{PV}), \vec{P}_B, \vec{P}_h]}{|\vec{P}_B \times \vec{P}_h|}. \quad (5.10)$$

For events with a resolved π^0 , the minimum γ CL over the two photons is also used. Figures 5.8 and 5.9 show the distributions of the input variables for events with a merged or resolved π^0 . Other variables were tested in addition to those presented here but gave marginal improvements on the multivariate selection.

Selection of the multivariate classifier

Figure 5.10 shows the performances of the three classifiers in terms of background rejection versus signal efficiency. Those curves are obtained with the test samples, not used during the training of the classifiers. The three methods have relatively similar performances, especially for resolved π^0 events. The BDT is chosen as it gives the best background rejection for any signal efficiency.

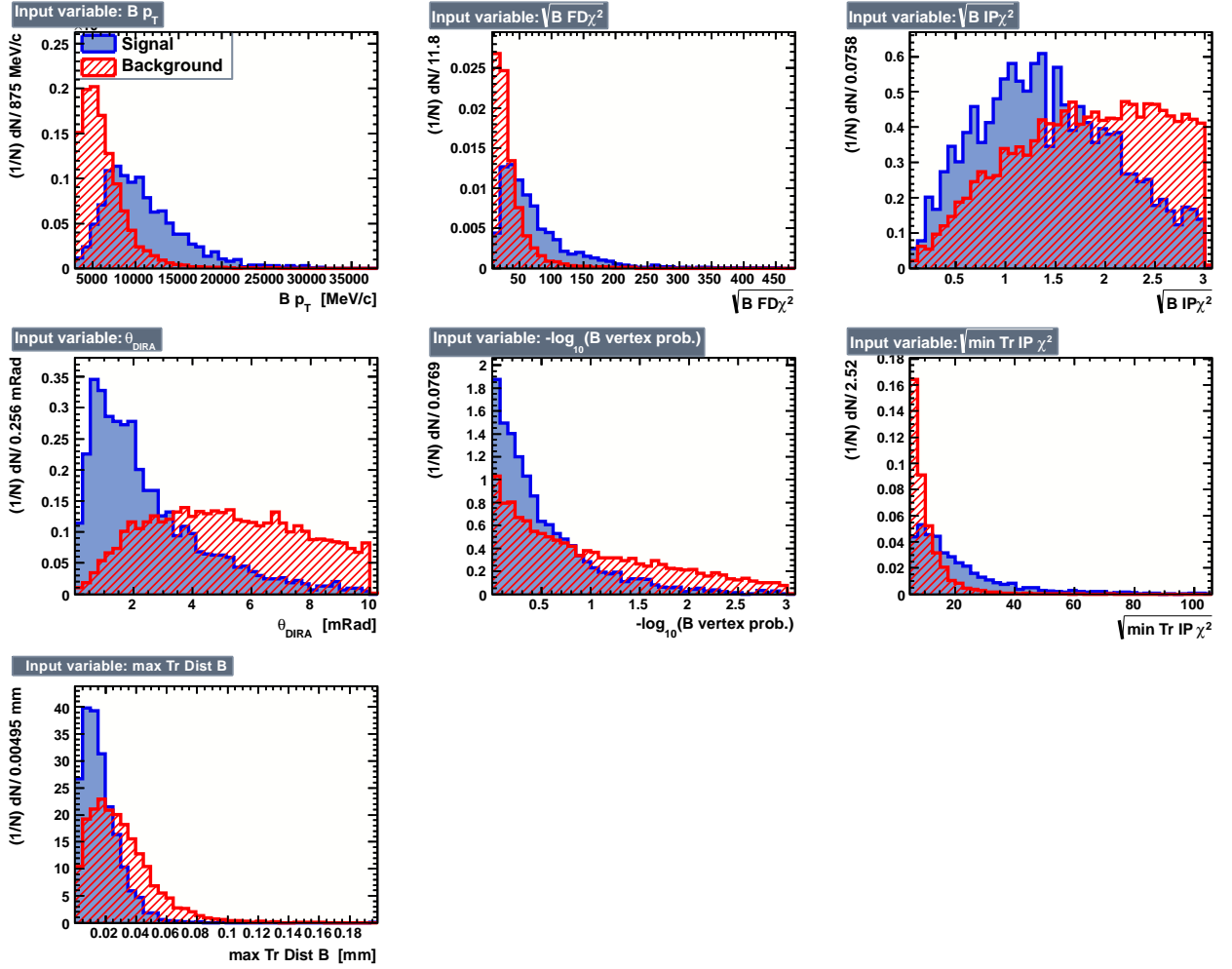


Figure 5.8: Distributions of the TMVA input variables in the case of merged π^0 events (see table 5.17). The distributions in blue are for signal, the ones in red for background.

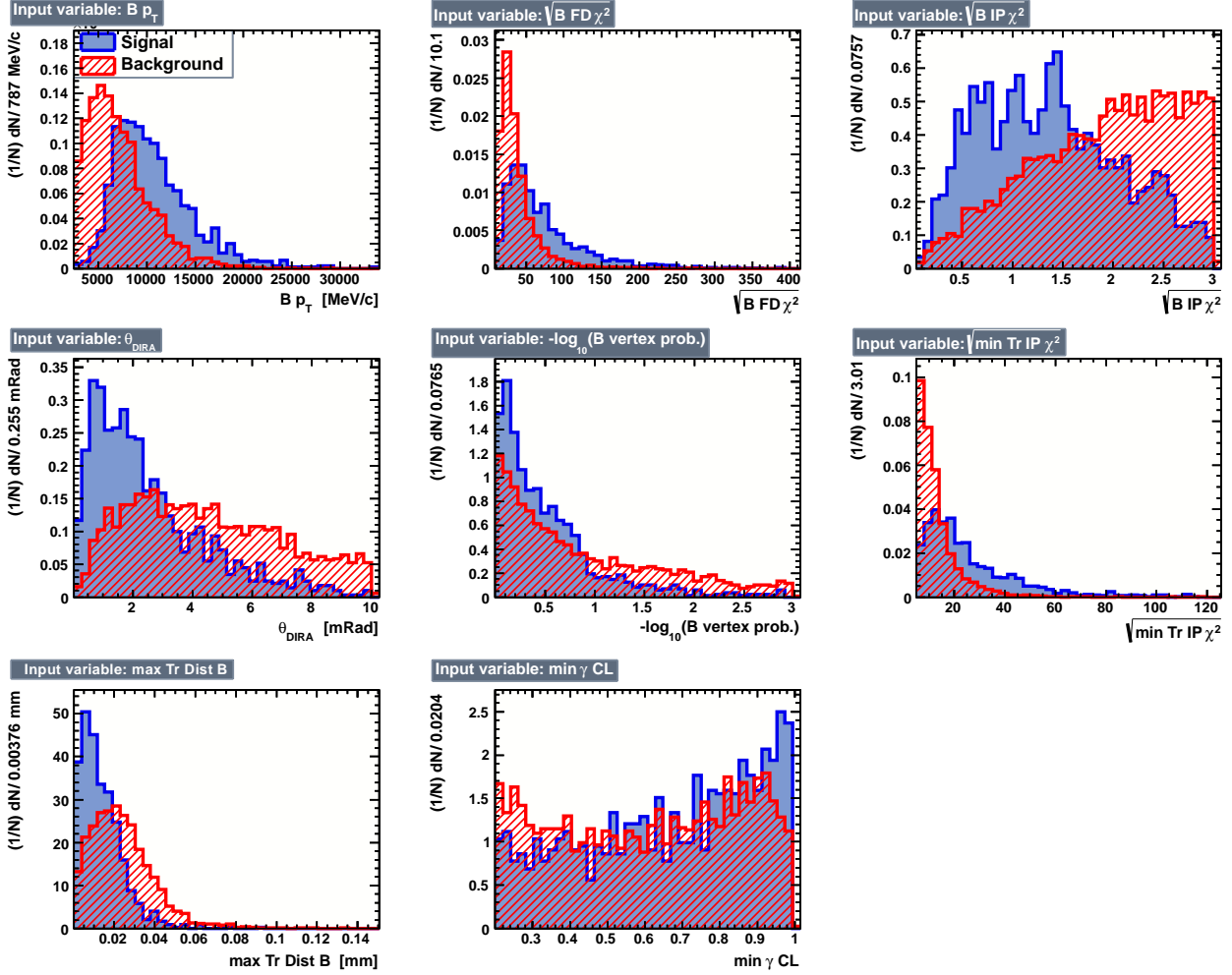


Figure 5.9: Distributions of the TMVA input variables in the case of resolved π^0 events (see table 5.17). The distributions in blue are for signal, the ones in red for background.

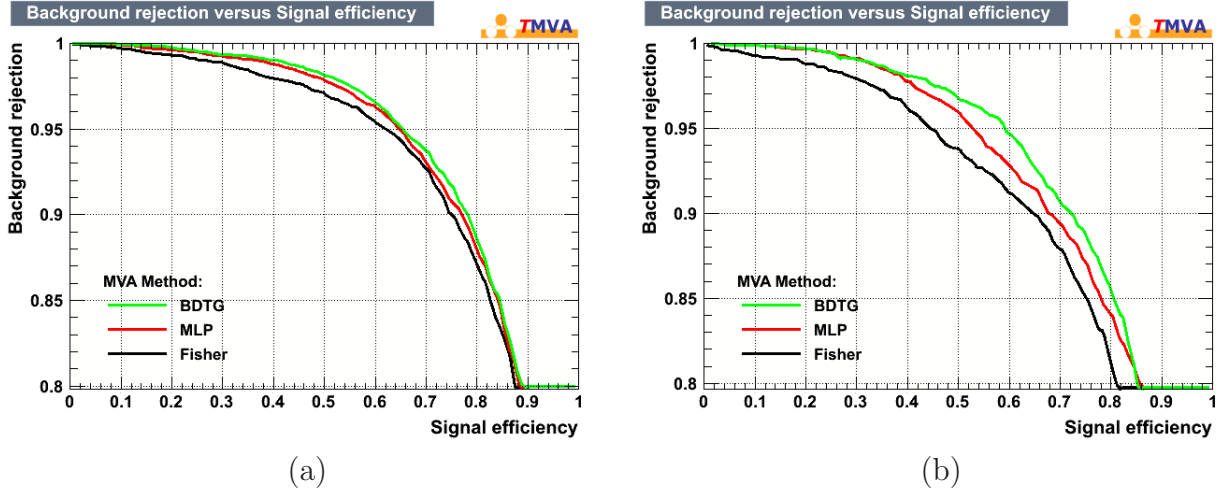


Figure 5.10: Background rejection vs signal efficiency for merged (a) and resolved (b) π^0 events. The performances of the three methods are shown.

The BDT output distributions for signal and background are presented in figure 5.11. The distributions are similar for the test and training samples. This shows the classifier is not over-trained.

The choice of the cut applied on the BDT output is discussed in the next chapter. The optimal cut value will be obtained using signal and background yields in real data. In the next section, a very loose cut at $\text{BDT} > -0.8$ will be applied to reject most of the combinatorial background and study the remaining specific backgrounds.

5.4.6 Radiative background

The presence of radiative decays of neutral B mesons is a critical source of background for the observation of $B_{d,s}^0 \rightarrow h^+ h'^- \pi^0$ decays. This is more important in the case of merged π^0 that are reconstructed from a single ECAL cluster.

The study of the contamination from radiative decays can be done at the level of the preselection as the multivariate classifier is not expected to discriminate those from signal. The expected yields after the preselection are reported in tables 5.18 to 5.20. Those are more illustrative numbers than real expectations. They rely in particular on the decay dynamics introduced in the simulation considering the fact that the efficiency varies along the Dalitz plot. They were calculated from equations 5.2, 5.4 and 5.5 using the branching fractions of table 5.2, the Monte Carlo efficiencies of tables 5.1, 5.7 and 5.13 and the PID efficiencies of table 5.10. For $\Lambda_b \rightarrow \Lambda(1520)\gamma$ and $\Lambda_b \rightarrow \Lambda(1670)\gamma$ we pessimistically assume individual branching fractions equal to the one estimate for all the $\Lambda \rightarrow \Lambda^* \gamma$ decays globally. For the

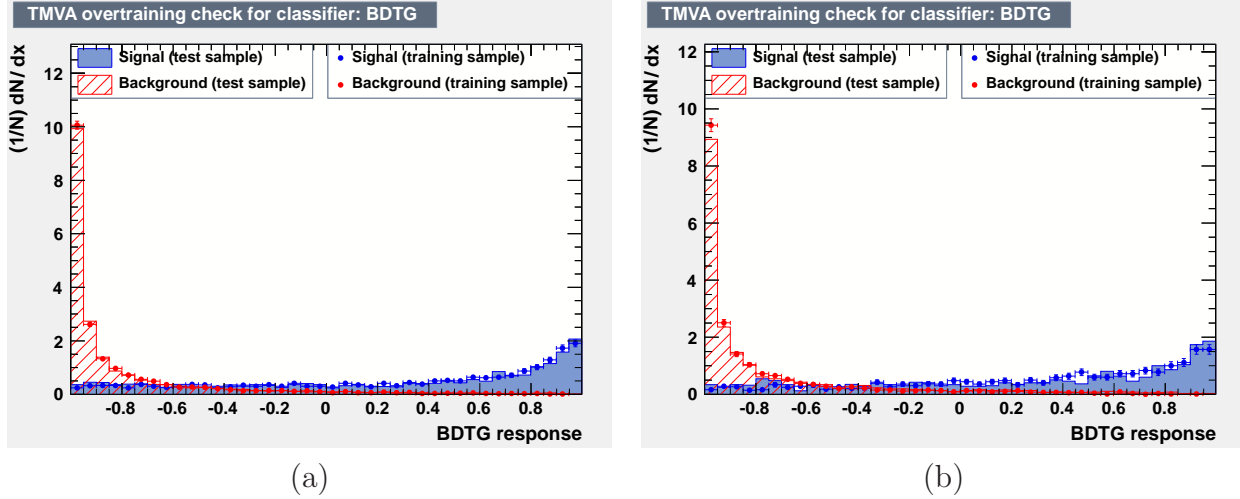


Figure 5.11: BDT output in the case of merged (a) and resolved (b) π^0 events. The distributions in blue are for signal, the ones in red are for background. The points correspond to the training samples and the areas to the test samples.

unobserved $B_s^0 \rightarrow K^- \pi^+ \pi^0$ and $B_s^0 \rightarrow K^+ K^- \pi^0$ modes, branching fractions of 2.5×10^{-5} , identical to what is measured for $B^0 \rightarrow \rho \pi$, are assumed. For the $B_s^0 \rightarrow K^+ K^- \pi^0$ decay, as no Monte Carlo sample was available, the Monte Carlo efficiencies were taken from the $B_s^0 \rightarrow K^- \pi^+ \pi^0$ sample.

Tables 5.18 to 5.20 show that large contamination from radiative decays are expected. For merged π^0 events preselected as $\pi^+ \pi^- \pi^0$ B meson decays, the yields evaluated for $B^0 \rightarrow K^{*0} \gamma$ and $B^0 \rightarrow \rho^0 \gamma$ represent about 20% and 10% of the signal one respectively. In the case of $K^\pm \pi^\mp \pi^0$, the $B^0 \rightarrow K^{*0} \gamma$ yield is more than twice higher than the $B^0 \rightarrow K^+ \pi^- \pi^0$ one for merged π^0 events. Even for events with a resolved π^0 it is around 15% of the signal one. For the $B_s^0 \rightarrow K^+ K^- \pi^0$ mode, with the branching fraction of 2.5×10^{-5} taken for this unobserved mode, the calculated signal yield for merged π^0 events is smaller than the $B_s^0 \rightarrow \phi \gamma$ one. In addition the $B^0 \rightarrow K^{*0} \gamma$ and $\Lambda_b \rightarrow \Lambda^* \gamma$ decays represent in this case about 30% and 20% of the signal one, respectively.

Another way to study the specific backgrounds is to produce the two-body invariant mass distributions for events passing the preselection and a loose cut on the output of the multivariate classifier in order to remove most of the combinatorial background. The cut used for this study is $\text{BDT} > -0.8$. Events are also required to have a reconstructed $B_{d,s}^0$ mass in the signal region as we are particularly interested by the peaking backgrounds, the most dangerous ones. A $\pm 150 \text{ MeV}/c^2$ mass window is used for resolved π^0 events. In the case of merged π^0 events, for which the mass resolution is higher as we will see in the next chapter, a $\pm 200 \text{ MeV}/c^2$ mass window is used. The nominal mass is taken as the B^0 mass for the

Sample	Merged	Resolved
$B^0 \rightarrow \pi^+\pi^-\pi^0$	1545.8 ± 32.6	806.0 ± 23.6
$B^0 \rightarrow K^+\pi^-\pi^0$	127.9 ± 2.5	67.2 ± 1.8
$B_s^0 \rightarrow K^-\pi^+\pi^0$	29.6 ± 0.5	11.8 ± 0.3
$B_s^0 \rightarrow K^+K^-\pi^0$	1.38 ± 0.02	0.55 ± 0.01
$B^0 \rightarrow \rho^+\rho^-$	663.1 ± 27.4	299.3 ± 18.4
$B^+ \rightarrow \rho^+\rho^0$	381.8 ± 21.0	137.9 ± 12.7
$B^0 \rightarrow \rho^0\gamma$	134.6 ± 1.5	4.4 ± 0.3
$B^0 \rightarrow K^{*0}\gamma$	312.0 ± 1.8	9.9 ± 0.3
$B_s^0 \rightarrow \phi\gamma$	1.79 ± 0.01	0.050 ± 0.002
$\Lambda_b \rightarrow \Lambda(1520)\gamma$	0.5 ± 0.5	0.5 ± 0.5
$\Lambda_b \rightarrow \Lambda(1670)\gamma$	0.2 ± 0.2	0.2 ± 0.2

Table 5.18: Illustration of the expected yields for events preselected as $B_{d/s}^0 \rightarrow \pi^+\pi^-\pi^0$ decays.

Sample	Merged	Resolved
$B^0 \rightarrow \pi^+\pi^-\pi^0$	90.4 ± 1.9	47.0 ± 1.4
$B^0 \rightarrow K^+\pi^-\pi^0$	2477.3 ± 47.4	1297.7 ± 34.3
$B_s^0 \rightarrow K^-\pi^+\pi^0$	573.8 ± 9.6	226.6 ± 6.0
$B_s^0 \rightarrow K^+K^-\pi^0$	58.2 ± 1.0	23.0 ± 0.6
$B^0 \rightarrow \rho^+\rho^-$	39.2 ± 1.6	17.6 ± 1.1
$B^+ \rightarrow \rho^+\rho^0$	22.7 ± 1.2	8.0 ± 0.7
$B^0 \rightarrow \rho^0\gamma$	7.9 ± 0.1	0.26 ± 0.02
$B^0 \rightarrow K^{*0}\gamma$	6031.0 ± 35.3	191.2 ± 6.2
$B_s^0 \rightarrow \phi\gamma$	75.4 ± 0.5	2.16 ± 0.09
$\Lambda_b \rightarrow \Lambda(1520)\gamma$	4.5 ± 1.6	0.6 ± 0.6
$\Lambda_b \rightarrow \Lambda(1670)\gamma$	7.6 ± 1.2	0.6 ± 0.3

Table 5.19: Illustration of the expected yields for events preselected as $B_{d/s}^0 \rightarrow K^\pm\pi^\mp\pi^0$ decays.

Sample	Merged	Resolved
$B^0 \rightarrow \pi^+\pi^-\pi^0$	11.8 ± 0.2	6.1 ± 0.18
$B^0 \rightarrow K^+\pi^-\pi^0$	62.2 ± 1.2	32.6 ± 0.9
$B_s^0 \rightarrow K^-\pi^+\pi^0$	14.4 ± 0.2	32.6 ± 0.9
$B_s^0 \rightarrow K^+K^-\pi^0$	559.3 ± 9.4	221.1 ± 5.9
$B^0 \rightarrow \rho^+\rho^-$	5.1 ± 0.2	2.3 ± 0.1
$B^+ \rightarrow \rho^+\rho^0$	2.9 ± 0.2	1.0 ± 0.1
$B^0 \rightarrow \rho^0\gamma$	1.02 ± 0.01	0.033 ± 0.002
$B^0 \rightarrow K^{*0}\gamma$	151.8 ± 0.9	4.8 ± 0.1
$B_s^0 \rightarrow \phi\gamma$	726.7 ± 5.3	20.8 ± 0.9
$\Lambda_b \rightarrow \Lambda(1520)\gamma$	34.9 ± 4.4	0.6 ± 0.6
$\Lambda_b \rightarrow \Lambda(1670)\gamma$	75.1 ± 3.9	0.2 ± 0.2

Table 5.20: Illustration of expected yields for events preselected as $B_{d/s}^0 \rightarrow K^+K^-\pi^0$ decays.

$\pi^+\pi^-\pi^0$ and $K^\pm\pi^\mp\pi^0$ samples and as the B_s^0 mass for the $K^+K^-\pi^0$ one.

Figure 5.12 shows the resulting $h^+h'^-$ mass distributions. In the case of $\pi^+\pi^-\pi^0$ and $K^\pm\pi^\mp\pi^0$, the Monte Carlo distributions from the $B^0 \rightarrow \pi^+\pi^-\pi^0$ and $B^0 \rightarrow K^+\pi^-\pi^0$ samples are also shown for comparison. Compared to Monte Carlo and to resolved π^0 events, distributions for merged π^0 events exhibit clear peaks associated to radiative decays:

- certainly a mixture of $B^0 \rightarrow K^*(892)^0\gamma$ and $B^0 \rightarrow \rho^0\gamma$ decays, according to table 5.18, for $\pi^+\pi^-\pi^0$ events;
- $B^0 \rightarrow K^*(892)^0\gamma$ and $B^0 \rightarrow K_2^*(1430)^0\gamma$ decays for $K^\pm\pi^\mp\pi^0$ events;
- $B_s^0 \rightarrow \phi\gamma$, polluted by $B^0 \rightarrow K^*(892)^0\gamma$ events, according to table 5.20, and $\Lambda_b \rightarrow \Lambda^*\gamma$ decays, with possibly also a contribution of $B_s^0 \rightarrow f_2'(1525)\gamma$, for $K^+K^-\pi^0$ events.

No unexpected peaks were found on the $h^+\pi^0$ and $h'^-\pi^0$ distributions.

Radiative backgrounds are localized at the low $h^+h'^-$ invariant mass. According to this, the samples are divided in two: a low $m_{h^+h'^-}$ region where the radiative decays will be important, and a high $m_{h^+h'^-}$ region where they will be negligible. For the $\pi^+\pi^-\pi^0$ sample, almost 95% of the $B^0 \rightarrow \pi^+\pi^-\pi^0$ simulated sample is such that the minimum of the two body invariant masses is lower than $1.2 \text{ GeV}/c^2$. This clearly appears on figure 2.4: $B^0 \rightarrow \pi^+\pi^-\pi^0$ events accumulates on the border of the Dalitz plot. Discarding the center of the Dalitz plot applying such a cut has very little impact on the signal and allows to reject an important fraction of background. For this reason the division in two regions is done here defining a $\rho^0\pi^0$ region, $m_{\pi^+\pi^-} < 1.2 \text{ GeV}/c^2$, and a $\rho^\pm\pi^\mp$ region, $\min(m_{\pi^0\pi^+}, m_{\pi^0\pi^-}) < 1.2 \text{ GeV}/c^2$.

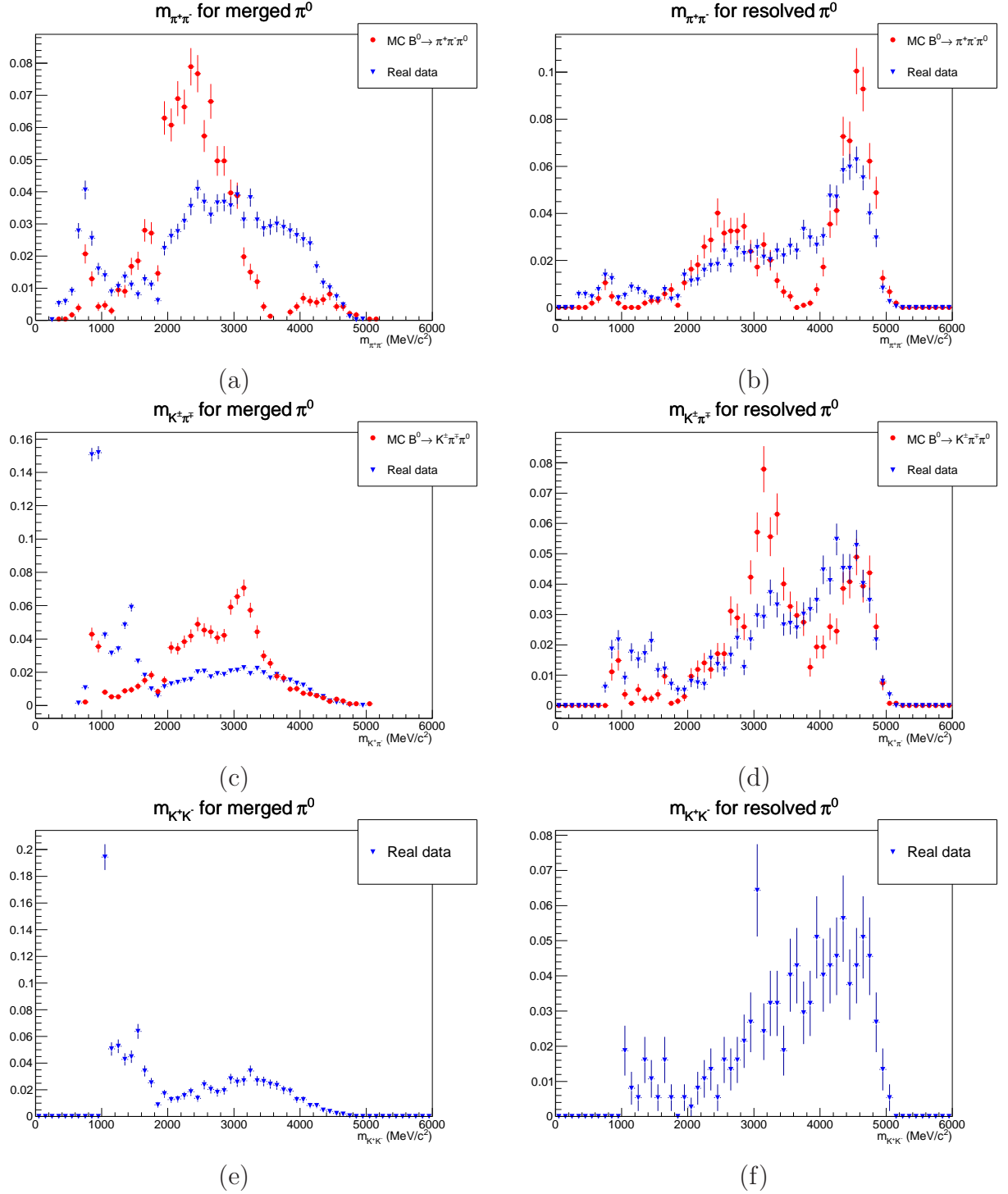


Figure 5.12: Distributions of the two tracks invariant mass in the case of merged (left) and resolved (right) π^0 events preselected as $\pi^+\pi^-\pi^0$ (top), $K^\pm\pi^\mp\pi^0$ (middle) and $K^+K^-\pi^0$ (bottom). In addition to the preselection, a loose cut on the multivariate classifier, $\text{BDT} > -0.8$, is applied. Red circles correspond to Monte Carlo, blue triangles to real data.

Sample	Merged		Resolved	
	$\rho^0\pi^0$ region	$\rho^\pm\pi^\mp$ region	$\rho^0\pi^0$ region	$\rho^\pm\pi^\mp$ region
$B^0 \rightarrow \pi^+\pi^-\pi^0$	75.1 ± 7.2	1382.5 ± 30.9	17.9 ± 3.5	710.9 ± 22.1
$B^0 \rightarrow K^+\pi^-\pi^0$	12.4 ± 0.8	92.8 ± 2.1	2.2 ± 0.3	51.3 ± 1.6
$B_s^0 \rightarrow K^-\pi^+\pi^0$	8.6 ± 0.3	8.6 ± 0.3	1.7 ± 0.1	3.8 ± 0.2
$B_s^0 \rightarrow K^+K^-\pi^0$	0.40 ± 0.01	0.40 ± 0.01	0.080 ± 0.005	0.178 ± 0.008
$B^0 \rightarrow \rho^+\rho^-$	18.1 ± 4.5	617.9 ± 26.4	1.1 ± 1.1	259.8 ± 17.1
$B^+ \rightarrow \rho^+\rho^0$	169.7 ± 14.1	200.3 ± 15.4	53.0 ± 7.90	63.6 ± 8.6
$B^0 \rightarrow \rho^0\gamma$	126.9 ± 1.5	0.22 ± 0.06	4.0 ± 0.3	0.02 ± 0.02
$B^0 \rightarrow K^{*0}\gamma$	307.4 ± 1.8	0.27 ± 0.05	9.6 ± 0.3	0.04 ± 0.02
$B_s^0 \rightarrow \phi\gamma$	1.78 ± 0.01	0.0003 ± 0.0002	0.05 ± 0.002	0.0004 ± 0.0002
$\Lambda_b \rightarrow \Lambda(1520)\gamma$	0.6 ± 0.6	0.6 ± 0.6	0.6 ± 0.6	0.6 ± 0.6
$\Lambda_b \rightarrow \Lambda(1670)\gamma$	0.2 ± 0.2	0.2 ± 0.2	0.2 ± 0.2	0.2 ± 0.2

Table 5.21: Illustration of expected yields for events preselected as $B_{d/s}^0 \rightarrow \pi^+\pi^-\pi^0$ decays in the $\rho^0\pi^0$ region ($m_{\pi^+\pi^-} < 1.2 \text{ GeV}/c^2$) and the $\rho^\pm\pi^\mp$ region ($\min(m_{\pi^0\pi^+}, m_{\pi^0\pi^-}) < 1.2 \text{ GeV}/c^2$).

For the $K^\pm\pi^\mp\pi^0$ and $K^+K^-\pi^0$ samples, the $m_{h+h'}$ cut should be sufficiently far away from the highest resonances from radiative decays, $K_2^*(1430)^0$ or $\Lambda(1670)$ respectively. As the $D^0 \rightarrow \pi^+\pi^-$, $D^0 \rightarrow K^-\pi^+$ and $D^0 \rightarrow K^+K^-$ peaks are explicitly cutted in the preselection, the value of the $m_{h+h'}$ cut is chosen to be the D^0 mass.

Tables 5.21 to 5.23 give the expected yields in the two regions for each sample. Those yields are evaluated as previously and again they should be taken more as illustrative numbers than real expectations. The fraction of events in each region itself rely on the decay dynamics used in the simulation. This is especially true for the unobserved $B_s^0 \rightarrow K^-\pi^+\pi^0$ and $B_s^0 \rightarrow K^+K^-\pi^0$ modes for which the decay models introduced in the simulation are not supported by any measurement.

For the $\pi^+\pi^-\pi^0$ sample, considering the $B^0 \rightarrow \rho^0\pi^0$ and $B^0 \rightarrow \rho^\pm\pi^\mp$ branching fractions, most of the signal is expected in the $\rho^\pm\pi^\mp$ region. Table 5.21 shows that in the case of merged π^0 events, the $\rho^0\pi^0$ region is dominated by $B^0 \rightarrow K^{*0}\gamma$ and $B^0 \rightarrow \rho^0\gamma$ decays. For resolved π^0 events, the expected signal yield is very small in the $\rho^0\pi^0$ region. In addition, the sum of the $B^0 \rightarrow K^{*0}\gamma$ and $B^0 \rightarrow \rho^0\gamma$ contributions is almost as high as the signal one.

According to BaBar and Belle studies of the $B^0 \rightarrow K^+\pi^-\pi^0$ mode [41, 46], most of the B^0 signal is expected to be in the high $m_{K^\pm\pi^\mp}$ region of the $K^\pm\pi^\mp\pi^0$ sample. For the unobserved $B_s^0 \rightarrow K^-\pi^+\pi^0$ mode, the yields reported in table 5.22 are very arbitrary as they rely on

Sample	Merged		Resolved	
	$m_{K^\pm\pi^\mp} < m_{D^0}$	$m_{K^\pm\pi^\mp} > m_{D^0}$	$m_{K^\pm\pi^\mp} < m_{D^0}$	$m_{K^\pm\pi^\mp} > m_{D^0}$
$B^0 \rightarrow \pi^+\pi^-\pi^0$	11.2 ± 0.7	79.1 ± 1.8	1.8 ± 0.3	45.2 ± 1.3
$B^0 \rightarrow K^+\pi^-\pi^0$	408.6 ± 19.3	2068.6 ± 43.3	71.7 ± 8.1	1225.9 ± 33.4
$B_s^0 \rightarrow K^-\pi^+\pi^0$	305.8 ± 7.0	268.1 ± 6.6	64.8 ± 3.2	161.8 ± 5.1
$B_s^0 \rightarrow K^+K^-\pi^0$	31.0 ± 0.7	27.2 ± 0.7	6.6 ± 0.3	16.4 ± 0.5
$B^0 \rightarrow \rho^+\rho^-$	5.6 ± 0.6	33.6 ± 1.5	0.6 ± 0.2	17.0 ± 1.1
$B^+ \rightarrow \rho^+\rho^0$	11.5 ± 0.9	11.2 ± 0.9	3.5 ± 0.5	4.5 ± 0.6
$B^0 \rightarrow \rho^0\gamma$	7.72 ± 0.09	0.15 ± 0.01	0.25 ± 0.02	0.007 ± 0.003
$B^0 \rightarrow K^{*0}\gamma$	6025.2 ± 35.3	6.2 ± 1.1	189.8 ± 6.3	1.4 ± 0.5
$B_s^0 \rightarrow \phi\gamma$	75.3 ± 0.5	0.05 ± 0.01	2.14 ± 0.09	0.020 ± 0.009
$\Lambda_b \rightarrow \Lambda(1520)\gamma$	4.5 ± 1.6	0.6 ± 0.6	0.6 ± 0.6	0.6 ± 0.6
$\Lambda_b \rightarrow \Lambda(1670)\gamma$	7.6 ± 1.2	0.2 ± 0.2	0.6 ± 0.3	0.2 ± 0.2

Table 5.22: Illustration of expected yields for events preselected as $B_{d/s}^0 \rightarrow K^\pm\pi^\mp\pi^0$ decays in the regions $m_{K^\pm\pi^\mp} < m_{D^0}$ and $m_{K^\pm\pi^\mp} > m_{D^0}$.

Sample	Merged		Resolved	
	$m_{K^+K^-} < m_{D^0}$	$m_{K^+K^-} > m_{D^0}$	$m_{K^+K^-} < m_{D^0}$	$m_{K^+K^-} > m_{D^0}$
$B^0 \rightarrow \pi^+\pi^-\pi^0$	0.82 ± 0.07	11.0 ± 0.2	0.14 ± 0.03	6.0 ± 0.2
$B^0 \rightarrow K^+\pi^-\pi^0$	7.1 ± 0.4	55.1 ± 1.1	1.3 ± 0.2	31.3 ± 0.8
$B_s^0 \rightarrow K^-\pi^+\pi^0$	6.9 ± 0.2	7.5 ± 0.2	1.47 ± 0.08	4.2 ± 0.1
$B_s^0 \rightarrow K^+K^-\pi^0$	267.6 ± 6.5	291.9 ± 6.8	57.2 ± 3.0	163.9 ± 5.1
$B^0 \rightarrow \rho^+\rho^-$	0.30 ± 0.05	4.8 ± 0.2	0.009 ± 0.009	2.3 ± 0.1
$B^+ \rightarrow \rho^+\rho^0$	1.4 ± 0.1	1.6 ± 0.1	0.42 ± 0.06	0.63 ± 0.07
$B^0 \rightarrow \rho^0\gamma$	1.00 ± 0.01	0.028 ± 0.002	0.0321 ± 0.002	0.0014 ± 0.0004
$B^0 \rightarrow K^{*0}\gamma$	151.4 ± 0.9	0.41 ± 0.05	4.7 ± 0.2	0.05 ± 0.02
$B_s^0 \rightarrow \phi\gamma$	726.2 ± 5.3	0.5 ± 0.1	20.6 ± 0.9	0.2 ± 0.1
$\Lambda_b \rightarrow \Lambda(1520)\gamma$	34.9 ± 4.4	0.6 ± 0.6	0.6 ± 0.6	0.6 ± 0.6
$\Lambda_b \rightarrow \Lambda(1670)\gamma$	75.1 ± 3.9	0.2 ± 0.2	0.2 ± 0.2	0.2 ± 0.2

Table 5.23: Illustration of expected yields for events preselected as $B_{d/s}^0 \rightarrow K^+K^-\pi^0$ decays in the regions $m_{K^+K^-} < m_{D^0}$ and $m_{K^+K^-} > m_{D^0}$.

Sample	Cut	Eff (%)	
		Resolved	Merged
$B_d^0 \rightarrow \pi^+ \pi^- \pi^0$	$\min(m_{\pi^+ \pi^0}, m_{\pi^- \pi^0}) < 1.2 \text{ GeV}/c^2$	90.4 ± 1.2	90.5 ± 0.9
$B_d^0 \rightarrow K^+ \pi^- \pi^0$	$m_{K^\pm \pi^\mp} > m_{D^0}$	95.4 ± 0.9	83.7 ± 1.1
$B_s^0 \rightarrow K^- \pi^+ \pi^0$		72.2 ± 1.3	46.1 ± 0.9
$B_s^0 \rightarrow K^+ K^- \pi^0$	$m_{K^+ K^-} > m_{D^0}$	74.1 ± 2.9	52.1 ± 2.1

Table 5.24: Dalitz cut applied to reject radiative decays and corresponding Monte Carlo efficiencies.

the assumed branching fraction (2.5×10^{-5}) and the dynamics used in the simulation. Table 5.22 shows that for both merged and resolved π^0 events the low $m_{K^\pm \pi^\mp}$ region is dominated by $B^0 \rightarrow K^{*0} \gamma$ decays. In the case of the $K^+ K^- \pi^0$ sample, the yields reported for the $B_s^0 \rightarrow K^+ K^- \pi^0$ mode are, as for $B_s^0 \rightarrow K^- \pi^+ \pi^0$ in the $K^\pm \pi^\mp \pi^0$ sample, very arbitrary. Table 5.23 shows that for merged π^0 events the low $m_{K^+ K^-}$ region is dominated by $B_s^0 \rightarrow \phi \gamma$ decays. The hypothesis done here leads to an expected signal yield of only about 60 events in the low $m_{K^+ K^-}$ region for resolved π^0 events. The $B_s^0 \rightarrow \phi \gamma$ and $B^0 \rightarrow K^{*0} \gamma$ contributions sum up to about half of this.

The situation is relatively similar for the $\pi^+ \pi^- \pi^0$, $K^\pm \pi^\mp \pi^0$ and $K^+ K^- \pi^0$ samples. The signal is expected to populate mostly the high $m_{h^+ h'^-}$ region. In this region, the background from radiative decays is negligible. In the low $m_{h^+ h'^-}$ region, the expected signal yields are smaller or much smaller and the radiative backgrounds contribute very significantly or can even be dominant. To see if it would anyhow be possible to extract the $h^+ h'^- \pi^0$ modes in the low $m_{h^+ h'^-}$ region, an attempt was made to use the decay helicity angle and the π^0/γ separation tool discussed in Chapter 4. As the photon is a vector while the π^0 is a pseudo-scalar the helicity angle distributions are different for $h^+ h'^- \pi^0$ decays and radiative modes. The helicity angle follows a \sin^2 distribution for $B \rightarrow V \gamma$ decays (where V stands for a vector meson) and a \cos^2 distribution for $B \rightarrow V \pi^0$ modes. While the π^0/γ separation tool only concerns merged π^0 events, helicity angle cuts are possible for both merged and resolved π^0 events. In all cases, it was found that it is not possible to obtain acceptable signal to background ratios without significant reduction of the signal efficiency, leading to expected signal yields of few dozens of events at most. It was then decided to limit the study to the high $m_{h^+ h'^-}$ region. The corresponding cuts are reminded in table 5.24. The efficiencies reported here are directly coming from the Monte Carlo samples. As already explained, if the numbers are relatively reliable in the case of $B^0 \rightarrow \pi^+ \pi^- \pi^0$ and $B^0 \rightarrow K^+ \pi^- \pi^0$, they are on the other hand arbitrary for the unobserved $B_s^0 \rightarrow K^- \pi^+ \pi^0$ and $B_s^0 \rightarrow K^+ K^- \pi^0$ decays. However the predictions of table 2.1 seem to indicate that for those modes also most of the events would be in the high $m_{h^+ h'^-}$ region.

5.5 Summary

The whole selection chain implemented for $h^+h'^-\pi^0$ charmless B meson decays has been presented in this chapter. The trigger and stripping selections are followed by additional cleaning cuts and PID criteria to form three independent samples ($\pi^+\pi^-\pi^0$, $K^\pm\pi^\mp\pi^0$ and $K^+K^-\pi^0$). A multivariate classifier is used for the final selection. The input variables and the choice of the classifier itself have been discussed. The optimization of the cut on the classifier output is one of the object of the next chapter.

The Monte Carlo efficiencies and the expected signal yields presented in this chapter are just indicative as they come directly from the simulation and rely on the decay dynamics introduced for the different Monte Carlo samples. Formally, the efficiencies have to be evaluated accounting for the Dalitz distributions as obtained from the data.

Finally, we have seen that the study has to be limited to the part of the Dalitz plane where the radiative decays are negligible. This corresponds to high $m_{h+h'}$ values (see table 5.24) where most of the signal is expected. In the complementary part of the Dalitz plane, the radiative decays contribute very significantly or are even dominant.

CHAPTER 6

Estimation of the $B_{d/s}^0 \rightarrow h^+ h'^- \pi^0$ signal yields

The signal yields are obtained by fitting the reconstructed B mass spectra in the $\pi^+ \pi^- \pi^0$, $K^\pm \pi^\mp \pi^0$ and $K^+ K^- \pi^0$ samples. A combined fit of the three samples is used to account for the signal crossfeeds. It also allows to use common parameters to describe the signal shape in the different samples, assuring coherent signal descriptions and stabilizing the fit results.

The fit used gives a good description of the reconstructed B mass spectra in the three samples over a large range of cuts on the multivariate classifier output. The actual value of the cut is then optimized on data using the signal and background yields obtained from the fit. As the $B_s^0 \rightarrow K^+ K^- \pi^0$ mode has not been observed previously, this optimization is done blinding the signal region in the $K^+ K^- \pi^0$ sample.

This chapter first presents the probability density functions (PDFs) used to describe the signals, the crossfeeds and the backgrounds. The fit model and the optimization of the cut on the multivariate classifier output are then discussed. Finally the results are presented in terms of signal yields and Dalitz plots.

6.1 Signal and background PDFs

Except for the combinatorial background, the PDFs that will be used to fit the reconstructed B mass spectra of the $\pi^+ \pi^- \pi^0$, $K^\pm \pi^\mp \pi^0$ and $K^+ K^- \pi^0$ samples are obtained from fully simulated events. The Monte Carlo samples are reported in table 5.1. For signal, resonant samples of $B^0 \rightarrow \pi^+ \pi^- \pi^0$, $B^0 \rightarrow K^+ \pi^- \pi^0$ and $B_s^0 \rightarrow K^- \pi^+ \pi^0$ decays are used. The $B^0 \rightarrow \rho^+ \rho^-$ and $B^+ \rightarrow \rho^+ \rho^0$ modes are assumed to be representative of the partially reconstructed backgrounds.

Simulated events are required to pass the whole selection described in chapter 5. For the crossfeed PDFs, the PID cut are not applied as they would reduce by a lot the statistics. In any case, they do not affect significantly the reconstructed B mass distributions. The actual value of the cut on the multivariate classifier output also has little effect on the reconstructed B mass distributions. The PDFs reported here are the ones obtained with the cut that will be found to be optimal in section 6.3, i.e. $\text{BDT} > 0.4$.

6.1.1 Signal

The reconstructed B mass distributions obtained from the three signal Monte Carlo samples are reported in figures 6.1 to 6.3. In those figures, the B mass is reconstructed making the right hypothesis on the identification of the final state particles. The PDFs corresponding to the signal crossfeeds are discussed in the next section.

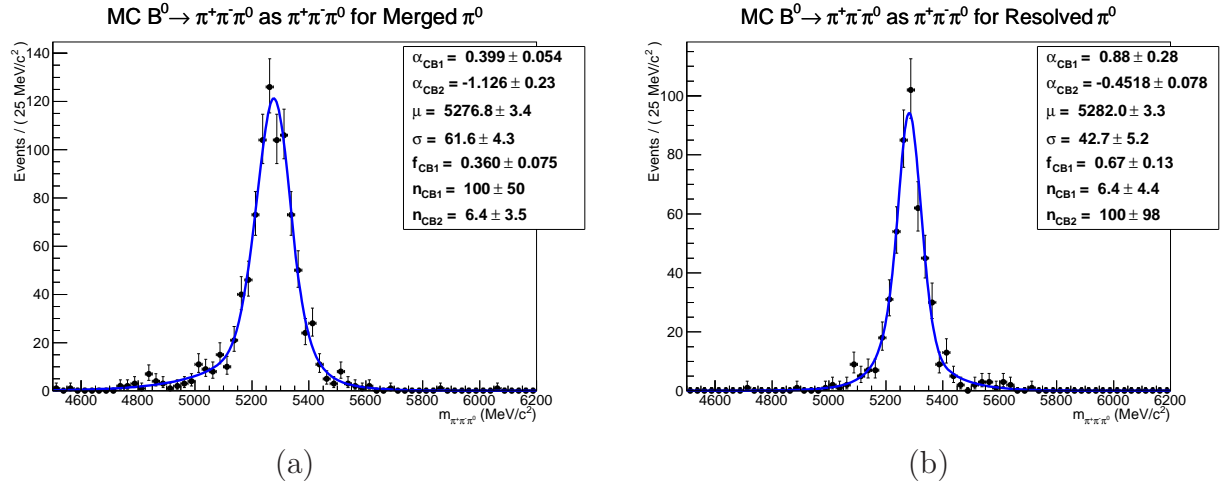


Figure 6.1: $m_{\pi^+\pi^-\pi^0}$ distribution from Monte Carlo $B^0 \rightarrow \pi^+\pi^-\pi^0$ events with a merged π^0 (a) and a resolved π^0 (b). The solid blue lines represent the fitted PDFs.

The distributions are fitted with PDFs combining two Crystal Balls (see section 4.4.2), one with a left handed tail ($\alpha > 0$), the other with a right handed tail ($\alpha < 0$). The two Crystal Balls share the same μ and σ . Given the available statistics, the n parameters of the Crystal Balls are limited to 100. For larger n the fitted Crystal Balls would give very similar shapes but their computation would be more and more time consuming.

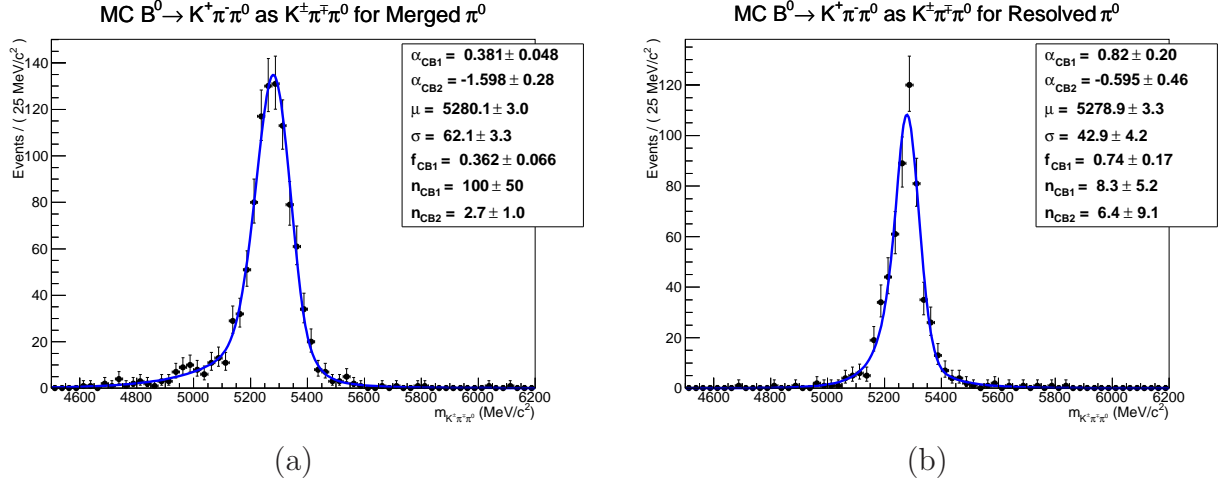


Figure 6.2: $m_{K^\pm \pi^\mp \pi^0}$ distribution from Monte Carlo $B^0 \rightarrow K^+ \pi^- \pi^0$ events with a merged π^0 (a) and a resolved π^0 (b). The solid blue lines represent the fitted PDFs.

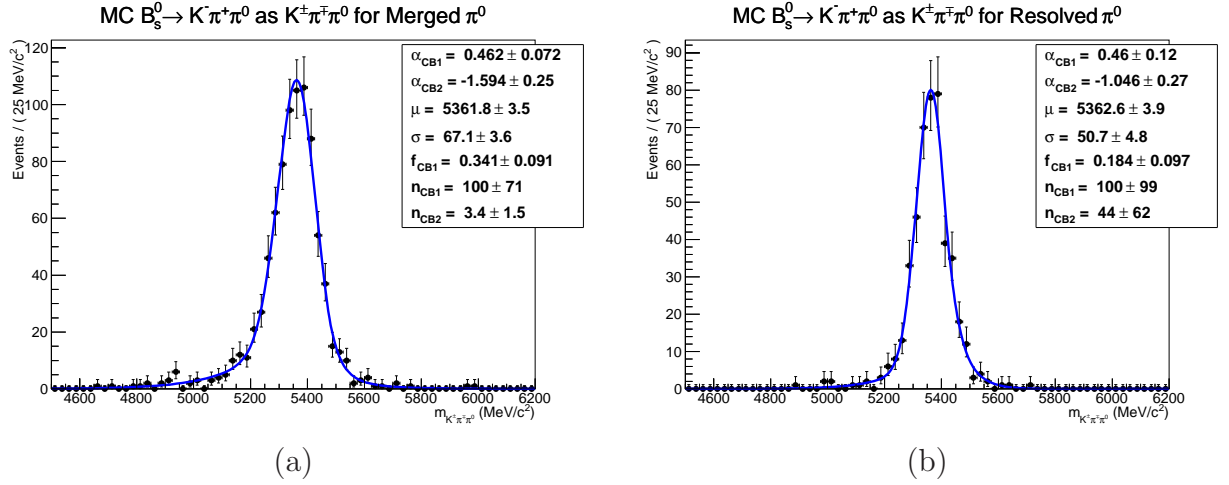


Figure 6.3: $m_{K^\pm \pi^\mp \pi^0}$ distribution from Monte Carlo $B_s^0 \rightarrow K^- \pi^+ \pi^0$ events with a merged π^0 (a) and a resolved π^0 (b). The solid blue lines represent the fitted PDFs.

For the $B_s^0 \rightarrow K^+ K^- \pi^0$ signal shape, since no resonant Monte Carlo sample is available, the fitted PDFs obtained from the $B_s^0 \rightarrow K^- \pi^+ \pi^0$ (see figure 6.3) will be used.

6.1.2 Crossfeed

Figures 6.4 to 6.6 show the reconstructed B mass distributions for the signal crossfeeds. According to table 5.10, crossfeeds corresponding to two misidentified tracks are of the order or 1 to 2 per mille and are then neglected. Thus the crossfeeds considered are coming from $K^\pm \pi^\mp \pi^0$ events identified as $\pi^+ \pi^- \pi^0$, $\pi^+ \pi^- \pi^0$ and $K^+ K^- \pi^0$ events identified as $K^\pm \pi^\mp \pi^0$, and $K^\pm \pi^\mp \pi^0$ events identified as $K^+ K^- \pi^0$.

As previously, the Monte Carlo distributions are fitted by the sum of two Crystal Balls sharing the same μ and σ . Again as there is no $B_s^0 \rightarrow K^+ K^- \pi^0$ resonant Monte Carlo sample, the crossfeed contribution of $B_s^0 \rightarrow K^+ K^- \pi^0$ events in the $K^\pm \pi^\mp \pi^0$ sample is assumed to have the same PDF as the one fitted on the $B_s^0 \rightarrow K^- \pi^+ \pi^0$ sample reconstructed as $\pi^+ \pi^- \pi^0$ (see bottom of figure 6.4). Apart from the shift in mass, the $B^0 \rightarrow K^+ \pi^- \pi^0$ and the $B_s^0 \rightarrow K^- \pi^+ \pi^0$ events give similar $m_{\pi^+ \pi^- \pi^0}$ distributions as one can see on figure 6.4.

6.1.3 Partially reconstructed background

Partially reconstructed backgrounds are events from B decays with one or more decay products in addition to the two tracks and the π^0 of the signal final state. They are modelled using the reconstructed $\pi^+ \pi^- \pi^0$ invariant mass distributions obtained from the $B^0 \rightarrow \rho^+ \rho^-$ and $B^+ \rightarrow \rho^+ \rho^0$ Monte Carlo samples. With respect to the $\pi^+ \pi^- \pi^0$ signal final state, the $\rho^+ \rho^-$ final state has an additional π^0 , the $\rho^\pm \rho^0$ an additional π^\pm . As we have seen in section 5.4.3, an important fraction of the partially reconstructed backgrounds with additional tracks are rejected requiring the B end vertex to be isolated. There is no such a criteria for those with additional π^0 .

Figure 6.7 shows the $m_{\pi^+ \pi^- \pi^0}$ distribution combining the $B^0 \rightarrow \rho^+ \rho^-$ and $B^+ \rightarrow \rho^+ \rho^0$ Monte Carlo samples. Within the limited statistics, the individual distributions of the two samples are found to be compatible. The distribution for merged π^0 events are fitted using the convolution of an Argus and a gaussian. An Argus PDF [115] can be written as

$$F(m; c, m_0) = A \cdot m \cdot \sqrt{1 - \frac{m^2}{m_0^2}} \cdot e^{c \left(1 - \frac{m^2}{m_0^2}\right)}, \quad (6.1)$$

where A is a normalization factor.

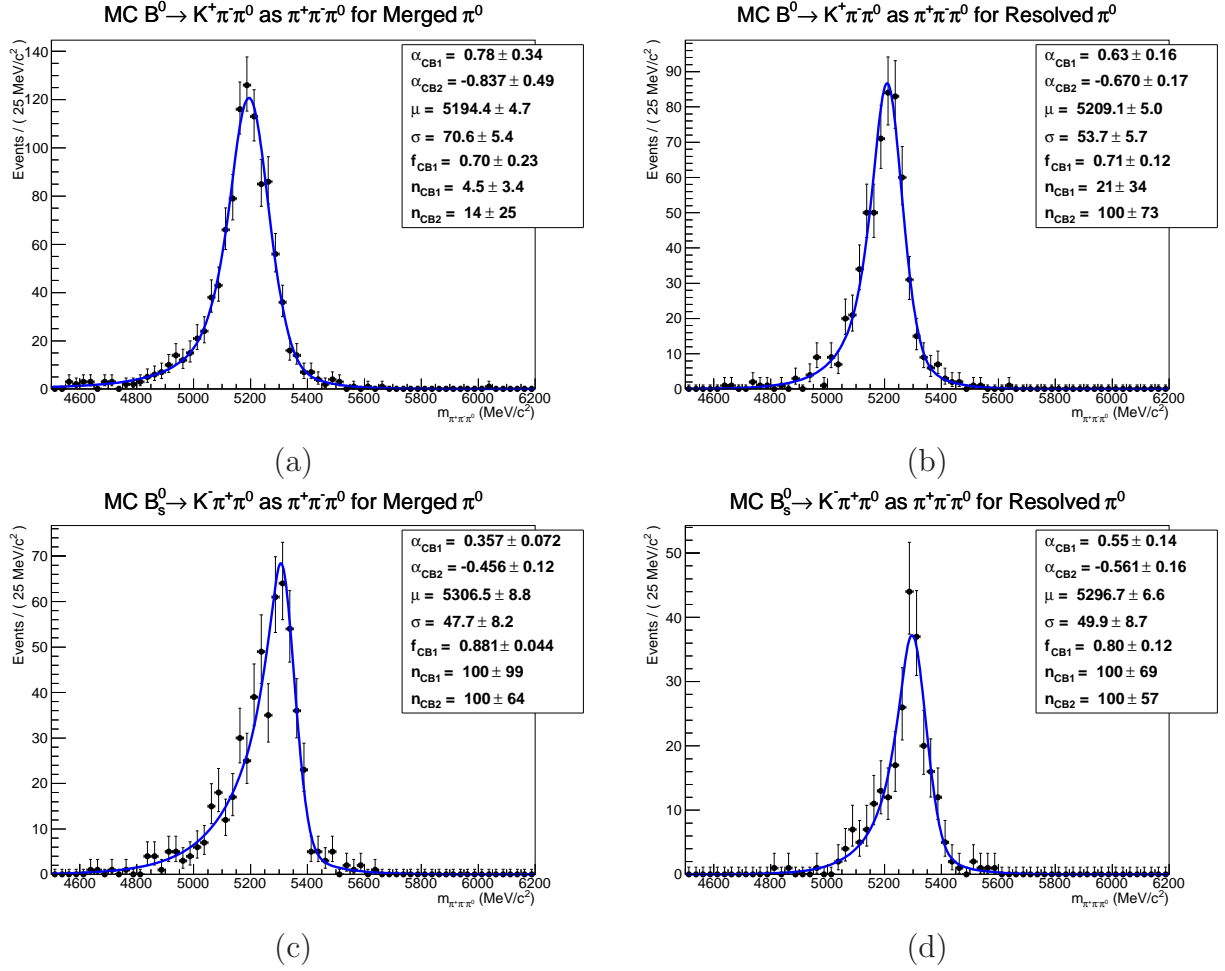


Figure 6.4: $m_{\pi^+\pi^-\pi^0}$ distribution from Monte Carlo $B^0 \rightarrow K^+\pi^-\pi^0$ (top) and $B_s^0 \rightarrow K^-\pi^+\pi^0$ (bottom) with a merged π^0 (left) and a resolved π^0 (right). The solid blue lines represent the fitted PDFs.

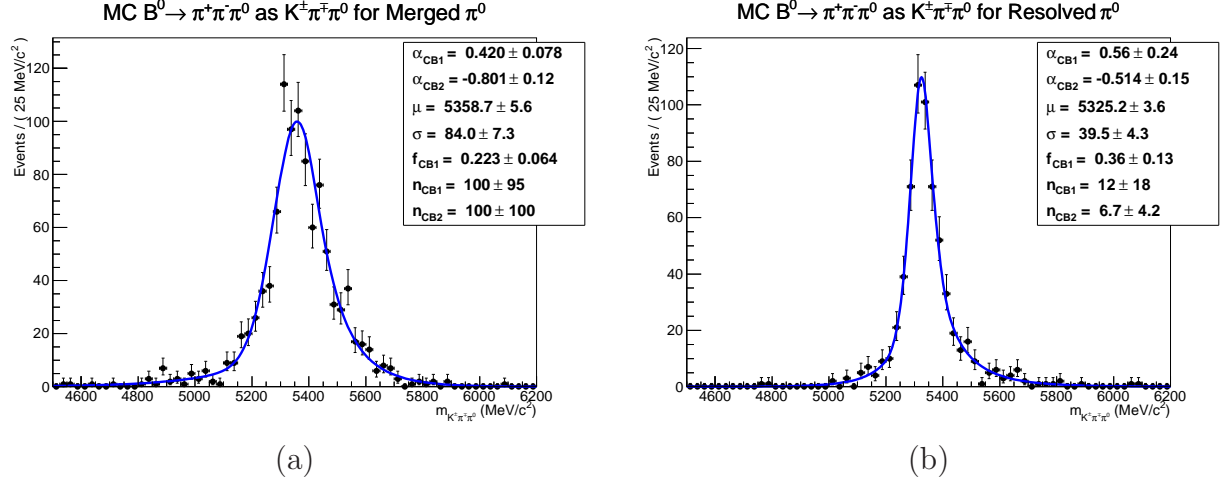


Figure 6.5: $m_{K^\pm\pi^\mp\pi^0}$ distribution for Monte Carlo $B^0 \rightarrow \pi^+\pi^-\pi^0$ events with a merged π^0 (a) and a resolved π^0 (b). The solid blue lines represent the fitted PDFs.

The width of the gaussian is fixed to the width obtained fitting by a gaussian the $m_{\pi^+\pi^-\pi^0}$ distribution from the $B^0 \rightarrow \pi^+\pi^-\pi^0$ signal sample as shown on figure 6.8. On this figure, the Monte Carlo distributions are the same as on figure 6.1. As they have non gaussian tails, the gaussian fits are limited to the core of the distributions. The ranges of the fits are defined from the μ and σ of the two Crystal Balls fits of figure 6.1, as $[\mu-2.5\sigma, \mu+2.5\sigma]$.

6.1.4 Combinatorial background

An exponential PDF will be assumed for the combinatorial background. To correctly fit the data, an additional flat component is needed for merged π^0 events in the $\pi^+\pi^-\pi^0$ sample. The fact that two components have to be used in this case in order to model the combinatorial background is not understood.

6.2 Fit Model

A simultaneous fit of the reconstructed B mass distributions in the three samples is performed. It allows to take into account the signal crossfeeds and to use common parameters for the signal shapes in order to have a coherent description across the three samples.

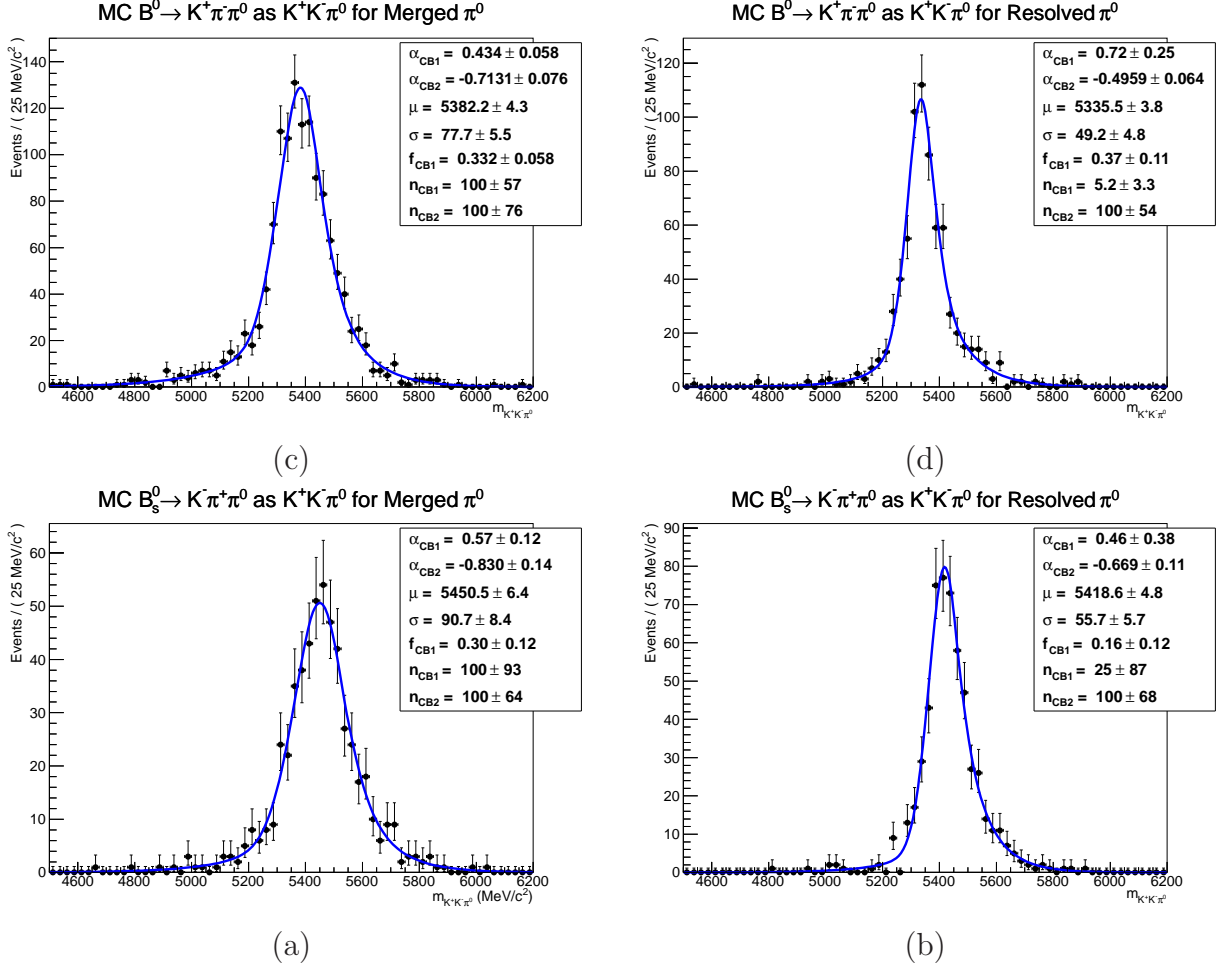


Figure 6.6: $m_{K^+K^-\pi^0}$ distribution from Monte Carlo $B^0 \rightarrow K^+\pi^-\pi^0$ (top) and $B_s^0 \rightarrow K^-\pi^+\pi^0$ (bottom) events with a merged π^0 (left) and a resolved π^0 (right). The solid blue lines represent the fitted PDFs.

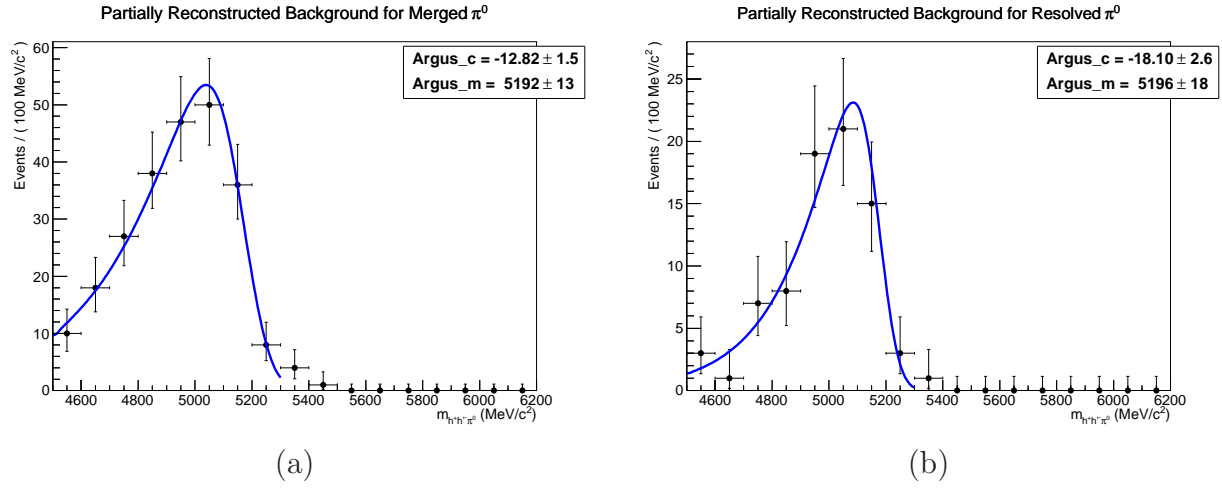


Figure 6.7: $m_{\pi^+\pi^-\pi^0}$ distribution from Monte Carlo $B^0 \rightarrow \rho^+\rho^-$ and $B^+ \rightarrow \rho^+\rho^0$ events with a merged π^0 (a) and a resolved π^0 (b). The solid blue lines represent the fitted PDFs.

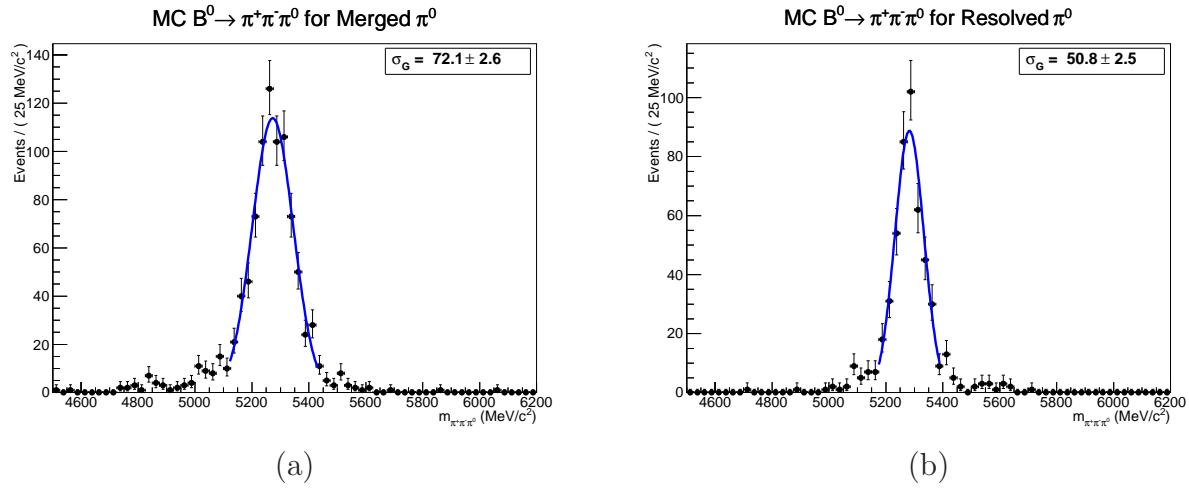


Figure 6.8: Gaussian fit of the $m_{\pi^+\pi^-\pi^0}$ distribution from Monte Carlo $B^0 \rightarrow \pi^+\pi^-\pi^0$ events with a merged π^0 (a) and a resolved π^0 (b).

6.2.1 Parametrisation of the PDFs

Only two free parameters are introduced for the signal PDFs, one corresponding to the peak values, one to the peak widths. The peak values for the $B^0 \rightarrow \pi^+\pi^-\pi^0$ and $B^0 \rightarrow K^+\pi^-\pi^0$ are constrained to be the same:

$$\mu_{B^0 \rightarrow \pi^+\pi^-\pi^0} = \mu_{B^0 \rightarrow K^+\pi^-\pi^0} = \mu_{B^0} . \quad (6.2)$$

For the $B_s^0 \rightarrow K^-\pi^+\pi^0$ and $B_s^0 \rightarrow K^+K^-\pi^0$ modes the mass difference between the B_s^0 and the B^0 [6] is used:

$$\mu_{B_s^0 \rightarrow K^-\pi^+\pi^0} = \mu_{B_s^0 \rightarrow K^+K^-\pi^0} = \mu_{B^0} + 86.8 \text{ MeV}/c^2 . \quad (6.3)$$

As one can see on figures 6.1 to 6.3, the results obtained fitting the Monte Carlo signal samples are compatible with the assumptions made in equations 6.2 and 6.3. Both for merged π^0 and resolved π^0 events, one has in the Monte Carlo: $\mu_{B^0 \rightarrow \pi^+\pi^-\pi^0} \simeq \mu_{B^0 \rightarrow K^+\pi^-\pi^0} \simeq \mu_{B_s^0 \rightarrow K^-\pi^+\pi^0} - 86.8 \text{ MeV}/c^2$.

For what concerns the widths, the free parameter corresponds to the width of the two Crystal Balls for the $B^0 \rightarrow \pi^+\pi^-\pi^0$ mode. The other signal widths are then defined with respect to the Monte Carlo fits as

$$\sigma_X = \sigma_X^{MC} \times \frac{\sigma_{B^0 \rightarrow \pi^+\pi^-\pi^0}^{MC}}{\sigma_{B^0 \rightarrow \pi^+\pi^-\pi^0}^{MC}} . \quad (6.4)$$

This formula is also used to scale the width of the gaussian that is convoluted with an Argus PDF to model the partially reconstructed backgrounds.

All the other shape parameters are directly taken from the Monte Carlo. The crossfeed PDFs are not modified. For the $K^+K^-\pi^0$ sample, the partially reconstructed background PDF is shifted by $86.8 \text{ MeV}/c^2$ to account for the mass difference between the B_s^0 and the B^0 . Apart from that, the Argus parameters are the ones obtained in the Monte Carlo.

6.2.2 Crossfeed Contributions

The crossfeed contribution of a given signal to another sample are evaluated using the efficiency ratios of the PID cuts and of the cuts in the Dalitz plane, according to:

Signal	Crossfeed to	PID eff. ratio (%)
$B^0 \rightarrow \pi^+ \pi^- \pi^0$	$K^\pm \pi^\mp \pi^0$	5.8 ± 1.3
$B_{d/s}^0 \rightarrow K^\pm \pi^\mp \pi^0$	$\pi^+ \pi^- \pi^0$	5.2 ± 1.5
	$K^+ K^- \pi^0$	2.5 ± 0.9
$B_s^0 \rightarrow K^+ K^- \pi^0$	$K^\pm \pi^\mp \pi^0$	10.8 ± 2.6

Table 6.1: PID efficiency ratios used to evaluate the different crossfeed contributions.

$$N_{B^0 \rightarrow \pi^+ \pi^- \pi^0}^{K^\pm \pi^\mp \pi^0} = N_{B^0 \rightarrow \pi^+ \pi^- \pi^0} \times \frac{\epsilon_{PID}(\pi\pi \rightarrow K\pi)}{\epsilon_{PID}(\pi\pi \rightarrow \pi\pi)} \times \frac{\epsilon_{m_{K\pi}}(B^0 \rightarrow \pi^+ \pi^- \pi^0)}{\epsilon_{m_{\pi\pi}}(B^0 \rightarrow \pi^+ \pi^- \pi^0)}, \quad (6.5)$$

$$N_{B_{d/s}^0 \rightarrow K^\pm \pi^\mp \pi^0}^{\pi^+ \pi^- \pi^0} = N_{B_{d/s}^0 \rightarrow K^\pm \pi^\mp \pi^0} \times \frac{\epsilon_{PID}(K\pi \rightarrow \pi\pi)}{\epsilon_{PID}(K\pi \rightarrow K\pi)} \times \frac{\epsilon_{m_{\pi\pi}}(B_{d/s}^0 \rightarrow K^\pm \pi^\mp \pi^0)}{\epsilon_{m_{K\pi}}(B_{d/s}^0 \rightarrow K^\pm \pi^\mp \pi^0)}, \quad (6.6)$$

$$N_{B_{d/s}^0 \rightarrow K^\pm \pi^\mp \pi^0}^{K^+ K^- \pi^0} = N_{B_{d/s}^0 \rightarrow K^\pm \pi^\mp \pi^0} \times \frac{\epsilon_{PID}(K\pi \rightarrow KK)}{\epsilon_{PID}(K\pi \rightarrow K\pi)} \times \frac{\epsilon_{m_{KK}}(B_{d/s}^0 \rightarrow K^\pm \pi^\mp \pi^0)}{\epsilon_{m_{K\pi}}(B_{d/s}^0 \rightarrow K^\pm \pi^\mp \pi^0)}, \quad (6.7)$$

$$N_{B_s^0 \rightarrow K^+ K^- \pi^0}^{K^\pm \pi^\mp \pi^0} = N_{B_s^0 \rightarrow K^+ K^- \pi^0} \times \frac{\epsilon_{PID}(KK \rightarrow K\pi)}{\epsilon_{PID}(KK \rightarrow KK)} \times \frac{\epsilon_{m_{K\pi}}(B_s^0 \rightarrow K^+ K^- \pi^0)}{\epsilon_{m_{KK}}(B_s^0 \rightarrow K^+ K^- \pi^0)}. \quad (6.8)$$

The PID efficiencies are reported in table 5.10. The corresponding efficiency ratios are presented in table 6.1. Considering the fact that the uncertainties of the PID efficiencies are correlated, their contributions to the uncertainty on the ratio are summed up linearly. The PID efficiency ratios range from 2.5% for the crossfeed of $K^\pm \pi^\mp \pi^0$ events into the $K^+ K^- \pi^0$ sample to 10.8% for $K^+ K^- \pi^0$ events crossfeeding in the $K^\pm \pi^\mp \pi^0$ sample. As one expects more $K^\pm \pi^\mp \pi^0$ events than $K^+ K^- \pi^0$ ones, this is safer than if it would be the other way round. The relative uncertainties on the PID efficiency ratios are between 23 and 35%.

The Dalitz cuts used in each sample are presented in table 5.24. Table 6.2 gives the corresponding efficiency ratios. The numbers were obtained from the resonant $B^0 \rightarrow \pi^+ \pi^- \pi^0$ and $B^0 \rightarrow K^+ \pi^- \pi^0$ Monte Carlo samples. The same efficiency ratios are assumed for $B_s^0 \rightarrow K^- \pi^+ \pi^0$ and $B^0 \rightarrow K^+ \pi^- \pi^0$. For $B_s^0 \rightarrow K^+ K^- \pi^0$, as there is no resonant Monte Carlo sample, efficiency ratios of 1 are assumed. Since the efficiencies of the Dalitz cuts depend on the actual Dalitz distributions, a conservative uncertainty of 15% will be used for those corrections. This is about as large as the larger correction. Given the uncertainties of the PID efficiency ratios, adding up this contribution in quadrature does not affect much the overall uncertainties on the crossfeed calculations. Overall, the relative uncertainties are between 27 and 38%.

Signal	Crossfeed to	Merged	Resolved
$B^0 \rightarrow \pi^+\pi^-\pi^0$	$K^\pm\pi^\mp\pi^0$	0.98	1.08
$B_{d/s}^0 \rightarrow K^\pm\pi^\mp\pi^0$	$\pi^+\pi^-\pi^0$	0.86	0.83
	$K^+K^-\pi^0$	1.06	1.01
$B_s^0 \rightarrow K^+K^-\pi^0$	$K^\pm\pi^\mp\pi^0$	1 (no MC)	

Table 6.2: Dalitz cut efficiency ratios used to evaluate the different crossfeed contributions. A relative uncertainty of 15% will be used for those corrections.

6.2.3 Free parameters

The fits of the distributions obtained from merged π^0 and resolved π^0 events are completely independent. According to the parametrisation discussed in section 6.2.1, in each of the two fits, the free parameters are the following:

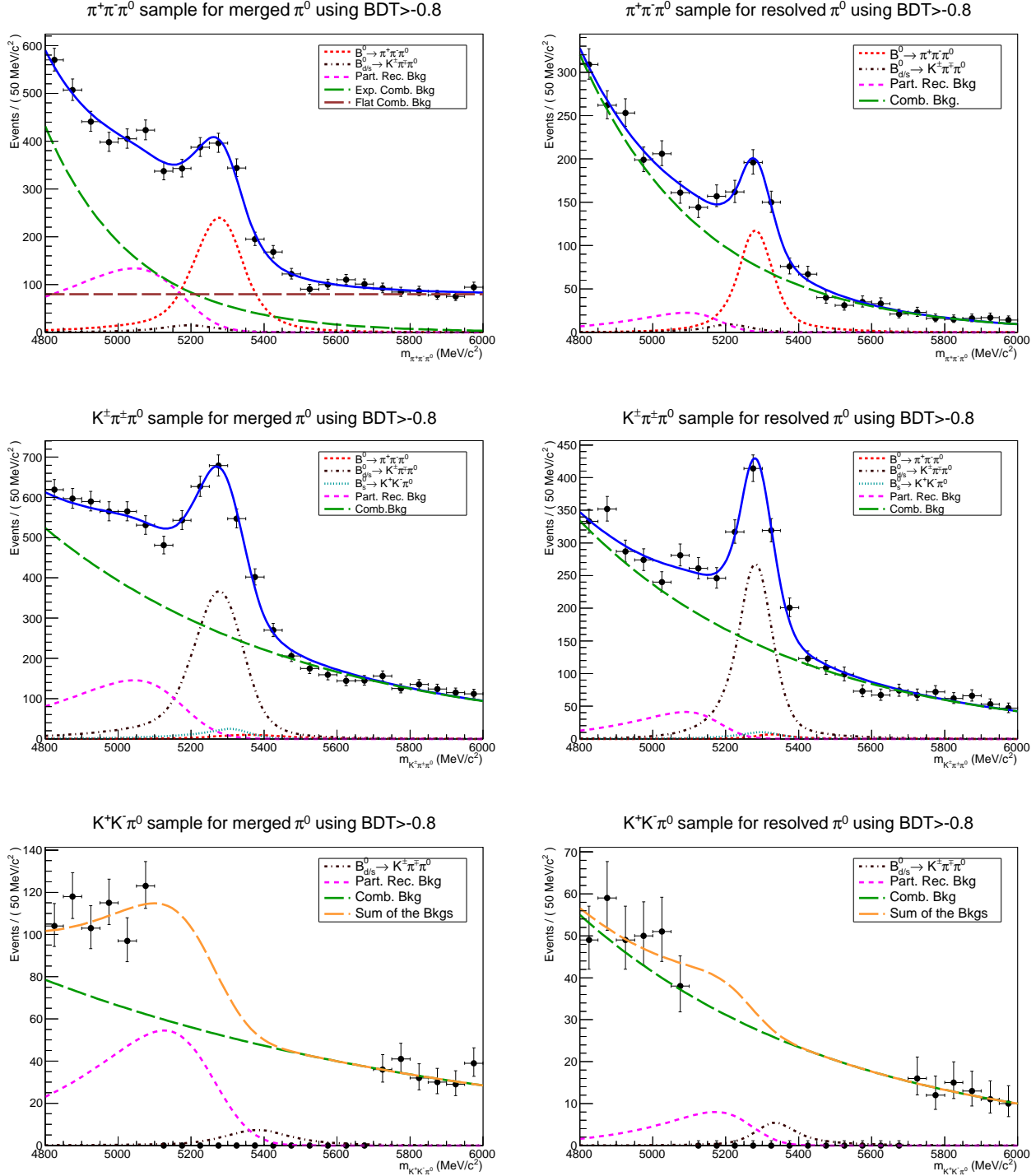
- μ_{B^0} and $\sigma_{B^0 \rightarrow \pi^+\pi^-\pi^0}$ for the signal shapes;
- the signal yields;
- the partially reconstructed background yields in the three samples;
- the yields and the exponents of the combinatorial backgrounds in the three samples.

In the case of merged π^0 events, an extra parameter is needed for the yield corresponding to the additional flat contribution in the $\pi^+\pi^-\pi^0$ sample.

6.3 Optimization of the BDT cut

The cut on the multivariate classifier output is optimized on the data estimating the signal and background yields thanks to the simultaneous fit described in the previous section. This is possible because the fit gives a good description of the data over a large range of cuts.

Figures 6.9 and 6.10 show the results obtained with two extreme values of the cut: $\text{BDT} > -0.8$ and $\text{BDT} > 0.9$. As the $B_s^0 \rightarrow K^+K^-\pi^0$ mode has not been observed previously, the signal region is blinded in the $K^+K^-\pi^0$ sample during the optimization. The data is not looked at in a wide range going from 5100 to 5700 MeV/ c^2 . The $B_s^0 \rightarrow K^+K^-\pi^0$ signal yield parameter is blinded and only the background PDFs are represented on the plots of the $K^+K^-\pi^0$ sample. In addition the crossfeed of $B_s^0 \rightarrow K^+K^-\pi^0$ events in the $K^\pm\pi^\mp\pi^0$ sample is evaluated from the $B^0 \rightarrow \pi^+\pi^-\pi^0$ yield instead of the $B_s^0 \rightarrow K^+K^-\pi^0$ one. In this way, it is not possible to asses, even indirectly, the $B_s^0 \rightarrow K^+K^-\pi^0$ yield.



For the optimization of the BDT cut, to simplify the fit and make in particular more robust the estimation of the signal yield in the $K^\pm\pi^\mp\pi^0$ sample, for which the most signal events are expected, no dedicated contribution is introduced for the $B_s^0 \rightarrow K^-\pi^+\pi^0$ mode. Only the $B^0 \rightarrow K^+\pi^-\pi^0$ PDF is used to model the signal. The obtained signal yield in this sample then corresponds to the sum of $B^0 \rightarrow K^+\pi^-\pi^0$ events and to a possible contribution from the B_s^0 .

One can see on figures 6.9 and 6.10 that the fits give a good description of the data for both merged and resolved π^0 events and in the three samples, at least for what concerns the sidebands in the $K^+K^-\pi^0$ sample.

As a figure of merit we choose a prescription from Punzi [116]. Considering a set of cuts t , the prescription is to maximize

$$F_{Punzi} = \frac{\epsilon(t)}{a/2 + \sqrt{B(t)}} , \quad (6.9)$$

where $\epsilon(t)$ and $B(t)$ are the signal efficiency and the background yield for the set of cuts t , and a is the desired significance for the signal observation. This maximization corresponds to minimize the number of signal events required for the desired significance.

We took a significance of $a = 5$. As only the evolution of the Punzi figure of merit is relevant, we replaced the signal efficiency of equation 6.9 by the signal yield. The ratio of signal yields between two cuts corresponds to their relative efficiencies.

The signal and background yields are estimated in a $\pm 3\sigma$ window around the signal peak with respect to the μ and the σ of the Crystal Balls. Since the signal region is blinded in the $K^+K^-\pi^0$ sample, the signal yield is replaced by the one of the $K^\pm\pi^\mp\pi^0$ sample. This relies on the fact that the BDT efficiency is supposed to be the same for the different signal modes.

Figure 6.11 shows the evolution of the Punzi figure of merit as a function of the BDT cut. A cut at 0.4 was selected for both merged and resolved π^0 events as it seems to be optimal for the various samples. Figure 6.12 shows, still with the $K^+K^-\pi^0$ signal region blinded, the corresponding distributions together with the results of the simultaneous fits.

The same value of the cut on the BDT output was found to be optimal using $(S/\sqrt{S+B})_{3\sigma}$ where S and B are the signal and background yields in a $\pm 3\sigma$ window around the signal peak, or the ratio between the fitted signal yields and their uncertainties as returned from the fit $(S/\Delta S)$. The figures presented here were obtained with the PDFs described in section 6.1. Those were themselves obtained with a cut at $\text{BDT} > 0.4$ but in fact there is not circularity

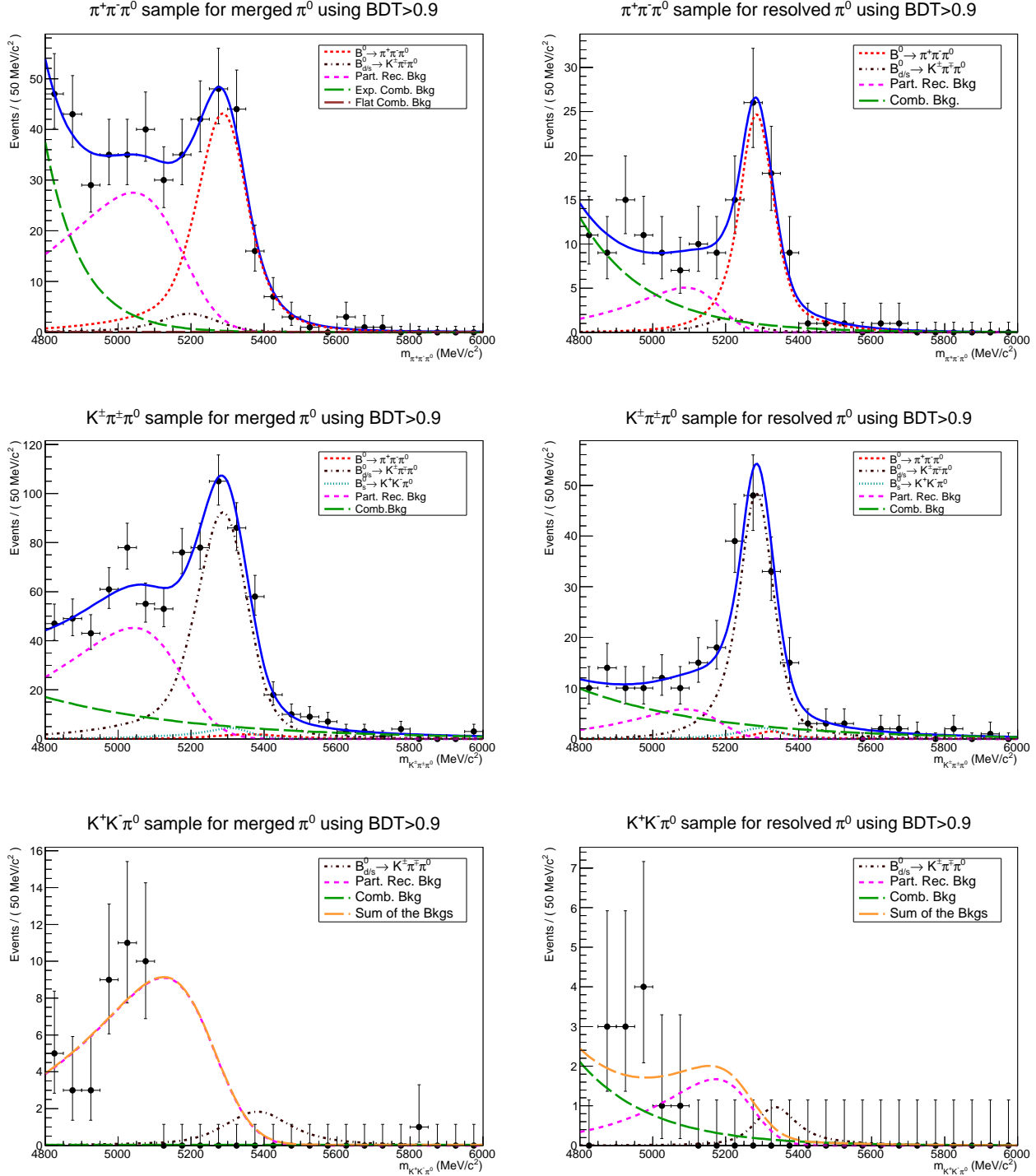


Figure 6.10: $m_{h^+ h^- \pi^0}$ distribution for merged π^0 (left) and resolved π^0 (right) events in the $\pi^+ \pi^- \pi^0$ (top), $K^\pm \pi^\mp \pi^0$ (middle) and $K^+ K^- \pi^0$ (bottom) samples cutting at $\text{BDT} > 0.9$. The blue lines represent the fitted PDFs. The different components are given in the legends. Here the signal region of the $K^+ K^- \pi^0$ sample is blinded.

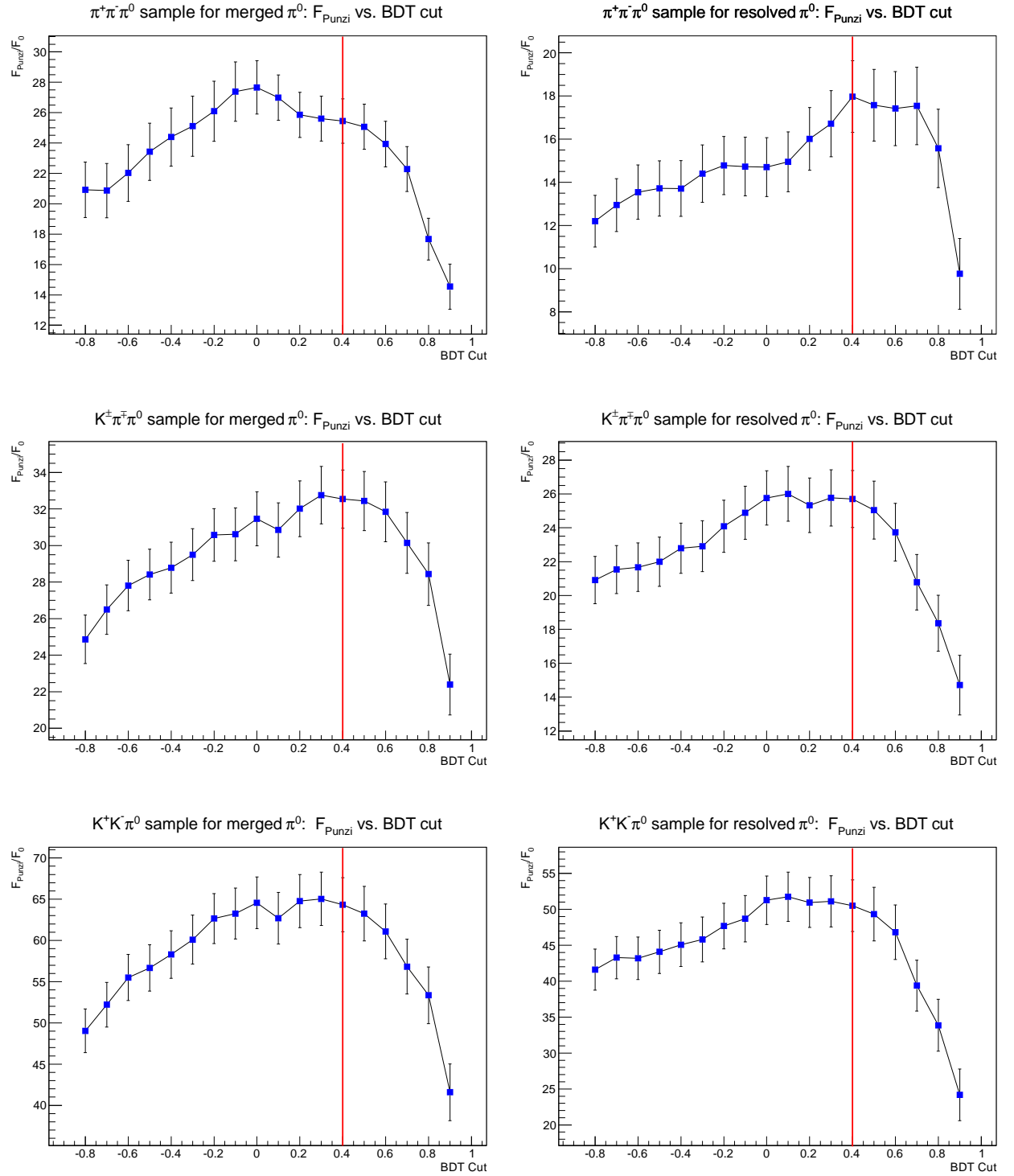


Figure 6.11: F_{Punzi} vs BDT cut for merged π^0 (left) and resolved π^0 (right) events in the $\pi^+\pi^-\pi^0$ (top), $K^+\pi^-\pi^0$ (middle) and $K^+K^-\pi^0$ (bottom) sample. Signal yields are used instead of signal efficiencies so the units of the vertical axes are arbitrary.

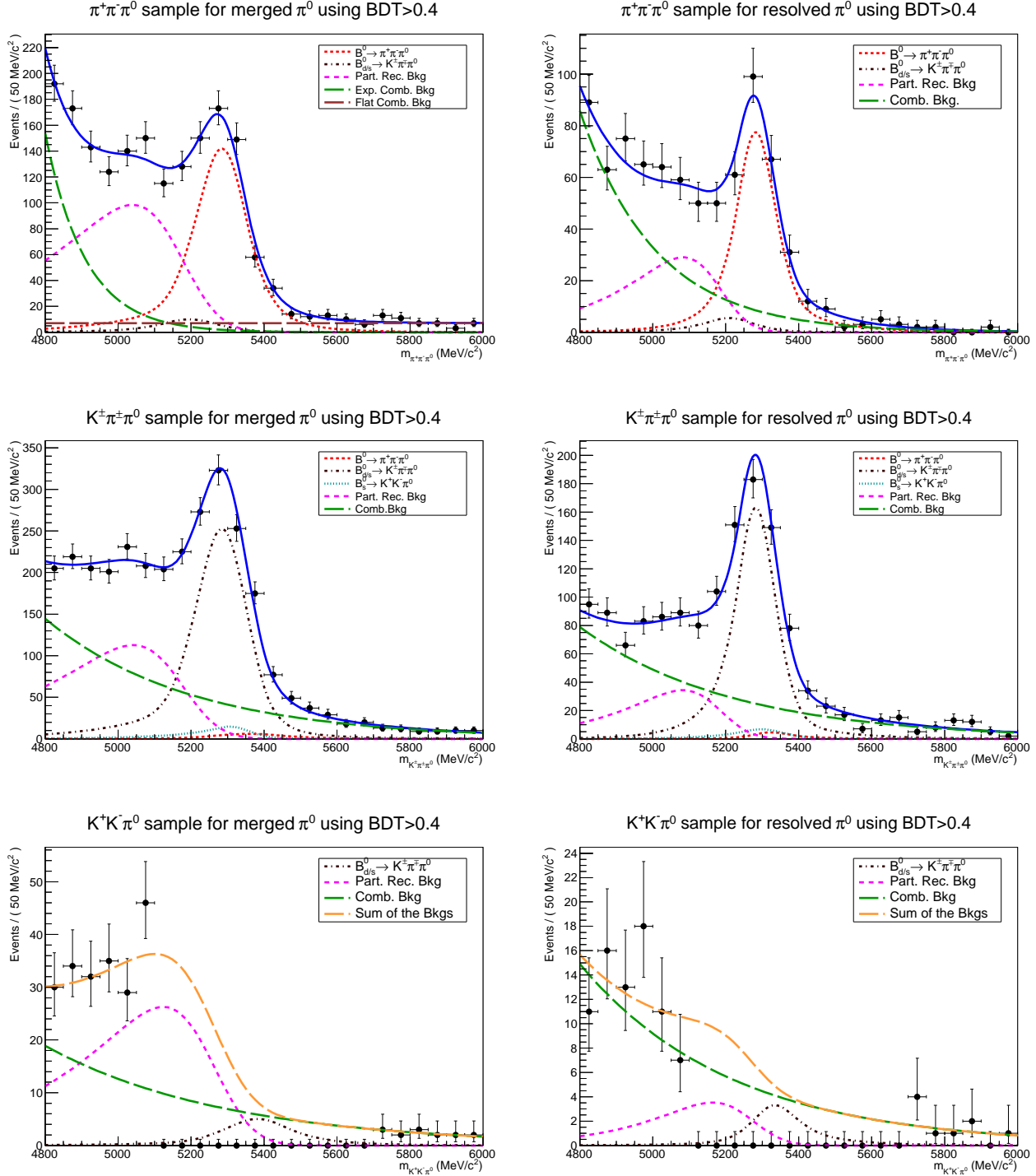


Figure 6.12: $m_{h^+ h^- \pi^0}$ distribution for merged π^0 (left) and resolved π^0 (right) events in the $\pi^+ \pi^- \pi^0$ (top), $K^\pm \pi^\mp \pi^0$ (middle) and $K^+ K^- \pi^0$ (bottom) samples cutting at $\text{BDT} > 0.4$. The blue lines represent the fitted PDFs. The different components are given in the legends. Here the signal region of the $K^+ K^- \pi^0$ sample is blinded.

Channel	Signal yield	$S/\Delta S$	$(S/\sqrt{S+B})_{3\sigma}$	$(S/B)_{3\sigma}$
$B^0 \rightarrow \pi^+\pi^-\pi^0$	592 ± 33	17.9	18.1 ± 1.0	1.54 ± 0.09
$B_{d/s}^0 \rightarrow K^\pm\pi^\mp\pi^0$	1073 ± 50	21.5	24.0 ± 1.1	1.43 ± 0.07
$B_s^0 \rightarrow K^+K^-\pi^0$	268 ± 23	11.7	12.7 ± 1.1	1.87 ± 0.16

Table 6.3: Signal yields, signal significances and signal over background ratios obtained for merged π^0 events before adding the $B_s^0 \rightarrow K^-\pi^+\pi^0$ contribution.

as the actual cut used has little effect on the PDFs. In reality, the first optimization was done with PDFs obtained with a cut at $\text{BDT} > -0.8$ and the same, $\text{BDT} > 0.4$, cut was found to be optimal.

6.4 Unblinding the $K^+K^-\pi^0$ signal region

Now that the value of the cut on the multivariate classifier output is fixed, as all the rest of the selection, the signal region of the $K^+K^-\pi^0$ sample is unblinded. At first, the fit without a dedicated $B_s^0 \rightarrow K^-\pi^+\pi^0$ contribution is still used to stay close to what was done during the optimization procedure. The only change in the fit model concerns the crossfeed of $B_s^0 \rightarrow K^+K^-\pi^0$ events in the $K^\pm\pi^\mp\pi^0$ sample that can now be evaluated from the corresponding signal yield.

Figures 6.13 and 6.14 show the data distributions and their fits for merged and resolved π^0 events respectively. There is a clear signal peak in the $K^+K^-\pi^0$ sample both for merged and resolved π^0 events. The fits well reproduce the data in the three samples over the full reconstructed B mass range, including the $K^+K^-\pi^0$ signal region. The fitted signal yields together with their statistical uncertainties are reported in tables 6.3 and 6.4. The yield in the $K^\pm\pi^\mp\pi^0$ sample has to be understood as the sum of the B^0 and B_s^0 contributions. The tables also present some crude estimations of the signal significance. The first one is the ratio between the fitted yield and its negative uncertainty ($S/\Delta S$), the second is $S/\sqrt{S+B}$ in a $\pm 3\sigma$ region around the signal peak (see end of previous section). The two estimators give similar numbers, well above 5 in all cases including the $B_s^0 \rightarrow K^+K^-\pi^0$ mode. The signal over background ratios in a $\pm 3\sigma$ range are also given. They are between 1.2 and 1.9 for merged π^0 events and around 2 in the case of resolved π^0 .

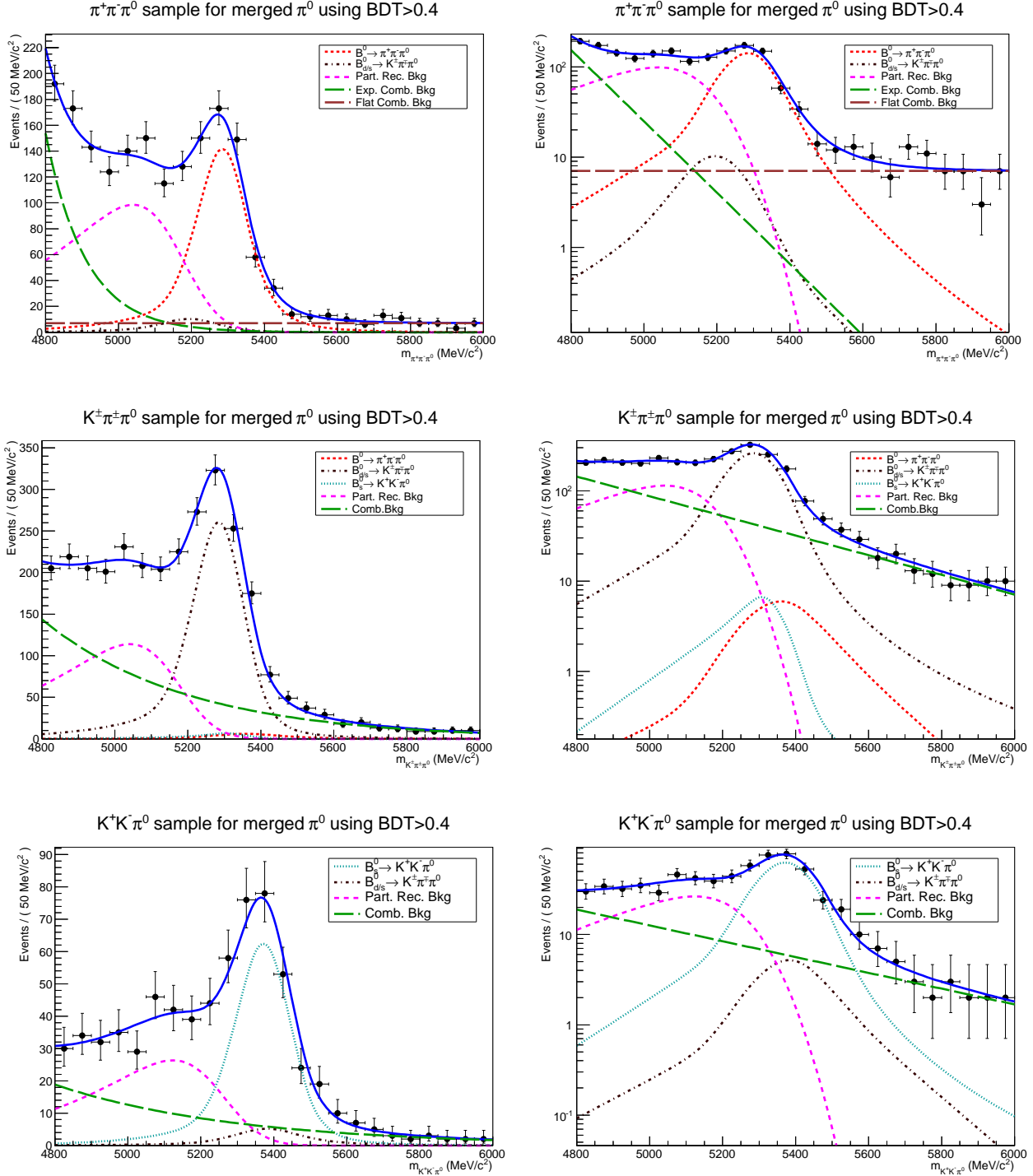


Figure 6.13: $m_{h^+h^-\pi^0}$ distribution for merged π^0 events in the $\pi^+\pi^-\pi^0$ (top), $K^\pm\pi^\mp\pi^0$ (middle) and $K^+K^-\pi^0$ (bottom) samples cutting at BDT>0.4. The distributions are presented on a linear (left) and a logarithmic (right) vertical scale. The blue lines represent the fitted PDFs. The different components are given in the legends.

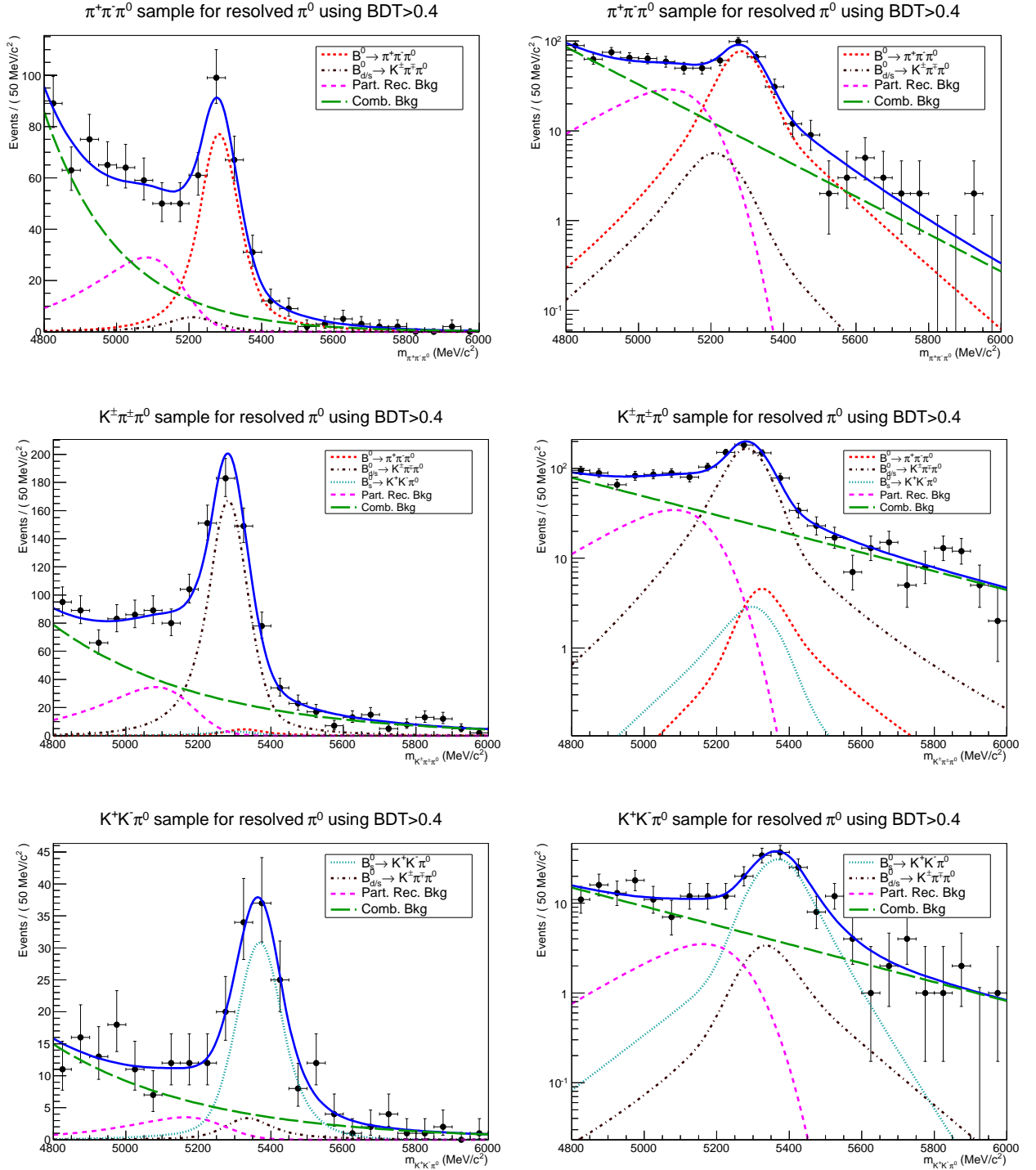


Figure 6.14: $m_{h^+ h^- \pi^0}$ distribution for resolved π^0 events in the $\pi^+ \pi^- \pi^0$ (top), $K^\pm \pi^\mp \pi^0$ (middle) and $K^+ K^- \pi^0$ (bottom) samples cutting at BDT>0.4. The distributions are presented on a linear (left) and a logarithmic (right) vertical scale. The blue lines represent the fitted PDFs. The different components are given in the legends.

Channel	Signal yield	$S/\Delta S$	$(S/\sqrt{S+B})_{3\sigma}$	$(S/B)_{3\sigma}$
$B^0 \rightarrow \pi^+\pi^-\pi^0$	257 ± 23	11.2	12.5 ± 1.1	2.15 ± 0.19
$B_{d/s}^0 \rightarrow K^\pm\pi^\mp\pi^0$	547 ± 34	16.1	18.1 ± 1.1	1.99 ± 0.12
$B_s^0 \rightarrow K^+K^-\pi^0$	110 ± 14	7.9	8.4 ± 1.0	2.10 ± 0.26

Table 6.4: Signal yields, signal significances and signal over background ratios obtained for resolved π^0 events before adding the $B_s^0 \rightarrow K^-\pi^+\pi^0$ contribution.

6.5 Signal yields

6.5.1 Final fit

While the $B_s^0 \rightarrow \pi^+\pi^-\pi^0$ and $B^0 \rightarrow K^+K^-\pi^0$ modes are expected to be negligible with respect to the $B^0 \rightarrow \pi^+\pi^-\pi^0$ and $B_s^0 \rightarrow K^+K^-\pi^0$ ones [51, 52], the situation is more complicated in the $K^\pm\pi^\mp\pi^0$ sample in which a possible contribution from the $B_s^0 \rightarrow K^-\pi^+\pi^0$ mode [52] has to be taken into account. The final fit then introduces separated PDFs for the $B^0 \rightarrow K^+\pi^-\pi^0$ and $B_s^0 \rightarrow K^-\pi^+\pi^0$ modes in the $K^\pm\pi^\mp\pi^0$ sample, and also in the other samples for what concerns their crossfeeds.

Figures 6.15 and 6.16 show the fit results for merged and resolved π^0 events respectively. For merged π^0 , the additional $B_s^0 \rightarrow K^-\pi^+\pi^0$ allows to marginally improve the fit. This is visible in particular in the $K^\pm\pi^\mp\pi^0$ sample between 5.35 and 5.60 GeV/ c^2 : the five consecutive data points are a bit above the fitted PDF in figure 6.13 while this is not the case here. Another effect is that the signal widths are reduced a little as one could expect since the previous fit would have the tendency to enlarge them to account for a $B_s^0 \rightarrow K^-\pi^+\pi^0$ contribution. However, it is clear that the fitted $B_s^0 \rightarrow K^-\pi^+\pi^0$ yield should not be taken too seriously. Given the invariant mass resolution for merged π^0 events, the B^0 and the B_s^0 contributions are only separated by about 1.3σ . Here, with a fitted B_s^0 yield of only around 15% of the B^0 one, small changes on the right hand tail of the B^0 shape would greatly affect the fitted B_s^0 yield. For resolved π^0 events, the fitted $B_s^0 \rightarrow K^\pm\pi^\mp\pi^0$ yield is negligible so the fit is almost identical with the previous one.

Table 6.5 presents the comparison of the signal shape parameters, μ_{B^0} and $\sigma_{B^0 \rightarrow \pi^+\pi^-\pi^0}$, between data and Monte Carlo. They are in good agreement. The fitted signal yields and their statistical uncertainties are reported in tables 6.6 and 6.7. As previously, the crude estimations of the signal significance give numbers well above 5 for all the modes but $B_s^0 \rightarrow K^-\pi^+\pi^0$. The fitted $B_s^0 \rightarrow K^-\pi^+\pi^0$ yield is 2.3 times larger than its negative uncertainty for merged π^0 events. It is compatible with 0 for resolved π^0 events. The signal over background ratios in a $\pm 3\sigma$ range are a bit higher than before for merged π^0 events due to the small reduction

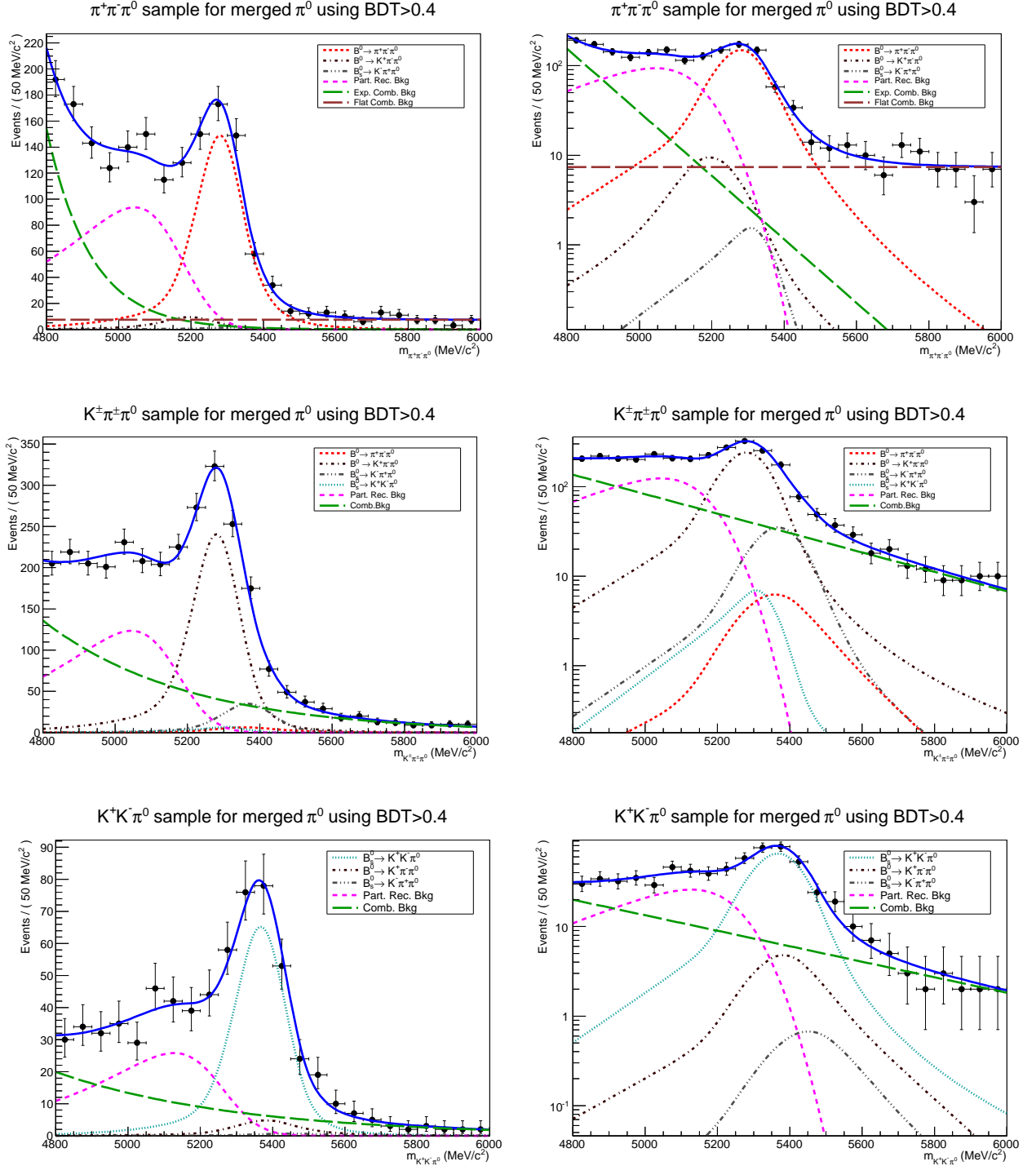


Figure 6.15: $m_{h^+\pi^-\pi^0}$ distribution for merged π^0 events in the $\pi^+\pi^-\pi^0$ (top), $K^\pm\pi^\mp\pi^0$ (middle) and $K^+K^-\pi^0$ (bottom) samples cutting at $\text{BDT} > 0.4$. A dedicated $B_s^0 \rightarrow K^-\pi^+\pi^0$ contribution is used in the fit presented here. The distributions are presented on a linear (left) and a logarithmic (right) vertical scale. The blue lines represent the fitted PDFs. The different components are given in the legends.

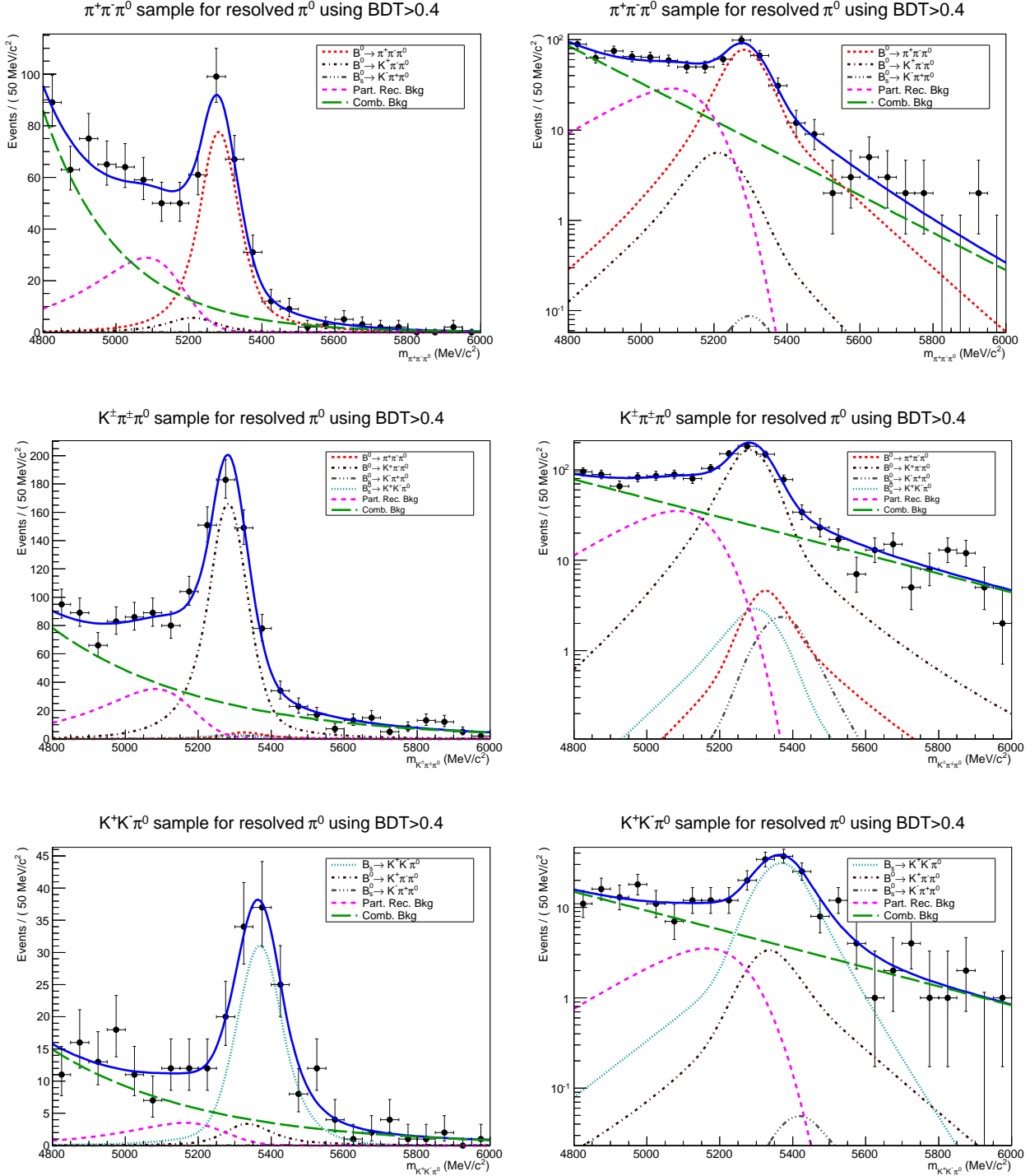


Figure 6.16: $m_{h+h'-\pi^0}$ distribution for resolved π^0 events in the $\pi^+\pi^-\pi^0$ (top), $K^\pm\pi^\mp\pi^0$ (middle) and $K^+K^-\pi^0$ (bottom) samples cutting at BDT>0.4. A dedicated $B_s^0 \rightarrow K^-\pi^+\pi^0$ contribution is used in the fit presented here. The distributions are presented on a linear (left) and a logarithmic (right) vertical scale. The blue lines represent the fitted PDFs. The different components are given in the legends.

Parameter	Merged π^0		Resolved π^0	
	Data	Monte Carlo	Data	Monte Carlo
μ_{B^0} (MeV/ c^2)	5280.1 $^{+3.7}_{-3.9}$	5276.8 \pm 3.4	5282.0 $^{+3.7}_{-4.1}$	5282.0 \pm 3.3
$\sigma_{B^0 \rightarrow \pi^+ \pi^- \pi^0}$ (MeV/ c^2)	64.5 $^{+3.5}_{-3.4}$	61.6 \pm 4.3	52.3 $^{+3.9}_{-4.0}$	42.7 \pm 5.2

Table 6.5: Comparison of the signal shape parameters between Data and $B^0 \rightarrow \pi^+ \pi^- \pi^0$ Monte Carlo.

Channel	Signal yield	$S/\Delta S$	$(S/\sqrt{S+B})_{3\sigma}$	$(S/B)_{3\sigma}$
$B^0 \rightarrow \pi^+ \pi^- \pi^0$	586 $^{+34}_{-41}$	11.3	18.2 \pm 1.1	1.64 \pm 0.10
$B^0 \rightarrow K^+ \pi^- \pi^0$	934 $^{+75}_{-72}$	13.0	24.6 \pm 1.6	1.57 \pm 0.11
$B_s^0 \rightarrow K^- \pi^+ \pi^0$	142 $^{+62}_{-61}$	2.3		
$B_s^0 \rightarrow K^+ K^- \pi^0$	264 $^{+23}_{-22}$	12.0	13.6 \pm 1.2	2.39 \pm 0.20

Table 6.6: Signal yields, signal significances and signal over background ratios for merged π^0 events.

of the signal widths. They are here between 1.6 and 2.4.

6.5.2 First observation of the $B_s^0 \rightarrow K^+ K^- \pi^0$ mode

To better quantify the signal significance of the $B_s^0 \rightarrow K^- \pi^+ \pi^0$ and $B_s^0 \rightarrow K^+ K^- \pi^0$ modes, previously unobserved, their log-likelihood profiles are drawn as one can see on figures 6.17 and 6.18. The differences of the log-likelihoods between the fitted values and the no signal hypothesis give significances ($\Delta LL = -\chi^2/2$) of 2.3 for the $B_s^0 \rightarrow K^- \pi^+ \pi^0$ mode in merged π^0 events and of 15.6 (10.5) for the $B_s^0 \rightarrow K^+ K^- \pi^0$ mode in merged (resolved) π^0 events.

Even statistically only, the evidence level is not reached for the $B_s^0 \rightarrow K^- \pi^+ \pi^0$ mode.

Channel	Signal yield	$S/\Delta S$	$(S/\sqrt{S+B})_{3\sigma}$	$(S/B)_{3\sigma}$
$B^0 \rightarrow \pi^+ \pi^- \pi^0$	256 $^{+24}_{-23}$	11.1	12.5 \pm 1.1	2.14 \pm 0.19
$B^0 \rightarrow K^+ \pi^- \pi^0$	538 $^{+42}_{-50}$	10.8	18.2 \pm 2.0	2.03 \pm 0.21
$B_s^0 \rightarrow K^- \pi^+ \pi^0$	8 $^{+37}_{-8}$	-		
$B_s^0 \rightarrow K^+ K^- \pi^0$	109 \pm 14	7.8	8.4 \pm 1.0	2.12 \pm 0.27

Table 6.7: Signal yields, signal significances and signal over background ratios for resolved π^0 events.

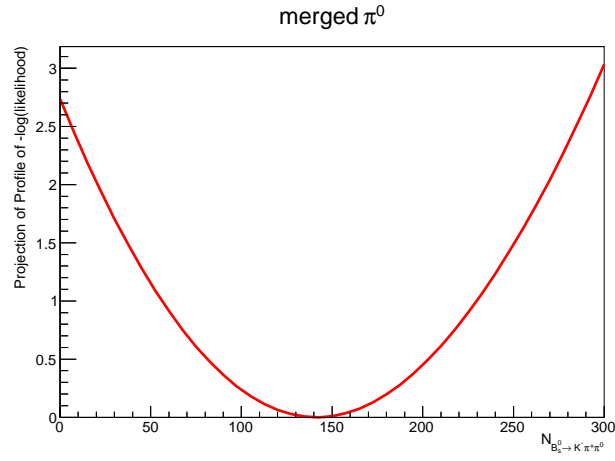


Figure 6.17: Log-likelihood profile as a function of $N_{B_s^0 \rightarrow K^- \pi^+ \pi^0}$ for merged π^0 events.

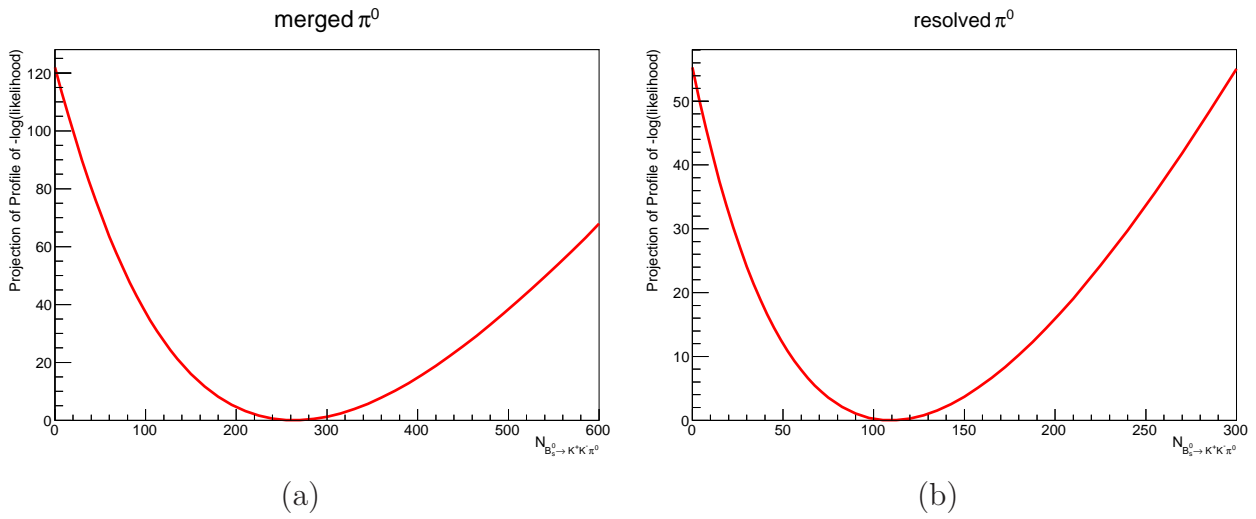


Figure 6.18: Log-likelihood profile as a function of $N_{B_s^0 \rightarrow K^+ K^- \pi^0}$ for merged π^0 (a) and resolved π^0 (b) events.

Channel	Merged π^0	resolved π^0
$B^0 \rightarrow \pi^+\pi^-\pi^0$	8.2 ± 2.7	9.2 ± 3.0
$B^0 \rightarrow K^+\pi^-\pi^0$	6.6 ± 1.8	5.2 ± 1.4
$B_s^0 \rightarrow K^+K^-\pi^0$	10.9 ± 4.2	12.8 ± 4.9

Table 6.8: Crossfeed over signal ratios (%) for the different channels and for merged or resolved π^0 events.

As previously discussed, considering systematic uncertainties on the right hand tail of the $B^0 \rightarrow K^+\pi^-\pi^0$ would in addition considerably reduce the significance. On the other hand, the first observation of the $B_s^0 \rightarrow K^+K^-\pi^0$ mode can be claimed with no doubt.

6.5.3 Crossfeed contributions

From the fitted signal yields in the three samples and the efficiency ratios of the PID and Dalitz cuts, reported in tables 6.1 and 6.2, the crossfeed contributions can be evaluated. The crossfeed over signal ratios are presented in table 6.8. For the $B^0 \rightarrow \pi^+\pi^-\pi^0$ and $B_s^0 \rightarrow K^+K^-\pi^0$ channels the crossfeeds correspond to the sum of the $B^0 \rightarrow K^+\pi^-\pi^0$ and $B_s^0 \rightarrow K^-\pi^+\pi^0$ contributions. For the $B^0 \rightarrow K^+\pi^-\pi^0$ channel, the reported ratio consider for the signal only the $B^0 \rightarrow K^+\pi^-\pi^0$ fitted yield, not the $B_s^0 \rightarrow K^-\pi^+\pi^0$ one, and for the crossfeed the sum of the $B^0 \rightarrow \pi^+\pi^-\pi^0$ and $B_s^0 \rightarrow K^-\pi^+\pi^0$ contributions.

The uncertainties given in table 6.8 correspond to the sum in quadrature of the uncertainties on the PID efficiency ratios, see table 6.1, and the Dalitz efficiency ratios, for which we assume a $\pm 15\%$ relative uncertainty as already mentioned in section 6.2.2.

6.5.4 Results

Since the signal and crossfeed shapes are not that different, the uncertainties reported in table 6.8 directly translate into relative uncertainties on the signal yields. Table 6.9 shows the signal yields together with their statistical uncertainties and the systematic uncertainties related to the crossfeeds. The yields obtained summing up merged and resolved π^0 events are also presented. The uncertainty related to the crossfeeds is here obtained summing linearly the uncertainties for merged and resolved π^0 events as they are fully correlated.

Uncertainties on the signal and background shapes also affect the signal yields. However, they cancel out at first order when calculating yields ratios to evaluate ratio of branching fractions and should then be evaluated on the yield ratios not on the yields themselves. A possibility here would be to measure the branching fraction of the previously unobserved

Channel	merged π^0	resolved π^0	merged + resolved π^0
$B^0 \rightarrow \pi^+\pi^-\pi^0$	$586^{+34}_{-41} \pm 16$	$256^{+24}_{-23} \pm 8$	$842^{+42}_{-47} \pm 24$
$B^0 \rightarrow K^+\pi^-\pi^0$	$934^{+75}_{-72} \pm 17$	$538^{+42}_{-50} \pm 8$	$1472^{+86}_{-88} \pm 25$
$B_s^0 \rightarrow K^+K^-\pi^0$	$264^{+23}_{-22} \pm 11$	$109 \pm 14 \pm 5$	$373^{+27}_{-26} \pm 16$

Table 6.9: Signal yields. The first uncertainty is statistical, the second is the systematic related to the crossfeeds.

$B_s^0 \rightarrow K^+K^-\pi^0$ mode relative to the $B^0 \rightarrow \rho^\pm\pi^\mp$ one. The $B^0 \rightarrow K^+\pi^-\pi^0$ branching fraction is known with a relative uncertainty of 8.5% [6], which is a bit better than the 10% of the $B^0 \rightarrow \rho^\pm\pi^\mp$ mode [6], but may not be used as a normalization because of the possible $B_s^0 \rightarrow K^-\pi^+\pi^0$ contribution. To measure a ratio of branching fractions, one needs the yield ratio but also the ratio of efficiencies. Here, the efficiency would have to be mapped on the Dalitz plane and applied to the observed Dalitz distributions in the two modes. The Dalitz distributions are the object of the forthcoming section.

6.6 Dalitz distributions

The Dalitz distributions have been obtained by subtracting statistically the partially reconstructed and combinatorial backgrounds thanks to the sPlot technique [109]. The Dalitz variables are calculated refitting the B decay constraining $m_{h+h'-\pi^0}$ to the nominal B mass. Doing so, they are not correlated with the unconstrained $m_{h+h'-\pi^0}$ which is fitted to evaluate the sWeights. The sum of the sWeighted distributions putting together merged and resolved π^0 are presented on figure 6.19. Those distributions are not corrected for variations of efficiency across the Dalitz plane nor for crossfeed contributions. Those represent of the order of 8% of the overall distribution for $B^0 \rightarrow \rho^\pm\pi^\mp$, 5% for $B^0 \rightarrow K^+\pi^-\pi^0$ and 10% for $B_s^0 \rightarrow K^+K^-\pi^0$. The $B^0 \rightarrow K^+\pi^-\pi^0$ mode is also potentially polluted by $B_s^0 \rightarrow K^-\pi^+\pi^0$ events. The fit presented in the previous section evaluates those events to contribute at the level of 9% of the overall distribution.

The corresponding two-body invariant mass spectra are shown on figures 6.20 to 6.22. Contributions from $\rho(770)^\pm$ and $K^*(892)^\pm$ can be clearly identified on those plots. The $B^0 \rightarrow \rho^\pm\pi^\mp$ distributions are in relatively good agreement with the Monte Carlo expectations. The $B^0 \rightarrow K^+\pi^-\pi^0$ ones seem to agree with BaBar and Belle measurements [41, 46].

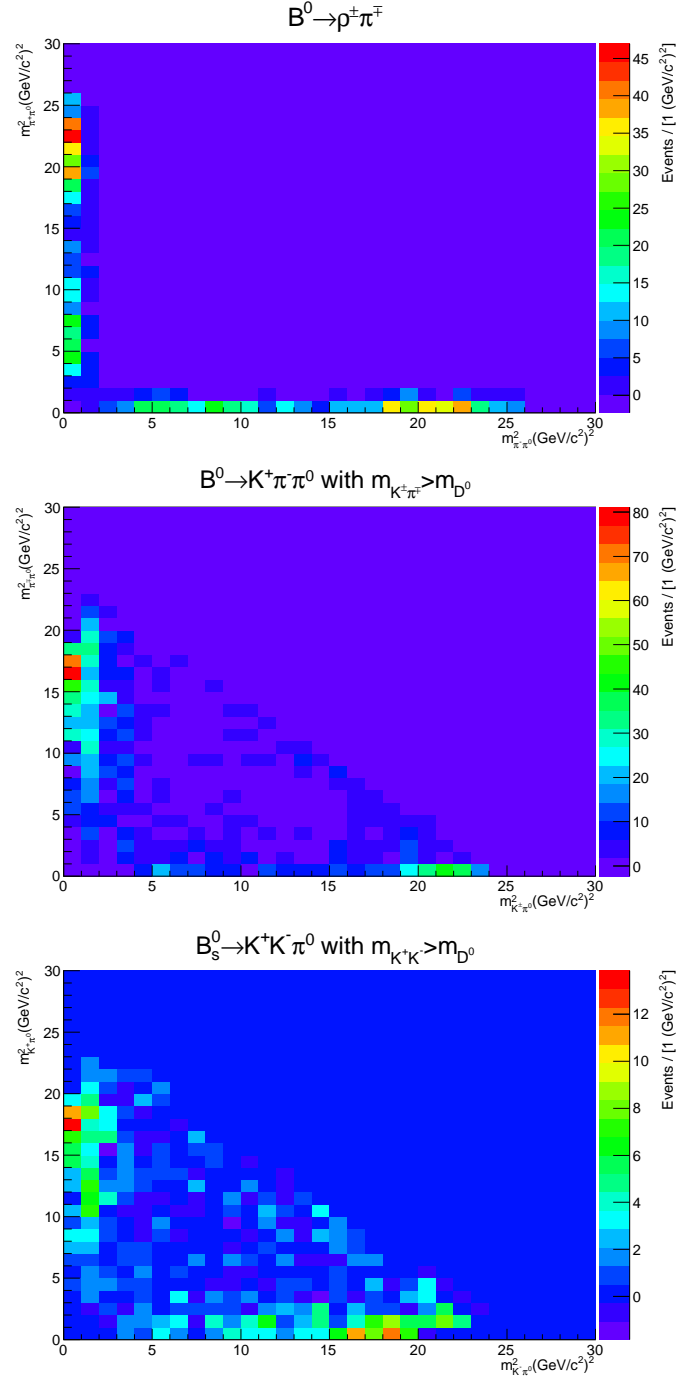


Figure 6.19: Dalitz distributions for $B^0 \rightarrow \pi^+\pi^-\pi^0$ events in the $\rho^+\pi^-$ region (top), $B^0 \rightarrow K^+\pi^-\pi^0$ events with $m_{K^+\pi^-} > m_{D^0}$ (middle), and $B_s^0 \rightarrow K^+K^-\pi^0$ events with $m_{K^+K^-} > m_{D^0}$ (bottom).

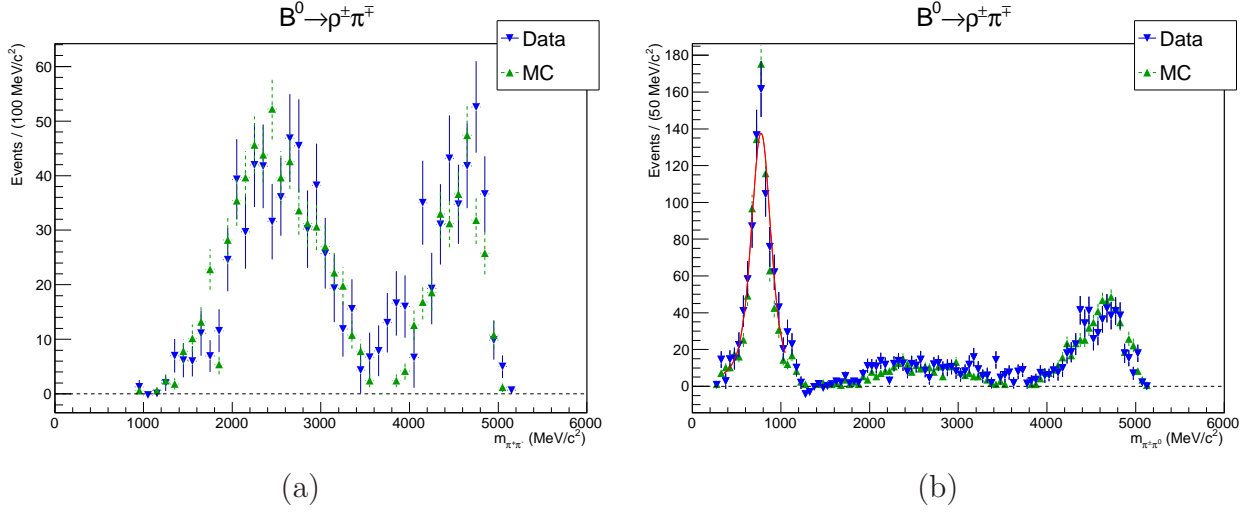


Figure 6.20: $m_{\pi^+\pi^-}$ (a) and $m_{\pi^\pm\pi^0}$ (b) distributions for $B^0 \rightarrow \pi^+\pi^-\pi^0$ events in the $\rho^\pm\pi^\mp$ region. The data are in blue, the Monte Carlo in green. The red line represents a simple Breit-Wigner fit of the $\rho(770)^\pm$ peak.

6.7 Summary

A simultaneous fit has been developed to extract the $B_{d/s}^0 \rightarrow h^+h'^-\pi^0$ yields. It allows to account for the signal crossfeeds and gives a good description of the data. The value of the cut on the multivariate classifier output has been optimized on data blinding the $B_s^0 \rightarrow K^+K^-\pi^0$ mode. The unblinding leads to the first observation of this mode.

The signal yields are of the order of 840, 1470 and 370 for the $B^0 \rightarrow \pi^+\pi^-\pi^0$, $B^0 \rightarrow K^+\pi^-\pi^0$ and $B_s^0 \rightarrow K^+K^-\pi^0$ modes respectively. The systematic uncertainties related to the crossfeeds have been evaluated. They range from 1.7% of the yield for the $B^0 \rightarrow K^+\pi^-\pi^0$ mode to 4.3% for the $B_s^0 \rightarrow K^+K^-\pi^0$ one.

The Dalitz distributions, background subtracted but not corrected for variations of efficiency across the Dalitz plane non for crossfeed contributions, have been presented. They seem to agree with expectations and previous measurements for the $B^0 \rightarrow \pi^+\pi^-\pi^0$ and $B^0 \rightarrow K^+\pi^-\pi^0$ modes. A possible extension of this work would be to measure the $\mathcal{B}(B_s^0 \rightarrow K^+K^-\pi^0)_{m_{K^+K^-} > D^0} / \mathcal{B}(B^0 \rightarrow \rho^\pm\pi^\mp)$ ratio of branching fractions.

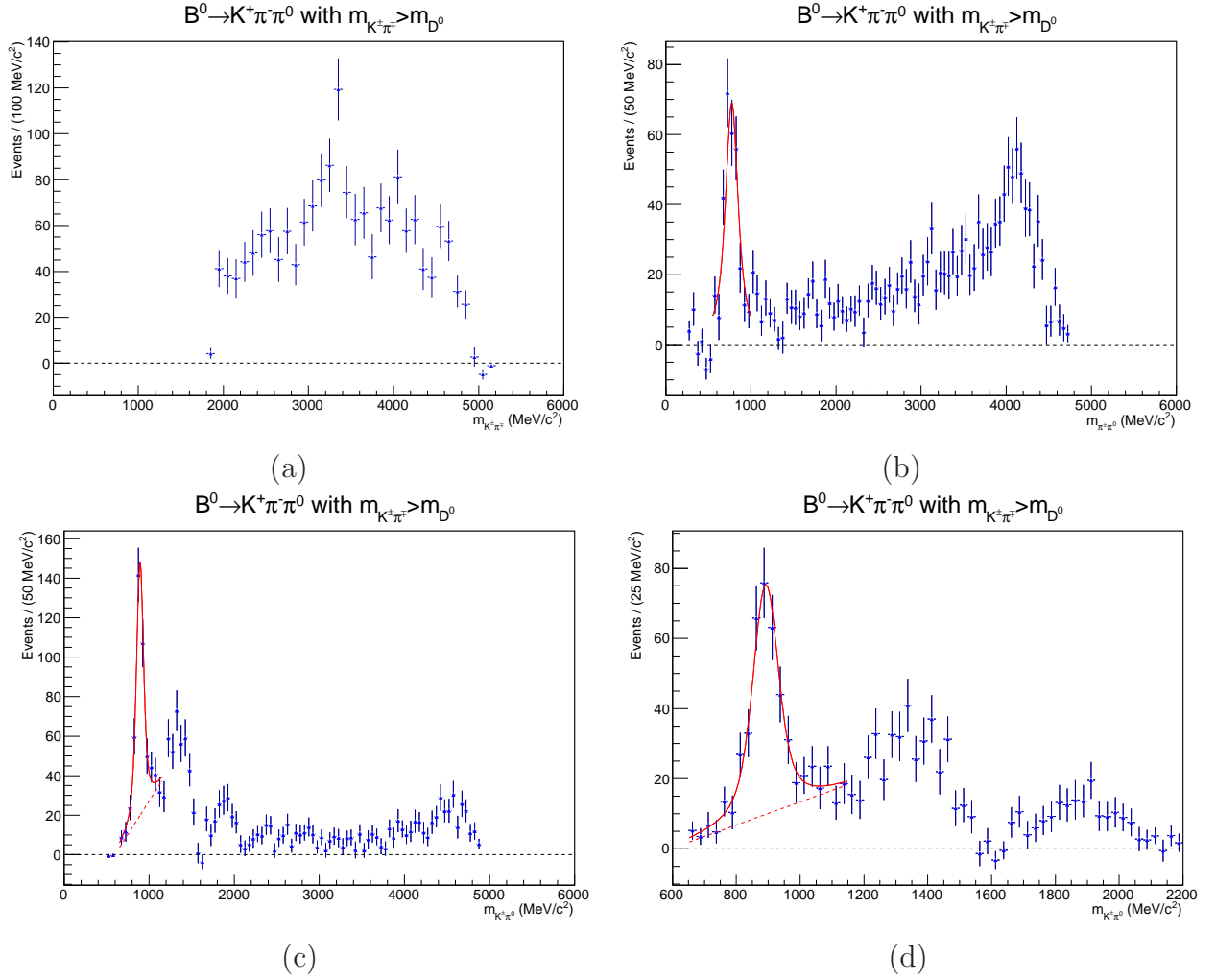


Figure 6.21: Obtained $m_{K^\pm \pi^\mp}$ (a), $m_{\pi^\pm \pi^0}$ (b) and $m_{K^\pm \pi^0}$ (c) distributions for $B^0 \rightarrow K^+ \pi^- \pi^0$ events with $m_{K^\pm \pi^\mp} > m_{D^0}$; (d) $m_{K^\pm \pi^0}$ distribution below 2.2 GeV/c². The red lines represent simple Breit-Wigner fits of the $\rho(770)^\pm$ (a) and $K^*(892)^\pm$ (c and d) peaks.

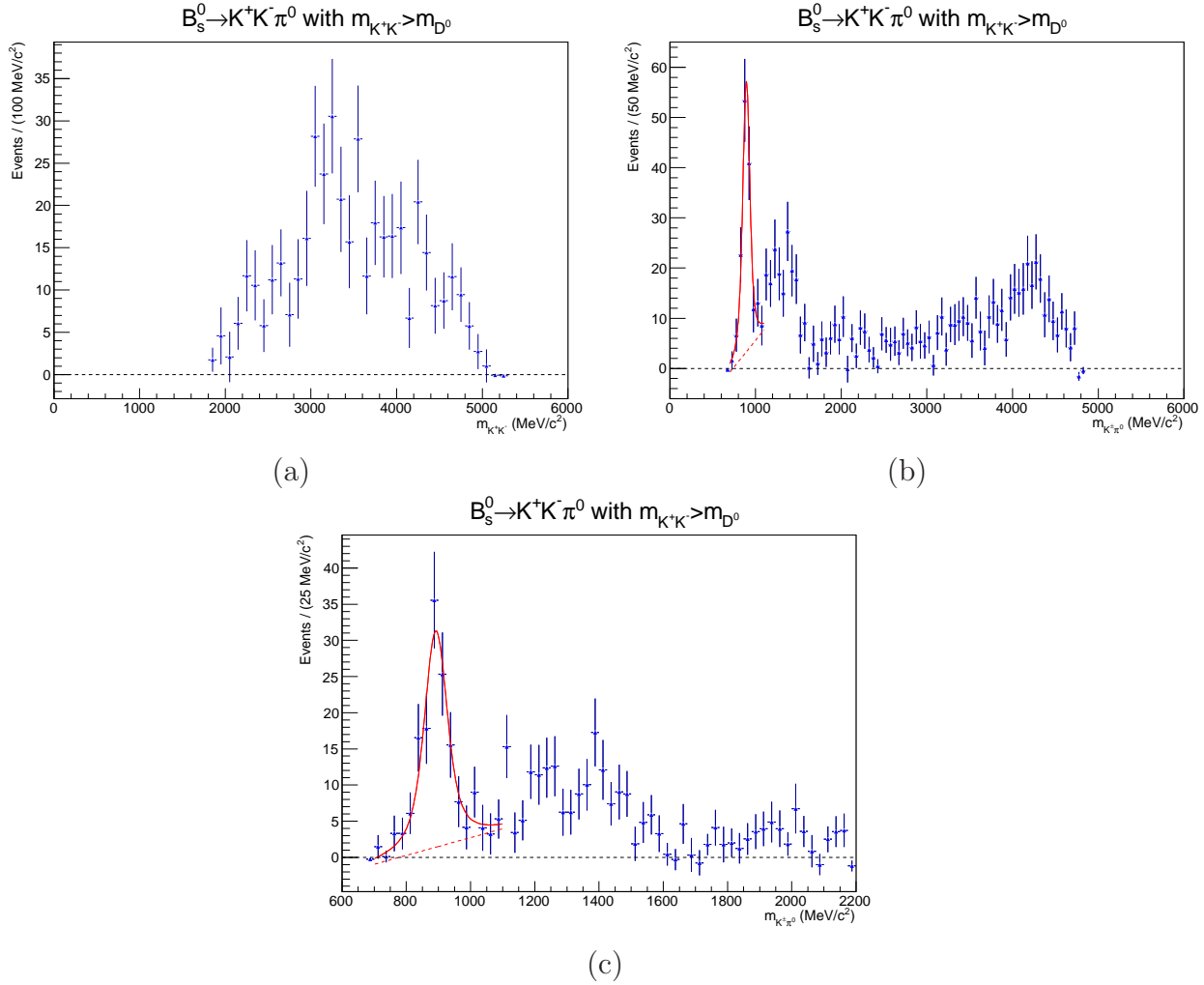


Figure 6.22: $m_{K^+ K^-}$ (a) and $m_{K^\pm \pi^0}$ (b) distributions for $B_s^0 \rightarrow K^+ K^- \pi^0$ events with $m_{K^+ K^-} > m_{D^0}$; (c) $m_{K^\pm \pi^0}$ distribution below 2.2 GeV/c². The red lines represent a simple Breit-Wigner fit of the $K^*(892)^\pm$ peak.

Conclusion

Charmless three body decays of neutral b-mesons with a π^0 in the final state are sensitive to the angles α and γ of the unitarity triangle. For instance, the cleanest way to extract α from the theoretical point of view is the time dependent Dalitz analysis of the $B^0 \rightarrow \pi^+\pi^-\pi^0$ mode. It is however very challenging experimentally. In this work charmless $B_{d,s}^0 \rightarrow h^+h'^-\pi^0$ decays have been studied using the 1.0 fb^{-1} data sample collected by LHCb in 2011.

In a first stage, the π^0 energy calibration and the π^0/γ discrimination have been studied thanks to a clean and high statistics sample of π^0 obtained considering $D^*(2010)^+ \rightarrow D^0(\rightarrow K^-\pi^+\pi^0)\pi^+$ decays. For this, a dedicated $D^0 \rightarrow K^-\pi^+\pi^0$ stripping line was implemented. The $D^*(2010)^+ \rightarrow D^0\pi^+$ sample contains about 2.5×10^5 and 3.6×10^5 signal events with merged and resolved π^0 respectively.

A full selection chain has been implemented for $B_{d,s}^0 \rightarrow h^+h'^-\pi^0$ decays. It includes dedicated trigger and stripping lines. The combinatorial background is reduced thanks to a multivariate classifier. It was found that radiative B decays dominate at low $m_{h+h'^-}$. The study was then limited to the $\rho^\pm\pi^\mp$ region for the $\pi^+\pi^-\pi^0$ sample and to $m_{h+h'^-} > m_{D^0}$ for the $K^\pm\pi^\mp\pi^0$ and $K^+K^-\pi^0$ one. Only about 10% of the signal events are expected in the excluded regions of the Dalitz planes.

A simultaneous fit of the three samples is used to extract the signal yields. It allows to take into account the signal crossfeeds and to have a coherent description of the signal shape over the three samples. The fit gives a good description of the reconstructed B mass spectra. The $B_s^0 \rightarrow K^+K^-\pi^0$ mode is observed for the first time. The signal yields are of the order of 840, 1470 and 370 for the $B^0 \rightarrow \pi^+\pi^-\pi^0$, $B^0 \rightarrow K^+\pi^-\pi^0$ and $B_s^0 \rightarrow K^+K^-\pi^0$ modes respectively. The Dalitz distributions were presented. They still need to be corrected for variations of efficiency in the Dalitz plane and for crossfeed contributions, which range from 5 to 10%. For $B^0 \rightarrow \pi^+\pi^-\pi^0$ and $B^0 \rightarrow K^+\pi^-\pi^0$ modes, they seem to agree with B-factories measurements. A possible extension of this work is to measure the $B_s^0 \rightarrow K^+K^-\pi^0$ branching fraction normalized to the $B^0 \rightarrow \rho^\pm\pi^\mp$ one.

APPENDIX A

π^0 calibration from $D^0 \rightarrow K\pi\pi^0$ decays

In this appendix the tables present the obtained correction factors on the π^0 4-momentum in the case of merged π^0 and resolved π^0 . The corresponding reconstructed D^0 mass distributions before correction are presented in the figures following those tables. The sample of events with merged π^0 is divided in six sub-samples depending on the position of the π^0 in the ECAL (inner, middle, outer) and considering separately π^0 with or without associated signal in the SPD. For resolved π^0 , six subsamples are also considered requiring both photons to be in the inner, middle or outer part of the ECAL and considering separately π^0 with two non-converted photons or with two converted photons. The fit model is the same as in 4.4.4.

	Inner	Middle	Outer
No SPD signal	1.0126 ± 0.0005	1.0035 ± 0.0004	0.9759 ± 0.0006
With SPD signal	1.0270 ± 0.0004	1.0073 ± 0.0005	0.9684 ± 0.0007

Table A.1: Correction factors obtained for merged π^0 . The uncertainties are statistical only.

	Both γ inner	Both γ middle	Both γ outer
Both γ non-converted	0.9812 ± 0.0007	0.9860 ± 0.0006	0.9734 ± 0.0011
Both γ converted	0.9949 ± 0.0009	0.9983 ± 0.0009	0.9702 ± 0.0019

Table A.2: Correction factors obtained for resolved π^0 . The uncertainties are statistical only.

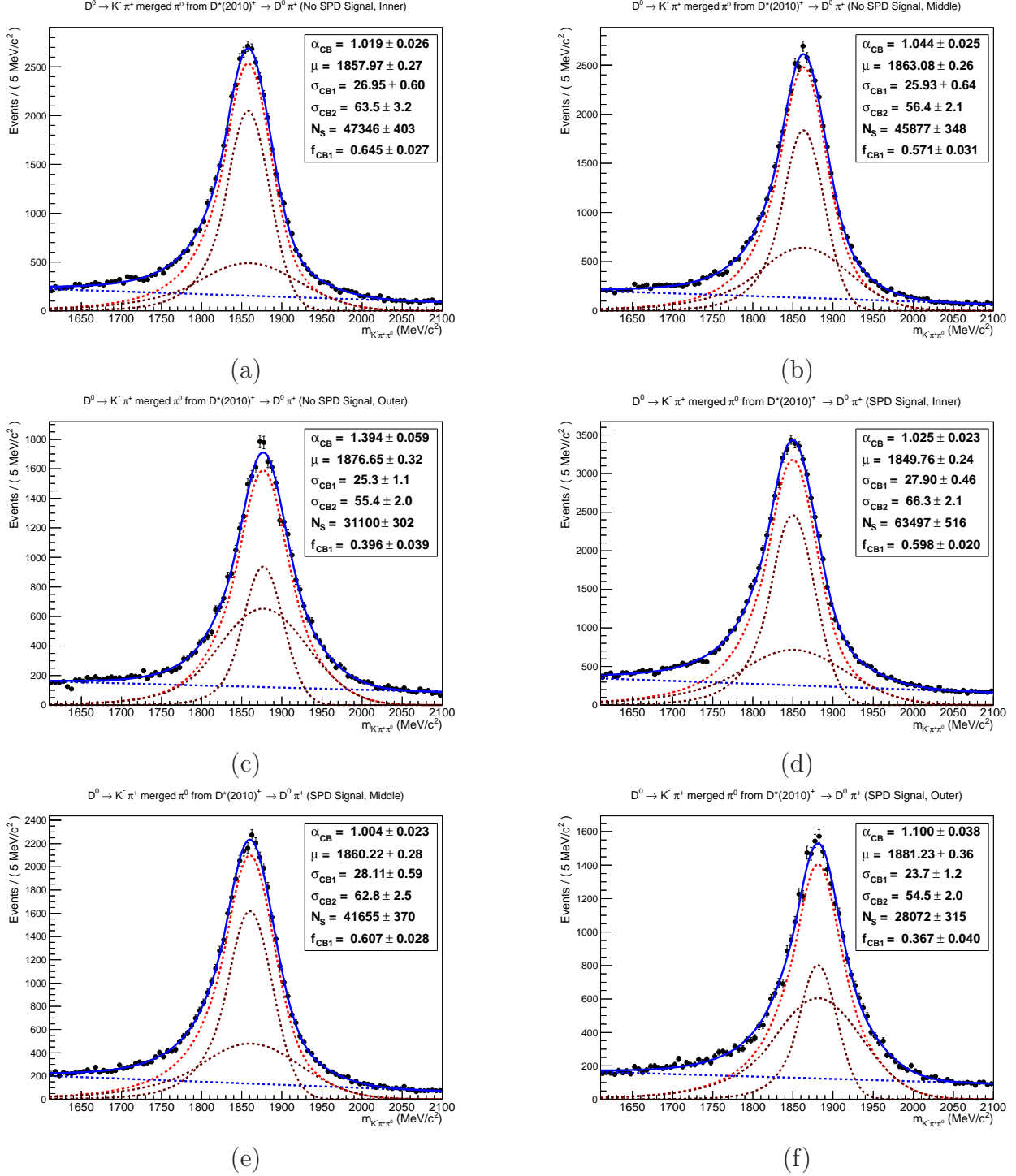


Figure A.1: $K^- \pi^+ \pi^0$ invariant mass distributions before correction for events with merged π^0 in the six subsamples considered. (a) Inner no SPD signal, (b) middle no SPD signal, (c) outer no SPD signal, (d) inner with SPD signal, (e) middle with SPD signal, (f) outer with SPD signal.

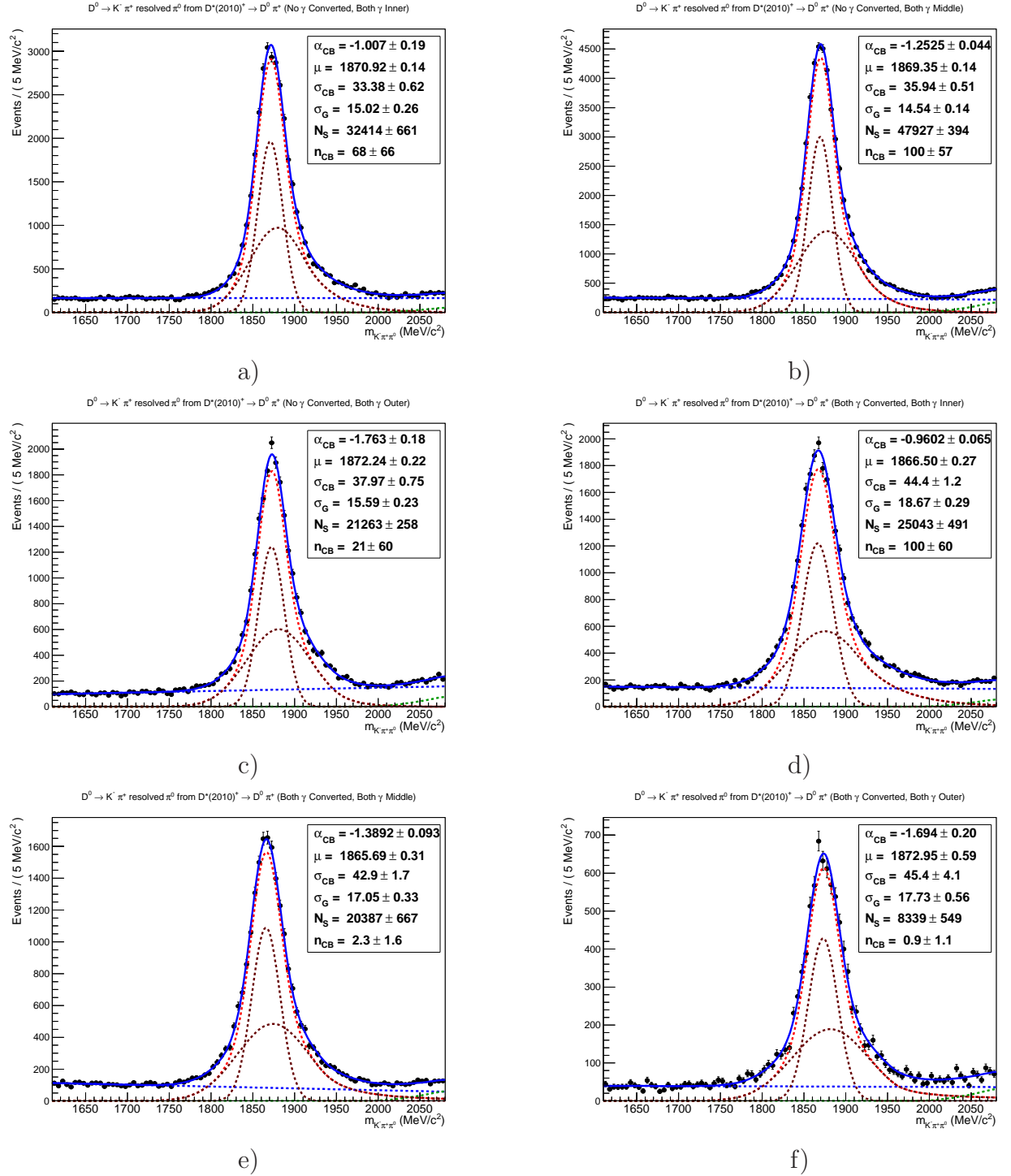


Figure A.2: $K^- \pi^+ \pi^0$ invariant mass distributions before correction for events with resolved π^0 in the six subsamples considered. (a) Inner both γ non-converted, (b) middle both γ non-converted, (c) outer both γ non-converted, (d) inner both γ converted, (e) middle both γ converted, (f) outer both γ converted.

APPENDIX B

Stripping Selection

This appendix illustrates the cuts used in the $B_{d/s}^0 \rightarrow h^+ h'^- \pi^0$ stripping line. The samples used are $B_d^0 \rightarrow \pi^+ \pi^- \pi^0$ Monte Carlo events for signal, Monte Carlo $b\bar{b}$ events and real data minimum bias events. In each plot, the corresponding cut is drawn. In the figure, the plots on the left are for events with merged π^0 and the plots on the right for events with resolved π^0 . The plots were obtained applying a loose preselection presented in table B.1.

Observable	Cut
Tracks p_T	$> 0.3 \text{ GeV}/c$
Tracks minimum $\text{IP}\chi^2$	> 9
π^0 p_T	$> 1 \text{ GeV}/c$
B vertex χ^2 prob.	$> 10^{-6}$
B minimum $\text{IP}\chi^2$	< 100
$ m_B - m_{B^0}^{PDG} $	$< 1.7 \text{ GeV}/c^2$

Table B.1: Cuts of the loose preselection used to study the stripping selection.

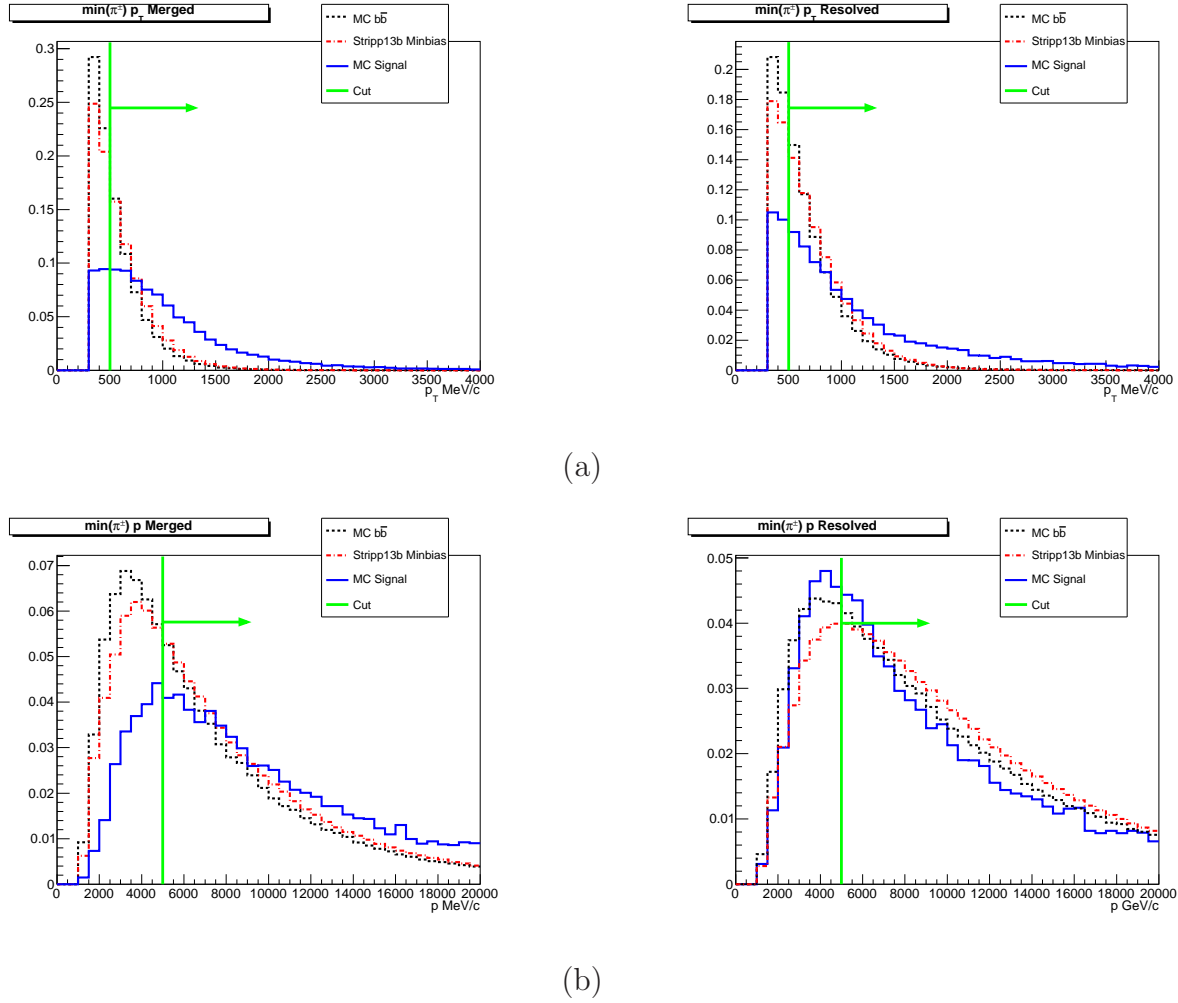


Figure B.1: Distributions of (a) the minimum p_T over the two tracks and (b) the minimum p over the two tracks. The cuts on the tracks p and p_T correspond to the ones used in the trigger which are imposed by the trigger tracking reconstruction.

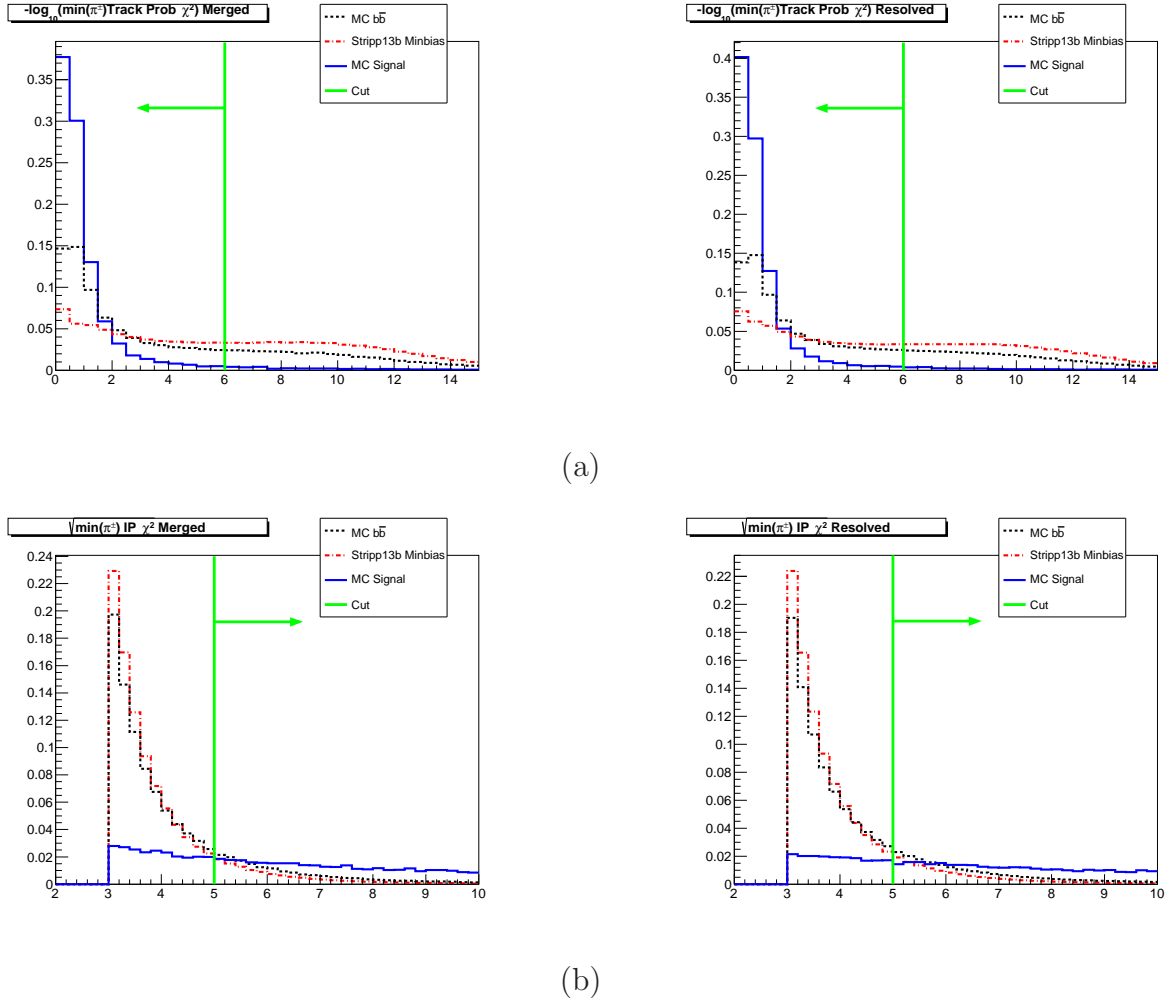
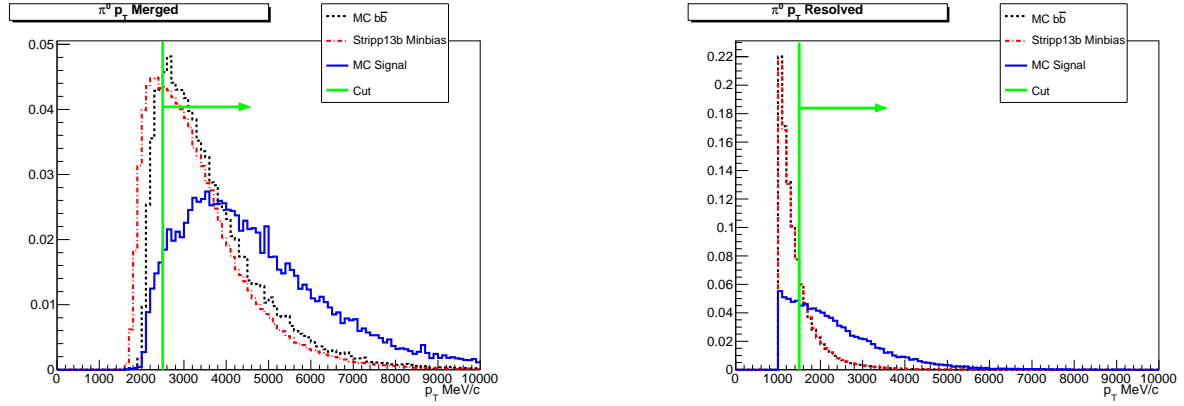
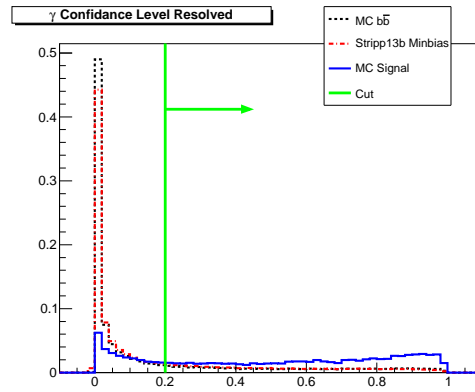


Figure B.2: Distributions of (a) the negative of logarithm in base 10 of the minimum track fit χ^2 probability over the two tracks and (b) the square root of the minimum IP χ^2 over the two tracks.

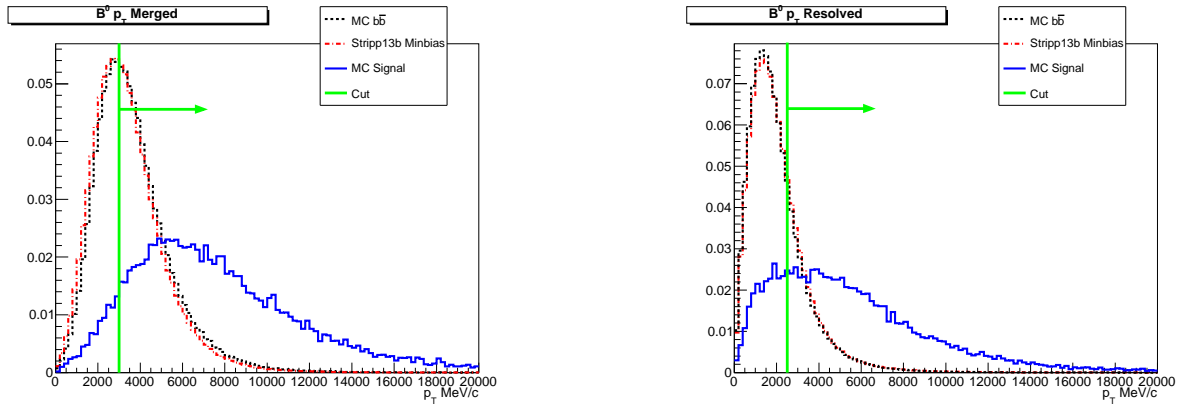


(a)

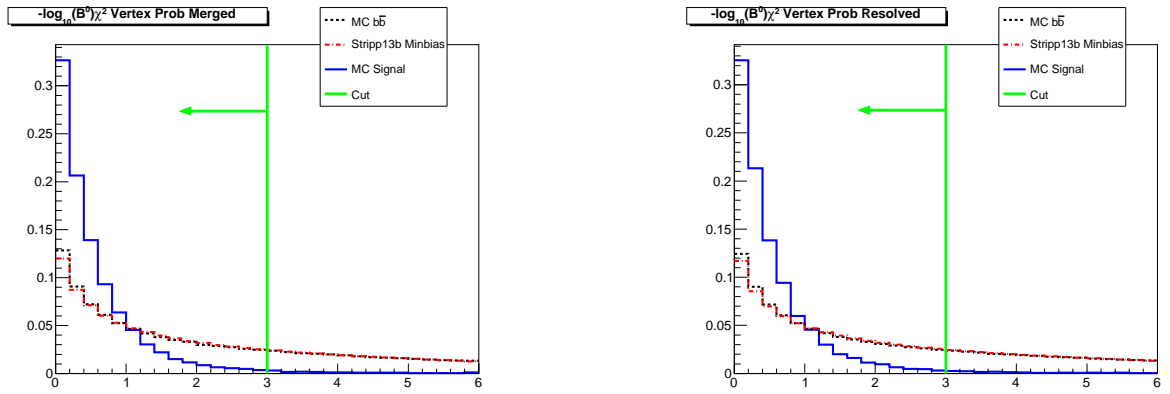


(b)

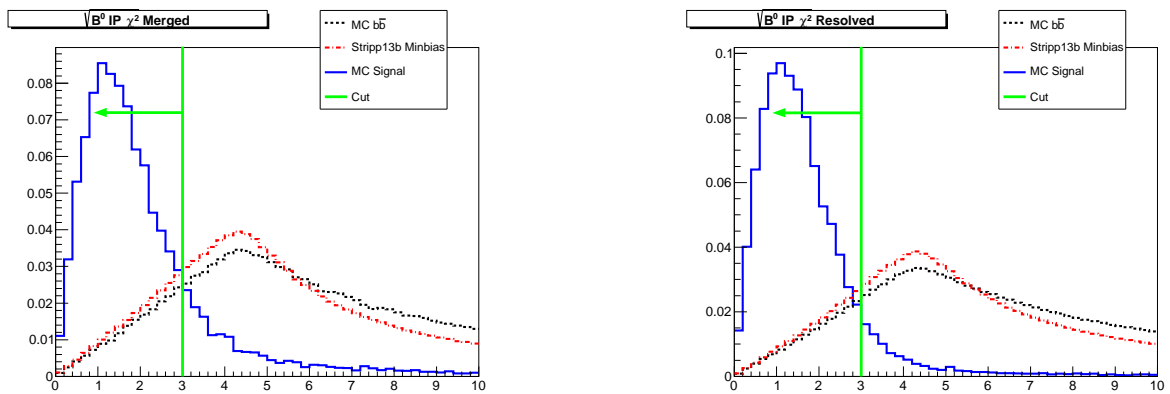
Figure B.3: Distributions of (a) the $\pi^0 p_T$ and (b) the minimum γ CL over the two photons for resolved π^0 .



(a)

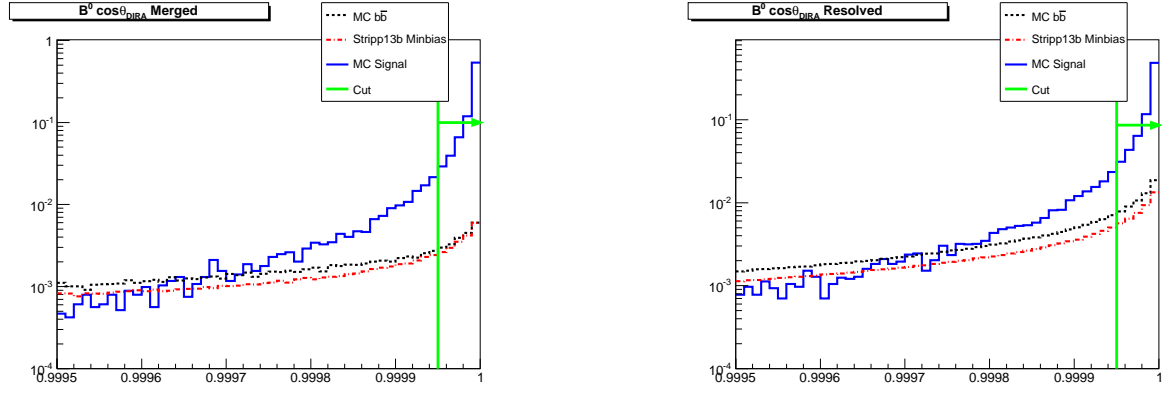


(b)

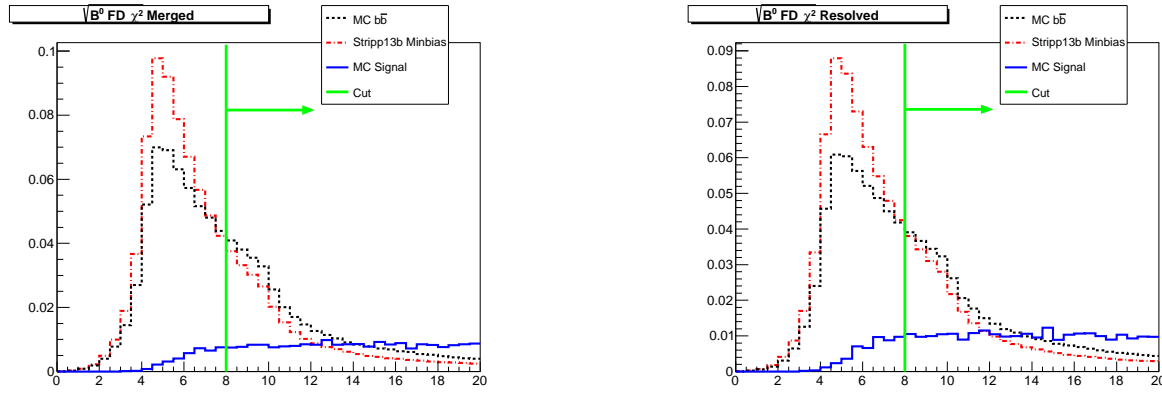


(c)

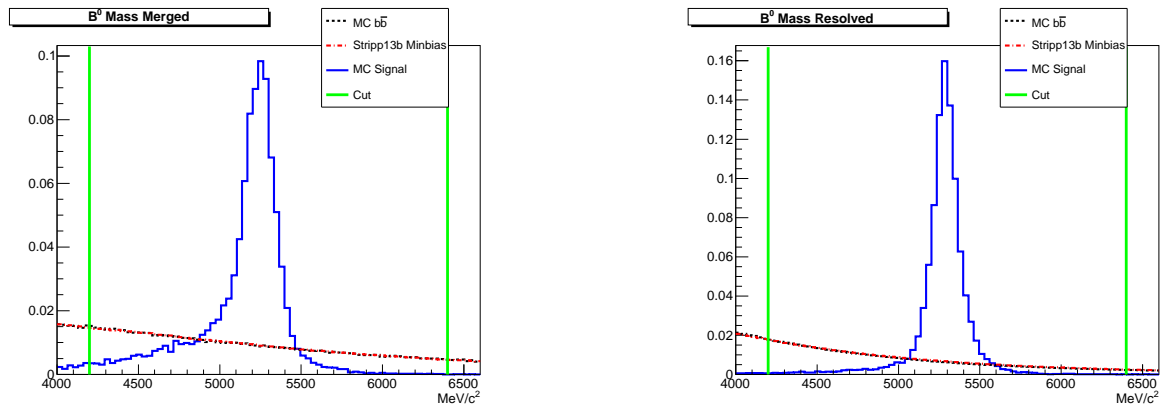
Figure B.4: Distributions of (a) the B^0 candidate p_T , (b) the negative of logarithm in base 10 of the B^0 candidate end vertex fit χ^2 probability and (c) the square root of the B^0 candidate minimum $\text{IP}\chi^2$.



(a)



(b)



(c)

Figure B.5: Distributions of (a) the cosine of the B^0 candidate θ_{DIRA} , (b) the square root of the B^0 candidate FD χ^2 and (c) the reconstructed mass of the B^0 candidate.

Bibliography

- [1] D. Perkins, *Introduction to High Energy Physics*, Cambridge, Cambridge University Press (2000).
- [2] L. Anchordoqui and F. Halzen, *Lessons in Particle Physics*, arXiv:0906.1271v2 (2009).
- [3] N. Cabbibo, *Unitary Symmetry and Leptonic Decays*, Phys. Rev. Lett. **10** (1963) 531.
- [4] I. Bigi and A. Sanda, *CP Violation*, Cambridge, Cambridge University Press (2000).
- [5] P. Harrison and H. Quinn, *The BaBar Physics Book*, SLAC Report (1998).
- [6] J. Beringer *et al.* [Particle Data Group], *Review of particle physics*, Phys. Rev. **D86** (2012) 010001.
- [7] L. Wolfenstein, *Parametrization of the Kobayashi-Maskawa Matrix*, Phys. Rev. Lett. **51** (1983) 1945.
- [8] P. Paganini *et al.*, *Measurements of the ρ and η Parameters of the V_{CKM} Matrix and Perspectives*, Phys. Scr. **58** (1998) 556.
- [9] C. Jarlskog, *Commutator of the quark mass matrices in the standard electroweak model and a measure of maximal CP nonconservation*, Phys. Rev. Lett. **55** (1985) 1039.
- [10] <http://www.physics.uoguelph.ca/Nucweb/superaligned.html>
- [11] J.C. Hardy and I.S. Towner, *Superaligned $0^+ \rightarrow 0^+$ nuclear β decays: A new survey with precision tests of the conserved vector current hypothesis and the standard model*, Phys. Rev. C. **79** (2009) 055502.
- [12] P.A. Boyle *et al.*, *K_{I3} Semileptonic Form Factor from (2+1)-Flavor Lattice QCD*, Phys. Rev. Lett. **100**, (2008) 141601 [arXiv:0710.5136].
- [13] E. Follana *et al.* [HPQCD and UKQCD collaborations], *High-Precision Determination of the π , K , D , and D_s Decay Constants from Lattice QCD*, Phys. Rev. Lett. **100** (2008) 062002 [arXiv:0706.1726].

- [14] M. Antonelli *et al.* [flaviaNet working group on kaon decays], *An evaluation of —Vus— and precise tests of the Standard Model from world data on leptonic and semileptonic kaon decays*, Eur. Phys. J. C **69** (2010) 399 [arXiv:1005.2323v2].
- [15] L. Widhalm, *Measurement of $D^0 \rightarrow \pi l \nu (K l \nu)$ form factors and absolute branching fractions*, Phys. Rev. Lett. **97** (2006) 061804.
- [16] P. Vilain *et al.* [CHARM II collaboration], *Leading-order QCD analysis of neutrino-induced dimuon events*, Eur. Phys. J.C **11** (1999) 19.
- [17] CMS collaboration, *First measurement of $R = B(t \rightarrow Wb)/B(t \rightarrow Wq)$ in the dilepton channel in pp collisions at $\sqrt{s}=7$ TeV*, CMS-PAS-TOP-11-029 (2011).
- [18] J. Charles *et al.* [CKMfitter group], *CP Violation and the CKM Matrix: Assessing the Impact of the Asymmetric B Factories*, Eur. Phys. J. C **41** (2005) 1-131 [hep-ph/0406184]. Updated results and plots available at <http://ckmfitter.in2p3.fr>
- [19] M. Gronau and D. London, *How to determine all the angles of the unitarity triangle from $B_d^0 \rightarrow DK_S$ and $B_s^0 \rightarrow D\phi$* , Phys. Lett. B **253** (1991) 483.
- [20] M. Gronau and D. Wyler, *On determining a weak phase from charged B decay asymmetries*, Phys. Lett. B **265** (1991) 172.
- [21] D. Atwood *et al.*, *Enhanced CP Violation with $B \rightarrow KD^0(\bar{D}^0)$ modes and extraction of the Cabibbo-Kobayashi-Maskawa Angle γ* , Phys. Rev. Lett. **78** (1997) 3257.
- [22] A. Poluektov *et al.* [Belle collaboration], *Measurement of ϕ_3 with Dalitz plot analysis of $B^\pm \rightarrow D^{(*)}K^\pm$ decay*, Phys. Rev. D **70** (2004) 072003 [hep-ex/0406067].
- [23] A. Giri *et al.*, *Determining γ using $B^\pm \rightarrow DK^\pm$ with multibody D decays*, Phys. Rev. D **68** (2003) 054018 [hep-ph/0303187].
- [24] A. Lenz *et al.*, *Constraints on new physics in $B - \bar{B}$ mixing in the light of recent LHCb data*, Phys. Rev. D **86** (2012) 033005 [hep-ph:1203.0238]
- [25] S. W. Herb *et al.*, *Observation of a Dimuon Resonance at 9.5 GeV in 400-GeV Proton-Nucleus Collisions*, Phys. Rev. Lett. **39** (1977) 252.
- [26] C. Bebek *et al.*, *Evidence for New-Flavor Production at the $\Upsilon(4S)$* , Phys. Rev. Lett. **46** (1981) 84.
- [27] M. Battle *et al.*, *Observation of B^0 decay to two charmless mesons*, Phys. Rev. Lett. **71** (1993) 3922.
- [28] A. Buras, *Weak Hamiltonian, CP Violation and Rare Decays, Lectures in high energy physics*, hep-ph/9806471 (1998).

- [29] A. Ali, G. Kramer, and C. Lu, *Experimental tests of factorization in charmless nonleptonic two-body B decays*, Phys. Rev. D **58** (1998) 094009 [hep-ph/9804363].
- [30] G.Kramer, W.F. Palmer and H. Simma, *CP violation and strong phases from penguins in $B^\pm \rightarrow VV$ decays*, Nucl. Phys. B **428** (1994) 77 [arXiv:hep-ph/9402227].
- [31] C. W. Bauer, S. Fleming and M. E. Luke, *Summing Sudakov logarithms in $BBX_s\gamma$ in effective field theory*, Phys. Rev. D **63** (2000) 014006 [arXiv:hep-ph/0005275]; S. Fleming, *Soft Collinear Effective Theory*, AIP Conf. Proc. **842** (2006) 923-928 [arXiv:hep-ph/0601257].
- [32] M. Gronau and D. London, *Isospin analysis of CP asymmetries in B decays*, Phys. Rev. Lett. **65** (1990) 3381.
- [33] M. Pivk and F.R. Le Diberder, *Isospin constraints from/on $B \rightarrow \pi\pi$* , Eur. Phys. J. C **39** (2005) 397 [arXiv:hep-ph/0406263v1].
- [34] B. Aubert *et al.* [BaBar collaboration], *Limit on the $B^0 \rightarrow \rho^0\rho^0$ branching fraction and implications for the CKM angle alpha*, Phys. Rev. Lett. **94** (2005) 131801.
- [35] B. Aubert *et al.* [BaBar collaboration], *Observation of the decay $B^0 \rightarrow \rho^+\rho^-$ and measurement of the branching fraction and polarization*, Phys. Rev. D **69** (2004) 031102.
- [36] A.Snyder and H. Quinn, *Measuring CP asymmetry in $B \rightarrow \rho\pi$ decays without ambiguities*, Phys. Rev. D **48** (1993) 2139.
- [37] R. H. Dalitz, *On the analysis of τ -meson data and the nature of the τ -meson*, Phil. Mag. **44** (1953) 1068; Kopp *et al.* [CLEO collaboration], *Dalitz analysis of the decay $D^0 \rightarrow K^-\pi^+\pi^0$* , Phys. Rev. D **63** (2001) 092001.
- [38] H. Lipkin, Y. Nir, A.Snyder and H. Quinn, *Penguin trapping with isospin analysis and CP asymmetries in B decays*, Phys. Rev. D **44** (1991) 1454.
- [39] J.P. Lees *et al.* [BaBar collaboration], *Measurement of CP-violating asymmetries in $B^0 \rightarrow (\rho\pi)^0$ using a time-dependent Dalitz plot analysis*, BABAR-PUB-12-026 (2013) [arXiv:1304.3503].
- [40] A. Kusaka *et al.* [Belle collaboration], *Measurements of CP asymmetries and branching fractions in a time-dependent Dalitz analysis of $B^0 \rightarrow (\rho\pi)^0$ and a constraint on the quark mixing angle ϕ_2* , Phys. Rev. D **77** (2008) 072001 [arXiv:0710.4974].
- [41] P. Chang, *et al.* [Belle collaboration], *Observation of the decays $B^0 \rightarrow K^+\pi^-\pi^0$ and $B^0 \rightarrow \rho^-K^+$* , Phys. Lett. B **599** (2004) 148 [arXiv:hep-ex/0406075v1].

- [42] M. Ciuchini, M. Pierini and L. Silvestrini, *New bounds on the Cabibbo-Kobayashi-Maskawa matrix from $B \rightarrow K\pi\pi$ Dalitz plot analyses*, Phys.Rev. D **74** (2006) 051301 [hep-ph/0601233v4].
- [43] L. A. Pérez Pérez, *Time-dependent amplitude analysis of $B^0 \rightarrow K_S^0 \pi^+ \pi^-$ decays with the BaBar experiment and constraints on the CKM matrix using the $B \rightarrow K^* \pi$ and $B \rightarrow \rho K$ modes*, document présenté pour obtenir le grade de docteur d'université, Université Paris Diderot - Paris VII, Paris (2008).
- [44] I. Bediaga, G. Guerrier and J. Miranda, *CKM γ phase from $B \rightarrow K\pi\pi$* , 4th International Workshop on the CKM Unitarity Triangle, 2006 [arXiv:hep-ph/0703131].
- [45] G. Buchalla, J. Buras and E. Lautenbacher, *Weak Decays Beyond Leading Logarithms*, Rev. Mod. Phys. **68** (1996) 1125 [hep-ph/9512380v1].
- [46] B. Aubert *et al.* [BaBar collaboration], *Amplitude analysis of $B^0 \rightarrow K^+ \pi^- \pi^0$ and evidence of direct CP violation in $B \rightarrow K^* \pi$ decays*, Phys. Rev. D **83** (2011) 112010 [arXiv:1105.0125v1].
- [47] M. Ciuchini, M. Pierini and L. Silvestrini, *Hunting the CKM weak phase with time-integrated Dalitz analyses of $B_s \rightarrow K\pi\pi$ decays*, Phys. Lett. B **645** (2007) 201 [hep-ph/0602207v3].
- [48] J. Beringer *et al.* [Particle Data Group], *Review of particle physics*, Phys. Rev. D **86** (2012) 010001, section “Production and decay of b-Flavored hadrons”.
- [49] A. Ali, G. Kramer *et al.*, *Charmless non-leptonic B_s decays to PP , PV , and VV final states in the perturbative QCD approach*, Phys. Rev. D **76** (2007) 074018 [arXiv:hep-ph/0703162v2].
- [50] LHCb collaboration, *Branching fraction measurements of $B_{d,s}^0$ decays to $K_S^0 h^\pm h'^\pm$ final states, including first observation of $B_s^0 \rightarrow K_S^0 K^\pm \pi^\pm$* , 36th International Conference on High Energy Physics, LHCb-CONF-2012-023 (2012); *The quest for $B_{d,s}^0$ decays to $K_S^0 h^\pm h'^\pm$ at LHCb*, LHCb-ANA-2012-026 (2012).
- [51] X. Li and Y. Yang, *Reexamining charmless $B \rightarrow PV$ decays in the QCD factorization approach*, Phys.Rev. D **73** (2006) 114027 [arXiv:hep-ph/0602224v3].
- [52] M. Beneke and M. Neubert, *QCD factorization for $B \rightarrow PP$ and $B \rightarrow PV$ decays*, Nucl. Phys. B **675** (2003) 333 [arXiv:hep-ph/0308039v2].
- [53] H.Y. Cheng, *Vector dominance effects in weak radiative decays of B mesons*, Phys. Rev. D **51** (1995) 6228 [arXiv:hep-ph/9411330v1].

-
- [54] B. Aubert *et al.* [BaBar collaboration], *Measurements of branching fractions for $B^+ \rightarrow \rho^+ \gamma$, $B^0 \rightarrow \rho^0 \gamma$, and $B^0 \rightarrow \omega \gamma$* , Phys. Rev. D **78** (2008) 112001.
- [55] N. Taniguchi *et al.* [Belle collaboration], *Measurement of Branching Fractions, Isospin, and CP-Violating Asymmetries for Exclusive $b \rightarrow d \gamma$ Modes*, Phys. Rev. Lett. **101** (2008) 111801.
- [56] R. Aaij *et al.* [LHCb collaboration], *Measurement of the ratio of branching fractions $\mathcal{B}(B^0 \rightarrow K^{*0} \gamma)/\mathcal{B}(B_s^0 \rightarrow \phi \gamma)$* , Phys. Rev. D **85** (2012) 112013 [arXiv:1202.6267].
- [57] B. Aubert *et al.* [BaBar collaboration], *Search For T, CP, and CPT Violation in $B^0 - \bar{B}^0$ mixing with inclusive dilepton events*, Phys. Rev. Lett. **96** (2006) 251802.
- [58] E. Nakano *et al.* [Belle collaboration], *Charge asymmetry of same-sign dileptons in $B^0 - \bar{B}^0$ mixing*, Phys. Rev. D **73** (2006) 112002.
- [59] L. Evans and P. Bryant, *LHC Machine*, J. Instrum. **3** (2008) S08001.
- [60] G. Aad *et al.* [ATLAS collaboration], *The ATLAS Experiment at the CERN Large Hadron Collider*, J. Instrum. **3** (2008) S08003.
- [61] R. Adolphi *et al.* [CMS collaboration], *The CMS experiment at the CERN LHC. The Compact Muon Solenoid experiment*, J. Instrum. **3** (2008) S08004.
- [62] K. Aamodt *et al.* [ALICE collaboration], *The ALICE experiment at the CERN LHC. A Large Ion Collider Experiment*, J. Instrum. **3** (2008) S08002.
- [63] A. Alves *et al.* [LHCb collaboration], *The LHCb Detector at the LHC*, J. Instrum. **3** (2008) S08005.
- [64] J. Koutchouk and G. Sterbini, *An Early Beam Separation Scheme for the LHC Luminosity Upgrade*, LHC-PROJECT-Report-972 (2006).
- [65] LHCb computing project, *LHCb Computing Resource usage in 2011*, LHCb-PUB-2012-003 (2012).
- [66] LHCb computing project, *LHCb Computing Resource usage in 2012(I)*, LHCb-PUB-2012-013 (2012).
- [67] S. Viret *et al.*, *Alignment procedure of the LHCb vertex detector*, Nucl. Inst. and Meth. in Phys. Res. A **596** (2008) 157.
- [68] P. Rodriguez Perez, *The LHCb VERTEX LOCATOR performance and VERTEX LOCATOR upgrade*, 14th International workshop on radiation imaging detectors (2012).

-
- [69] T. Latham, *Performance of the LHCb Vertex Locator*, International Conference on Technology and Instrumentation in Particle Physics (2011).
- [70] C. Salzmann and J. Tilburg, *TT detector description and implementation of the survey measurements*, LHCb-2008-061 (2008).
- [71] J. Tilburg, *Studies of the Silicon Tracker resolution using data*, LHCb-PUB-2010-016 (2010).
- [72] L. Nicolas and M. Needham, *Alignment of the Inner Tracker Stations Using First Data*, CERN-LHCb-PUB-2009-012 (2009).
- [73] LHCb collaboration, *LHCb Outer Tracker Technical Design Report*, CERN-LHCC-2001-024 (2001).
- [74] A. Jaeger *et al.*, *Measurement of the track finding efficiency*, LHCb-PUB-2011-025 (2011).
- [75] T. Ypsilantis and J. Seguinot, *Theory of ring imaging Cherenkov counters*, Nucl. Instrum. Meth. A **343** (1994) 30.
- [76] LHCb collaboration, *LHCb calorimeters Technical Design Report*, CERN-LHCC-2000-036 (2000).
- [77] S. Monteil, *Mesures de precision electrofaibles*, Habilitation à diriger des recherches, Université Blaise Pascal, HDR 280 (2010).
- [78] LHCb collaboration, *LHCb Muon System Technical Design Report*, CERN-LHCC-2001-010 (2001).
- [79] LHCb collaboration, *Second Addendum to the Muon System Technical Design Report*, CERN-LHCC 2005-012 (2005).
- [80] L. Gruber and W. Riegler, *Time resolution limits of the MWPCs for the LHCb muon system*, Nucl. Inst. and Meth. in Phys. Res. A **632** (2011) 69.
- [81] R. Aaij *et al.* [LHCb collaboration], *Absolute luminosity measurements with the LHCb detector at the LHC*, J. Instrum. **7** (2012) P01010 [LHCb-PAPER-2011-015].
- [82] LHCb collaboration, *Measurement of J/ψ production in pp collisions at $\sqrt{s}=7$ TeV*, LHCb-PUB-2011-003 (2011).
- [83] M. Williams *et al.*, *The LHCb Topological Lines*, LHCb-PUB-2011-002 (2011).

- [84] H. Yang, B. Roe and J. Zhu, *Studies of boosted decision trees for MiniBooNE particle identification*, Nucl. Inst. and Meth. in Phys. Res. A **555** (2005) 370 [arXiv:physics/0508045].
- [85] M. Cattaneo *et al.*, *Status of the GAUDI event-processing framework*, Proc. of CHEP (2001); G. Barrand *et al.*, *GAUDI - A software architecture and framework for building LHCb data processing applications*, Proc. of CHEP (2000).
- [86] I. Belyaev *et al.*, *Handling of the generation of primary events in Gauss, the LHCb simulation framework*, Nuclear Science Symposium Conference Record (NSS/MIC) 325 IEEE (2010) 1155.
- [87] T. Sjöstrand, S. Mrenna and P. Skands, *PYTHIA 6.4 physics and manual*, JHEP 05 322 (2006) 026 [arXiv:hep-ph/0603175].
- [88] D. J. Lange, *The EvtGen particle decay simulation package*, Nucl. Instrum. Meth. A **462** (2001) 152.
- [89] P. Golonka and Z. Was, *PHOTOS Monte Carlo: a precision tool for QED corrections in Z and W decays*, Eur. Phys. J. C **45** (2006) 97 [arXiv:hep-ph/0506026].
- [90] J. Allison *et al.* [GEANT4 collaboration], *Geant4 developments and applications*, IEEE Trans. Nucl. Sci. **53** (2006) 270; S. Agostinelli *et al.* [GEANT4 collaboration], *GEANT4: A simulation toolkit*, Nucl. Instrum. Meth. A **506** (2003) 250.
- [91] M. Cattaneo, *The Boole project*, <http://lhcb-release-area.web.cern.ch/LHCb-release-area/DOC/boole/> (2012).
- [92] LHCb collaboration, *The Moore project*, <http://lhcb-release-area.web.cern.ch/LHCb-release-area/DOC/moore/> (2012).
- [93] M. Cattaneo *et al.* *Brunel LHCb Reconstruction Program: User Guide*, (2001).
- [94] P. Koppenburg and L. Fernández, *Da Vinci for Busy People*, LHCb Note 2005-016 (2005); P. Koppenburg, *The DAVINCI project*, <http://lhcb-release-area.web.cern.ch/LHCb-release-area/DOC/davinci/>
- [95] W. Herr and B. Muratori. *Concept of luminosity*, CAS - CERN Accelerator School: Intermediate Course on Accelerator Physics (2003) 361.
- [96] LHCb collaboration, *The beam-gas method for luminosity measurement at LHCb*, Rencontres de Moriond EW, arXiv:1005.4398v1 (2010)
- [97] A. Powell, *Particle ID at LHCb*, 35th International Conference on High Energy Physics (ICHEP 2010), Paris, France, 2010.

- [98] LHCb collaboration, *Prompt charm production in pp collisions at $\sqrt{s} = 7$ TeV*, 6th International Workshop on the CKM Unitarity Triangle, LHCb-CONF-2010-013 (2010).
- [99] M. Adinolfi, R. Aglieri *et al.*, *Performance of the LHCb RICH detector at the LHC*, CERN-LHCb-DP-2012-003 (2012).
- [100] O. Deschamps *et al.*, *Photon and neutral pion reconstruction*, LHCb 2003-091 (2003).
- [101] T. Skwarnicki, *A study of the radiative cascade transitions between the Upsilon-prime and Upsilon resonances*, PhD thesis, Cracow Institute of Nuclear Physics, 1986, DESY-F31-86-02.
- [102] R. Aaij *et al.* [LHCb collaboration], *Evidence for CP Violation in Time-Integrated $D^0 \rightarrow h^- h^+$ Decay Rates*, Phys. Rev. Lett. **108** (2012) 111602 [arXiv:1112.0938v2].
- [103] J. Brehmer, J. Albrecht and P. Seyfert, *Ghost probability: an efficient tool to remove background tracks*, LHCb-INT-2012-025 (2012).
- [104] G. Cowan, *Topics in statistical data analysis for high-energy physics*, Lectures given at the 2009 European School of High-Energy Physics (2009), CERN-2010-002 (2010) 197 [arXiv:1012.3589v1].
- [105] <http://tmva.sourceforge.net/>
- [106] <http://root.cern.ch/drupal/>
- [107] <http://www.dtrek.com/mlfn.htm>
- [108] LHCb collaboration, *Measurement of the ratio of branching fractions $\mathcal{B}(B^0 \rightarrow K^{*0} \gamma) / \mathcal{B}(B_s^0 \rightarrow \phi \gamma)$ and direct CP violation in $B^0 \rightarrow K^{*0} \gamma$* , LHCb-ANA-2012-014 (2012).
- [109] M. Pivk and F. R. Le Diberder, *sPlot: a statistical tool to unfold data distributions*, Nucl. Instrum. Meth. A **555** (2005) 356 [arXiv:physics/0402083].
- [110] R. Aaij *et al.* [LHCb collaboration], *Measurement $\sigma(pp \rightarrow b\bar{b}X)$ at $\sqrt{s} = 7$ TeV in the forward region*, Phys. Lett. B **694** (2010) 209 [hep-ex arXiv:1009.2731].
- [111] LHCb collaboration, *Measurement of the fragmentation fraction ratio f_s/f_d and its dependence on B meson kinematics*, LHCb-PAPER-2012-037 (2012).
- [112] R. Aaij *et al.* [LHCb collaboration], *Measurement of b hadron production fractions in 7 TeV pp collisions*, Phys. Rev. D **85** (2012) 032008.
- [113] V. Gligorov, *A single track HLT1 trigger*, LHCb-PUB-2011-003 (2011).

-
- [114] R.A. Fisher, *The use of multiple measurements in taxonomic problems*, Annals of Eugenics **7** (1936) 179.
- [115] H. Albrecht *et al.* [ARGUS collaboration], *Observation of charmless B meson decays*, Phys. Lett. B **209** (1988) 1
- [116] G. Punzi, *Sensistivity of Searches for New Signals and Its Optimization*, Proceedings from Phystat (2003) [arXiv:physics/0308063]